Plastic shrinkage cracking and other evaporation-related impairments in 3D printed and cast concrete

by

Gerrit Marius Moelich

Dissertation presented for the degree of Doctor of Philosophy in Engineering in the Faculty of Engineering at Stellenbosch University

Supervisor: Prof. Riaan Combrinck

December 2021

Declaration

By submitting this dissertation electronically, I declare that the entirety of the work contained therein is my own, original work, that I am the sole author thereof (save to the extent explicitly otherwise stated), that reproduction and publication thereof by Stellenbosch University will not infringe any third party rights and that I have not previously in its entirety or in part submitted it for obtaining any qualification.

Date: December 2021

Abstract

Plastic shrinkage cracking and other evaporation-related impairments in 3D printed and cast concrete

Gerrit Marius Moelich

Department of Civil Engineering,
Stellenbosch University,
Private Bag X1, Matieland 7602, South Africa.

Dissertation: PhD (Civil Engineering)

December 2021

The Fourth Industrial Revolution (Industry 4.0) aims to make manufacturing more agile, flexible and responsive to the customer through intelligent and autonomous solutions. One Industry 4.0 technology that shows great potential for the construction industry is 3D concrete printing as it eliminates the need for formwork and is so-called formfree. Early estimations show the formfree attribute can reduce construction costs and time by 28% and 50%, respectively. Furthermore, 3D printing concrete (3DPC) increases design freedom, produces less waste material and improves workplace safety.

The advantages of 3DPC's formfree attribute are noteworthy. However, the absence of formwork leaves 3DPC vulnerable to rapid pore water evaporation immediately after extrusion, causing plastic shrinkage, plastic shrinkage cracking (PSC) and an impaired long-term durability and mechanical performance. On-site printing in dry and windy climates, common in Southern Africa, Australia, Central America and the Middle East, is of concern since the evaporation rates tend to be more severe. However, for 3DPC, the more benign evaporation rate of indoor climates cannot be precluded from evaporation-related damage.

This research aims to improve the resilience of concrete printed or cast in adverse climatic conditions by quantifying, understanding, modelling and mitigating the consequences of rapid early age pore water evaporation. Ultimately, this study contributed several novel findings that amounted to seven journal publications.

First, a method was proposed for using weather data to characterise the expected on-site evaporation rate for a specific location. Active PSC mitigation

measures were recommended based on the result. Thereafter, the effect of solar radiation exposure on the accuracy of the available evaporation estimation equations and severity of PSC were evaluated. The results showed that high levels of solar radiation exposure significantly increase the severity of PSC, and the Jansen-Haise model was recommended to estimate the pore water evaporation rate in these conditions.

A test method was proposed to induce and measure plastic shrinkage and early age cracking in 3DPC. 3DPC exhibited severe plastic shrinkage that started immediately after extrusion. Early age cracks appeared and increased in severity within the first one to two hours at a moderate evaporation rate. This behaviour was attributed to the low bleeding rate, absence of coarse aggregates, the high quantities of fines, and high surface area to volume ratio of 3DPC.

It is estimated that the risk of PSC in 3DPC is three times as high as cast concrete. Decreasing the magnitude or delaying the evaporation rate decreased the plastic shrinkage and reduced the risk of cracking. Based on this result, an empirical model for the risk of PSC was proposed for 3DPC. To minimise the risk, the evaporation rate should be reduced to below 0.1 $kg/m^2/h$ until the final setting time. Evidently, 3DPC is also vulnerable to PSC at lower evaporation rates, typical in indoor climates.

The efficacy of several mitigation measures for early age cracking in 3DPC was evaluated with the proposed test method. At a low dosage, short polypropylene microfibres prevented (100% reduction) the formation of PSC without adversely affecting the printability or buildability. Alternatively, increasing the structuration rate, with additives, can reduce early age cracking while improving buildability. Superabsorbent polymers also improved buildability by increasing the stiffening rate through continued pore water absorption.

Discontinuities in the transfer of plastic shrinkage from one layer to the next were noticed and coined as interlayer slip. Interlayer slip and microcracking, caused by pore water evaporation from a restrained 3DPC specimen, did not reduce the mechanical and durability performance significantly. Therefore, visibly uncracked 3DPC shows satisfactory durability performance for a short pass time.

Finally, internal curing, with superabsorbent polymers, increased the long-term flexural strength (19%) and interlayer adhesion (10%) of printed concrete by promoting the hydration of anhydrous cementitious particles near the interlayer. Evaporation of the interlayer moisture has the direct opposite effect. An analytical model for the interlayer adhesion was proposed based on the amount of interlayer surface moisture which was estimated from the initial surface moisture, the pass time, bleeding rate and evaporation rate. The model was validated for an interlayer bond strength reduction from 30% to 50%. However, applying the model to the experimental results of other researchers suggest that this range is extendable.

Uittreksel

Plastiese krimpkrake en ander verdampingsverwante skade aan gietbeton en beton 3D-drukwerk

("Plastic shrinkage cracking and other evaporation-related impairments in 3D printed and cast concrete")

Gerrit Marius Moelich

Departement Siviele Ingenieurswese,
Universiteit van Stellenbosch,
Privaatsak X1, Matieland 7602, Suid Afrika.

Proefskrif: PhD (Siviel Ingenieurswese)

Desember 2021

Die Vierde Industriële Rewolusie beoog om vervaardiging meer buigsaam en reaktief tot die behoeftes van die kliënt te maak deur middel van intelligente en outonome oplossings. 3D-drukwerk met beton (3DDB) toon groot potensiaal vir die konstruksiebedryf aangesien dit vormwerk vry is. Vroeë beramings toon dat 3DDB die konstruksiekoste en konstruksietyd kan verlaag met tenminste 54% en 75%. Verder verhoog 3DDB ontwerpvryheid, produseer minder afvalmateriaal en verbeter werkplek veiligheid.

Die voordele van vormvrye beton is opmerklik, maar die afwesigheid van vormwerk stel 3DDB bloot aan poriewaterverdamping onmiddellik na plasing wat kan lei tot aansienlike plastiese krimp, ernstige plastiese krimpkrake en 'n vermindering in die langtermyn duursaamheid en sterkte. Die verdamping van poriewater is veral 'n bron van kommer vir terrein drukwerk in droë en winderige klimaatstoestande; algemeen in Suiderlike Afrika, Australië, Sentraal-Amerika en die Midde-Ooste. 3DDB is egter ook kwesbaar vir plastiese krimpkrake in meer gematigde klimaatstoestande. Die doel van hierdie navorsing is om die weerstand van 3DDB geplaas in ongunstige klimaatstoestande te verbeter. Die nadelige gevolge a.g.v. vroeë ouderdom poriewater verdaping word bestudeer, gekwantifiseer, gemodeleer en versagmaatreëls word aanbeveel.

'n Metode word voorgestel vir die gebruik van liggingspesifieke weerdata om die verwagte verdampingstempo te karakteriseer. Aktiewe plastiese krimpingsversagmaatreëls word aanbeveel op grond van die resultate. Die effek van sonstraling blootstelling op die akkuraatheid van die beskikbare verdampingsberamingsvergelykings word geëvalueer en die Jansen-Haise model word aanbeveel vir toestande met hoë sonstraling. Die erns van plastiese krimpkrake in gegote beton word ook geëvalueer en die resultate toon dat sonbestraling plastiese krake aansienlik verhoog. 3DDB toon ernstige plastiese krimping, selfs teen 'n lae tot matige verdampingstempo. 'n Toetsmetode word voorgestel om plastiese krimp en krake in vroeë ouderdom 3DDB te veroorsaak en te meet. 'n Groot hoeveelheid en hoë tempo plastiese krimping vind plaas onmiddellik na plasing met vroeë ouderdom krake wat verskyn binne die eerste een tot twee uur van verdamping. Hierdie gedrag word toegeskryf aan die lae bloeitempo, die afwesigheid van growwe aggregaat, groot hoeveelhede fynstof en die hoë oppervlak-tot-volume-verhouding van 3DDB. Daar word beraam dat die risiko van plastiese krimpkrake in 3DDB tot drie keer so hoog is soos gietbeton. As die verdampingstempo verlaag of vertraag word verminder die plastiese kraakrisiko. Op grond van hierdie resultate word 'n empiriese model voorgestel vir die risiko van plastiese krimpkrake in 3DDB.

Die doeltreffendheid van verskillende versagtingsmaatreëls vir plastiese krimpkrake in 3DDB word geëvalueer met die voorgestelde toetsmetode. 'n Lae dosis polypropyleen vesels voorkom plastiese krimpkrake sonder om die drukbaarheid of boubaarheid nadelig te beïnvloed. Die verhoging van die struktureringstempo, m.b.v. bymiddels, is voordelig in terme van kraakversagting sowel as boubaarheid.

Diskontinuïteite in die oordrag van plastiese krimping van een laag na die volgende is opgemerk en die verskynsel is benoem tussenlaagglip. Inklemming van die 3DDB monster onder 'n verdampingslas veroorsaak beide tussenlaagglip en mikrokrake. Die verdampingsverwante skade het egter nie die meganiese en duursaamheidsverrigting aansienlik verminder nie. Die gevolgtrekking is dat 3DDB met 'n kort laagtyd goeie duursaamheid toon.

Interne kuring, met superabsorberende polimere, het die langtermyn buigsterkte en tussenlaaghegting van 3DDB verhoog deur die hidrasie van sement partikels naby die tussenlaag te bevorder. Verdamping van die tussenlaagvog het die teenoorgestelde effek. 'n Analitiese model vir die tussenlaaghegting word voorgestel gebaseer op die hoeveelheid tussenlaagvog teenwoordig wanneer die daaropvolgende filament geplaas word. Die oppervlakvog word bereken vanaf die aanvanklike waarde, laagtyd, bloeitempo en verdampingstempo. Die model kan die tussenlaaghegting vermindering akkuraat voorspel tussen 30% en 50%. Hierdie perke sal waarskynlik in toekomstige navorsing uitgebrei word.

Acknowledgements

I want to express my sincere gratitude to the following people and organisations:

- My supervisor, Riaan Combrinck, for his support and guidance during my studies. Thank you for trusting in my abilities, giving me the freedom to pursue my curiosity and facilitating my growth as a researcher and person.
- Jacques Kruger, for his valuable insight in 3DPC, interesting ideas and intellectually challenging conversations. Thank you for all the encouragement and advice.
- My fellow postgraduate students, for the discussions, the suggestions and support during the long hours in the laboratory.
- The laboratory and workshop staff, for their assistance with the experimental work.
- The Wilhelm Frank Trust, for their financial support and for showing interest in my research.
- The products provided by Chryso South Africa, Pretoria Portland Cement (PPC) and SNF Floerger France are much appreciated.
- My family, for their unwavering support and love. Thank you for teaching me perseverance, stimulating curiosity, and always showing interest in my research.
- My friends, for seeking adventures with me and for keeping me motivated.
- My partner, Petra Marais, for her love and support. Thank you for challenging me, being a hard-working office mate, listing to my stories, cooking amazing food, encouraging me to pursue my hobbies and providing much-needed distraction at times.

Contents

List of Figures

List of Tables

List of Abbreviations and Symbols

Abbreviations

3DPC	3D printed concrete/3D concrete printing
AFH	Al-Fadhala-Hover evaporation estimation equation
ALT	Atlantis
ANOVA	Analysis of variance
B-CSA	Calcium sulfoaluminate-belite
BREB	Bowen-ratio energy-budget
BW	Beaufort-Wes
CA	Curing agent
CCI	Chloride Conductivity Index
CEM	Cement
CR	Crack risk
CS	Compressive strength
CSA	Calcium sulfoaluminate cement
CSH	Calcium-Silicate-Hydrate
CS_R	Reduction in compressive strength
CT	Cape Town
CV/CoV	Coefficient of variation
DIC	Digital image correlation
DHI	Diffused horizontal irradiation
DNI	Direct normal irradiation
FORM	First Order Reliability Method
FS	Flexural strength
GHI	Global horizontal irradiation
HPCM	High-performance concrete mixes
IA/S_r	Lack of interlayer adhesion

IBS	Interlayer bond strength
KMU	Kohler-Menzel-Uno evaporation estimation equation
LVDT	Linear variable differential transformer
RET	Retentive SAP
OPI	Oxygen Permeability Index
PoE	Probability of exceedance
RS	Restrained shrinkage
PSC	Plastic shrinkage cracking
SAP	Superabsorbent polymers
SF	Silica fume
SP	Superplasticizer
SR	Self-releasing SAP
SRA	Shrinkage reducing admixture
TER	Tolerable evaporation rate
Th	Binary threshold value
ToL	Top of layer
w/c	Water to cement ratio
w/b	Water to binder ratio

Symbols

λ_t	Thixotropy index
A_{thix}	Structuration rate
B_{pt}	Amount of bleeding at the pass time
c_c	Cloud cover
ΔL	Horizontal change in length
E_w/ER/ER_{pt}	Evaporation rate
L	Gauge length
$L\#$	Layer number from base
RH	Relative humidity
R_{thix}	Re-flocculation
pt	Pass time
SM_f	Surface moisture at placement of the overlayer
SM_i	Initial surface moisture
T_a	Ambient temperature

T_c	Concrete placement temperature
Th	Binary threshold value
V	Wind speed

Chapter 1

Introduction

1.1 Introduction

1.1.1 Context

Globally, the productivity of the construction industry has stagnated [1]. The industry has experienced minimal innovation in the past few decades and is still heavily reliant on low-skilled labour. The ageing population and the dwindling interest of the youth are resulting in labour skill shortages [2]. Construction remains a hazardous work environment, costing the lives of many each year [3].

Adoption of the Fourth Industrial Revolution (Industry 4.0) promises a paradigm shift in the construction industry and provides solutions to some of these challenges. In general, Industry 4.0 aims to make manufacturing more agile, flexible and responsive to the customer with intelligent and autonomous solutions such as 3D printing, the Internet of Things, autonomous vehicles, nanotechnologies, cyber-physical systems, cloud computing, artificial intelligence, machine learning, deep learning and big data [4–6].

The Global South, and Africa in particular, is facing a challenge of a different nature. As Prof Marwala explains in his book "Closing the Gap: The Fourth Industrial Revolution in Africa [4]", in the past three industrial revolutions the Global South has lagged in adopting new technologies provided by industrial revolutions and, as a result, has not reaped the benefits. Yet again, the Global South is falling behind in Industry 4.0, even though it is here in Africa and the broader Global South, where innovation is needed most of all. The levels of unemployment and poverty remain alarming, and the food, water and energy insecurity persists. In South Africa alone, it is estimated that 13.5% of households (more than 8.1 million people) live in informal housing [7]. This is particularly concerning considering the rise in climate change-related natural disasters and increasing rate of urbanisation.

1.1.2 Background

In 1986, Charles Hull was issued a patent for his stereolithography apparatus. The system used a computer-controlled concentrated ultraviolet light beam to solidify a liquid photopolymer in a layer-by-layer fashion to build a three-dimensional object. The process was first used in prototyping and appropriately called rapid prototyping, but with advancements, the focus shifted to mass production, and the umbrella term additive manufacturing gained popularity. The term 3D printing was popularised by mainstream media because some additive manufacturing technique's followed a similar process as conventional 2D inkjet printing. Ultimately, rapid prototyping, additive manufacturing and 3D printing rely on the same principle—adding material in a layer-by-layer fashion to transform a digital model into an actual object [8–10]. This new technology has been identified as one of the leading technologies of Industry 4.0.

Pegna [11] was the first to use the additive manufacturing process with a cementitious material. In a formwork-free process, sand and Portland cement were deposited in thin subsequent layers, and steam was used to cure the element. Khoshnevis [12] suggested extruding a ceramic paste with the additive manufacturing process and filling the cavity with concrete to eliminate the need for formwork. Thereafter, Buswell et al. [2] illustrated the value of this formfree concrete for large-scale construction. These studies and recent advancements in concrete material science [13, 14] laid the foundation of 3D concrete printing. Today, 3D concrete printing refers to the additive manufacturing process with extruded cementitious materials for structural or architectural elements. This technology provides many cost, environmental and safety benefits in construction.

Cast concrete relies on formwork for support under gravitational forces in the fresh state. For reinforced concrete structures, it is estimated that the formwork amounts to between 28% and 54% of the total cost and consumes between 50% and 75% of the construction time [15, 16]. 3D printing concrete does not require formwork, and this reduces the aforementioned construction cost and time as well as the waste material. The manufacturing process allows for more design freedom and complex geometries without any additional financial or environmental cost [17, 18]. In the long-term, easily customisable structures can put the end-user at the centre of the design process. Additionally, geometric flexibility allows for topology-optimisation, meaning that the extruded material is placed only where it bears the load; the so-called "form follows force" principle [19, 20]. This results in leaner structural elements that requires less material. Ultimately, it is the beauty of these elements that capture the imagination of architects, engineers and the public alike.

In the past decade, an increasing number of international companies have started using additive manufacturing for large-scale construction. More and more

applications are coming to light and the economic, environmental and aesthetic value is slowly being realised.

Although the general materials science aspects of cementitious material are still valid for printable concrete, many challenges still remain. Several review papers have been published, but a relatively low number of experimental studies have been conducted. Specifically, the durability (defined as the ability to withstand wear, damage, and adverse conditions) of 3D printed concrete has not received much attention. This dissertation aims to address the lacuna by conducting experimental research and providing a feasible solution and/or a fundamental understanding. Occasionally, a tone of criticism against the technology may be perceived but it is by no means the intent of the author. Rather, this dissertation attempts to highlight areas where improvement and a better understanding are required.

1.2 Problem statement

The absence of formwork leaves 3D printed concrete vulnerable to rapid pore water evaporation immediately after extrusion. Covering the concrete element is the conventional prevention method but is only feasible once the element has gained adequate strength. Therefore, from extrusion to a concrete age of about 4 to 6 hours (initial setting time), the element is exposed to the environment's drying rate. Adverse environmental conditions can evaporate large amounts of concrete water during this period. This can have negative consequences for the aesthetics, durability and mechanical performance of the printed structure. More specifically, rapid and excessive early age pore water evaporation can cause plastic shrinkage and related cracking, reduce the degree of hydration, damage the concrete's microstructure and reduce the long-term bond strength between printed filaments.

1.3 Research significance

Early age cracks are aesthetically unpleasing and allow for the ingress of corrosive agents that reduce the concrete's durability. A reduction in the degree of hydration and drying-induced microstructural damage also impair the concrete's durability. Ultimately, durability indicates the structure's service life, and its integrity is essential in reducing CO^2 emissions, construction and maintenance costs and preventing premature structural collapse. Furthermore, modelling the bond strength is fundamental for the design of structural printed elements. Accurately doing so would optimise structural performance and reduce construction cost.

Addressing the problem of early age pore water evaporation is imperative for adopting 3D concrete printing on a large scale, especially for on-site printing in ad-

verse drying conditions. The problem is of particular concern in Southern Africa, Australia, Central America and the Middle East due to the harsh climatic conditions, but also in more benign, indoor climates. A solution is essential for the advancement of 3D concrete printing as a construction technique.

1.4 Research aim

This research aims to quantify, understand, model and mitigate the adverse consequences that arise due to rapid pore water evaporation from early age printed and cast concrete. Enforceable solutions should be proposed to improve the resilience of concrete printed and cast in adverse climatic conditions.

1.5 Objectives

The objectives, in methodological order, are:

1. Characterise the expected on-site evaporation rate.
2. Evaluate the accuracy of the available evaporation estimation equations and investigate the effect of solar radiation exposure on the severity of plastic shrinkage cracking (PSC) in cast concrete.
3. Develop a test method to study PSC in printed concrete.
4. Use the method to evaluate the efficacy of PSC mitigating measures in 3D printed concrete and recommend a feasible solution.
5. Develop a mathematical model for the risk of PSC in printed concrete.
6. Evaluate the durability of printed concrete exposed to severe early age drying.
7. Evaluate the effect of surface moisture evaporation on the interlayer bond strength of printed concrete.

1.6 Report structure

This dissertation is presented to obtain a PhD by publication with each content chapter being published or submitted to an academic journal.

- Chapter 1 aims to introduce the research topic and provides the context, background, problem statement, research significance and objectives.

- Chapter 2 provides background on the main topics discussed in this dissertation. A more technical literature review is provided in each of the subsequent chapters.

- Chapter 3 characterises the expected on-site evaporation rate through a novel weather data analysis method. Published as: **G.M. Moelich**, R. Combrinck, A weather data analysis method to mitigate and prevent plastic shrinkage cracking, Construction and Building Materials, vol. 253, August 2020. Online

- Chapter 4 investigates the accuracy of the available evaporation estimation equations for concrete exposed to solar radiation. The effect of solar radiation on the severity of plastic shrinkage cracking in cast concrete is also investigated. Published as: **G.M. Moelich**, J.E. van Zyl, N. Rabie, R. Combrinck, The influence of solar radiation on plastic shrinkage cracking in concrete, Cement and Concrete Composites, vol. 123, October 2021, 104182. Online

- Chapter 5 investigates the behaviour of plastic shrinkage cracking in printed concrete. A test method to induce and measure plastic shrinkage and related cracking in 3D printed concrete is proposed. Published as: **G.M. Moelich**, P.J. Kruger, R. Combrinck, Plastic shrinkage cracking in 3D printed concrete, Composites Part B: Engineering, vol. 200, November 2020. Online

- Chapter 6 quantifies the efficacy of available early age crack mitigation measures and recommends a feasible solution from printed concrete. Submitted to Cement and Concrete Research as: **G.M. Moelich**, P.J. Kruger, R. Combrinck, Mitigating early age cracking in 3D printed concrete using fibres, superabsorbent polymers, shrinkage reducing admixtures, B-CSA cement and curing measures.

- Chapter 7 studies the fundamental behaviour of plastic shrinkage cracking in printed concrete and models the risk thereof. An improved version of this chapter was submitted to Cement and Concrete Composites as: **G.M. Moelich**, P.J. Kruger, R. Combrinck, A plastic shrinkage cracking risk model for 3D printed concrete exposed to different environments.

- Chapter 8 investigates the effect of early age pore water evaporation on the durability of printed concrete. Published as: **G.M. Moelich**, P.J. Kruger, R. Combrinck, The effect of restrained early age shrinkage on the interlayer bond and durability of 3D printed concrete, Journal of Building Engineering, vol. 43, November 2021. Online

- Chapter 9 investigates the effect of interlayer surface moisture evaporation on the long-term mechanical strength of printed concrete. An analytical model is developed to predict the interlayer bond strength from the evaporation rate and superabsorbent polymers are used to improve performance. Published as: **G.M. Moelich**, P.J. Kruger, R. Combrinck, Modelling the interlayer bond strength of 3D printed concrete with surface moisture, Cement and Concrete Research, vol. 150, December 2021. Online
- Chapter 10 presents a conclusion and recommendations for future research.

Chapter 2

Background study

This chapter aims to provide a background on the main topics discussed in the dissertation. The terminology and mechanisms are addressed with engineers as the target audience. A more technical literature review is available in each chapter.

2.1 Concrete

2.1.1 Conventional cast concrete

Conventional concrete is a mixture of coarse (>4.75 mm) and fine (<4.75 mm) aggregates, water and cementitious binders. The latter constituent contains Portland cement, which reacts with water to bind the aggregates and harden the concrete in a chemical reaction called hydration. Portland cement is often supplemented with additions, inorganic powders with a similar particle size to improve the mix's properties, reduce cost or provide environmental benefits. The additions typically include fly ash, condensed silica fume and ground granulated blast furnace slag, while calcium sulfoaluminate cement (CSA) is classified as an alternative cement type. Additions containing active silica show pozzolanic behaviour, meaning that it contributes to developing the mechanical and durability properties of concrete, similar to Portland cement. For this reason, Portland cement with additions is referred to as a cementitious binder. Admixtures are often added during the mixing phase to improve the fresh, early age and hardened state properties. These include superplasticizer, viscosity modifying agent, fibres, shrinkage reducing admixtures (SRA) and superabsorbent polymers (SAP) [21].

For the first few hours after mixing, the concrete's fluidity remains fairly consistent, and any loss thereof can be partially recovered through agitation. This period is called the dormant period and is used for casting and vibrating. Once the hydration reaction starts, the stiffening occurs at a faster rate, and this gain in

stiffness is permanent and irrecoverable. The solidification of the mix is commonly measured with the initial and final setting times of the Vicat needle apparatus. Although somewhat arbitrary, the initial set is commonly regarded as the end of the handling and placement phase of the concrete. The final setting time is used to indicate the start of the mechanical strength development [21–23].

For the rest of this dissertation, the term fresh concrete is used to indicate that the concrete has not attained any irrecoverable stiffening. From placement until the final setting time, the term plastic concrete is used. The early age is used to define the first 24 h after placement. Hardened state or long-term is used to indicate a concrete age more than 28 days. Mortar is defined as a mixture between the fine aggregates, water and cementitious binders, while cement paste is just a mix of water and cementitious binders. Concrete water refers to the total amount of water added during the mixing phase, while pore water refers to the water inside the concrete element at a given time.

Since conventional concrete cannot sustain its own weight in the fresh state, formwork is used as a mould. Once the concrete gains adequate strength, the formwork is removed. Curing techniques are then applied to prevent water loss to the environment through evaporation, and additional water is supplied to promote a higher degree of hydration.

2.2 Rheology

Rheology is the study of the flow of matter, and is the building block of 3D concrete printing. It is widely accepted that fresh concrete shows Bingham material behaviour. The rheology can be used to determine the fresh state workability or the loss of fluidity in the plastic state. Workability is the ease at which concrete can be mixed, pumped and placed while remaining homogeneous (not segregating). The loss in fluidity, also referred to as the structuration, is a measure of the rate at which the mix stiffens [24, 23].

A rheology test provides a better alternative to the slump cone and Vicat needle tests commonly used to quantify the workability and structuration. Understanding the workings of a rheometer (instrument measuring rheology) is the best way to explain how to interpret the results and, ultimately, why the study of rheology is fundamental to 3D concrete printing [25, 26].

A rheometer measures the torque needed to rotate a vane in fresh concrete. Either the flow or stress growth test can be conducted. In a flow curve test, the torque is measured for the vane rotating at different speeds. The speed is plotted against the resulting torque, and a straight line is fitted. The intersection of the straight line with the vertical axis is the dynamic yield stress, where the slope is the plastic viscosity. In a stress growth test, the stress exerted on the material is

gradually increased until flow is initiated. This point is defined as the static yield stress. Therefore, the static yield stress is the stress required to initiate flow, and the dynamic yield stress is the minimum stress required to maintain flow. The plastic viscosity is a measure of the resistance to flow, with a high plastic viscosity indicating a high resistance to flow [27, 28].

2.3 3D concrete printed

The topic of concrete printing has a robotic and material aspect. The former aims to move a nozzle along a pre-defined path. The latter is the focus of this discussion.

2.3.1 Robotics of concrete printing

First, a 3D concrete element is designed in Computer-Aided Design software. The 3D model is then transformed into a toolpath in a digital process called slicing. The toolpath controls the movement of the printer nozzle, which determines the shape of the element. Different printing systems are used commercially, but the main types are a gantry, robotic arm or crane system [16, 19, 24].

2.3.2 Concrete printing process

The printing of a concrete element can be discussed based on the three main construction steps, namely: pumping, extrusion and building, as presented in Fig. 2.1. These steps determine the material requirements [29].

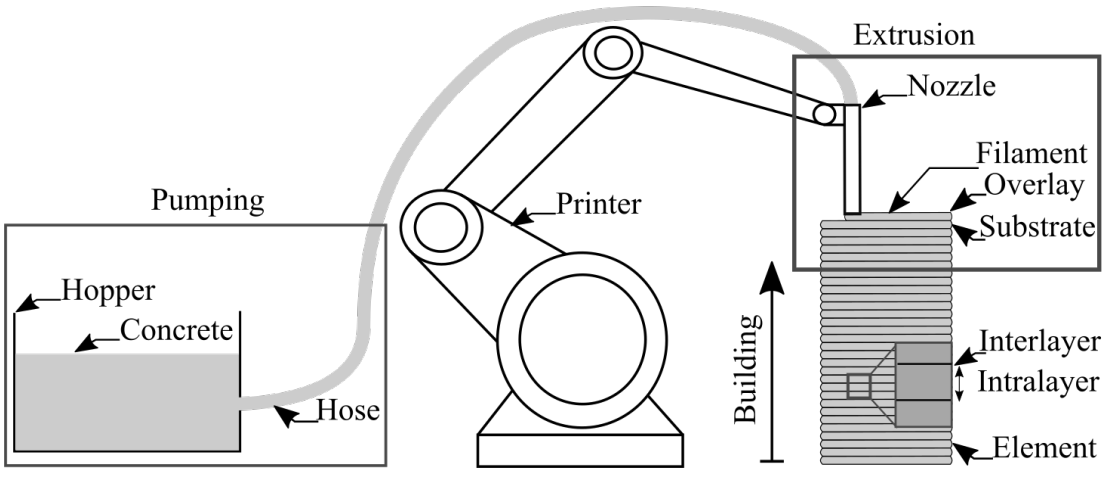

Figure 2.1: The three construction steps of concrete printing.

The concrete constituents can be mixed in a batch or continuous mixer. The latter is preferred since it allows for better control of the stiffening process and provides material on-demand. Once mixed, a continuously rotating screw forces the material into the hose. The ease with which the material can be pumped from the hopper to the nozzle, without segregating, is defined as pumpability. Pumpability is quantified by the dynamic yield stress and plastic viscosity for the specific transportation system (pump, hose and nozzle combination) used in printing. The dynamic yield stress should be low to avoid strain on the pump's motor, while the plastic viscosity should be adequate to resist segregation [14, 16, 30, 31].

In the hose, the material flow state can be classified as shear or plug flow. The flow state can be determined through a visual inspection and depends on the rheological properties of the mix as well as the transportation system. Generally, materials with a low static yield stress tend to undergo shear flow. In this case, admixtures are sometimes added to the nozzle to stiffen the material before extrusion. Plug flow occurs for higher static yield stress mixes and is accompanied by a lubrication layer. As the material is moved in the hose, the shear stress at the pipe wall forces the larger particles to the hose centre, a process called flow-induced particle migration. This leaves behind the rich cement paste, which forms the lubrication layer. Since shearing occurs at the hose wall, the bulk material remains unsheared to form the "plug". Ultimately, the lubrication layer reduces the pumping energy required [32, 29].

The material is extruded into the gap between the previous layer and the nozzle to form the filament. The change in flow direction bond the filament (overlay) to the previous layer (substrate) while the plastic viscosity and the flow rate determines the filament width. Shape retention is defined as the ability of the extruded material to form a filament with a desired cross-section in the gap between the nozzle and substrate under the gravitational forces of its self-weight. Extrudability is defined as the ability to place the filament with a constant cross-section, with minimal deformation or tearing. Extrudability is a function of the transportation system, the printing parameters and the material's rheology. Inconsistencies in the cross-section can occur when the flow rate is incompatible with the print speed for the material's plastic viscosity. Tearing occurs when the print speed (nozzle speed) is too high, or the flow rate is too low, for the material properties. Extrusion-induced tearing is also common in high-volume fibre mixes since the addition of fibres tend to increase the plastic viscosity [30, 24, 33].

Buildability is defined as the ability of the material to support the weight of consecutive filaments. It is quantified by the number of layers printed before structural failure at a defined printing speed and element geometry. The print speed determines the time between depositing the layers, referred to as the pass time.

During the pass time, the material stiffens. Therefore, if the print speed is decreased, the buildability increases. The structural failure mode can be classified as stability failure (elastic buckling) or materials failure (plastic yielding). The buildability is controlled by the static yield stress and its development (re-flocculation and structuration). In terms of buildability, the initial static yield stress and its development rate should be as high as possible [24, 34, 35].

Therefore, a high initial static yield stress and development rate are required for buildability, while a low dynamic yield stress is required for printability. Both requirements can be satisfied by using a thixotropic concrete mix, which gives the concrete the extraordinary ability to flow when it is agitated and retain shape when placed. The former satisfies the pumpability requirement while the latter satisfies the buildability [16, 36].

Agitation (e.g. pumped, vibrated) of a thixotropic mix breaks the intermolecular forces between particles, resulting in de-flocculation. This only occurs when the applied force is larger than the static yield stress. The mix flows at the lower dynamic yield stress in the de-flocculated state, allowing it to be pumped and placed. When the agitation stops, the particles re-orientate to the equilibrium position and regain the intermolecular bonds, a process known as re-flocculation. With time, the static yield stress increases due to re-flocculation and structuration. The former is a physical process, resulting in recoverable stiffening that provides buildability for short pass times. The latter occurs due to hydration and provides irrecoverable stiffening in the longer term and, ultimately, hardens the element [37–39].

Thixotropic concrete mixes typically contain a high amount of fines and often no coarse aggregates for a maximum particle packing density. Adding coarse aggregates can reduce the degree of thixotropy. Superplasticizer and viscosity modifying agents are often added to increase workability. Using low water to binder ratios in the high-performance to the ultra-high-performance range is also beneficial since, due to the high mechanical strength, less material is required, and this ultimately reduces costs [14, 16].

2.4 Plastic shrinkage cracking

In the early age, concrete undergoes unavoidable volume changes, which can lead to cracking in adverse circumstances. The main early age volume changing mechanisms are plastic settlement, plastic shrinkage, chemical shrinkage and thermal shrinkage. These mechanisms often occur simultaneously and can be difficult to decouple. In conventional cast concrete, plastic settlement typically occurs first, followed by plastic shrinkage and chemical shrinkage [40, 41].

2.4.1 Bleeding and plastic settlement

Bleeding is the process where the settlement of aggregates, under the gravitational force, displaces the mixing water to the surface of the concrete element to form a bleeding film. The resulting one-dimensional vertical volume reduction is called plastic settlement. The process stops when the concrete gains sufficient stiffness to prevent aggregate settlement. With time, the bleeding water is re-absorbed by the hydrating binders or evaporates into the environment. It is common for high-performance concrete mixes to exhibit minimal bleeding due to the low amount of mixing water and high fines content [22, 42–47].

2.4.2 Pore water evaporation

Evaporation is the process of transforming a molecule from a liquid to a gas. The process was first described mathematically with Dalton's Law which states that the evaporation is proportional to the wind speed and the saturation deficiency. The latter is defined as the difference in vapour pressure between the liquid and the environment. Dalton's Law has been used to estimate the evaporation rate of the bleeding film and the pore water by several researchers [48–52].

If the evaporation rate exceeds the bleeding rate, the bleeding film is depleted. This point is referred to as the drying time. Thereafter, the pore water can evaporate. For the first few hours after the drying time, the rate of pore water loss is almost equal to the evaporation load of the environment. With time, the rate of pore water evaporation decreases due to hydration, stiffening and desiccation of the concrete element [43, 53, 51, 54].

2.4.3 Capillary pressure

As the pore water evaporation continuous, water menisci form between the solid particles at the surface of the concrete. These water menisci are strong enough to squeeze the element volumetrically. The pressure that is exerted by the pore network is measured as the capillary pressure. As more pore water evaporates, the radii of these water menisci become smaller. At some stage, the radii become too small to bridge the gap between the solid particles, and air enters the pore network. This point is defined as air entry. The capillary pressure (P) can be modelled according to the Young-Laplace equation:

$$P = \frac{-2\gamma cos\theta}{r} \tag{2.1}$$

where γ is the surface tension of the pore solution, θ is the contraction angle and r is the radius of the menisci. Having more small particles in the concrete mix

results in more small menisci radii (lower r) and a higher capillary pore pressure [55–59].

2.4.4 Plastic shrinkage and related cracking

The horizontal contraction produced by the rise in capillary pressure is defined as plastic shrinkage. When the capillary pressure can freely deform the concrete, the term unrestrained or free shrinkage is used. When this shrinkage is prevented, the term restrained shrinkage is used.

Plastic shrinkage cracks (PSC) form when plastic shrinkage is restrained due to formwork, reinforcement, or internal restraint. Shrinkage restraint causes the tensile strain capacity to be exceeded, and this results in cracking. The tensile strain capacity tends to decrease from placement to about the final setting time. The shrinkage strain load increases from the drying time to about the final setting time. Typically, PSC becomes visible after the initial setting time and rapidly widens until the final setting time [60–63, 47, 64–68].

Printed concrete is vulnerable to plastic shrinkage cracking for several reasons. Firstly, printed concrete has no formwork to prevent early age pore water evaporation. Secondly, the low bleeding rate provides minimal protection against pore water evaporation. Thirdly, incorporating coarse aggregates is ill-advised due to the rheological and surface finish requirements of printed concrete but can provide dimensional stability and reduce shrinkage. Fourthly, the large quantities of fines in the thixotropic mix result in a higher capillary pressure before air entry, causing a larger magnitude free shrinkage. And finally, the thin-walled nature of printed elements means that a large amount of pore water can evaporate for an equivalent amount of shrinkage resistance—printed elements have a high surface area to volume ratio. This topic is further discussed in Chapters 5, 6 and 7.

2.5 Autogenous shrinkage

Chemical shrinkage can be defined as the volumetric reduction associated with the hydration reaction. The volume of the products formed by the hydration reaction is less than that of the original constituents, resulting in chemical shrinkage. Chemical shrinkage is the internal volume reduction, while autogenous shrinkage is the external volume reduction measured under a sealed, isothermal condition. Therefore, for autogenous shrinkage, no substances are lost or added, the temperature remains constant, and no external forces are applied—the shrinkage is self-produced. Continuous hydration creates internal pores and reduces internal humidity, a process known as self-desiccation. When the internal water is insufficient to fully hydrate the cementitious particles, as for mixes with w/c ratios lower

than 0.42, this self-desiccation results in a capillary tension in the internal pore network and ultimately autogenous deformation [40, 69, 70, 41, 71, 72]. The low w/c ratios and high quantity of binders predispose printed concrete to significant autogenous shrinkage. This topic is further discussed in Chapters 5 and 6.

2.6 Mechanical performance

The early age material properties have a more significant effect on the long-term mechanical performance of printed concrete than for cast concrete. This is because the interlayer is weak compared to the element's intralayer—printed elements show orthotropic material behaviour. Because of this, the printed element's mechanical performance is not only influenced by the degree of hydration but also by the early age thixotropy and rheology, the surface moisture and entrapped air on the interlayer, as well as the printing system parameters (print speed, pump speed, nozzle height, etc.). The complexity results in a notable variability in mechanical performance, large design uncertainties and less-cost effective structures [73–80]. This topic is further discussed in Chapters 8 and 9.

The integration of reinforcement is one of the main challenges facing printed concrete, with many research groups focussed on the topic [19, 81–83]. Although reinforcement is essential in many cases, the rigidity added to the plastic concrete can potentially exacerbate early age cracking.

2.7 Concrete durability

Concrete durability is defined as the ability to remain serviceable in the structure and its environment. The degradation processes are controlled by the rate at which air, moisture and aggressive agents enter the concrete. Degradation agents flow through the concrete by 1) permeation, movement due to differential pressure, 2) diffusion, movement of ions due to a concentration gradient and 3) sorptivity, capillary absorption of a fluid. These transport processes can be quantified by the oxygen permeability, water sorptivity and chloride conductivity tests [84–86]. This topic is further discussed in Chapter 8.

Chapter 3

A weather data analysis method to mitigate and prevent plastic shrinkage cracking

Abstract

Placing fresh concrete in high evaporation conditions can increase the permeability and risk of plastic shrinkage cracking in concrete elements. Prevention measures can be time-consuming and expensive and are often neglected or incorrectly applied. This study proposes a data analysis method to identify the best time for concrete placement, most effective active curing measures, limits on weather condition for concrete placement and adequate testing conditions from location-specific weather data to reduce and mitigate the adverse effects of extreme weather concreting. The aim of this study is to characterise the evaporativity of a region and identify common trends that may be useful for planning concrete projects. The method can be applied to weather data from any location to produce more specific plastic shrinkage crack prevention and extreme weather concreting guidelines. To show the potential of this method, it is applied to four geographically and meteorologically different locations. The selected locations have a hot and dry climate, but the method can also be applied to a cold and dry climate which can, in some cases, produce even higher evaporation rates. The results indicate that for the selected locations specific active curing measures should be rigidly enforced throughout the year and that additional passive prevention measures are required in summer months. The necessity for additional passive prevention can be significantly mitigated by selecting a placement time with a lower evaporation rate.

Article information

Chapter 3 has been published as a journal article and can be cited as: **G.M. Moelich**, R. Combrinck, A weather data analysis method to mitigate and prevent plastic shrinkage cracking, Construction and Building Materials, vol. 253, August 2020. Online

Contribution declaration

With regard to this chapter, the nature and extent of the contributions of the candidate and the co-authors were as follow:

Name	Nature of contribution	Extent
G.M. Moelich (candidate)	Conceptualisation, Methodology, Validation, Formal analysis, Writing - original draft, Visualization, Investigation	95%
Dr R. Combrinck (rcom@sun.ac.za)	Conceptualisation, Validation, Writing - review & editing, Supervision	5%

The undersigned hereby confirm that:

- The declaration above accurately reflects the nature and extent of the contributions of the candidate and the co-authors to this chapter.
- No other authors contributed to this chapter besides those specified above.
- Potential conflicts of interest have been revealed to all interested parties and that the necessary arrangements have been made to use the material in this chapter of the dissertation.

Signature of authors	Institutional affiliation	Date
	Department of Civil Engineering, Stellenbosch University	09/06/2021
	Department of Civil Engineering, Stellenbosch University	09/06/2021

3.1 Introduction

Plastic shrinkage cracking (PSC) is one of the first types of cracks that form in both reinforced and unreinforced concrete elements, appearing from 30 minutes to a few hours after placement. Elements with a high surface to volume ratio (such as slabs, pavements and bridge decks) exposed to high evaporation conditions at an early-age are prone to PSC [42]. Furthermore, exposing the fresh concrete to these conditions can also influence the hardened properties [87]. Although prevention measures can be implemented to reduce the adverse effects of extreme weather concreting, these measures are often neglected.

Immediately after placement gravity forces cause settlement of the solid particles forcing free pore water to the surface where a water film forms, a phenomenon known as bleeding [88, 89]. If the evaporation and reabsorption rate is higher than the bleeding rate the water film dissipates [55, 90]. The absence of a water film exposes the pore water to the environment where it can evaporate, causing a volume reduction and a negative pressure in the pore system [56, 58]. The negative pressure results in a contraction of the concrete body, known as plastic shrinkage. Restraint of the shrinkage causes an accumulation of tensile strain which, if it exceeds the tensile strain capacity, can result in the formation of plastic shrinkage cracking [91, 47, 92].

Evaporation is the main driver of plastic shrinkage [88, 91, 87] and is commonly used as an indication of the risk of PSC [93, 90]. Bleeding mitigates the extent to which the external evaporation conditions translate to the internal shrinkage by providing water to the surface of the concrete that acts as a protection layer which prevents or delays internal pore water evaporation. Other factors such rate of hydration, setting time, element depth, plastic settlement, size and distribution of fine particles and finishing operations may influence the shrinkage caused by the pore water evaporation [47, 42, 94]. Differential settlement, thermal dilation and autogenous shrinkage may also contribute to the severity of PSC [60, 57]. The concrete temperature can influence PSC by controlling the rate of the hydration reaction [95, 53, 96] and influence the difference in vapour pressure between the evaporating water and the air to effect the evaporation rate [49].

In early-age concrete, the faster formation of hydration products, caused by a high early-age temperature, can result in an unstructured pore framework [87, 97]. Almusallam [53] showed that placement at elevated temperatures may lead to a decrease in long-term compression strength and increase in coarse pore volume. The higher permeability, associated with an increase in coarse pore volume, may lead to a great deal of durability issues [87].

Prevention measures can be implemented to reduce the adverse effects of casting concrete in extreme weather and can be divided into two groups: active and passive measures [98]. Active measures are based on reducing the evaporation

rate through adequate curing methods and construction procedures [50, 99, 100]. Recently, passive measures, based on modifying the material properties, have received a great deal of attention with fibres [60, 101] and super absorbent polymers (SAP's) showing promising results [98, 102, 101]. However, neglecting the active measures can leave the passive measures ineffective in preventing the adverse effects of extreme weather concreting.

3.1.1 Research significance

Weather data can be used to estimate the evaporativity of an environment. Common trends in the weather conditions and evaporativity can indicate the risk of PSC and provide guidance on selecting active and passive PSC prevention measures. The trends can be used for planning and tendering for concrete construction projects. The weather data can also be used to determine appropriate, location specific, PSC testing conditions.

3.1.2 Estimating evaporation

Menzel's [48] model has been suggested to estimate evaporation potential [100, 103, 104]. The model was originally proposed by Kohler et al. [105] to estimate open water evaporation. Kohler monitored the evaporation rate from evaporation pans from 24 April 1950 to 31 August 1951. A model, based on Dalton's law, was fitted to the daily (24 hour) mean evaporation rate with a correlation index of 91% and standard error of 19%. In Kohler's study, wind speed was measured 0.5 m above the evaporation pan. It is presumed, from the ACI nomograph, that the Kohler-Menzel model was intended for air temperatures from 5 to 35°C, concrete temperatures from 4 to 38°C, a wind speed from 0 to 11 m/s to produce evaporation rates from 0 to 4 kg/m^2/h [100]. The model can be rewritten as a function of wind speed, concrete temperature, air temperature and the relative humidity as done by Uno [50] as follow:

$$E_w = 5\big((T_c + 18)^{2.5} - RH \cdot (T_a + 18)^{2.5}\big)(3.6V + 4) \cdot 10^{-6} \tag{3.1}$$

where E_w is the evaporation (kg/m^2/h), T_c is the concrete temperature (°C), T_a is the air temperature (°C), RH is the relative humidity (%/100) and V is the wind speed (m/s). Form here on, this study refers to the Kohler-Menzel-Uno model as KMU.

Al-Fadhala and Hover [51] conducted 94 water pan evaporation tests to propose a new model for liquid temperatures for 10 to 30°C, air temperatures from 25 to 30°C, relative humidity from 42% to 65% and wind speed from 2 m/s to 15.3 m/s. These limits produce an evaporation rate from 0.56 to 1.82 kg/m^2/h.

$$E_w = 0.4238(e_o - e_a) + 0.0485V - 0.305 \tag{3.2}$$

where e_0 is the vapour pressure on the surface of the liquid (kPa), e_a is the vapour pressure in the atmosphere above (kPa) and V is the wind speed (m/s). Form here on, this study refers to the Al-Fadhala-Hover model as AFH.

Bakhshi et al. [52] proposed an evaporation model based on the boundary-layer theory, mass transfer, diffusion and convection which predicted evaporation rates with higher accuracy. Due to its complexity the model is ill-suited for general estimation purposes.

3.1.3 Accuracy of evaporation estimations and the influencing factors

Hover [106] showed that the KMU model estimates the evaporation rate ±25% from the actual rate for evaporation rates up to 1 kg/m^2/h and can overestimate the actual rate by up to 50% at 1.8 kg/m^2/h. Kohler averaged the wind speed, 3-hour air temperatures and maximum and minimum water temperature for a 24-hour period. The actual evaporation was recorded once a day. A least squares fit was made to the daily averaged data to obtain the coefficients for the estimation model. The KMU model was proposed from data which were averaged over an extended period for any season which may lead to an error in short-term applications.The model does however provide a reasonable estimate of the evaporation rate, as stated by Hover [106].

Bakhshi et al. [52] accounted for the size of the sample when estimating the evaporation rate. Other factors such as surface roughness, wind fluctuations, sample shape, water depth, atmospheric pressure and evaporative cooling affects evaporation of open water. Solar radiation is considered one of the main variables when estimating evaporation from open water [107]. Neglecting these effects can result in large errors.

Consequently, the interpretation of the KMU and AFH models have shifted from forecasting the evaporation rate from the concrete surface to estimating the evaporativity of a environment [106, 90]. It is the intent of this study to use these evaporation models as an indication of the evaporativity of the environment to show common trends rather than forecasting the exact evaporation rate. The KMU and AFH models have been widely accepted in the PSC community to indicate the evaporativity of the environment.

3.1.4 Tolerable evaporation rates

The ACI 305.1 [100] suggests that evaporation control measures should be initiated when the evaporation rate exceeds 1 kg/m^2/h. Uno [50] referenced the Australian Pre-Mixed Concrete Association stating that pore water evaporation should be limited to 0.5 kg/m^2/h. The European Standards [108] limited the placement of concrete to an ambient temperature of 30°C with no limit on evaporation. The CCAA [103] suggests the evaporation rate should not exceed 0.75 kg/m^2/h.

Lerch [55] suggested that PSC is likely when the evaporation rate exceeds the bleeding rate. The above-mentioned tolerable evaporation rates were determined from the bleeding rates, which were based on experiments conducted many years ago [50]. Modern-day concrete mixtures have bleeding rates significantly less than 1 kg/m^2/h with some high-performance concretes producing no bleeding water [106]. The tolerable evaporation rate may, for this reason, be even lower.

3.1.5 Testing conditions found in literature

In the past, different testing conditions have been used to study PSC (Table 3.1). The vast range in testing conditions is clear. Since PSC is thermally dependent, the choice of testing temperature can affect the fundamental behaviour of the PSC phenomena. Information on the weather conditions at different evaporation rates can be used to identify more appropriate testing conditions. Several of the more recent studies have been conducted with the experimental setup proposed by ASTM C1579 [109].

Table 3.1: Testing conditions found in literature.

Reference	Initial T_c (°C)	T_a (°C)	RH (%)	V (m/s)	E_w (kg/m^2/h) KMU	AFH	PSC formed?
Ravina and Shalon [91]	-	20†, 30	45†, 35	5.7†, 2.5	0.60	0.52	Y
Wittmann [56]	-	20	50	4	0.41	0.38	Y
Berhane [110]	-	30†, 40	95, 70†, 35	0, 4.67†	0.50	0.46	-
Shaeles and Hover [42]	-	25†-35	10-25†	3.1†-3.6	0.69	0.85	Y
Cohen et al. [111]	-	40	0.83	-			Y
Almusallam et al. [43]	-	45	50	4.67	1.64	1.96	Y
Hammer [112]	-	20	50	0			-
Qi et al. [60]	-	38	50	6.67	1.64	1.43	Y
Banthia and Gupta [113]	-	50	5	-			Y
Turcry and Loukili [62]	-	20	50	5	0.49	0.43	Y
Azenha et al. [54]	-	20†, 35, 60	60†, 30	1.8†, 3.3, 4.2	0.19	0.18	-
Lura et al. [57]	30	30	50	6.67	1.12	0.92	Y
Slowik et al. [58]	-	20, 22†	45, 30†	4.8†	0.75	0.71	Y
Bakhshi et al. [52]	-	24	34	0.5	0.22	0.56	-
Boshoff and Combrinck [47]*	23	40	15	3.61	1.85	2.53	Y
Leemann et al. [64]*	-	30	60	7	0.93	0.76	Y
Combrinck et al. [94]*	23	40	10	6.4	3.12	2.83	Y
Ghourchian et al. [98]*	22	33	40	7.5	1.73	1.34	Y
Sirajuddin and Gettu [66]*	-	42	35	4.5	1.83	2.18	Y
Zhao et al. [114]*	26	42.5	15	9.1	4.45	3.18	Y

∗ studies conducted with ASTM C1579 [109]; - no data available;
† value used to calculate the evaporation rate in this table.

3.1.6 Other related studies

The influence of a change in air temperature, wind speed and relative humidity on the evaporation rate can be seen in Fig. 3.1 a-c) [55, 87]. Fig. 3.1 d) was included by the authors of this article to illustrate the effect of a change in the difference between concrete and air temperature.

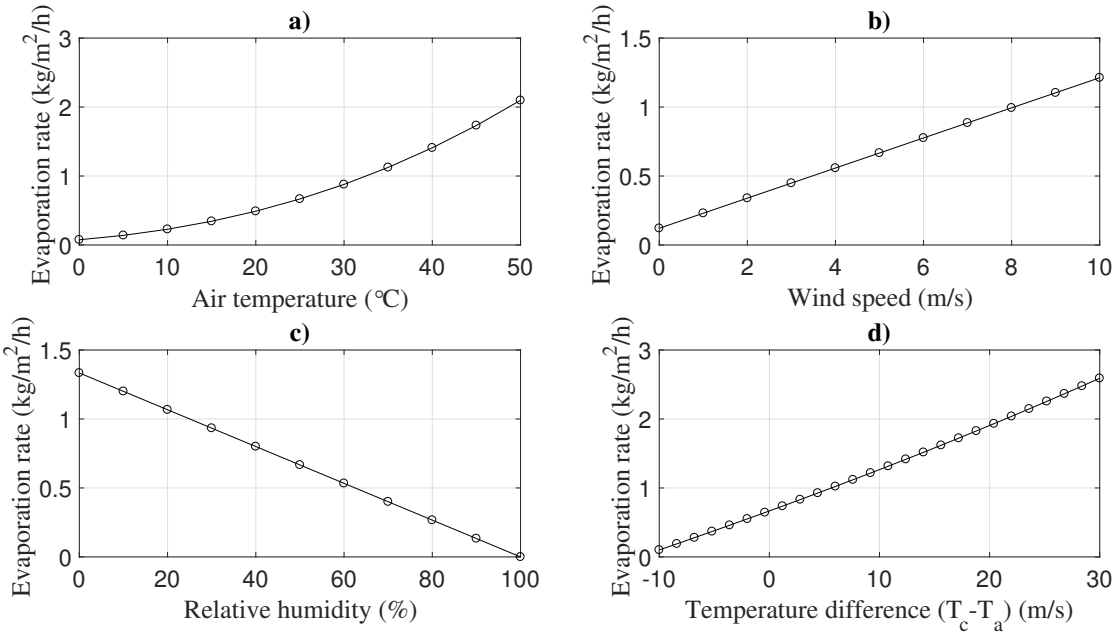

Figure 3.1: The influence of different weather condition on the KMU evaporation rate [87] with a) a change in air temperature and Tc=Ta, RH=50%, V=5 m/s, b) a change in wind speed and Tc=Ta=25°C, RH=50%, c) a change in relative humidity and Tc=Ta=25°C, V=5 m/s, d) a change in temperature difference and RH=50%, V=5 m/s.

Al-Fadhala and Hover [51] showed the daily and monthly evaporation rate fluctuations with different concrete temperatures using weather data of a few days for Kuwait in the Arabian Gulf. Carden and Ramey [115] conducted a study on weather conditions in Alabama, United States of America, to propose curing requirements for bridge decks from experience, engineering judgement and theoretical considerations. Data on monthly and daily mean fluctuations in the weather conditions and evaporation rates were used to propose curing requirements in four categories (Table 3.2). The research suggested that at evaporation rates exceeding 1 kg/m^2/h or wind speeds exceeding 9 m/s concrete should not be placed. Between 0.75 and 1 kg/m^2/h actions (Category A and C) should be taken to reduce the evaporation rate to below 0.5 kg/m^2/h in order to place concrete. Between 0 and 0.5 kg/m^2/h minimal actions (Category B and D) are suggested.

Table 3.2: Proposed curing requirements for bridge decks [115].

Category	Time after placement	Requirements
A	0.5 h - 4 h	Fogging or evaporation retarder
	4 h - 8 h	Double layer of wet burlap
	8 h - 7 days	Soaker hose on wet burlap and covered with layer white polyethylene
	7 days	Spray-on liquid curing compound
B	0.5 h - 4 h	None
	4 h - 8 h	Double layer of wet burlap
	8 h - 7 days	Soaker hose on wet burlap and covered with layer white polyethylene
	7 days	Spray-on liquid curing compound
C	0.5 h - 4 h	Fogging or evaporation retarder
	4 h - 8 h	Spray-on liquid curing compound
	8 h - 7 days	Cover with layer white polyethylene
	7 days	None
D	0.5 h - 4 h	None
	4 h - 8 h	Spray-on liquid curing compound
	8 h - 7 days	Cover with layer white polyethylene
	7 days	None

Carden and Ramey [115] neglected to acknowledge the importance of the concrete mixture's bleeding rate when suggesting curing measures on absolute evaporation rates. The evaporation rate of 0.5 kg/m^2/h may have been adopted from common bleeding rates, but it is not clear from their study. As an alternative, this study suggests that the bleeding rate of the specific mixture used should be adopted as a tolerable evaporation rate as suggested by Lerch [55]. Selecting a tolerable evaporation rate blindly can lead to a significant underestimation of PSC risk.

This study goes further to propose a statistical method of evaluating weather data to recommend curing methods specific to a location and placement times to mitigate the risk of PSC. The recommendations by Carden and Ramey [115] are used in the discussion of the results of this study.

3.2 Proposed method

The proposed method is a combination of statistical data analysis techniques used when working with large data sequences. An outline of the proposed method can be seen in Fig. 3.2. A discussion of each step follows. The application of the method is discussed in the next section followed by the results.

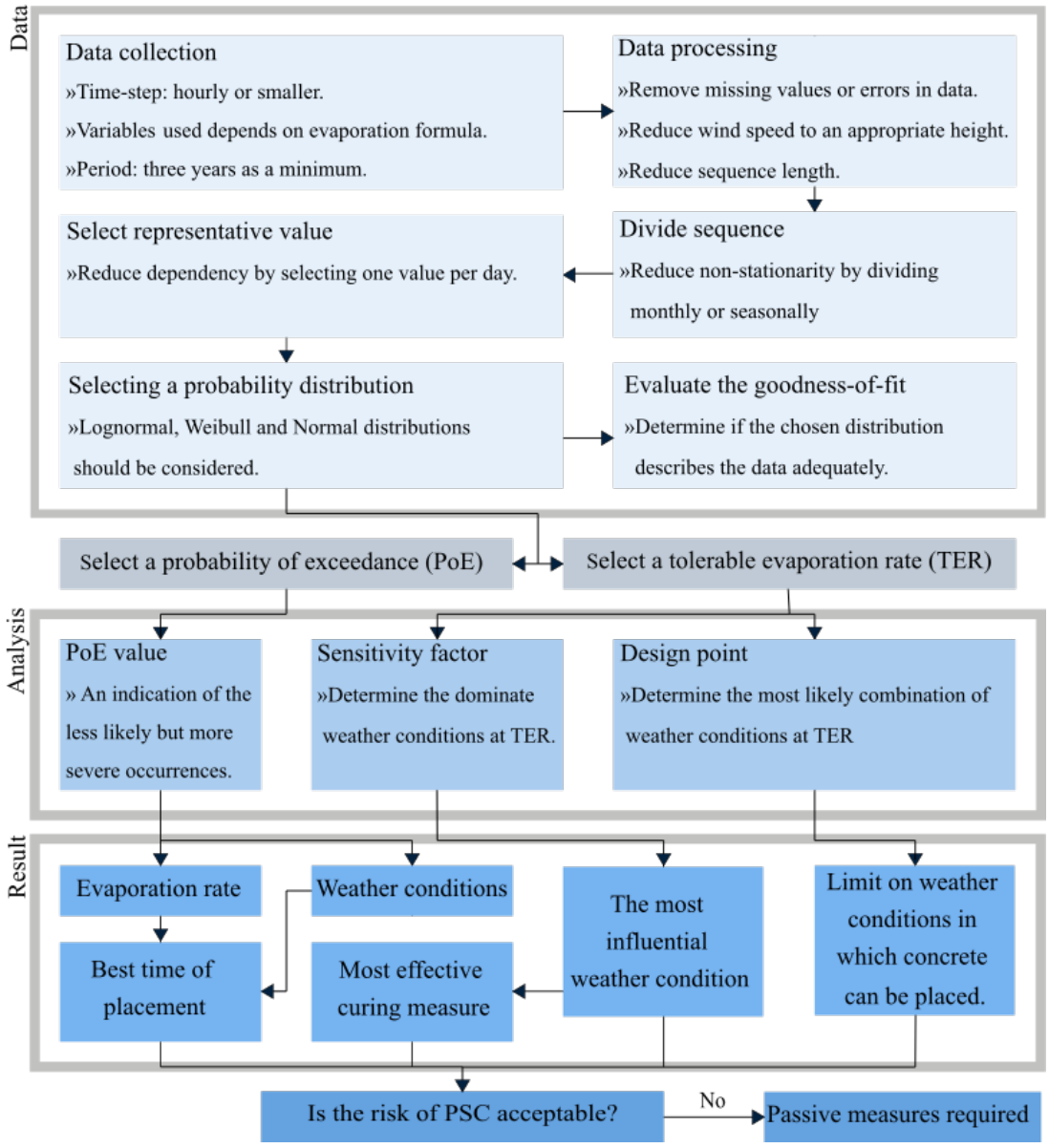

Figure 3.2: Thought process of the proposed method.

3.2.1 Data collection

First, weather data is obtained from a weather station. Weather data can be collected at the project-specific site or at a central weather station. By installing an automatically mobile weather station on the site, the data collected can be useful in predicting the magnitude of the evaporation rates, since it accounts for the local effects such as surrounding structures, water bodies, reflective surfaces, terrain roughness, geography, heat sources and sinks [107]. The main disadvantage is that the data would be site-specific. By selecting a central weather station, that follows the protocols set by the World Meteorological Organization [107], the aforementioned local effects can be significantly reduced. The results obtained from using a central weather station can be particularly valuable in identifying hourly and monthly trends in the weather conditions and evaporation rate for climatically similar regions but can lead to errors when used to forecast the evaporation rate on a specific site.

The data variables collected depend on the evaporation model used. Measurements taken every few seconds or every few minutes are averaged to determine an hourly value. The data sequence should at least span a period of three consecutive years to ensure that a sufficient number of data points are available to represent the entire population of the variable.

The period in which evaporation is critical to PSC commonly lasts for a few hours. An increase in air temperature or wind speed from one hour to the next would increase evaporativity of the environment and the total amount of pore water evaporation resulting in more severe PSC. The hourly fluctuations in the weather variables are therefore relevant for this study.

3.2.2 Data processing

The data is then processed to remove errors or missing data points. Wind speed measurements at weather stations are often taken at 10 m above the ground and should be reduced to a suitable height [50]. The data sequence length can be reduced by considering only possible working hours.

3.2.3 Reducing the non-stationarity and dependency of weather data

To determine the probability of a specific event occurring, a probability distribution is fitted to a sample space. A sample space is defined as a set of outcomes from an experiment with a unique set of conditions [116]. If the sample space is large enough it can be assumed that the probability distribution represents all the outcomes of the experiment (the entire population).

The seasonality of a weather data sequence violates the statistical assumption concerning the unique set of conditions [117]. The set of conditions vary for different seasons, resulting in a non-stationary sequence. Furthermore, due to small hourly time-steps, every data point is related to the recent history of the sequence, resulting in a dependency [117]. Since the modelling of a non-stationary sequence is complex, a simpler approach is recommended. The non-stationarity can be mitigated by dividing the sequence monthly or seasonally. The dependency can be reduced by selecting only one value per day [118]. The selection of dividing the data monthly or seasonally or selecting a maximum, mean or random value per day is crucial to the outcome of the method. Neglecting to cluster data seasonally or monthly would produce inaccurate and trivial results.

Firstly, the selections should be based on the desired outcome and statistical requirements. Secondly, the selections should acknowledge that maximising the number of data points will improve the accuracy of the model. Clustering the monthly subset data (e.g only January) into hours (e.g. 8:00, 9:00 ... 20:00) and fitting a different distribution to every hour is the most effective way of using the data. However, the results are specific to the selected month (January in this case). To determine the monthly and seasonal fluctuations of a variable would require clustering (e.g January, February ... December or summer and winter) of the data, selecting one value per day (e.g the maximum or mean) and fitting a different distribution to the values of each month or season. In this case, taking a maximum value per day would produce the most germane and conservative results. The sensitivity factor and design point analyses require that data are clustered seasonally, taking a random value to represent a day. Here, different times of the day may be related to different combinations of the weather variables which is accounted for if a random value is selected.

3.2.4 Selecting a probability distribution

Dividing the weather data sequence produces multiple subsets, each a sample space with a unique set of conditions. A probability distribution can then be fitted to each subset. The Maximum Likelihood method can be used to determine the parameters of the distribution from the sample space [119]. It is recommended that Lognormal, Weibull and Normal probability distributions are considered. The probability distributions with the best fit should be selected.

3.2.5 Evaluating the goodness-of-fit

The fit can be evaluated graphically, with a Probability plot (P-P) or a Quantile plot (Q-Q). For this study, the data at the upper tail end is of interest and not the data at the lower tail end. The graphical method can be used to select a

probability distribution that adequately represents the data at the upper tail end [119]. The Anderson-Darling (A-D) test and Kolmogorov-Smirnov (K-S) test was also used to evaluate the fit numerically [120, 121]. A significance level of 0.05 is recommended.

3.2.6 PoE analysis and potential results

The probability of exceedance (PoE) is the probability that a specific value is exceeded and can be used to give an indication of less likely but more severe occurrences. The above-mentioned steps can be applied to the weather conditions data or to the evaporation data (estimated from the weather conditions). The results can give valuable information on the magnitude and fluctuations of the variable at different PoEs.

The 10% probability of exceedance correspond to a 1 in 10 day return period. This means that if, for example, the 10% PoE is 8 m/s, one day of the next ten days is likely to have a wind speed >8 m/s that lasts for 1 hour or more. The PoE is more comprehensible for the contractor than the standard deviation since it quantifies the fluctuations.

3.2.7 TER analysis and potential results

The tolerable evaporation rate (TER) should be selected based on the bleeding rate of normal concrete. A First Order Reliability Method (FORM) analysis can then be used to determine the sensitivity factor and design point. The sensitivity factor identify the weather conditions that are most influential to the evaporation rate at the selected TER. The design point determines the most likely combination of weather conditions at the selected TER.

3.2.8 FORM analysis

The First Order Reliability Method (FORM) is in general conducted to determine the reliability of structures or systems. In this study, a FORM analysis was performed to determine the magnitude of the weather conditions at a TER (design point) as well as the most influential of the weather conditions at the TER (sensitivity factor). This study utilises a Matlab code by Kostandyan and Sørensen [122] to execute the FORM analysis but various other FORM software products are available. The method is summarised as follows [123]:

- The limit state function is formulated as follows, with G(T_a, RH, V)<0 a failure,

$$G(T_a, RH, V) = TER - EvaporationRate(T_a, RH, V) \tag{3.3}$$

- The probability distributions fitted to T_a, RH and V are transformed into a space of standard normal variables, U. For the first iteration, the origin is chosen at the mean of T_a, RH and V which denotes to the most likely combination of variables. The limit state function, G(T_a, RH, V), is also transformed to the space of standard normal variables G'(U)=0.
- The design point, where G(T_a, RH, V) is the closest to the origin, is determined through iteration. This point can be interpreted as the most likely point of failure.
- The reliability index, β, is the distance between the design point and origin. β can be used to calculate the probability of failure with a smaller value indicating a higher probability of failure.
- The sensitivity factor is the partial derivative of β with respect to a variable (T_a, RH or V) and is a measure of how β would change if a particular variable is changed slightly, near the design point.

The design point should be interpreted as the most likely combination of weather conditions that would result in a specific evaporation rate. The sensitivity factor quantifies the effect that a change in a specific weather condition would have on the evaporation rate while keeping the other variables constant.

3.3 Application of the method

3.3.1 Data collection

The evaporation rate was estimated with the Kohler-Menzel-Uno (KMU) and Al-Fadhala-Hover (AFH) models. Air temperature, relative humidity and wind speed data were obtained from four weather stations in the Western Cape of South Africa (Fig. 3.3). This study used central weather stations to identify and show common trends in the weather conditions and evaporation rate. All the data measurements were performed according to the standards of the WMO [107]. The wind speed was measured 10 m above ground level every five minutes and averaged over an hour. The temperature and relative humidity measurements were taken 1.25 m above ground level every 20 seconds and averaged over an hour.

The Cape Town (CT) and Beaufort-Wes (BW) weather stations, located at two meteorologically different locations, were selected to show the effect of the climate on the results. Atlantis (ALT), situated 41.22 km from the Cape Town station, has a similar climate to Cape Town. A visual inspection was conducted of all the sites to ensure the WMO protocols were followed. Of the four stations, the Douglas on site weather station, situated 1.78 km from the Cape Town station, was

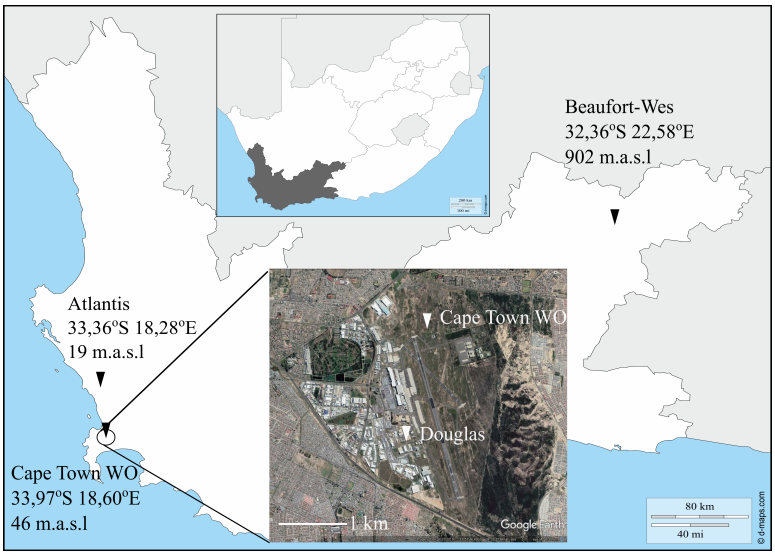

Figure 3.3: The four weather stations used in this study from Western Cape, South Africa.

selected as an example which violates the WMO terrain roughness protocols. The Douglas station is surrounded by buildings that affect the weather measurements and was included in this study to simulate an actual construction site scenario as close as possible. This method can also be applied to weather data obtained from a specific site to account for any local effects. Measurements taken every second were averaged to obtain hourly values for each location. The period from 01/01/2013 to 31/12/2017 (five years) was under study. Seasons were defined according to the South African Weather Service [124] as autumn from 1 March to 31 May, winter from 1 June to 31 August, spring from 1 September to 30 November and summer from 1 December to 29 February.

3.3.2 Data processing and assumptions

The following assumptions were made to produce practical results:

- In the case of a missing variable, all the variables were discarded for that hourly time-stamp.
- Wind speed values were adjusted to 2 m above ground level, unless stated otherwise. The influence of the elevation on the evaporation estimate is evaluated later in this study. The method suggested by the Wind action code is used [125]. The Power Law, as suggested by Uno [50], can also be used.

- The concrete temperature was assumed to the equal to the air temperature unless stated otherwise. In the case of exposure to solar radiation, the concrete temperature is assumed to be 5°C higher than the air temperature. This increase corresponds to a solar radiation of about 500 W/m^2 which is common in South Africa. The temperature increase to mean air temperature ratio is also similar to Al-Fadhala and Hover [51].

3.3.3 Reducing the non-stationarity and dependency of weather data

The selections made to reduce the non-stationarity and dependency in the weather sequence can be seen in Table 3.3.

Table 3.3: Selections made to reduce the non-stationarity and dependency of hourly weather sequences.

Method of analysis	Non-stationarity	Dependency
Design point	seasonally	randomly every day
Sensitivity	seasonally	randomly every day
Evaporation	monthly	the maximum value in every day
	monthly	every hour
Weather conditions	monthly	the maximum value in every day
	monthly	every hour

3.3.4 Evaluating the goodness-of-fit

Lognormal (LN), General Extreme Value (GEV), Weibull and Normal distributions were fitted to the estimated evaporation rates. When considering the monthly divided evaporation rates, the K-S tests failed to reject the LN and GEV distributions. The A-D test gives more weight to the tails and rejected the LN distribution for a few samples. Graphical methods, as seen in Fig. 3.4 for example, were then used to evaluate the fit. In this case, both the LN and GEV distributions were deemed adequate for evaporation rates from 0.5 to 3 kg/m^2/h, even though the A-D test rejected the LN distribution. It is clear that both the LN and GEV distributions describe the data well from 0.5 to 3.5 kg/m^2/h. In such an case, the LN distribution was chosen and preferred for its simplicity. Considering the evaporation rate estimation uncertainty, the error in choosing a simpler distribution is negligible.

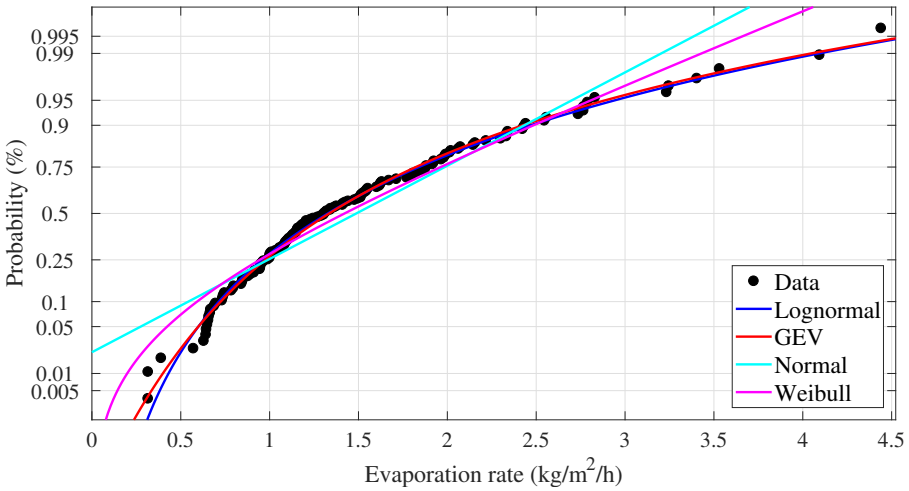

Figure 3.4: Probability distributions fitted to daily maximum evaporation rates of Beaufort-Wes in February.

A similar procedure was followed for the monthly and hourly divided air temperature, wind speed and relative humidity data. The LN distribution was assigned to air temperature and Weibull to wind speed and relative humidity. Here, the choice of distribution had a negligible effect on the result.

3.3.5 PoE analysis and TER analysis

This study selected a PoE of 10% and 50%. A 50% PoE corresponds to the mean value. Only the 10% and 50% PoE results are discussed in the results section of this study. To show the value of the proposed method the design point and sensitivity analysis was conducted at an evaporation rate of 1 and 2 kg/m^2/h. To discuss the results, a TER of 0.5 kg/m^2/h was selected based on the recommendation of Carden and Ramey [115] and common bleeding rates in the region. It is the responsibility of the contractor to interpret the results according to the bleeding rate of the mixtures used. The results for all the months of the year are available but are not discussed in this paper.

3.4 Results of method application

3.4.1 The design point and sensitivity

The design point and sensitivity factors for the two locations, Cape Town and Beaufort-Wes, were successfully determined with FORM. The sensitivity factor gives an indication of how a small change in one of the variables (T_a, RH or

V) can change the outcome evaporation rate and can be used to determine the most dominate weather condition. Table 3.4 shows the results from the sensitivity analyses for a tolerable evaporation rate (TER) of 1 kg/m^2/h.

Table 3.4: The sensitivity factors of Cape Town and Beaufort-Wes.

Location and season	G(T_a, RH, V)	T_a (°C)	V (m/s)	RH (%)
Cape Town in summer	1-KMU	42%	41%	17%
	1-AFH	69%	12%	20%
Cape Town in winter	1-KMU	66%	22%	11%
	1-AFH	87%	3%	10%
Beaufort-Wes in summer	1-KMU	67%	30%	3%
	1-AFH	91%	4%	6%
Beaufort-Wes in winter	1-KMU	87%	49%	12%
	1-AFH	98%	17%	12%

The evaporation rates of Cape Town in summer is almost equally effected by air temperature than by wind speed according to KMU. With AFH, the air temperature has a more significant effect than wind speed. In winter, when the wind speeds in Cape Town are generally lower, the evaporation rate is more dependent on air temperature. The evaporation rate of Beaufort-Wes in summer is largely dependent on temperature according to AFH. KMU shows that temperature and, to a lesser extent, wind speed has an effect. For Beaufort-Wes in winter the wind speed has a more significant effect on the evaporation than in summer due to the higher wind speeds in winter. Table 3.5 shows the most likely weather conditions that would result in a TER of 0.5, 1 and 2 kg/m^2/h.

Table 3.5: Design points of Cape Town and Beaufort-Wes.

		Summer			Winter		
Location	G(T_a, RH, V)	T_a (°C)	V (m/s)	RH (%)	T_a (°C)	V (m/s)	RH (%)
Beaufort-Wes	0.5-AFH	23.3	2.79	44.8	17.1	4.40	28.4
	1-AFH	27.7	3.47	27.9	23.8	5.43	16.4
	2-AFH	35.1	4.14	12.6	33.3	6.16	7.8
Cape Town	0.5-KMU	22.8	5.56	60.47	18.8	5.66	50.1
	1-KMU	25.4	7.51	47.5	23.5	6.95	36.9

For Beaufort-Wes in summer the most likely weather conditions that would result in a TER of 1 kg/m^2/h are: 27.7°C, 3.47 m/s and 27.9%. If, at these conditions, the wind speed is reduced by 50% the evaporation rate would reduce to

0.52 kg/m^2/h. However, at an air temperature and relative humidity of 35.1°C and 12.6%, a wind speed of 2 m/s would result in exceeding a evaporation rate of 1 kg/m^2/h. The location's climate has a significant effect on the design point with Cape Town requiring a lower temperature, higher relative humidity and almost double the wind speed to exceed the value of 1 kg/m^2/h when compared to Beaufort-Wes. Results differ from winter to summer. For Beaufort-Wes in winter a lower temperature and relative humidity and much higher wind speed are required to exceed the evaporation rate of 1 kg/m^2/h compared to summer.

3.4.2 Temperature

The fluctuations in monthly air temperature at a 10% and 50% probability of exceedance (PoE) throughout the year for Cape Town and Beaufort-Wes can be seen in Fig. 3.5. In Cape Town the mean (PoE=50%) daily maximum temperature is the highest in January at 24.7°C and the lowest in July at 15.1°C. Both the highest and lowest mean temperatures are higher in Beaufort-Wes at 32.2°C in January and 16.8°C occurring in August. For Beaufort-Wes in January, there is a 10% probability that the value of 38.5°C can be exceeded. In Cape Town the 10% PoE temperature is 30.9°C in January. The difference between the 10% PoE temperature and 50% PoE is larger in autumn and spring that in summer and winter in both Cape Town and Beaufort-Wes. In spring and autumn the air temperatures is more variable which may result in unexpected evaporation rates.

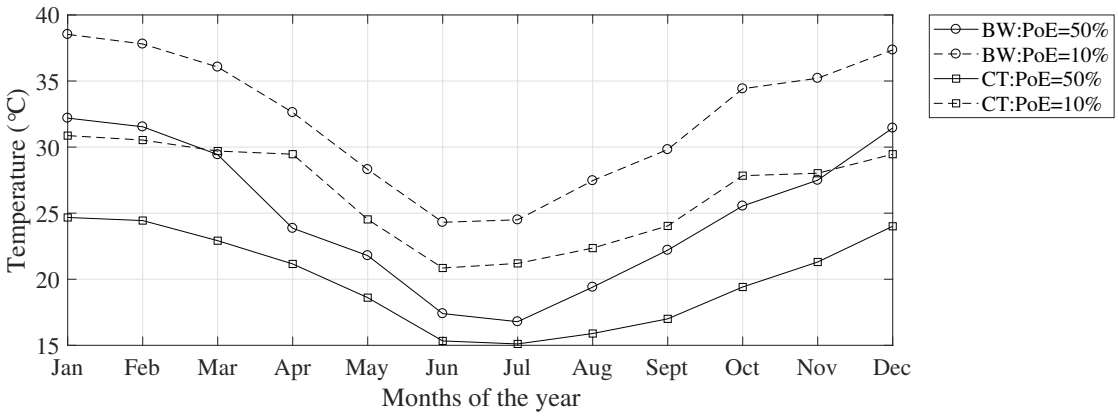

Figure 3.5: Probability of exceedance (PoE) air temperature during the year for Cape Town (CT) and Beaufort-Wes (BW).

Fig. 3.6 shows the hourly variation of temperature in Cape Town and Beaufort-Wes during January. From 1:00 to 10:00 the temperature in Beaufort-Wes and Cape Town are similar. The temperature in Beaufort-Wes continues to rise to a maximum of 31.1°C at 16:00. In Cape Town the maximum of 26°C forms earlier

at 13:00. The temperature in Cape Town gradually declines to 18.3°C at 6:00. The decline is more rapid in Beaufort-Wes with a minimum temperature of 16.4 °C at 6:00. The maximum 10% PoE temperatures are 38°C at 16:00 and 30°C at 13:00 in Beaufort-Wes and Cape Town, respectively.

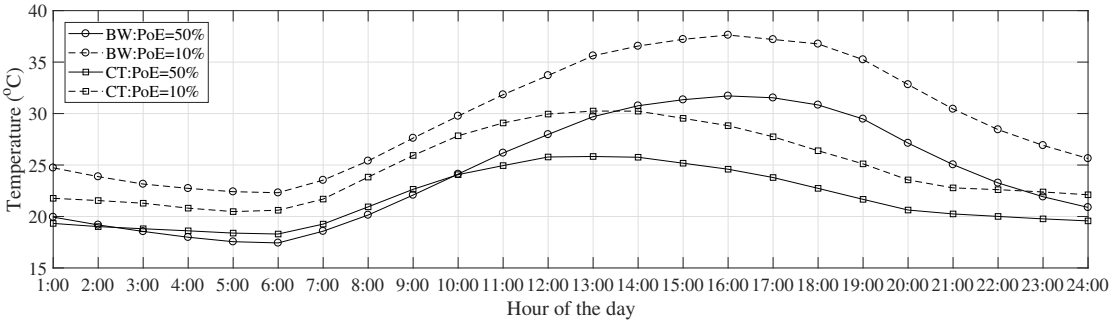

Figure 3.6: Air temperatures for different times in the day in Cape Town (CT) and Beaufort-Wes (BW) in January.

3.4.3 Wind

The maximum daily mean wind speed in Cape Town is 7.4 m/s in January and 3.9 m/s in June as seen in Fig. 3.7. In Beaufort-Wes the mean wind speed is more constant ranging between 4.8 m/s in April to 6 m/s in December. At a 10% PoE the wind speed is higher in Beaufort-Wes in winter months with a maximum of 10.8 m/s in June. Cape Town has a maximum 10% PoE wind speed of 11.3 m/s in January. In Beaufort-Wes the difference between the 10% PoE and 50% PoE wind speed is much higher in winter than in summer. In Cape Town the difference in wind speed is almost constant throughout the year.

The hourly fluctuation of wind speed for a normal day in January for Cape Town and Beaufort-Wes can be seen in Fig. 3.8. In Beaufort-Wes, the wind speed has a maximum at 20:00 and minimum at 10:00. In Cape Town, the maximum occur at 17:00 and minimum at 7:00.

3.4.4 Relative humidity

The monthly fluctuations in relative humidity can be seen in Fig. 3.9. In Cape Town the maximum daily mean relative humidity is 64% in winter months and 52% in summer months with Beaufort-Wes at 26% and 19%, respectively. The 10% PoE relative humidity is 9% in Beaufort-Wes and 33% in Cape Town throughout the year. The difference between the 10% PoE and 50% PoE relative humidity is higher in winter than in summer in both Cape Town and Beaufort-Wes.

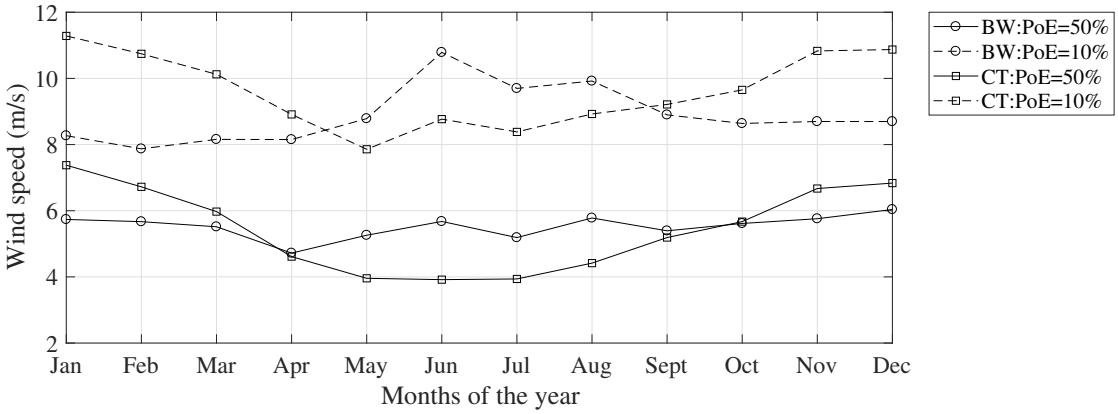

Figure 3.7: Probability of exceedance (PoE) wind speed during the year for Cape Town (CT) and Beaufort-Wes (BW).

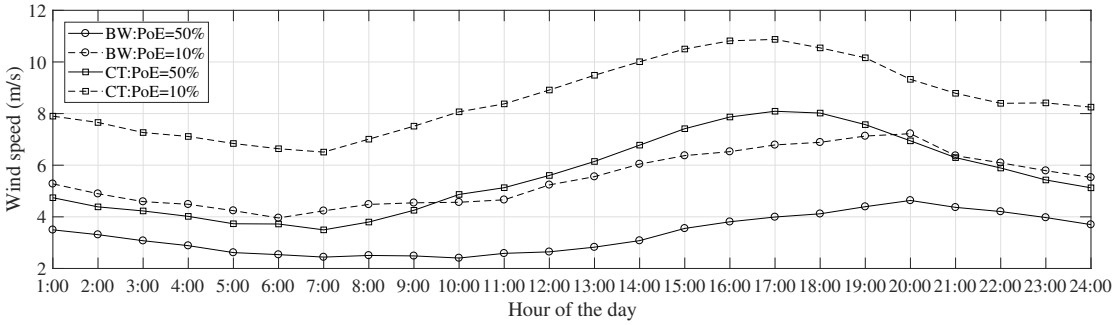

Figure 3.8: Wind speed for different times in the day in Cape Town (CT) and Beaufort-Wes (BW) in January

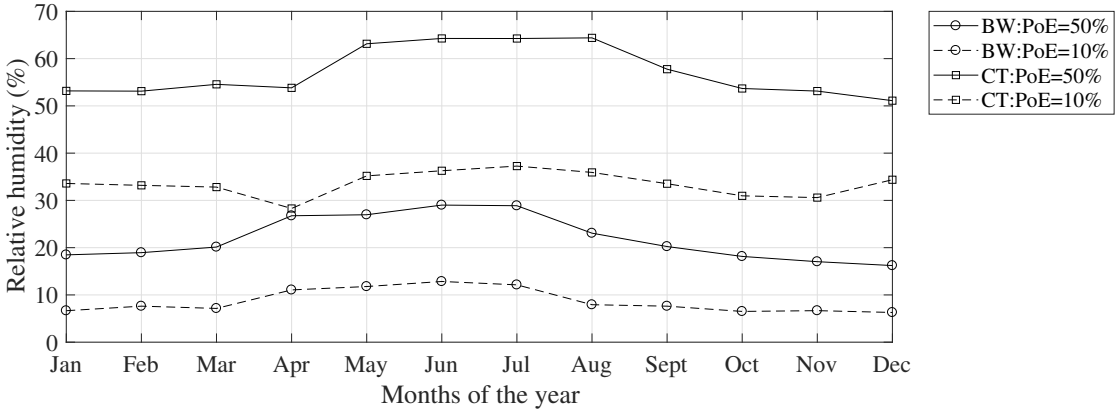

Figure 3.9: Probability of exceedance (PoE) relative humidity during the year for Cape Town (CT) and Beaufort-Wes (BW).

Fig. 3.10 shows the hourly fluctuations of relative humidity in January for Cape Town and Beaufort-Wes. In general, the relative humidity is inversely proportional to temperature. The low occurs between 12:00 and 13:00 in Cape Town and only at between 16:00 and 18:00 in Beaufort-Wes.

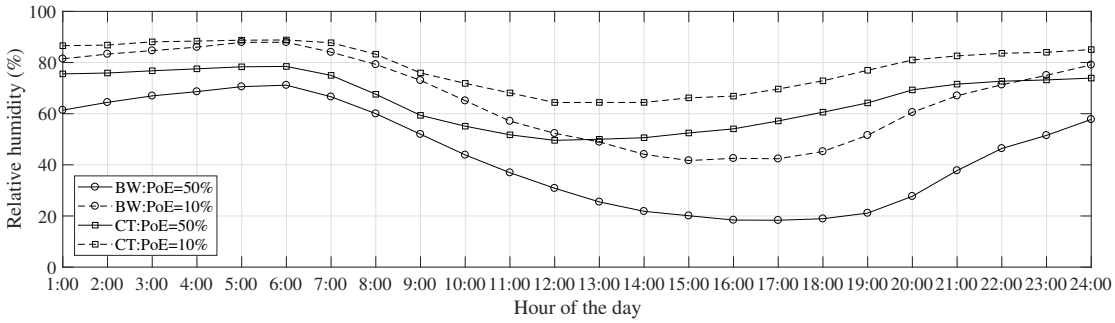

Figure 3.10: Relative humidity for different times in the day in Cape Town (CT) and Beaufort-Wes (BW) in January

3.4.5 Evaporation

The fluctuations of daily maximum evaporation rates, as estimated by KMU and AFH, for different exceedance probabilities (PoE) and months of the year in Cape Town and Beaufort-Wes can be seen in Fig. 3.11. In Beaufort-Wes with KMU and AFH, the maximum daily evaporation rate exceeds the value of 1 kg/m^2/h at least 50% of the days in the months from October to March. The maximum daily evaporation rate exceeds the value of 2.5 kg/m^2/h at least 10% of the days in the months from December to March. In Cape Town with KMU, the maximum daily evaporation rate exceeds the value of 1 kg/m^2/h at least 50% of the days only in January. There is a probability of at least 50% that the value of 0.5 kg/m^2/h is exceeded from September to April. The difference between the 10% PoE evaporation rate and 50% PoE is around 1.5 times larger in summer than winter for both Beaufort-Wes and Cape Town. Throughout the year the PoE difference is around 3 times higher in Beaufort-Wes than in Cape Town, showing the large variation in evaporation rates in Beaufort-Wes. AFH and KMU produced similar evaporation rate values in Beaufort-Wes and Cape Town. In Cape Town the KMU estimate is higher that AFH throughout the year. For Beaufort-Wes in summer the AFH estimate is higher than KMU due to the higher air temperatures and lower wind speeds.

The influence of radiation can be evaluated by assuming an increase in the concrete surface temperature by 5°C. The daily maximum evaporation rates, as estimated by AFH, for different exceedance probabilities (PoE) in Beaufort-Wes

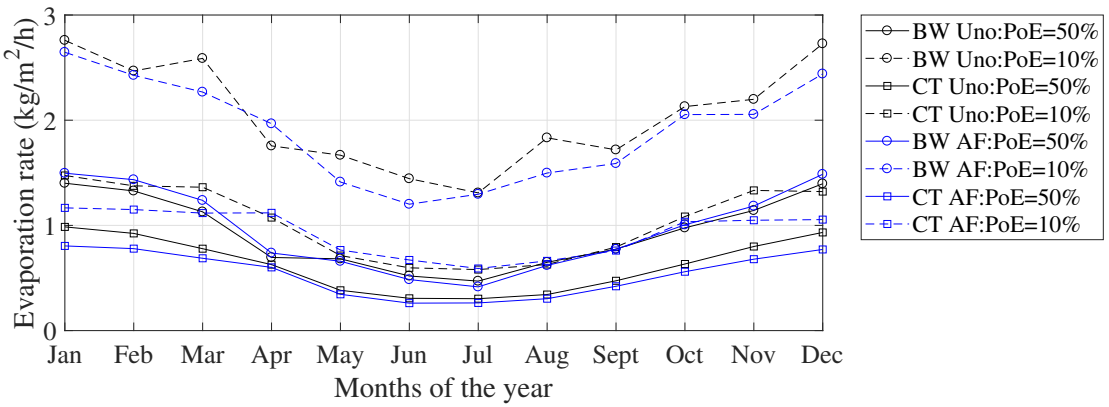

Figure 3.11: Probability of exceedance (PoE) evaporation rate during the year for Cape Town (CT) and Beaufort-Wes (BW) with KMU and AFH.

can be seen in Fig. 3.12. Only the AFH estimation is used since it is more sensitive to the temperature.

Assuming a 5°C increase in concrete temperature can increase the evaporation rate by up to 1.5 times in the summer of Beaufort-Wes. With this assumption, the 50% PoE exceeds the value of 1 kg/m^2/h for all the months of the year except June and July. For Cape Town in summer, assuming a 5°C increase in concrete temperature can increase the evaporation rate by up to 1.6 times.

The hourly fluctuation in air temperature, wind speed and evaporation rate (KMU) in Cape Town and Beaufort-Wes for January can be seen in Fig. 3.13 and Fig. 3.14, respectively.

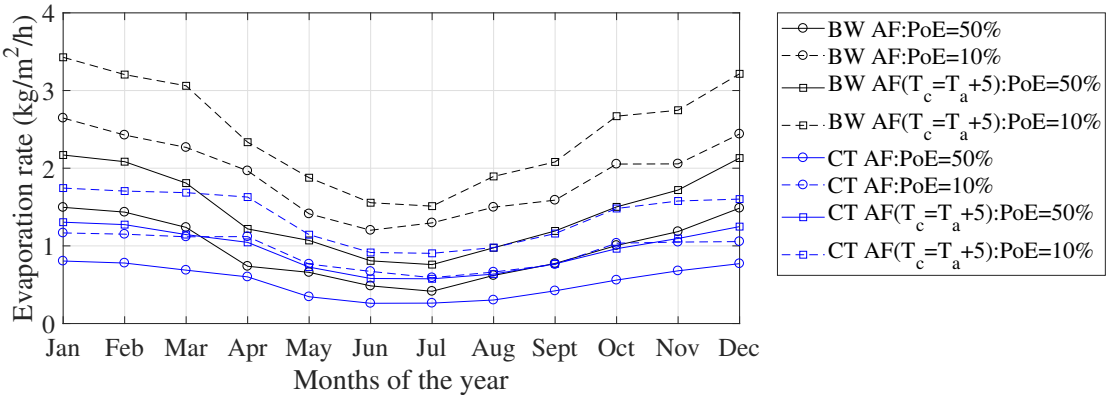

Figure 3.12: Probability of exceedance (PoE) evaporation rate during the year for Beaufort-Wes and Cape Town with AFH where $T_c = T_a$ and $T_c = T_a + 5$.

In Cape Town, at a 10% PoE the evaporation rate exceeds the value of 1 kg/m^2/h from 10:00 to 18:00. At a 50% PoE the evaporation rate exceeds with the value of

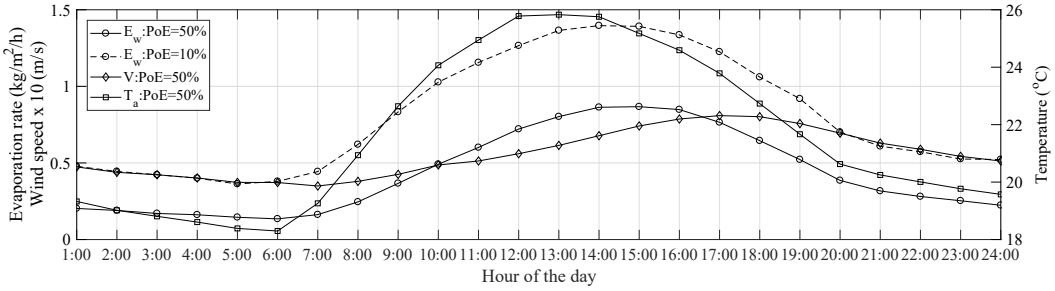

Figure 3.13: Probability of exceedance (PoE) evaporation rate at different hours of the day for Cape Town in January.

0.5 kg/m^2/h from 10:00 to 19:00. The evaporation rate peaks between 14:00 and 15:00 with the temperature peaking at 13:00.

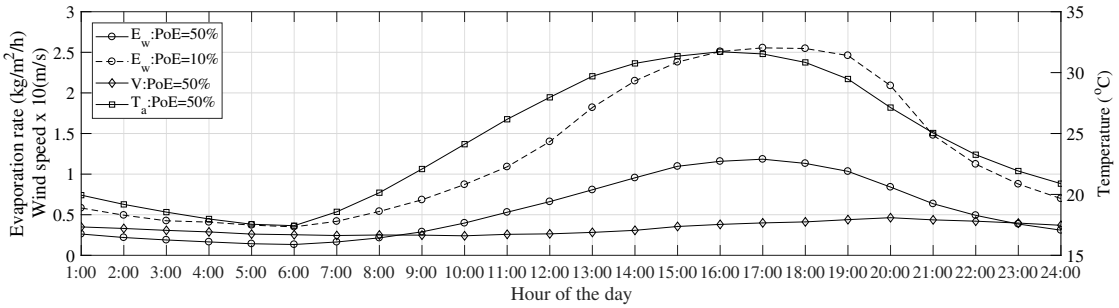

Figure 3.14: Probability of exceedance (PoE) evaporation rate at different hours of the day for Beaufort-Wes in January

In Beaufort-Wes, 10% PoE evaporation rate exceeds the value of 1 kg/m^2/h from 11:00 to 22:00. At a 50% PoE the evaporation rate exceeds with the value of 0.5 kg/m^2/h from 11:00 to 22:00. The evaporation rate peaks between 17:00 and 18:00 with the temperature peaking at 16:00. The evaporation rate peaks 2 to 3 hours later in Beaufort-Wes when compared to Cape Town, mainly due to the temperature peak occurring later.

3.4.6 Site specific conditions

The weather conditions at a specific site can be significantly different from the conditions at the weather station, even if the site is located in close proximity to the weather station. Fig. 3.15 shows the hourly 50% PoE air temperature and wind speed for Cape Town, Atlantis and at a specific site (Douglas) during January.

The air temperature fluctuation over 24 hours is similar at the Douglas and Cape Town weather station. Atlantis has a higher midday and lower night air tem-

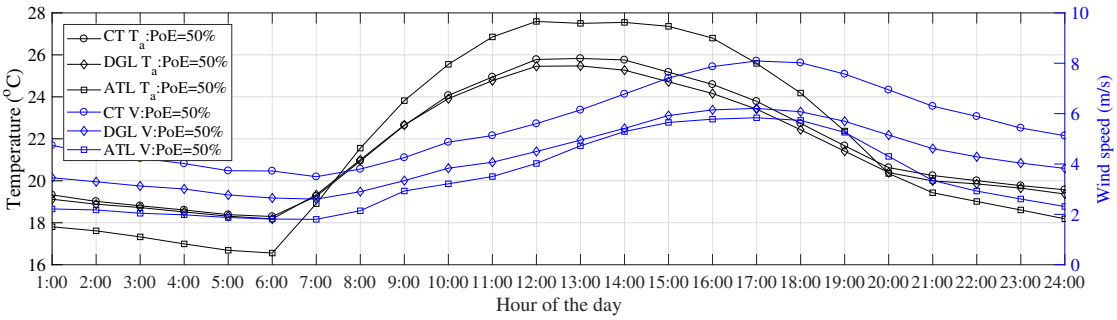

Figure 3.15: The 50% PoE air temperature and wind speed for different times of the day at Cape Town (CT), Atlantis (ALT) and Douglas (DGL).

perature compared to the other two stations. The magnitude of the 50% PoE wind speed differs for the three stations. The difference in wind speed between Cape Town and Douglas varies from 0.9 to 1.9 m/s, which is considerable considering that the stations are located only 1.78 km from each other. This considerable difference in wind speed measurements can be attributed to the buildings surrounding the site.

It should be noticed that the trends in the hourly air temperature and wind speed fluctuations are similar for all three stations. In all three stations, the peak wind speed and air temperature occur between 17:00 and 18:00 and 12:00 and 14:00, respectively. The factors driving the methodological process at these locations are similar and, therefore, also the trends in wind speed and air temperature development. In Beaufort-Wes, a methodologically different location, the peak wind speed and air temperature occur between 19:00 and 21:00 (Fig. 3.8) and 16:00 and 17:00 (Fig. 3.6), respectively. Fig. 3.16 shows the hourly 50% PoE KMU evaporation rate for Cape Town, Atlantis and at a specific site (Douglas) during January.

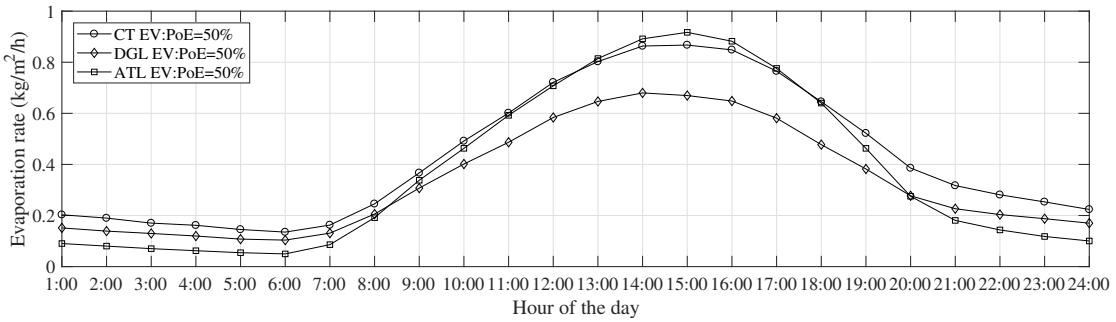

Figure 3.16: The 50% PoE KMU evaporation rate for different times of the day at Cape Town (CT), Atlantis (ALT) and Douglas (DGL).

The magnitude of the peak evaporation rate differs for Cape Town, Atlantis and Douglas. The evaporation rate at Douglas is lower than at Cape Town due to a lower wind speed. The combination of higher temperature and lower wind speed in Atlantis produced a similar evaporation rate than Cape Town.

The peak evaporation occurs between 14:00 and 15:00 in all three stations with the minimum occurring at 6:00. The maximum evaporation rate is 6 to 7 times the minimum. In Beaufort-Wes, a methodologically different location, the peak evaporation rate occurs three hours later, between 17:00 and 18:00 (Fig. 3.14).

Fig. 3.17 shows the monthly 50% and 90% PoE KMU evaporation rate for Cape Town, Atlantis and at a specific site (Douglas) throughout the year.

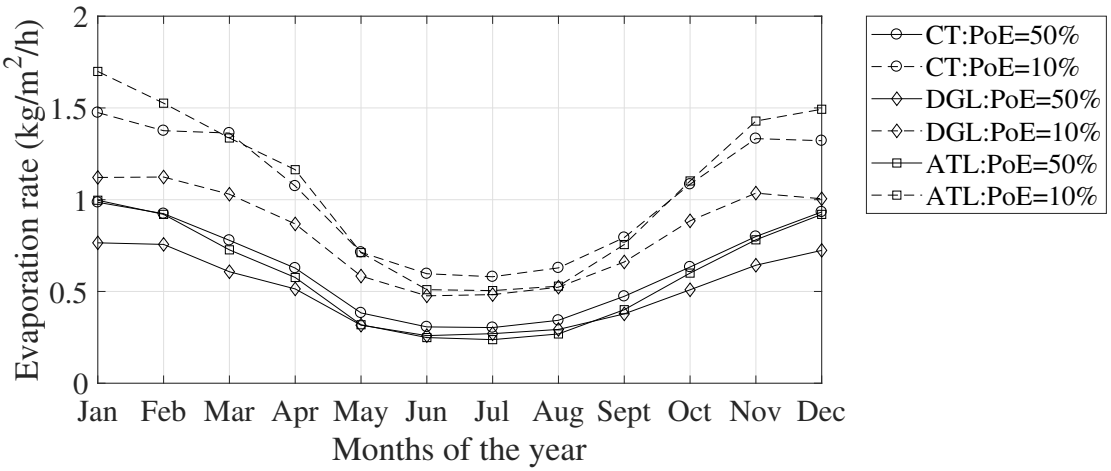

Figure 3.17: The 50% and 90% PoE KMU evaporation rate for different months of the year at Cape Town (CT), Atlantis (ALT) and Douglas (DGL).

In Cape Town, Atlantis and Douglas, the evaporation rate exceeded the evaporation rate of 0.5 kg/m^2/h from October to April with the peak occurring from January to December and minimum from May to August. In January, Douglas showed an 50% PoE evaporation rate 30% lower than Cape Town and Atlantis.

Wind speed increases with elevation. Fig. 3.18 shows the monthly KMU evaporation rate for Cape Town for a element at an elevation of 2, 5 and 10 m.

Wind speed increases with an increase in elevation, resulting in a marginal increase in evaporation rate. On average, increasing the elevation from 2 to 10 m resulted in a 15% increase in evaporation rate. The percentage increase was similar throughout the year.

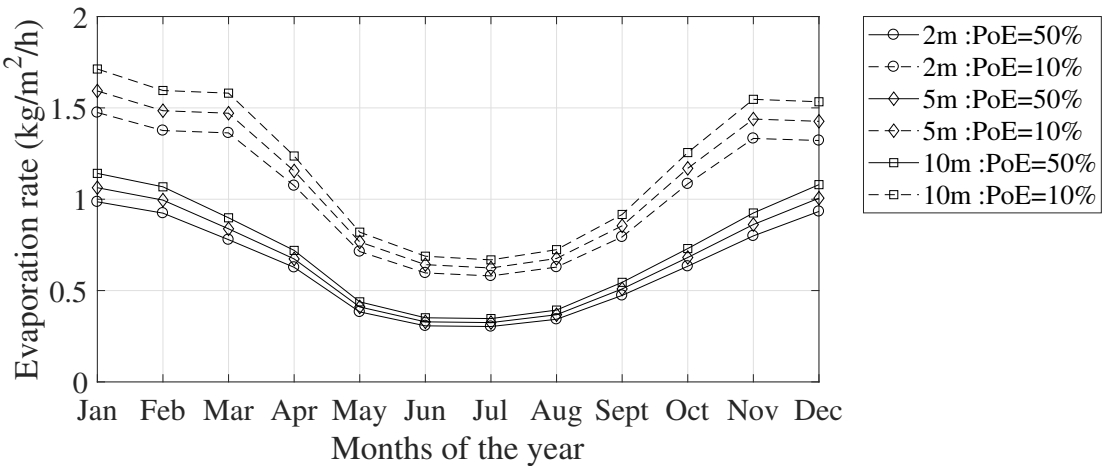

Figure 3.18: The 50% PoE KMU evaporation rate for different months of the year at Cape Town (CT) for an element elevation of 2, 5 and 10 m.

3.5 Discussion

3.5.1 Dominant weather condition

According to the sensitivity results, a change in air temperature has a more significant effect on the evaporation rate than a change in relative humidity for Beaufort-Wes. In Cape Town, both air temperature and wind speed have a significant effect on the evaporation rate while the relative humidity has less of an effect. The KMU model is more sensitive to wind whereas the AFH model is more sensitive to air temperature. The model choice has an insignificant effect on the evaporation rate considering the hourly and monthly fluctuations in evaporation, local effects and estimation errors.

3.5.2 Weather conditions limits

For Beaufort-Wes, especially in summer, air temperature is the dominant variable. Prevention measures should be implemented for air temperatures of >23.3°C, in summer, and >17.1°C, in winter, since these values would result in exceeding the evaporation rate of 0.5 kg/m^2/h suggested by Carden and Ramey [115]. Concrete placement should be avoided in temperatures >27.7°C since this would result in exceeding the evaporation rate of 1 kg/m^2/h. At a temperature of 30°C, the limit suggested by ENV 206 [108], is likely to result in an evaporation rate of 1.2 kg/m^2/h.

Wind is the dominant variable in Cape Town. Prevention measures should be implemented for wind speeds >5.5 m/s or temperatures >22.8°C, in summer, and >18.8°C in winter since these values would result in exceeding the evaporation

rate of 0.5 kg/m^2/h. Concrete placement should be avoided for temperatures >25.5°C and wind speeds >7 m/s since these values would result in exceeding the evaporation rate of 1 kg/m^2/h. By reducing the wind speed by 50% the evaporation rate can be reduced from 1 to 0.55 kg/m^2/h.

3.5.3 Testing conditions

The most likely combination of weather conditions resulting in an evaporation rate of 1 kg/m^2/h is 27.7°C, 3.47 m/s and 27.9% in Beaufort-Wes and 25.4°C, 7.51 m/s and 47.2% in Cape Town. It is recommended that one of these combinations of weather conditions are used as testing conditions to study PSC. The climate at the intended location should be used to select either the Cape Town or Beaufort-Wes combination.

3.5.4 Best time of placement

In Beaufort-Wes, the daily maximum mean temperature exceeds the temperature limit recommended by this study in all the months except June and July. The daily maximum mean temperature exceeds the 30°C limit suggested by ENV 206 [108] in December, January and February. The wind speed is higher in winter than in summer but the evaporation rate in summer is around 3 times higher than in winter. In January (in which the highest evaporation rate occurs) the hourly temperature exceeds the recommended limit between 10:00 and 22:00. The hourly evaporation rate of 0.5 kg/m^2/h, suggested by Carden and Ramey [115], is exceeded from 11:00 to 22:00 with the lowest evaporation rate occurring between 2:00 and 6:00. In Beaufort-Wes the evaporation rate peak occurs later in the day compared to Cape Town, mainly due to the temperature peaking later. From the hourly evaporation rate and air temperature results, it is recommended that concrete is placed as early in the mornings as possible, preferably reaching its final set before 10:00.

In Cape Town, the daily maximum temperature exceeds the temperature limit recommended by this study in all the months except June, July, August and September. During summer months wind speeds are extremely high. The evaporation rates in summer are around 3 times higher than in winter and less variable than Beaufort-Wes. In January, the hourly temperature exceeds the recommended limit between 9:30 and 17:30. The wind speed of 5.5 and 7 m/s are commonly exceeded after 10:00 and 14:00, respectively. In summer, the peak hourly evaporation rate occurs almost exactly in-between the peak temperature and wind speed. The hourly evaporation rate of 0.5 kg/m^2/h, suggested by Carden and Ramey [115], is exceeded from 10:00 to 19:00 with the lowest evaporation rate occurring between 2:00 and 7:00. From the hourly air temperature, wind speed and evaporation rate

results, early morning placement can be recommended, with the concrete reaching a final set before 10:00. Alternatively, evening placement may also be an option. After 19:00 the evaporation rate is likely to decrease below 0.5 kg/m^2/h. Ortiz et al. [97] has recommended placing concrete in the evening, after the peak evaporation rate. They argued that exposing the fresh concrete to lower temperatures during the night would result in a more structured formation of the hydration products and higher long-term strength.

3.5.5 Site specific conditions

The weather conditions at a specific site would not necessarily correspond to the conditions at the central weather station, even if they are in close proximity. Factors specific to the site can have a significant effect on the micro-climate. The results indicate that the magnitude of the wind speed at the site (Douglas) differs from that at the central weather station (Cape Town). However, similar trends in the hourly fluctuations of air temperature, wind speed and evaporation rate over time were noticed in Cape Town, Douglas (a specific site) and Atlantis (located 41.22 km from Cape Town). The methodological processes driving the weather conditions are similar for the broader area (location) and, therefore, also the trends in the development of these conditions.

Wind speed increases with elevation but this increase is not proportional to an increase in evaporation rate. In fact, the magnitude of the evaporation was not significantly affected by the increase in elevation.

3.5.6 Most effective curing methods

Literature [126, 53, 115, 127, 99, 51, 128] suggests that choosing an appropriate time for concrete placement, in combination with windbreaks, fogging and chemical curing between 0.5 and 4 hours after placement and plastic or wet burlap covering between 4 and 8 hours after placement is critical to reduce evaporation in extremely hot, dry and windy climates. In general, a reduction in the evaporation rate, achieved by any means possible, would reduce the risk op PSC and improve the long-term properties of the concrete.

In Beaufort-Wes, where evaporation is mainly dependent on air temperature, active curing measures such as fogging and evaporation reducing agents are recommended for air temperatures >23.3°C in summer, and >17.1°C in winter. Lowering the temperature of the concrete, by e.g. adding ice to the mixing water or suspending netting to reduce solar radiation, can also reduce evaporation [103, 100]. In Cape Town summers, fogging may be ineffective, due to the high wind speed. Windbreaks in combination with evaporation reducing agents are recommended for wind speeds >5.5 m/s and temperatures >22.8°C in summer, and >18.8°C in

winter. It has been shown that reducing the wind speed by 50% can almost half the evaporation rate.

3.5.7 PSC risk

The weather condition limits recommended by this study and evaporation rate limits suggested by ACI 305.1 [100], ENV 206 [108], CCAA [103], Carden and Ramey [115] are frequently exceeded in both the locations selected, especially in summer months. It is recommended that active curing measures are rigidly enforced throughout the year. Passive PSC prevention measures such as fibres, super absorbent polymers (SAP's) or shrinkage reducing admixtures (SRA) are advised for both locations in summer months. Selecting a placement time based on trends in weather data and the evaporativity of the environment is a cost effective and practical alternative to the aforementioned prevention measures.

3.6 Conclusion

A data analysis method to mitigate and reduce PSC was proposed. The method identifies the best time for concrete placement, most effective active curing methods and limits on weather condition for concrete placement from location-specific weather data. The results can provide guidance to concrete contractors and designers on the risk of PSC at the intended location as well as to researchers to determining appropriate testing conditions. The results are particularly valuable for concrete contractors who intend to choose placement times more than 7 days in advance, when weather forecasts are unreliable. The following conclusions can be drawn from this study:

- The Kohler-Menzel-Uno (KMU) evaporation estimation model is more sensitive to wind speed than the AFH model which is more sensitive to air temperature. However, the model choice does not have a significant effect on the evaporation rate result.
- The monthly and hourly fluctuations in evaporation rate were evaluated to suggest the best placement times. Both locations produced evaporation rates 3 times higher in summer than in winter. Regardless of the season, the evaporation rates are the lowest early in the morning.
- The weather conditions that dominate the evaporation rate is location-specific. The evaporation rate in one of the locations (Beaufort-Wes) is mainly dependent on air temperature. For the other location (Cape Town), the evaporation rate is equally dependent on air temperature and wind speed. Ac-

tive curing measures were recommended to reduce the identified dominant weather conditions.

- The most likely weather conditions at a specific evaporation rate were determined. From here, weather condition limits were recommended for which additional prevention measures are required.
- Although the magnitude of the weather conditions and the mean evaporation rates can differ from central weather station to a specific site, the trends in hourly and monthly fluctuations were very similar.
- Selecting a placement time based on the evaporativity of the environment can be a cost-effective solution to prevent and mitigate PSC.

Adequate curing is essential to any concrete project. Engineering judgement should be used to choose appropriate curing measures and placement times. This study attempts to provide assistance in this regard. Future work is required to implement the proposed method in other locations.

Chapter 4

The influence of solar radiation on plastic shrinkage cracking in concrete

Abstract

Plastic shrinkage cracking (PSC) in concrete is related to the amount and rate of free pore water loss due to evaporation. This study investigates the influence of solar radiation on evaporation, the concrete temperature, plastic shrinkage and cracking. Literature suggests that exposure to solar radiation can either: increase the concrete temperature and, consequently, increase the rate of tensile strength gain resulting in less severe PSC or can increase the concrete temperature, resulting in a higher amount and rate of pore water loss to produce more severe PSC. The results of this study indicate that exposure to solar radiation significantly increases the amount and rate of pore water loss as well as plastic shrinkage and severity of PSC. To study PSC, many authors have estimated the evaporation rate from wind speed, air and concrete temperature and humidity which would result in significantly underestimating the actual evaporation rate if the concrete is exposed to moderate or high solar radiation. The accuracy of several radiation-related evaporation estimation models was evaluated by comparing the models to the actual rate of evaporation from specimens placed in the sun. A more accurate model was identified to estimate the evaporation in concrete specimens when exposed to solar radiation.

Article information

Chapter 4 has been published as a journal article and can be cited as: **G.M. Moelich**, J.E. van Zyl, N. Rabie, R. Combrinck, The influence of solar radiation on plastic shrinkage cracking in concrete, Cement and Concrete Composites, vol. 123, October 2021, 104182. Online

Contribution declaration

With regard to this chapter, the nature and extent of the contributions of the candidate and the co-authors were as follow:

Name	Nature of contribution	Extent
G.M. Moelich (candidate)	Conceptualisation, Methodology, Validation, Formal analysis, Writing - original draft, Visualization, Investigation	85%
J.E. van Zyl	Conceptualisation, Methodology	5%
N. Rabie	Methodology	5%
Dr R. Combrinck (rcom@sun.ac.za)	Conceptualisation, Validation, Writing - review & editing, Supervision	5%

The undersigned hereby confirm that:

- The declaration above accurately reflects the nature and extent of the contributions of the candidate and the co-authors to this chapter.
- No other authors contributed to this chapter besides those specified above.
- Potential conflicts of interest have been revealed to all interested parties and that the necessary arrangements have been made to use the material in this chapter of the dissertation.

Signature of authors	Institutional affiliation	Date
	Department of Civil Engineering, Stellenbosch University	09/06/2021
	Department of Civil Engineering, Stellenbosch University	09/06/2021
	Department of Civil Engineering, Stellenbosch University	09/06/2021
	Department of Civil Engineering, Stellenbosch University	09/06/2021

4.1 Introduction

It is estimated that up to 40% of cracking in reinforced concrete structures forms before the concrete enters a solid state (further referred to as the plastic state), with roughly 80% of plastic cracking involving plastic shrinkage [129, 98]. The presence of any crack increases permeability and exposes the concrete and reinforcement to numerous physical and chemical processes that can lead to deterioration [130]. Plastic shrinkage cracking (PSC), in particular, propagates early in the service life of reinforced concrete structures and can result in a direct pathway for deterioration agents to corrode reinforcement. PSC can be a major concern, especially in flat concrete elements such as slabs, pavements and bridge decks exposed to rapid drying [42]. 3D printed concrete is also particularly vulnerable to PSC due to its high surface area to volume ratio [131, 132].

Ravina and Shalon [91] were one of the first to study the effect of evaporation on plastic shrinkage cracking. Their study accounted for air temperature, humidity, radiation and concrete temperature. An infrared light was used to mimic radiation, but the intensity was not quantified. The study showed that although radiation severely increased the rate and amount of shrinkage, plastic shrinkage cracking did not increase. It was shown that the temperature increase resulted in an increased rate of tensile strength gain and reduced plastic shrinkage cracking. Berhane [110] followed and studied the effect of air temperature, wind speed, humidity and concrete temperature on evaporation from concrete. The study ignored radiation, arguing that it would increase the concrete temperatures and, consequently, the rate of tensile strength gain. Shaeles and Hover [42] agreed, stating that the heat flux presented by radiation increases the rate of the hydration reaction and, consequently, the tensile strength gain. Ahmadi [95] and Schindler et al. [96] showed the extent to which concrete temperature can control the setting time—an indication of the progress of the stiffening and hydration processes in concrete. The setting time is relevant for PSC for the following reasons:

- Accelerating the setting time results in a decrease in the amount of pore water loss before the fresh concrete gains sufficient strength to resist shrinkage and can, therefore, decrease PSC [47].
- Combrinck and Boshoff [133] showed that the time-related tensile strength and strain capacity increased with an increase in concrete temperature. The earlier development of tensile strength resistance can mitigate PSC by resisting the stress caused by restraining plastic shrinkage [134].

On the other hand, radiation can supply pore water with additional energy to change from the liquid to the vapour phase and increase evaporation. Radiation can cause the concrete surface temperatures to rise above the air temperature,

creating a vapour pressure deficiency and increase evaporation [49, 135]. Cohen et al. [111] argued that earlier dissipation of the bleeding water would expose the concrete to shrinkage earlier when the tensile strength to resist the forces has not been fully developed, and result in more severe PSC. Hasanain et al. [126] conducted outdoor experiments and measured the evaporation for shaded and sun exposed concrete specimens. Radiation controlled the concrete surface temperature and mitigated the effect of evaporative cooling significantly. Shading resulted in a reduction of the total evaporation of up to 70%. The study did not measure shrinkage or cracking.

Both arguments are compelling. More recent studies that provide conclusive evidence on this topic could not be found. This study investigates the influence of radiation on the freshly place concrete temperature, the evaporation of the free pore water, plastic shrinkage and cracking experimentally. It is hypothesised that radiation would increase the loss in free pore water due to evaporation, the plastic shrinkage and the severity of cracking. The study goes further to evaluate evaporation estimation models which account for solar radiation experimentally. The models commonly used in the fields of Hydrology, Meteorology and Agriculture are adopted and adapted to estimate the water loss of concrete exposed to solar radiation.

4.2 Background

4.2.1 Radiation

Solar radiation is the electromagnetic waves emitted by the sun and arrives on the earth's surface in various forms, as seen in Fig. 4.1. The solar radiation is absorbed, reflected and scattered by gasses in the atmosphere to form diffused short-wave solar radiation (Diffused horizontal irradiation or DHI). The solar radiation that reaches the earth's surface without interference is known as direct short-wave solar radiation (Direct normal irradiation or DNI). The sum of the diffused solar radiation and direct solar radiation is the global short-wave solar radiation (Global horizontal irradiation or GHI). A portion of the short-wave solar radiation is absorbed by the earth and re-emitted as long-wave radiation (LW). The long-wave radiation can then be reflected back to the earth's surface by clouds or atmospheric gasses. The sum of all these radiations is known as the net radiation. Placing a specimen in the shade would eliminate the DNI component of the GHI. Furthermore, cloud cover would influence both DHI and LW significantly [136, 107].

This paper further refers to the specimen exposed to GHI as the sun specimen and to specimen not exposed to direct radiation (DNI) component of GHI as the

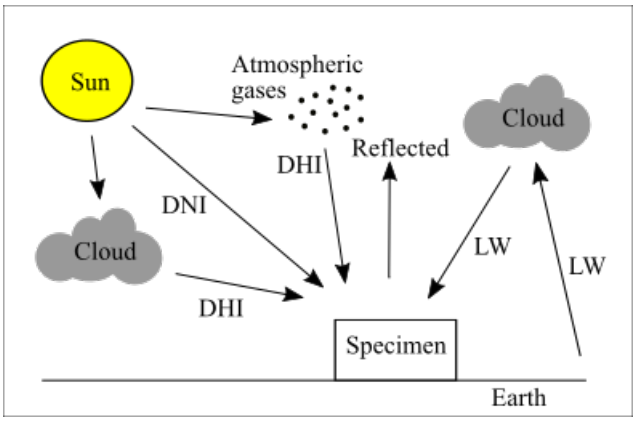

Figure 4.1: Incoming short-wave and long-wave radiation.

shaded specimen.

4.2.2 Evaporation estimation models currently used

To estimate evaporation from the concrete surface ACI 305.1 [100], CCAA [103] and PCA [104] specify that the Menzel [48] model should be used. This model was originally proposed by Kohler et al. [105] from the well-known Lake Hefner experiment. Although the experiments were conducted in the presence of solar radiation, the model does not require solar radiation as an input variable. The model can be rewritten as a function of wind speed, concrete temperature, air temperature and the relative humidity as done by Uno [50]. Uno [50] also proposed using the Penman [137] model to estimate pore water evaporation in the presence of solar radiation, but did not experimentally validate the recommendation. Al-Fadhala and Hover [51] proposed a different model from water-pan evaporation accounting for wind speed, relative humidity, initial concrete temperature and air temperature. Bakhshi et al. [52] estimated the evaporation of water from the concrete surface based on the boundary-layer theory, mass transfer, diffusion and convection. Both the Bakhshi and Al-Fadhala-Hover models did not account for radiation.

According to Allen et al. [138] and WMO [107], the radiation energy captured by a water body is one of the main factors driving evaporation. Winter et al. [139] stated that solar and atmospheric radiation are the most significant energy inputs to the water body. Currently, in the fields of Hydrology, Meteorology and Agriculture, most of the evaporation models are a function of radiation. It is for this reason that this study aims to evaluate and suggest appropriate radiation-related evaporation estimation models to estimate water evaporation from concrete.

4.3 Models to be evaluated

Hydrologists have studied evaporation from ponds and lakes for centuries. It is from these measurements that various models to estimate the open water evaporation have been proposed, even the Kohler-Menzel-Uno model. A great deal of research has been conducted to compare these models for different water bodies under different conditions.

The Bowen-ratio energy-budget (BREB) method is considered the standard when estimating evaporation from weather data [140, 141, 139, 142]. Numerous other evaporation estimation methods have also been proposed; eddy-covariance, surface-renewal, LIDAR and other laser-based methods [141]. For more on these methods, Drexler et al. [140] can be consulted.

4.3.1 Bowen-ratio energy-budget (BREB)

The energy-budget approach relates the net energy transfer to and from the body to evaporation. The method has been used by Anderson [143] on the same Lake Hefner experiment as Kohler et al. [105] with great accuracy. The evaporation rate can be calculated with:

$$E_{eb} = \frac{Q_S - Q_R + Q_{LW} - Q_{LWR} - Q_{BS} - Q_x}{\rho(L(1 + R_B) + cT_o)} \tag{4.1}$$

where E_{eb} is the energy-budget evaporation rate, Q_S is the incoming short-wave solar radiation (GHI), Q_R is the reflected short-wave solar radiation, Q_{LW} is the incoming long-wave atmospheric radiation, Q_{LWR} is the reflected long-wave atmospheric radiation, Q_{BS} is the long-wave atmospheric radiation emitted from the body, Q_X is the change in energy content of the body of water, ρ is the density of water, L is the latent heat due to the vaporisation of water, R_B is the Bowen ratio, c is the specific heat of water and T_o is the water surface temperature. With the net radiation (Q_N) as $Q_N = Q_S - Q_R + Q_{LW} - Q_{LWR} - Q_{BS}$. The Bowen ratio can be calculated with:

$$R_B = \frac{c_b P(T_o - T_a)}{(e_o - e_a)} \tag{4.2}$$

where c_b is an empirical constant (0.61°C), T_a is the temperature of the air, e_o is the vapour pressure of saturated air at the temperature of the water surface, e_a is the vapour pressure of the air and P is the atmospheric pressure.

For this study, Q_R, Q_{LW}, Q_{LWR} and Q_{BS} were estimated due to an absence of measuring equipment. The contributions of these forms of radiations to Q_N are relatively small when compared to Q_S. An estimation error would, therefore, have a insignificant effect on the resulting evaporation [141].

Q_{LW} was taken as $\alpha \times Q_S$, with α (the soil albedo value) equal to 0.05 as in Oke [144]. For a clear-sky Q_{LW} was estimated according to Brutsaert [145] as suggested by Duarte et al. [146]:

$$Q_{LW}clear = 0.643\left(\frac{e_a}{T_a}\right)^{1/7}\sigma T_a^4 \tag{4.3}$$

with σ the Stephan-Boltzman constant (5.67×10^{-8}). For overcast conditions the model suggested by Jacobs [147] is used as:

$$Q_{LW}cloudy = Q_{LW}clear(1 + \alpha c_c^{\beta}) \tag{4.4}$$

with α and β, equal to 0.263 and 0.69 respectively as suggested by Duarte et al. [146] and c_c the fractional cloud cover. The method showed excellent results when compared to measured downward long wave radiation [148]. Q_{LWR} was taken as 3% of Q_{LW} [143]. Q_{BS} was taken as:

$$Q_{BS} = \varepsilon\sigma T_o^4 \tag{4.5}$$

with ε the soil emissivity values, equal to 0.97 [143] or 0.9 [148]. Q_X was calculated according to Giadrossich et al. [149] as:

$$Q_X = \frac{\rho_w c_w}{A(t)\Delta t}\sum_{i=1}^{n_i} V_i \Delta T_i \tag{4.6}$$

with $A\Delta t$ the surface area, n_i is the number of layers where temperature is measured, $\Delta T_i = T_i(t) - T_i(t - \Delta t)$ is the temperature deference of the layer i over the time step Δt and V_i is the volume of layer i.

4.3.2 Other evaporation estimation models

Since the BREB model requires many complex inputs and expensive measuring instrumentation, simplified methods were developed. The Penman-Monteith model is the standard for estimating evaporation from vegetation-covered soil [138]. Combination models, such as Brutsaert-Sticker, Penman, deBruin-Keijman, Priestley-Taylor, include energy and aerodynamic terms and are regularly used to estimate open water evaporation. Stewart and Rouse [150] showed that for a half-hourly and daily estimation period, open water evaporation could be approximated closely by the Priestley-Taylor model. Rosenberry and Likens [141] showed the BREB model could be approximated with deBruin-Keijman, Priestley-Taylor and Penman with a regression (R^2) value of 0.97, 0.97 and 0.96, respectively. The models evaluated in this study can be seen in Table 4.1.

Table 4.1: Evaporation estimation models evaluated in this study

Model	Reference	Input variables
Penmen-Monteith	Penman [151]	$Q_N, Q_X, T_a, T_o, v, rh$
Penman	Penman [137]	$Q_N, Q_X, T_a, T_o, v, rh$
Brutsaert-Sticker	Brutsaert and Stricker [152]	$Q_N, Q_X, T_a, T_o, v, rh$
deBruin-Keijman	De Bruin and Keijman [153]	Q_N, Q_X, T_a, T_o, rh
Priestley-Taylor	Priestley and Taylor [154]	Q_N, Q_X, T_a, T_o, rh
Makkink	Rosenberry and Likens [141]	Q_S, T_a, T_o, rh
Jensen-Haise	Rosenberry and Likens [141]	Q_S, T_a
Uno	Uno [50]	T_a, T_o, v, rh
AlFadhala-Hover	Al-Fadhala and Hover [51]	T_a, T_o, v, rh

Q_N - net radiation; v - wind speed; rh - relative humidity.

4.4 Experimental program

4.4.1 Moulds

PVC moulds with inner dimensions of 200 × 200 × 100 mm, as seen in Fig. 4.2 a), were used to measure evaporation. The setup used to measure the concrete temperature can be seen in Fig. 4.2 b). The plastic shrinkage was measured with the setup in Fig. 4.3 a). The study used a PSC cracking mould as suggested by ASTM C1579 [109] with additional steel bars as seen in Fig. 4.3 b). Each mould was sealed with a silicone sealant to prevent water leakage. Mould release oil was applied to each mould before the experiment.

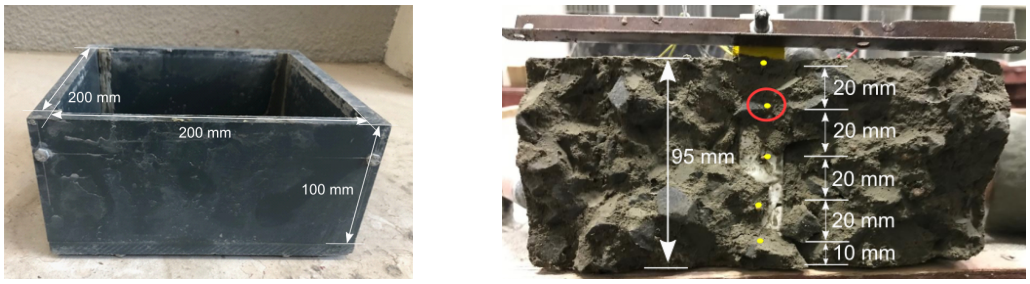

(a) **(b)**

Figure 4.2: a) Mould used to measure mass loss due to evaporation. b) Temperature sensors embedded at different depths in the concrete specimen.

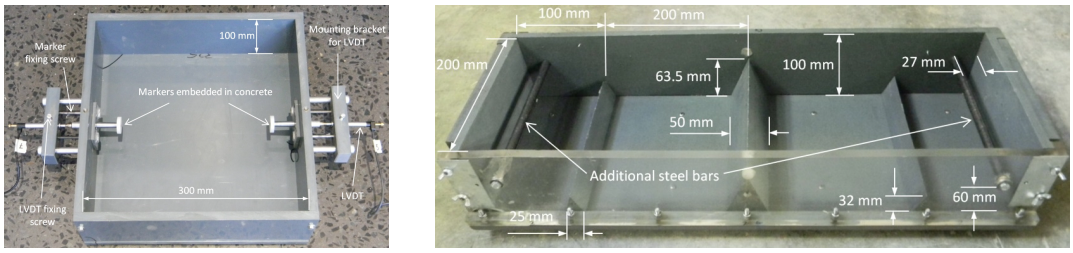

(a) (b)

Figure 4.3: a) Plastic shrinkage mould. b) Plastic shrinkage cracking mould. [94]

4.4.2 Mixes and mixing procedure

The mixtures can be seen in Table 4.2. For the SL mix, the cement was replaced with blast furnace slag to reduce water consumption due to hydration, but without significantly changing the particle size distribution. The SW mix only contained sand and water, eliminating hydration and changing the particle size distribution. CM2 has a higher W/C ratio, cement content and different type of cement when compared to CM1. Cement A contains 6% to 20% limestone extender and is used in CM1. Cement B contains 35% to 65% blast furnace slag and is used in CM2.

Table 4.2: Mixes used in this study.

Mixture	CM1	CM2	SL	SW
Water	205	205	205	339
Cement A - CEM II 52,5 N	350	-	-	-
Cement B - CEM III 42.5 N	-	466	-	-
Slag	-	-	350	-
Natural quarry sand	980	900	980	1732
13 mm Greywacke stone	874	850	850	-

The materials were placed in a climate-controlled room, with a temperature of 23°C and relative humidity of 60%, 24 h before each experiment. The materials were mixed for 1 minute dry, after which water was added and mixing continued for another 2 minutes. The specimens were vibrated for 5 minutes at a low intensity on a vibration table and finished with a steel float. It took 10 minutes to transport the specimens to the test site. Placement time is defined as 20 minutes after mixing is complete. The experiments were conducted in an area with nearly no surrounding obstacles (on the roof of a five story building, as seen in Figure 4.4). A weather station located at the test-site was used to track the weather conditions.

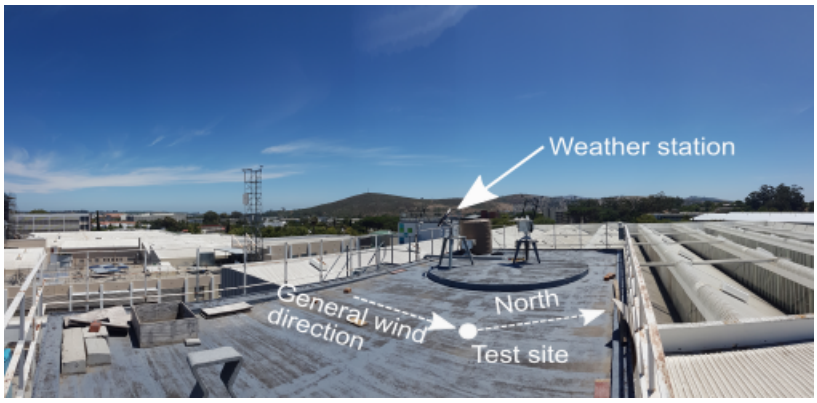

Figure 4.4: Test-site for all the experiments conducted in this study.

4.4.3 Measurements

In general, the individual specimens, tested on the same day, showed an excellent agreement with one another and had a small standard deviation. The evaporation rates were determined by weighing three samples every 30 minutes and taking the average of the results. The temperature measurements were taken from one additional specimen and used in the evaporation models. The temperature sensor embedded 25 mm below the surface was taken as a representation of the concrete temperature.

The shrinkage was measured as explained in Combrinck et al. [94] and Combrinck et al. [155]. The severity of cracking was measured by photographing cracks every 15 minutes and using image processing software (written in Matlab following the procedure set out by Qi et al. [60]) to determine the crack area. The results of the two PSC cracking moulds and the two shrinkage moulds were averaged.

Setting times of mortar specimens, sieved from the concrete using a 4.75 mm sieve, were determined in accordance with the procedure set out in **?**]. Two closed specimens were placed in the sun and two in the shade to expose the setting time specimens to the same temperature as the other sun and shaded specimens. The setting time specimens were only open when the penetration test was being conducted.

The instrumentation and measurement intervals used for the weather conditions and evaporation rate can be seen in Table 4.3. These instruments comply with international weather station standards [107]. The wind speed, air temperature, relative humidity and solar radiation measurement devices were located 1.5 m above the evaporation specimens.

The cloud cover (c_c) was determined every 30 minutes with a visual inspection. The sky was divided into segments to estimating the percentage of the sky covered with clouds. This method is recommended by Duarte et al. [146] and Choi

Table 4.3: Instruments used for measurements

Measurement	Measuring device	Interval
Air temperature	Campbell CS215 with radiation shield	60 s
Concrete temperature	NTC Thermistors and seen in Fig. 4.2 b)	60 s
Relative humidity	Campbell CS215 with radiation shield	60 s
Wind speed	Campbell R.M. Young 03001	60 s
Global radiance (GHI)	Kipp&Zone CMP11 pyranometer	60 s
Diffuse radiance (DHI)	Kipp&Zone CMP11 pyranometer	60 s
Evaporation	Micro scale 15kg x 0.1g	30 min

et al. [148] to estimate the incoming long-wave atmospheric radiation, used in the evaporation estimation models.

Although c_c gives a reasonable estimate of the cloud cover, a more scientific approach is required to classify the experiments and to discuss the results of this study. A variable R can be defined as:

$$R = \frac{DHI}{GHI} \tag{4.7}$$

R is the ratio of the radiation on a shaded surface (DHI) over the radiation on a surface exposed to the sun (GHI) and is used as an indication of cloud cover in this study. On days with a low c_c, R is small and closer to the value of 0. On days with a high c_c, R is higher and closer to the value of 1. The relationship between c_c and R for three cloudy days can be seen in Fig. 4.5.

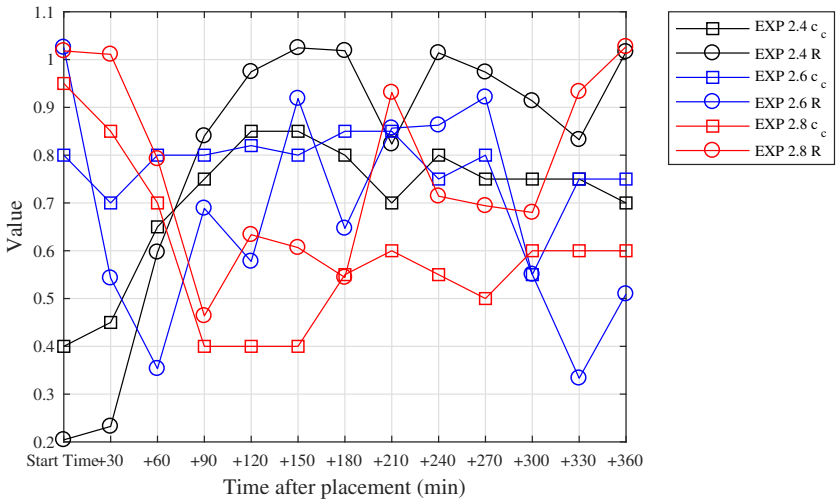

Figure 4.5: The relationship between c_c and R for three cloudy days (EXP 2.4, 2.6 and 2.8).

4.4.4 Test conditions

The temperature, wind speed, relative humidity, solar radiation, cloud cover and evaporation can be categorised in low, moderate and high (Table 4.4). These categories were chosen to ensure that a wide range of weather conditions were considered and that the test conditions represent the climate of the test location. The categories are specific to the test location and are necessary to improve the readability of the discussion.

Table 4.4: Testing condition categories.

	Temperature (^{o}C)	Wind (m/s)	GHI (W/m^2)	R (%)	ER ($kg/m^2/h$)
Low	<18	<2	<600	<15	<0.4
Moderate	18-25	2-4	600-800	15-50	0.4-0.6
High	>25	>4	>800	>50	>0.6

ER - Evaporation rate ; R - Cloud cover.

4.4.5 Experimental program

A summary of the experimental program can be seen in Table 4.5. EXP 1.1 to 1.6 were conducted to determine the influence of the mixture on the water loss due to evaporation. For EXP 2.1 to 2.8 and EXP 3.1 to 3.3, the direct solar radiation (DNI) was eliminated by placing the one set of specimens in the shade. The other set was placed in the sun (GHI) 2 m upwind, parallel to the first set, as seen in Fig. 4.6.

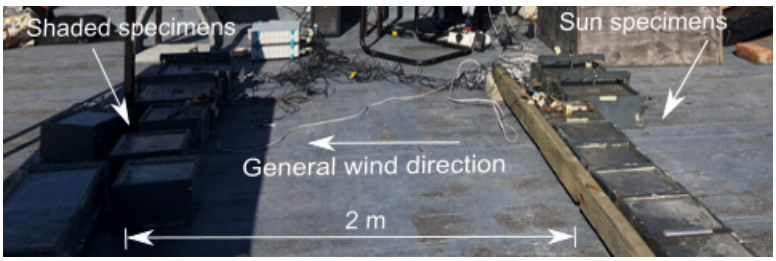

Figure 4.6: The shaded specimens placed 2 m downwind from the sun specimens.

Table 4.5: A summary of the experiments conducted.

	T_a (^oC)	Wind (m/s)	GHI (W/m^2)	DHI (W/m^2)	R (%)	AER sun ($kg/m^2/h$)	AER shade ($kg/m^2/h$)	Shrinkage measured	Cracking measured	Mix
EXP1.1	25.49	2.14	654.36	-	-	0.62	-	No	No	CM1, SL
EXP1.2	15.56	3.38	369.37	-	-	0.36	-	No	No	CM1, SL, SW
EXP1.3	15.24	0.66	456.37	-	-	0.31	-	No	No	CM1, SL, SW
EXP1.4	24.30	1.85	364.80	-	-	0.43	-	No	No	CM1, SL, SW
EXP1.5	16.17	2.46	390.86	-	-	0.34	-	No	No	CM1, SL, SW
EXP1.6	19.00	0.95	423.28	-	-	0.36	-	No	No	CM1, SL, SW
EXP2.1	18.50	2.11	485.50	63.25	13.03	0.34	0.158	Yes	Yes	CM1
EXP2.2	19.74	1.61	570.21	61.75	10.83	0.46	0.19	Yes	Yes	CM1
EXP2.3	19.87	2.11	505.33	145.8	28.85	0.41	0.19	Yes	Yes	CM1
EXP2.4	14.68	1.45	308.83	288.83	93.5	0.35	0.27	Yes	Yes	CM1
EXP2.5	20.15	1.78	575.36	273.54	47.54	0.5	0.26	Yes	Yes	CM1
EXP2.6	18.57	2.70	514.51	353.31	68.67	0.55	0.33	Yes	Yes	CM1
EXP2.7	21.00	2.50	644.00	100.62	15.64	0.6	0.23	Yes	Yes	CM2
EXP2.8	27.46	2.61	475.62	326.5	68.6	0.67	0.5	Yes	Yes	CM2
EXP3.1	27.73	4.08	933.70	91.73	9.8	0.80	0.55	Yes	Yes	CM2
EXP3.2	22.34	1.85	947.54	88.82	9.37	0.74	0.33	Yes	Yes	CM2
EXP3.3	23.70	5.67	975.36	70.09	7.19	0.76	0.48	Yes	Yes	CM2

EXP - Experiment; AER - Actual evaporation rate.

4.5 Results

4.5.1 Materials

The mean water loss of CM1, SL and SW can be seen in Fig. 4.7. The cumulative evaporation of CM1, SL and SW was calculated by averaging the results from EXP 1.1, 1.2, 1.3, 1.4, 1.5 and 1.6. The mean Uno evaporation rate of the five experiments was estimated using the 30 minutes averaged wind speed, air temperature and relative humidity of each experiment. Here, the concrete temperature was assumed to be equal to the air temperature.

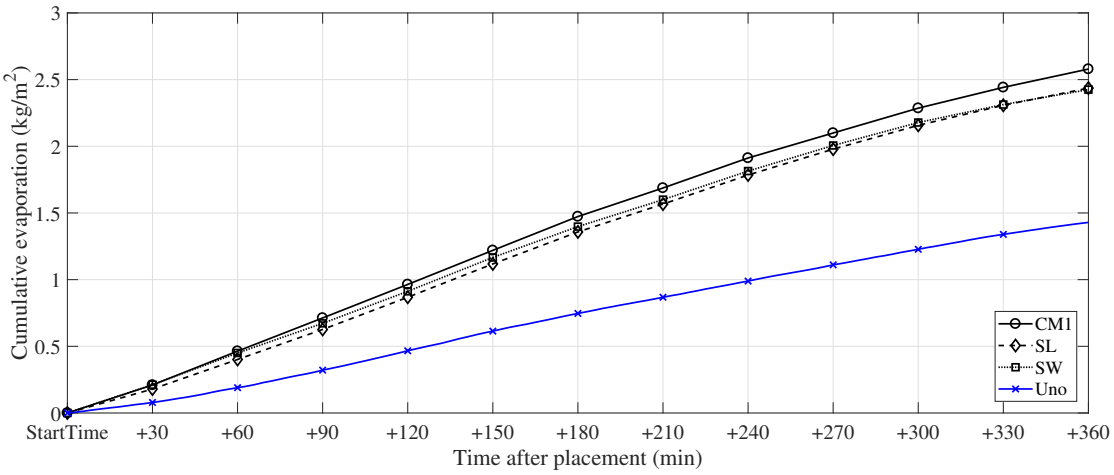

Figure 4.7: The mean cumulative evaporation of CM1, SL and SW. The cumulative mean evaporation rate as estimated by Uno is used as a reference.

The difference in evaporation between CM1 and SL, and CM1 and SW is minimal. The evaporation of the SL mixture is 14% lower after the first 30 minutes and 5.5% lower after 6 hours when compared to CM1. The water loss of the SW mixture is 1% higher after the first 30 minutes and 6% lower after 6 hours when compared to CM1. All the individual experiments show a similar trend. Under the test conditions, the results indicate that the environmental conditions dictate the evaporation rate for the first six hours after placement. In the test conditions, the hydration rate and particle size distribution have a minimal effect on the evaporation rate during this period.

4.5.2 Evaporation

4.5.2.1 The influence of cloud cover on evaporation

The difference in water loss between the specimens exposed to GHI (full sun) and non-direct (shade) radiation mainly depends on the cloud cover, solar radiation and wind speed. For the days with low cloud cover (R<15%), moderate air temperature (18-25 ^oC), low wind (<2 m/s) and low GHI (<600 W/m^2), the cumulative evaporation of EXP 2.1 and 2.2 were averaged. Fig. 4.8 shows the mean, maximum (EXP 2.2) and minimum (EXP 2.1) cumulative evaporation measured during the two experiments. The Uno evaporation rate is calculated from the air temperature, wind speed and relative humidity and assumes the concrete temperature to be equal to the air temperature. The Uno evaporation rate is used as a reference in this section and is only compared to other models later in this study.

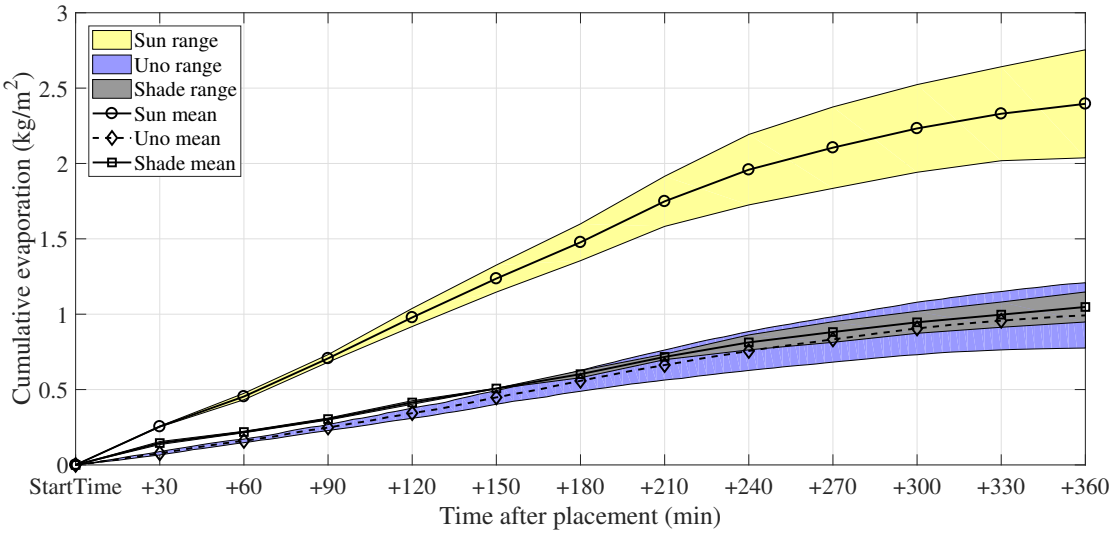

Figure 4.8: The cumulative evaporation of specimens exposed to global (GHI) and non-direct radiation (no DNI) on days (EXP 2.1 and 2.2) with low cloud cover, low wind speed and low GHI. The evaporation rate as estimated by Uno is used as a reference.

Exposure to direct normal radiation (DNI) resulted in a mean increase in evaporation rate of 108% in the first 60 minutes, with the peak increase of 145% occurring 180 minutes after placement. The cumulative evaporation after 6 hours was on average 129% higher in the sun specimens. It is clear that exposing specimens to the sun (GHI) produced a higher water loss than shading specimens (no DNI). Hasanain et al. [126] showed similar results, with a total increase of 70% due to exposure to direct normal radiation.

For the days with moderate cloud cover (R=38.15%), the cumulative evaporation of EXP 2.3 and 2.5 were averaged. Fig. 4.9 shows the mean, maximum (EXP 2.5) and minimum (EXP 2.3) cumulative evaporation measured during these experiments.

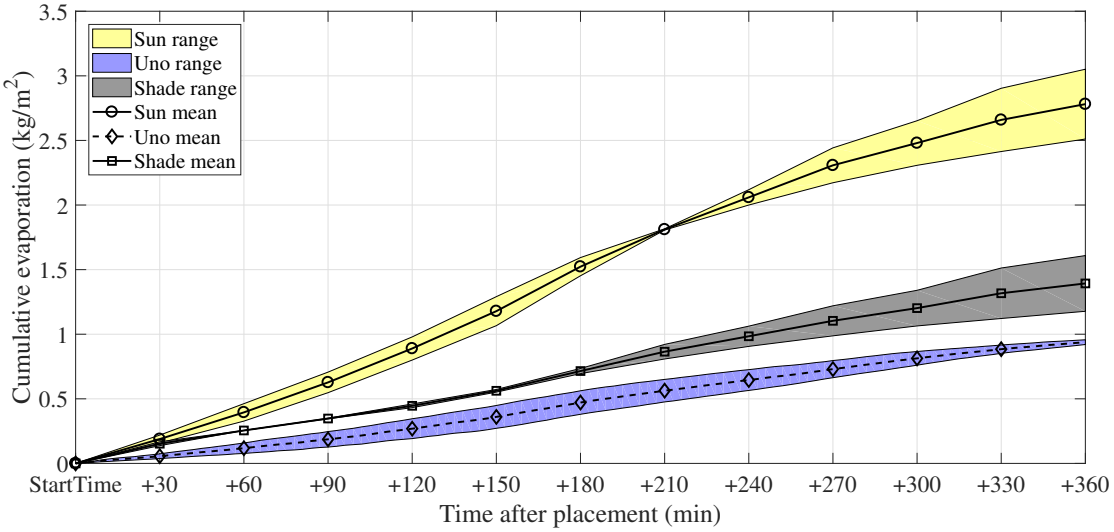

Figure 4.9: The cumulative evaporation of specimens exposed to global (GHI) and non-direct radiation (no DNI) on days (EXP 2.3 and 2.5) with moderate cloud cover, moderate temperature, low wind speed and low GHI.

Under moderate (R=38.15%) cloud cover direct normal radiation (DNI) exposure resulted in a mean cumulative evaporation increase of 55% in the first 60 minutes with the peak increase of 113% occurring 180 minutes after placement. The total water loss after 6 hours was 100% higher in the specimens exposed to DNI. The difference in total cumulative water loss between the sun and shaded specimens decreases from 129% (EXP 2.1 and 2.2, Fig. 4.8) to 100% (EXP 2.3 and 2.5, Fig. 4.9) due to an increase in cloud cover (R) from <15% to 38.15%. Exposing the specimens to the sun (GHI) produced a higher water loss than shading the specimens (no DNI) under minimal cloud cover. However, the increase in cloud cover increased the DHI to GHI ratio and, consequently, the total radiation on the shade specimens, resulting in a decrease in the difference in total water loss between the sun and shaded specimens.

For the days with substantial cloud cover (R=81.1%), the cumulative evaporation of EXP 2.4 and 2.6 were averaged. Fig. 4.10 shows the mean, maximum (EXP 2.6) and minimum (EXP 2.4) cumulative evaporation measured during these experiments.

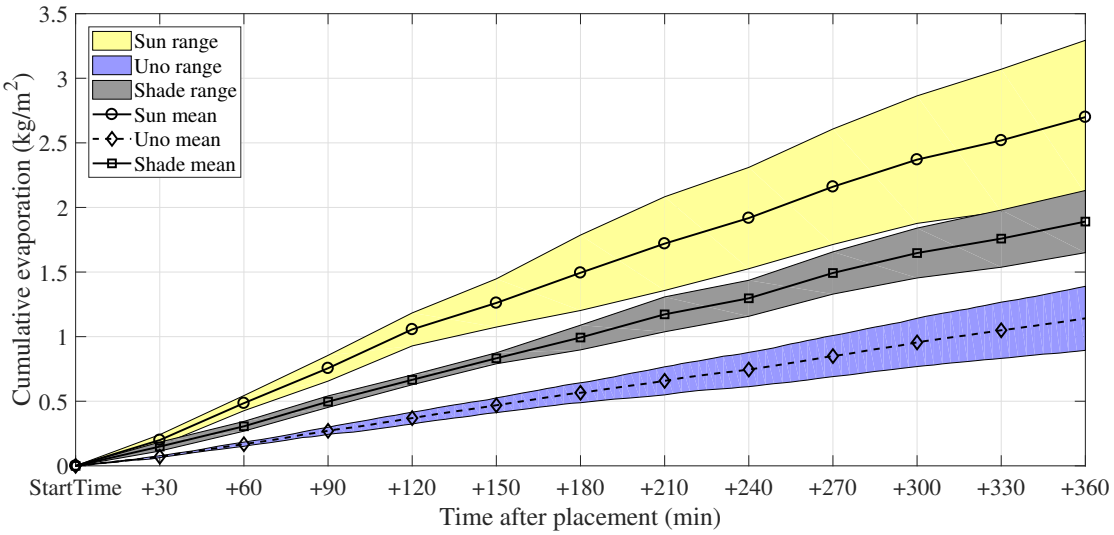

Figure 4.10: The cumulative evaporation of specimens exposed to global (GHI) and non-direct radiation (no DNI) on days (EXP 2.4 and 2.6) with substantial cloud cover, low temperature, low wind speed and low GHI.

The specimens exposed to the sun still exhibit a water loss higher than the shaded specimen with an increase in cumulative evaporation of 60% in the first 60 minutes and a peak increase of only 59%, 120 minutes after casting. The difference in total cumulative evaporation between the sun and shaded specimens decreases from 100% (EXP 2.3 and 2.5, Fig. 4.9) to 59% (EXP 2.4 and 2.6, Fig. 4.10) due to an increase in cloud cover from 38.15% to 81.1%. A similar trend is observed as when increasing the cloud cover (R) from <15% to 38.15%.

4.5.2.2 The influence of GHI on evaporation

For the days with low cloud cover (R<15%), moderate temperature (18-25 ^oC), moderate wind speeds (2-4 m/s) and high GHI (>800 W/m^2), the cumulative evaporation of EXP 2.7 and 3.2 were averaged. Fig. 4.11 shows the mean, maximum (EXP 3.2) and minimum (EXP 2.7) cumulative evaporation measured during these experiments.

Under a high GHI, direct normal radiation (DNI) exposure resulted in a mean increase in cumulative evaporation of 125% in the first 60 minutes with the peak increase of 172% occurring 210 minutes after placement. The total cumulative evaporation after 6 hours was 135% higher in the specimens exposed to direct normal radiation. The difference in total cumulative evaporation between the sun and shaded specimens increased from 129% (EXP 2.1 and 2.2, Fig. 4.8) to 135% (EXP 2.7 and 3.2, Fig. 4.11) due to an increase in GHI from 527 W/m^2 to 795 W/m^2. The increase in GHI is not proportional to an increase in DHI under

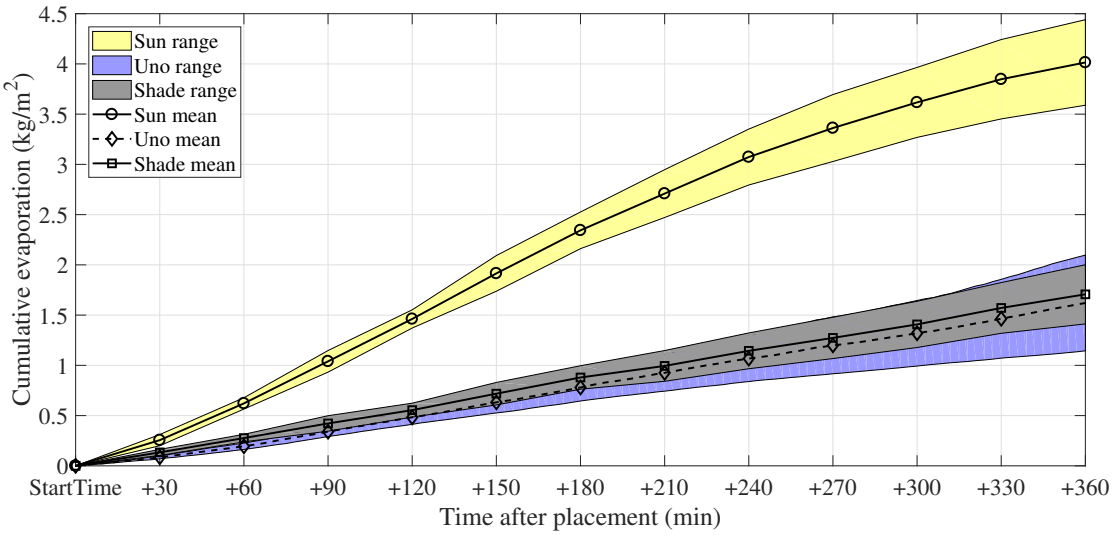

Figure 4.11: The cumulative evaporation of specimens exposed to global (GHI) and non-direct radiation (no DNI) on days (EXP 2.7 and 3.2) with a high GHI, low cloud cover, moderate wind speeds and moderate air temperatures.

clear skies. Therefore, an increase in GHI resulted in an even greater difference in mass loss between the sun and shaded specimens.

4.5.2.3 The influence of wind on evaporation

For the days with low cloud cover (R<15%), high wind speeds (>4 m/s) and a high GHI (>800 W/m^2), the cumulative evaporation of EXP 3.1 and 3.3 were averaged. Fig. 4.12 shows the mean, maximum (EXP 3.1) and minimum (EXP 3.3) cumulative evaporation measured during these experiments.

Under a high wind speed, direct radiation exposure resulted in a mean increase in cumulative evaporation of 102% in the first 60 minutes with the peak increase of 111% occurring 120 minutes after placement. The total cumulative evaporation after 6 hours was 53% higher in the specimens exposed to direct radiation. The difference in total cumulative evaporation between the sun and shaded specimens decreased from 135% (EXP 2.7 and 3.2, Fig. 4.11) to 53% (EXP 3.1 and 3.3, Fig. 4.12) due to an increase in wind speed from 2.1 to 4.8 m/s. A higher wind speed increased the cumulative evaporation in the sun and shaded specimen, but decreased the difference between the sun and shaded specimens. That being said, the specimens exposed to the sun still have a higher cumulative evaporation rate.

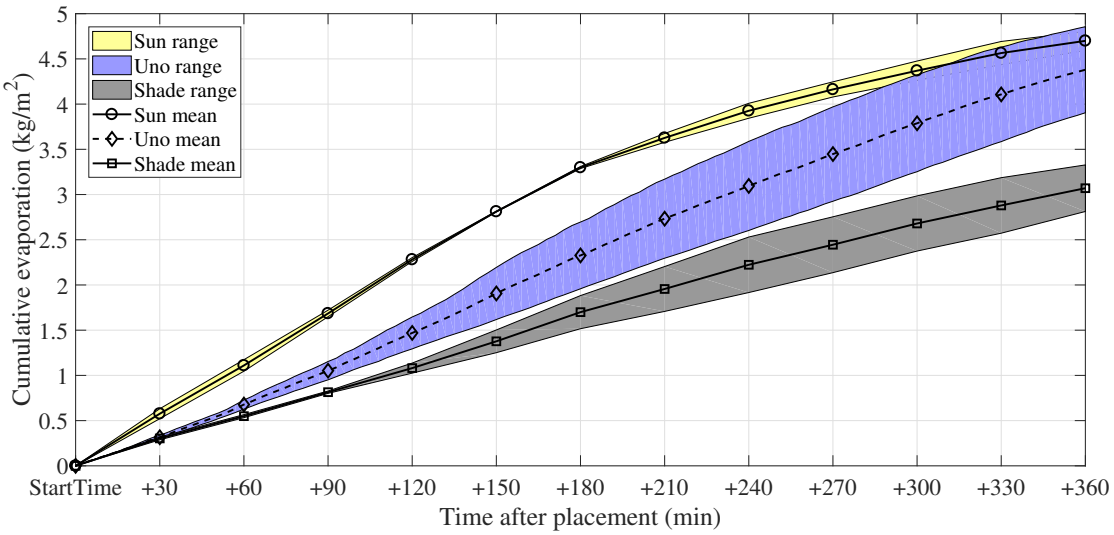

Figure 4.12: The cumulative evaporation of specimens exposed to global (GHI) and non-direct radiation (no DNI) on days (EXP 3.1 and 3.3) with a higher wind speeds, high GHI and low cloud cover.

4.5.3 Diffused radiation

The relationship between diffused radiation (DHI) and cloud cover can be seen in Fig. 4.13. As done previously, EXP 2.1 and 2.2 were categorised under low cloud cover (R<15%), EXP 2.3 and 2.5 under moderate cloud cover (R=38.15%) and EXP 2.4 and 2.6 under substantial cloud cover (R=81.1%).

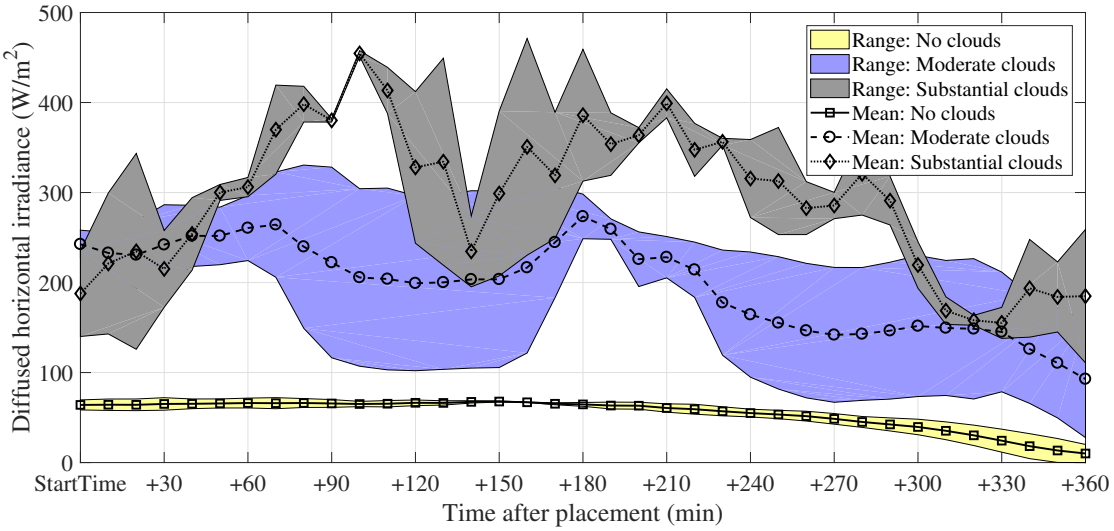

Figure 4.13: The diffused radiation for low, moderate and substantial cloud cover.

The diffused radiation (DHI) increased with an increase in cloud cover. An increase in cloud cover from <15% to 81.1% can increase the DHI up to 460%. Shaded specimens would, therefore, be exposed to higher radiation with an increase in cloud cover. This confirms the previous result regarding the difference in evaporation between the sun and shaded specimens decreasing with an increase in cloud cover.

4.5.4 Temperature

Exposing the specimens to direct radiation significantly affected the concrete temperatures. Fig. 4.14 shows the change in concrete temperatures (measured 25 mm below the surface) of the sun and shaded specimens over time. The results from EXP 3.1, 3.2 and 3.3 were averaged for Fig. 4.14.

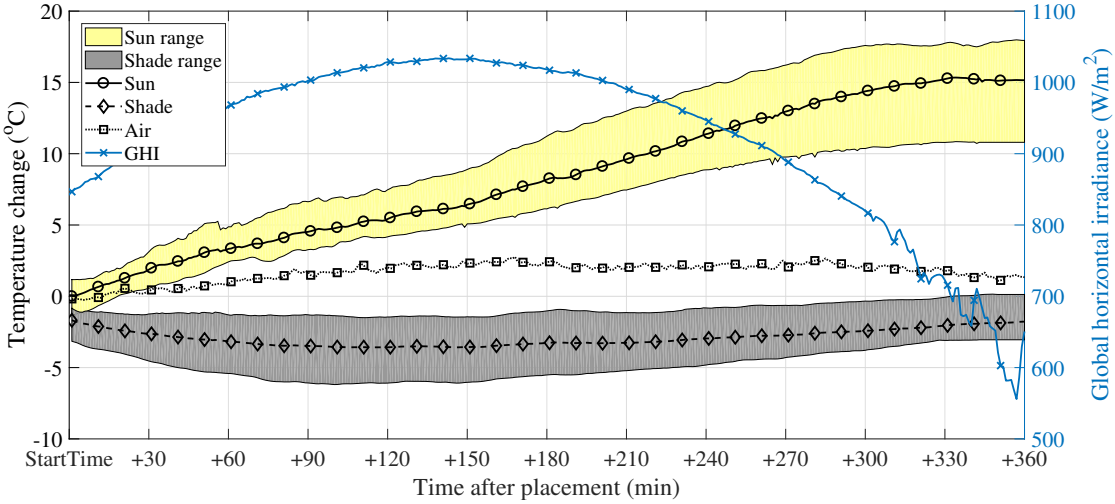

Figure 4.14: The change in concrete temperature after placement in the sun and shaded specimens. The air temperature and GHI can be used as a reference.

The concrete temperature is significantly higher in the sun specimen when compared to the shaded specimen. On average, the sun specimens experienced an increase in concrete temperature of 15°C over 6 hours due to a combination of GHI and air temperature. In the shaded specimens, the concrete temperature decreased by 3.4°C in the first 3 hours due to evaporative cooling. The evaporative cooling effect was not noticeable in the sun specimen due to the direct radiation dominating the concrete temperature. Hasanain et al. [126] also showed that direct radiation influenced the concrete temperature more than evaporated cooling.

The change in concrete temperatures can be affected by the cloud cover, as seen in Fig. 4.15. As done previously, EXP 2.1 and 2.2 were categorised under low

cloud cover (R<15%), EXP 2.3 and 2.5 under moderate cloud cover (R=38.15%) and EXP 2.4 and 2.6 under substantial cloud cover (R=81.1%).

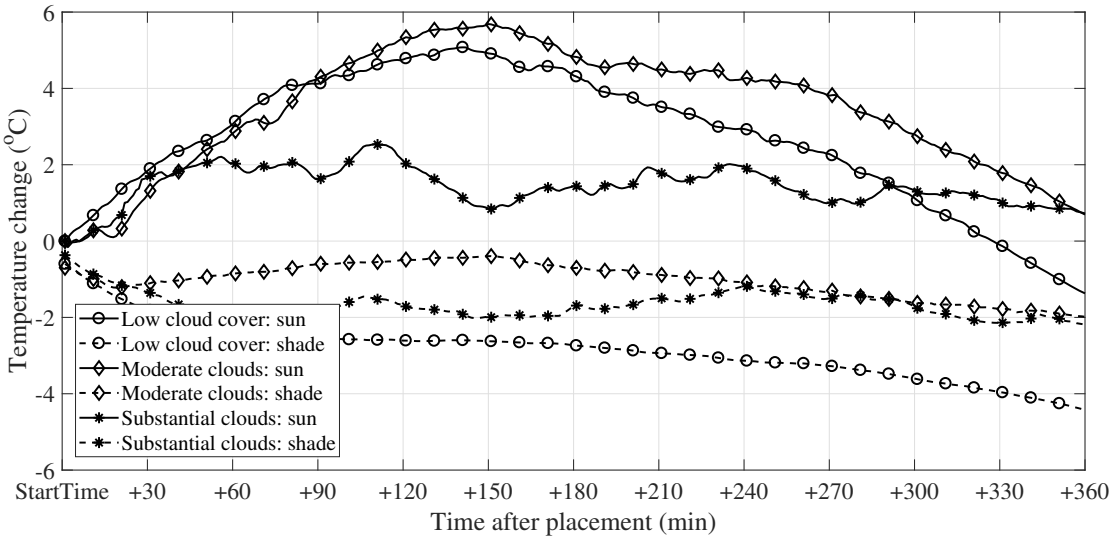

Figure 4.15: The change in concrete temperature of the sun and shaded specimens for different cloud covers.

The temperature difference between the sun and shade specimens decrease with an increase in cloud cover. The maximum temperature difference between the sun and shade specimens are 7.7^{o}C, 6^{o}C and 4^{o}C at 140, 150 and 60 minutes after placement for <15%, 38.15% and 81.1% cloud cover (R), respectively. This trend was also observed in the individual experiments.

4.5.5 Setting time

The setting times were only determined for EXP 3.1, 3.2 and 3.3. Both the initial and final setting times were less when the closed setting time specimens were placed in the sun. On average, the initial set occurred 37 minutes earlier and final set occurred 45 minutes earlier when placed in the sun. The decrease in setting time can be attributed to the increase in concrete temperature due to solar radiation.

4.5.6 Shrinkage

The shrinkage results of specimens exposed to the sun and shade with moderate and significant cloud cover can be seen in Fig. 4.16. For moderate cloud cover, the mean shrinkage of EXP 2.3 (R=28.85%) and EXP 2.5 (R=47.43%) were considered

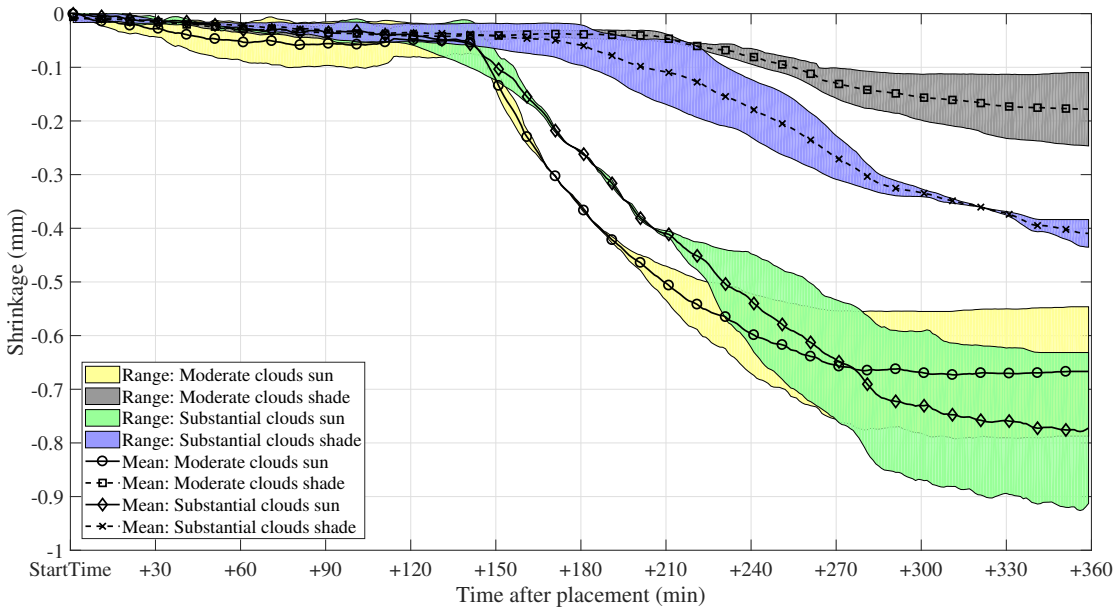

Figure 4.16: The total shrinkage of specimens exposed to the sun and shade for minimal and substantial cloud cover.

where as for significant cloud cover the mean shrinkage of EXP 2.4 (93.5%) and EXP 2.6 (68.67%) were considered.

The shrinkage of specimens exposed to the sun is significantly more than specimens placed in the shade. This trend was noticed in all the experiments conducted in this study and is coherent with the evaporation results. A increase in cloud cover, increased the shrinkage in the specimen placed in the shade significantly. The presence of clouds produces an increase in non-direct radiation, a higher evaporation and more shrinkage in the shaded specimens. Shrinkage started earlier and increased more rapidly in the specimens exposed to the sun.

Similar trends can be observed in Fig. 4.17 when comparing EXP 3.2, 2.7 and 2.8, where the mean cloud cover (R) was 9.37%, 15.6% and 68.6%, respectively.

The shrinkage in the specimens exposed to the sun is significantly more than specimens placed in the shade. When comparing EXP 2.7 to 2.8, it is clear that the difference in shrinkage between the sun and shade specimens are significantly lower with an increase in cloud cover. The magnitude of shrinkage in the specimen exposed to the shade is proportional to the evaporation rate with 0.23, 0.5 and 0.33 kg/m^2/h in EXP 2.7, 2.8 and 3.2, respectively. However, in the specimens exposed to the sun, the shrinkage in EXP 2.8 and 2.7 were similar even though the evaporation rate in EXP 2.8 (0.67 kg/m^2/h) was more than in EXP 2.7 (0.6 kg/m^2/h). EXP 3.2 exhibited the most shrinkage due to the high evaporation rate (0.74 kg/m^2/h) caused by the high GHI of 947.5 W/m^2. Shrinkage

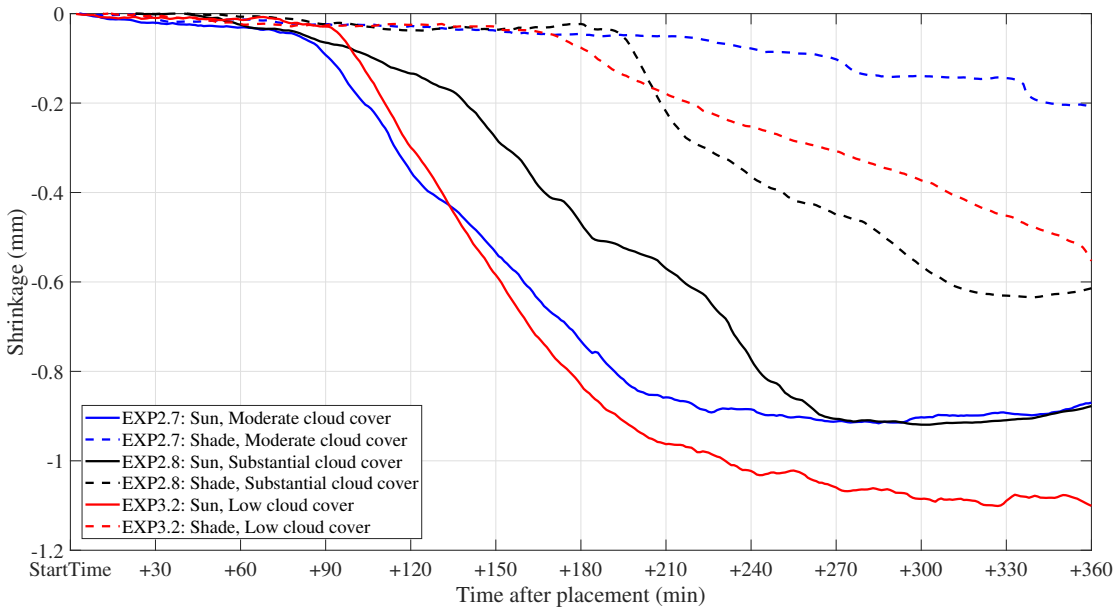

Figure 4.17: The mean total shrinkage of specimens exposed to global radiation and non-direct radiation of CM2.

also started much earlier in specimen exposed to the sun.

4.5.7 Plastic shrinkage cracking

The severity of plastic shrinkage cracking was determined by measuring the crack area. The total crack area of all specimens in each experiment can be seen in Fig. 4.18.

For all the experiments conducted, exposing specimens to the sun resulted in higher crack areas when compared to the shaded specimen except for EXP 2.8. Cracking also started later in the shaded specimens. For CM1, cracking occurred in the specimens exposed to an evaporation rate exceeding 0.35 kg/m^2/h. At 0.35 kg/m^2/h the cracks area was similar in the sun and shaded specimens. However, to produce an evaporation rate exceeding 0.35 kg/m^2/h in the shaded specimens required an extremely high wind speed and substantial cloud cover (to increase the diffused radiation). For CM2, cracks formed at an evaporation rate exceeding 0.25 kg/m^2/h. For further insight, the experiments are compared on an individual basis.

4.5.7.1 EXP 2.3 sun vs 2.4 sun vs 2.6 shade

For EXP 2.3 sun, 2.4 sun and 2.6 shade, the measured mean evaporation rates were similar with 0.41, 0.35 and 0.36 kg/m^2/h, respectively. However, the severity

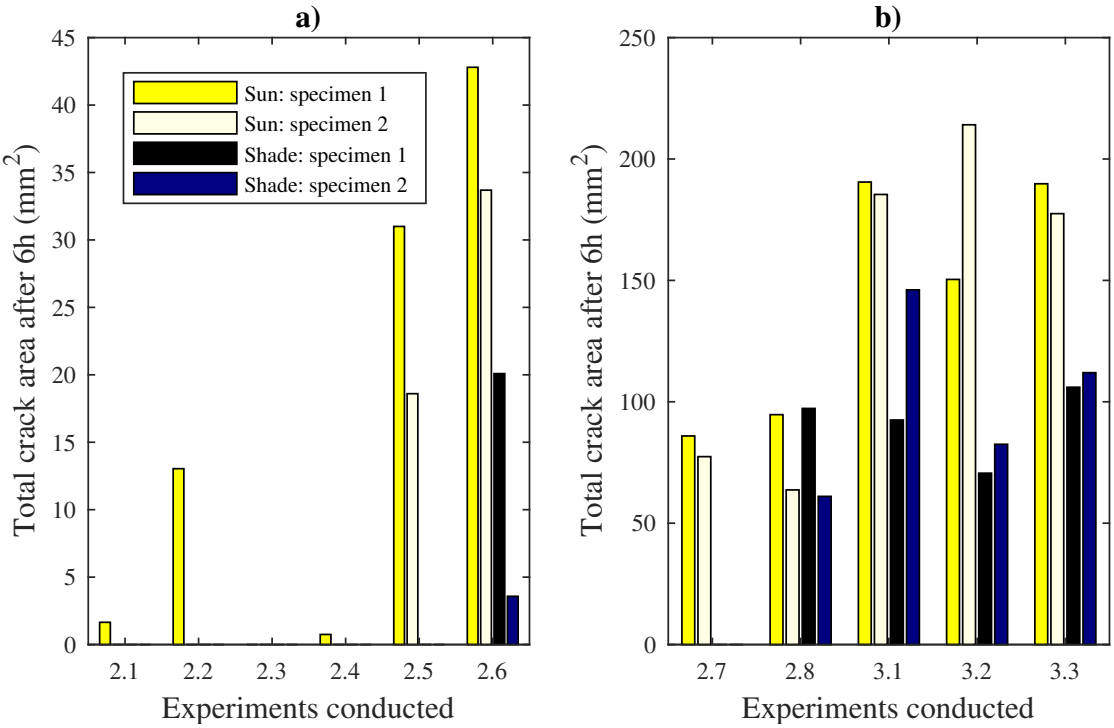

Figure 4.18: The total crack area 6 hours after placement for all the experiments conducted. The experiments in a) and b) were conducted with CM1 and CM2, respectively.

of PSC differs significantly with 0, 0.75 and 16.9 mm^2, respectively. The average shrinkage and concrete temperature of EXP 2.3 sun, 2.4 sun and 2.6 shade can be seen in Fig. 4.19.

The EXP 2.3 specimen exhibited no cracking whereas EXP 2.4 had cracks even though the evaporation rate was higher in EXP 2.3. This behaviour can be attributed to the lower concrete temperature in EXP 2.4, which delayed tensile strength gain and extended the shrinkage period. Severe cracks formed in the shaded specimen of EXP 2.6 but not in the sun specimen of EXP 2.3, even though the evaporation rates were almost exactly the same. This can also be attributed to the lower concrete temperature in EXP 2.6. In EXP 2.3 and 2.6, the shrinkage started at 140 and 180 minutes after placement and stopped 130 and >180 minutes later. Although the shrinkage after 360 minutes was lower for EXP 2.6, the lower concrete temperate delayed the tensile strength gain to such an extent that more severe PSC formed.

4.5.7.2 EXP 2.7 sun vs 2.8 sun vs 2.8 shade

The crack area growth over time can be seen in Fig. 4.20. The mean evaporation rate and radiation were 0.6, 0.67 and 0.5 kg/m^2/h and 644, 476, 326.5 W/m^2 in

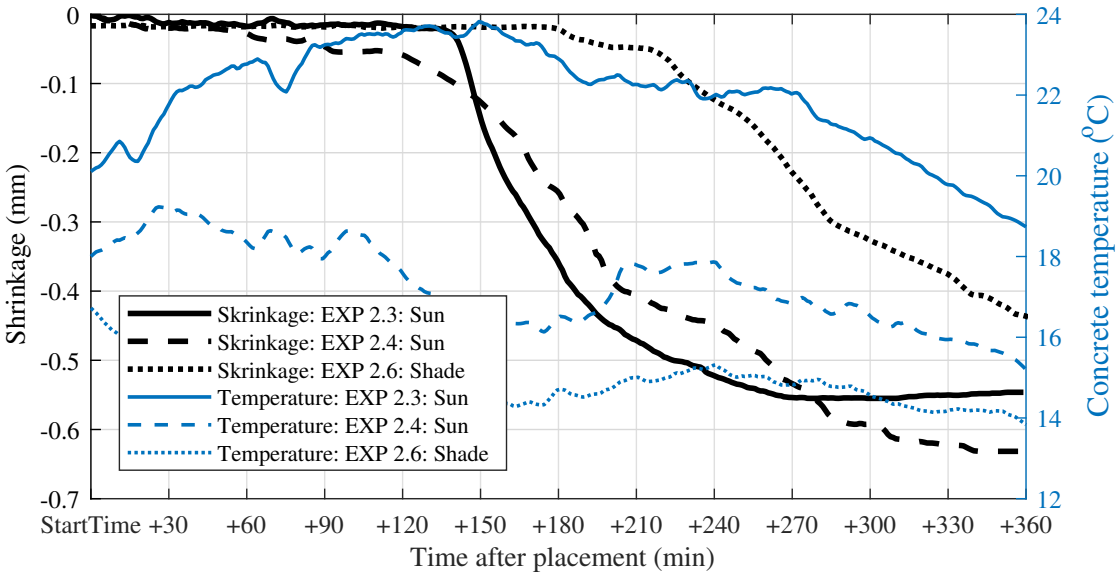

Figure 4.19: The concrete temperature and shrinkage of EXP 2.3 sun, 2.4 sun and EXP 2.6 shade.

EXP 2.7 sun, 2.8 sun and 2.8 shade, respectively.

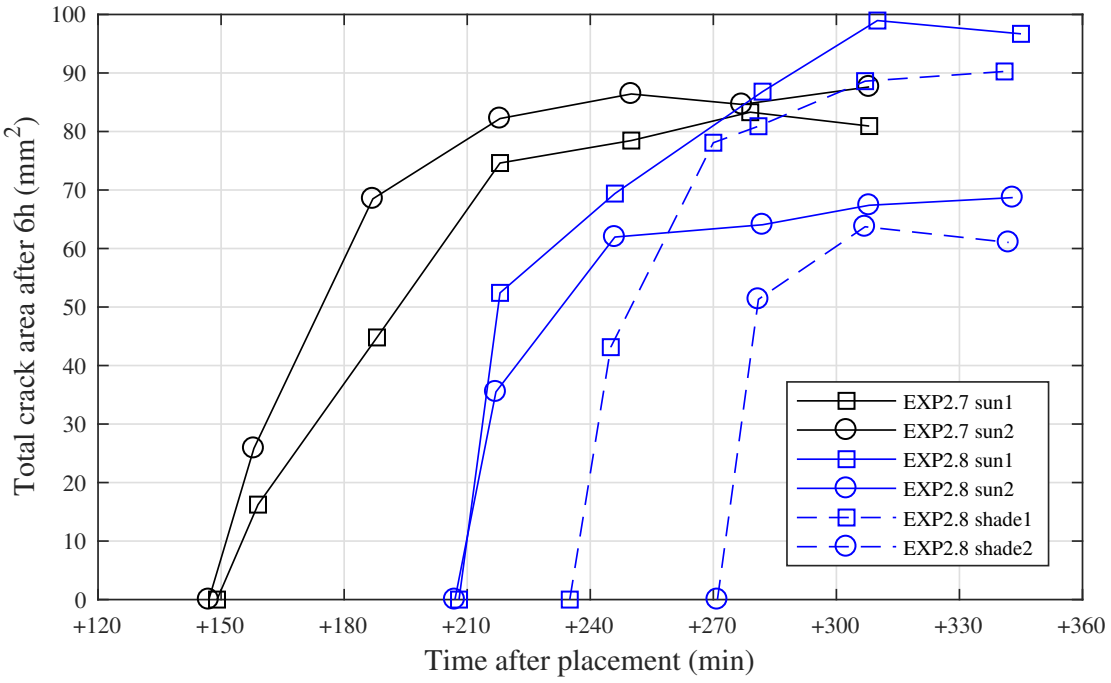

Figure 4.20: The crack growth over time of EXP 2.7 sun, 2.8 sun and 2.8 shade.

EXP 2.8 shade is exposed to high diffused radiation due to significant cloud cover, which resulted in a high evaporation rate (0.5 kg/m^2/h) and severe cracking. At an evaporation rate of 0.67 kg/m^2/h, EXP 2.8 sun was expected to crack more than EXP 2.8 shade and EXP 2.7 sun. However, the crack area of EXP 2.7 sun, 2.8 sun and 2.8 shade were fairly similar. The higher concrete temperature and evaporation rate of EXP 2.8 sun resulted in a similar crack area when compared to EXP 2.8 shade which had a slightly lower concrete temperature and evaporation rate. EXP 2.7 sun produced a similar crack area with a lower evaporation rate and higher concrete temperature when compared to EXP 2.8 sun. In EXP 2.7 sun, the cracks started to form earlier and increased in area more gradually when compared to the specimens with a lower concrete temperature (EXP 2.8 sun and 2.8 shade). The result shows the relationship between concrete temperature and PSC.

4.5.7.3 EXP 3.1 vs 3.2 vs 3.3

The crack area growth over time can be seen in Fig. 4.21. The evaporation rates in the specimen exposed to the sun were 0.8, 0.74 and 0.76 kg/m^2/h and 0.55, 0.33 and 0.48 kg/m^2/h in the shade for EXP 3.1, 3.2 and 3.3, respectively.

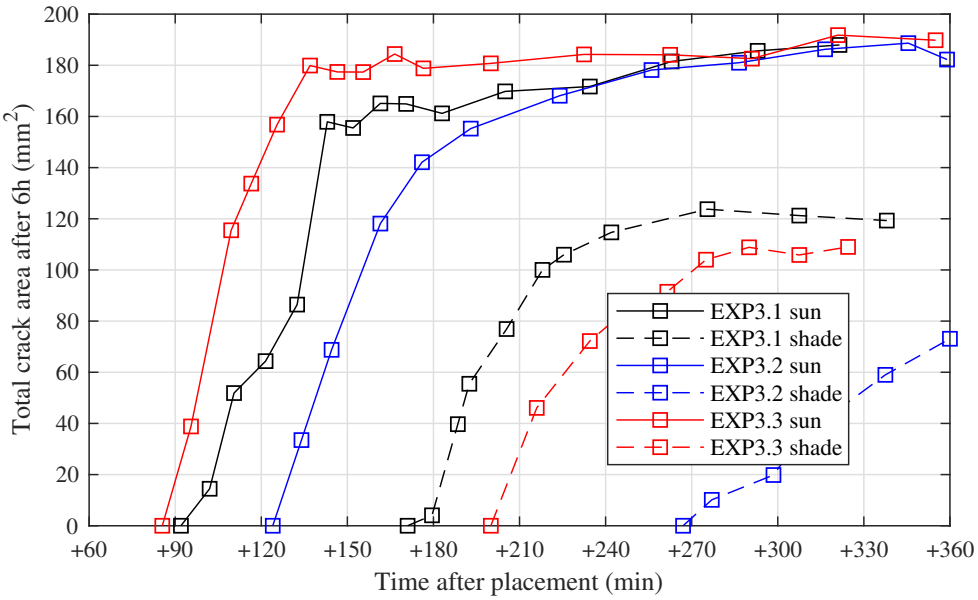

Figure 4.21: The crack growth over time of EXP 3.1, 3.2 and 3.3.

In the specimen exposed to the sun, cracking occurred between 80 and 140 minutes earlier than the specimen exposed to the shade. The total crack area was

between 60% and 140% higher due to exposure to direct radiation. This trend was noticed in all the experiments expect EXP 2.8.

4.5.8 The influence of weather conditions on PSC

Linear regression can be used to indicate the relationship between variables. Although only 11 experiments were conducted in this study, the trends observed are supported by the literature. A basic statistical significance test indicated that, at a probability of 0.05, r > 0.632 is significant [116]. Fig. 4.22 shows the relationship between the evaporation rate, radiation and wind speed for the conjunction of CM1 and CM2. As shown previously, the mixture had a minimal effect on the evaporation rate.

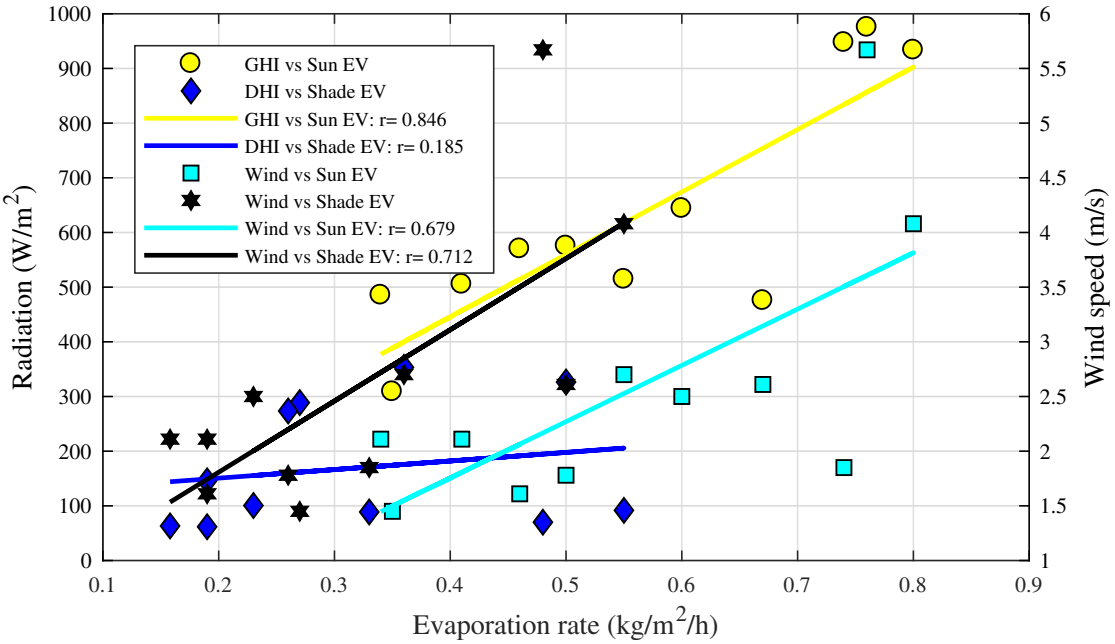

Figure 4.22: The relationship between the evaporation rate, radiation and wind speed for CM1 and CM2.

The GHI and evaporation rate of the sun specimens have a correlation coefficient (r) of 0.846 where the DHI and evaporation rate of the shade specimens have a correlation coefficient of 0.185. The correlation coefficient of the wind speed to evaporation rate for the sun and shade specimen were 0.68 and 0.71, respectively. The results indicate that the evaporation rate is more related to the GHI radiation than to the wind speed when the specimen is placed in the sun. The wind speed has a more pronounced effect on the evaporation rate if the specimen is placed in the shade.

Fig. 4.23 shows the relationship between the crack area and evaporation rate for each specimen for CM1 and CM2, independently.

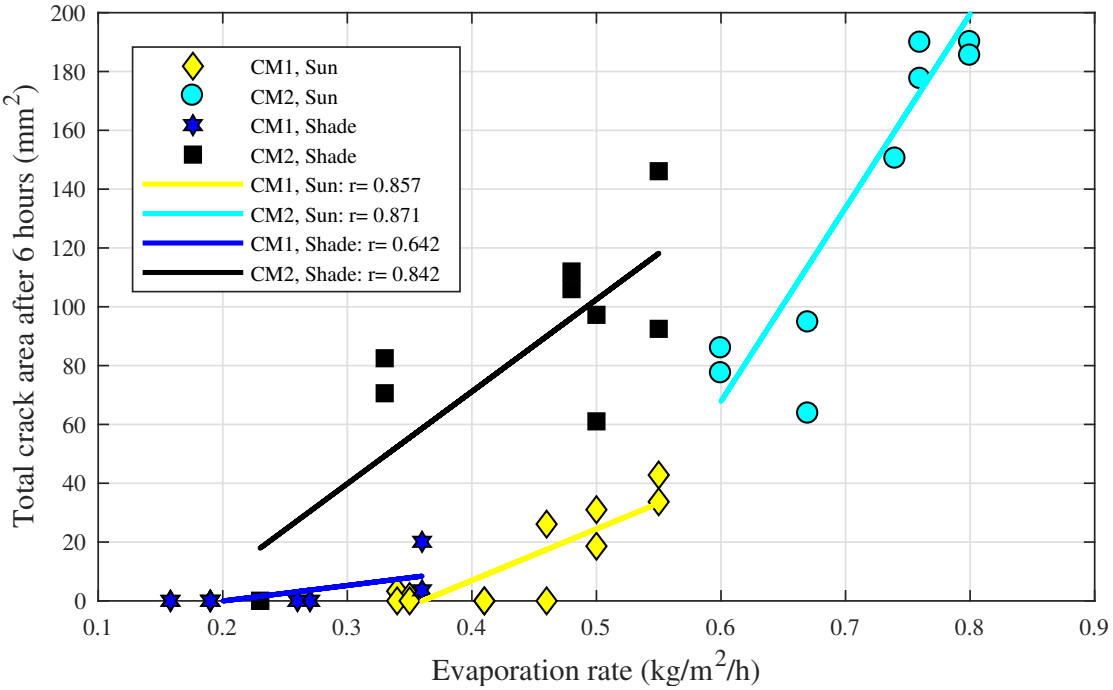

Figure 4.23: The relationship between crack area and evaporation rate for CM1 and CM2, independently.

Since the concrete mixture would have a significant effect on the crack size, CM1 and CM2 were analysed separately. A higher evaporation rate resulted in more shrinkage and, therefore, a larger crack area. For the specimen exposed to the sun, the correlation coefficient (r) is on average slightly higher at 0.864 compared to the shaded specimen with 0.742. The relationship between crack area and the evaporation rate is in agreement with literature [88, 40, 47].

Fig. 4.24 shows the relationship between the crack area and wind speed for CM1 and CM2, separately. Wind speed can have a significant effect on evaporation and crack area [50, 51]. The r-value is slightly lower in the specimen exposed to the sun (0.477) when compared to shaded specimen (0.6), an indication that direct radiation has some effect on the crack area.

Fig. 4.25 shows the relationship between crack area and radiation. For specimens exposed to the sun, the crack area and radiation have on average a correlation coefficient of 0.682 where as for specimens which were shaded, the crack area and radiation have a correlation coefficient of only 0.263. Therefore, in the sun specimens, the severity of PSC was affected to a greater extent by radiation (r=0.682)

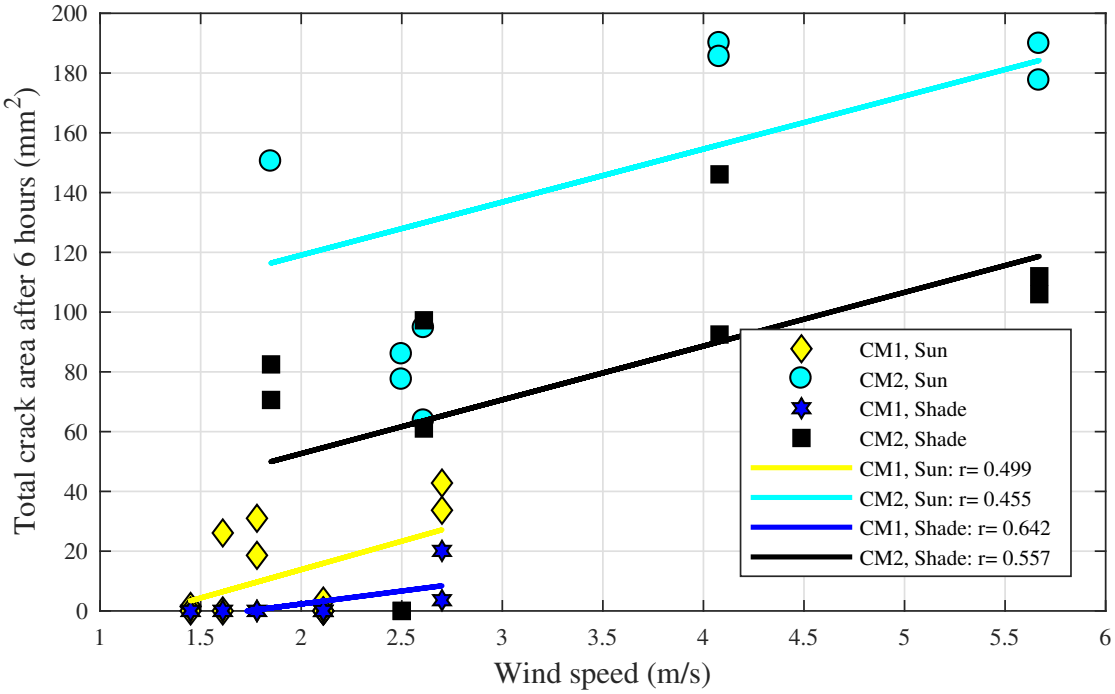

Figure 4.24: The relationship between crack area and wind speed for CM1 and CM2, independently.

than the wind speed (r=0.477), since the r-values are higher. On the contrary, for the shaded specimen, the wind speed (r=0.6) had a greater effect than the radiation (r=0.263).

4.5.9 Accuracy of the evaporation estimation models in the sun

A root mean square error (RMSE) analysis was conducted to determine the most accurate evaporation estimation model, as seen in Fig. 4.26. The experiments were placed in three categories with Category A corresponding to a low air temperature, low wind speed or low GHI. Category B correspond to a moderate air temperature, wind speed or GHI. Category C correspond to a high air temperature, wind speed or GHI. Table 4.4 define the values corresponding to a low, moderate or high air temperature, wind speed or GHI. For the Uno and Al-Fadhala-Hover models the concrete temperature of the specimen exposed to the sun is used in the model. The analysis compared the estimated evaporation rate to the actual evaporation rate in the specimens exposed to the sun for the first 5 hours. The variables used in these models can be seen in Table 4.1.

When solar radiation was high ($> 800\ W/m^2$), both the Uno and Al-Fadhala-

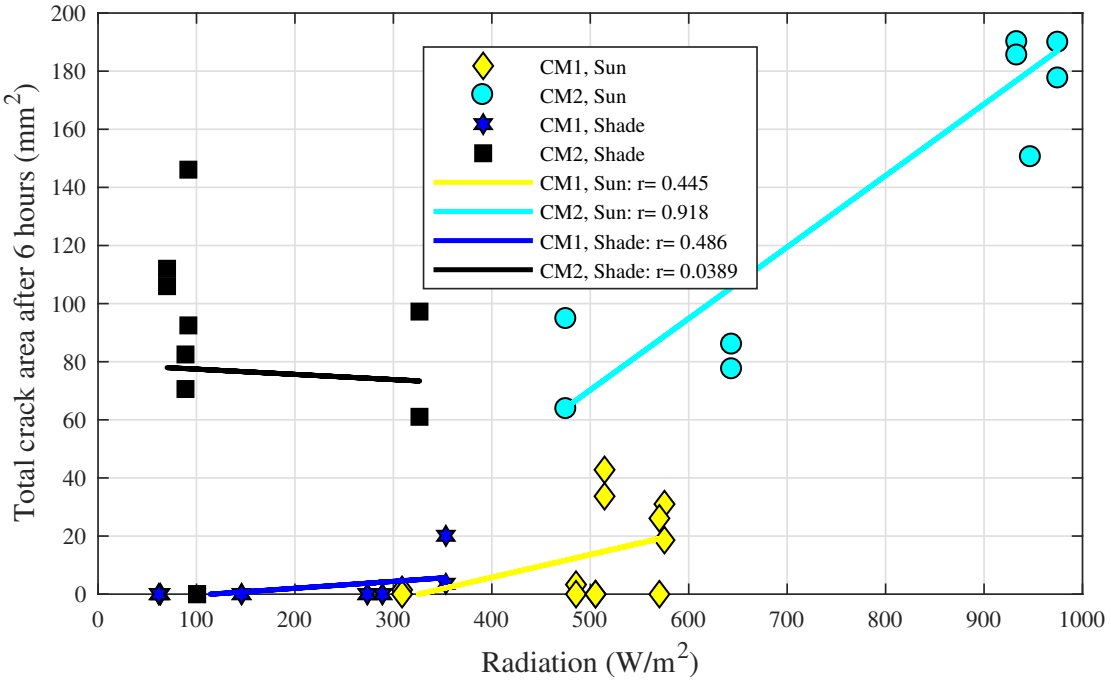

Figure 4.25: The relationship between crack area and radiation.

Hover models significantly underestimated the evaporation rate. However, the Al-Fadhala-Hover and, to a lesser extent, Uno produced relatively accurate results at a low solar radiation (300 to 600 W/m^2). These models are significantly influenced by wind speed when compared to the other models. When Al-Fadhala-Hover is compared to all the other models it performed particularly well at low wind speeds (<2 m/s) and low solar radiation (< 600 W/m^2).

Under the tested conditions, the Priestley-Taylor, deBruin-Keijman and Penman models performed the best. Of these, Penman consistently performed well and is on average marginally better than the rest. Jansen-Haise, Brutsaert-Sticker, Penmen-Monteith also performed well. On average, Uno and Al-Fadhala-Hover performed the worst of all the models. When specimens were exposed to a high solar radiation (Category C), the Al-Fadhala-Hover and Uno models produced an error twice that of the Penmen model.

The following models are recommended to estimate the pore water evaporation from concrete specimens placed in the sun based on the accuracy, ease of use, availability of data and the weather conditions:

- Penman is recommended as the most accurate model since it estimates the evaporation relatively well irrespective of the conditions. Net radiation (Q_N) and change in energy (Q_X) measurements are required to estimate the evaporation. If these variables are available, the Penman model is recommended.

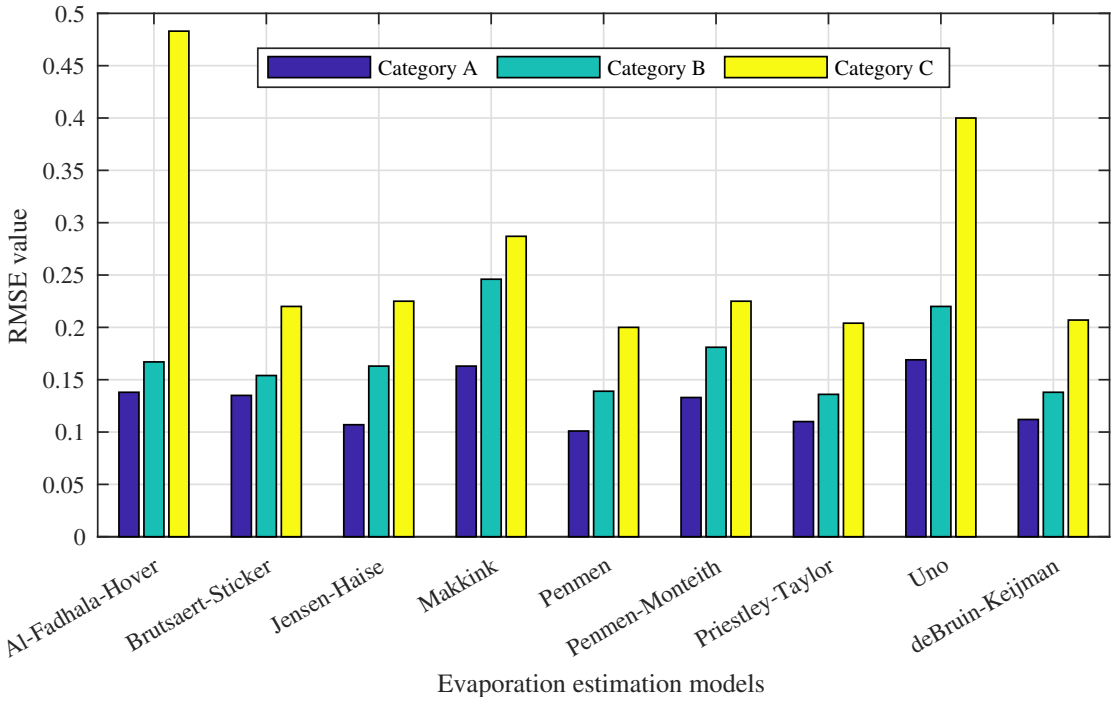

Figure 4.26: Root mean square error results for all the experiments conducted. Category A corresponding to a low air temperature, low wind speed or low GHI. Category B correspond to a moderate air temperature, wind speed or GHI. Category C correspond to a high air temperature, wind speed or GHI.

- Jansen-Haise is accurate at a moderate to high solar radiation. The model only requires solar radiation and air temperature measurements to estimate evaporation. Solar radiation data can be obtained from a nearby weather station, and air temperature can be measured on-site. The Jansen-Haise model is feasible and accurate and is therefore recommended for estimating the pore water evaporation from concrete placed in moderate to high solar radiation. The Jansen-Haise model follows:

$$E = (25.2T_a + 78)(Q_S \times 1.47 \times 10^{-6}) \tag{4.8}$$

  with T_a the air temperature in ^{o}C, Q_S the GHI in W/m^2 and E the evaporation rate in $kg/m^2/h$.

- Al-Fadhala-Hover is only recommended if no solar radiation data is available. The model can significantly underestimate the evaporation rate under moderate to high solar radiation ($> 600\ W/m^2$).

4.5.10 Accuracy of the evaporation estimation models in the shade

The Uno and Al-Fadhala-Hover models can also be used to estimate the evaporation from the shaded specimens. The RMSE results can be seen in Fig. 4.27. Categories A, B and C are defined as above. Here, the concrete temperature of the shaded specimens are used in the Uno and Al-Fadhala-Hover models. The other models were not developed for estimating the evaporation from shaded specimen and was therefore deemed unsuitable for estimating the evaporation from shaded specimens.

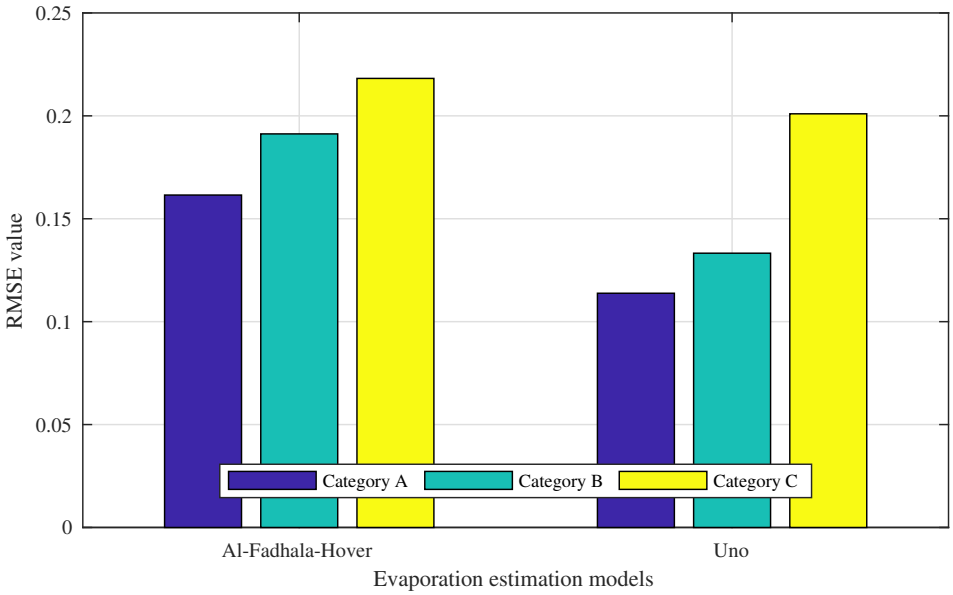

Figure 4.27: Root mean square error results for all the experiments conducted in the shade. Category A corresponding to a low air temperature or low wind speed. Category B correspond to a moderate air temperature or wind speed. Category C correspond to a high air temperature or wind speed.

In all the experiments conducted the two models underestimated the actual evaporation rate. The underestimation may be due to the diffused solar radiation on the shaded specimens.

For the three categories, the Uno model was a more accurate estimate of the actual evaporation from the shaded specimens than the Al-Fadhala-Hover model. The Uno model preformed particularly well under lower and moderate air temperatures and wind speeds compared to the Al-Fadhala-Hover model. The Uno model is therefore recommended to estimate the evaporation from concrete placed in the shade.

4.6 Conclusion

A strenuous experimental program was successfully executed to determine the influence of solar radiation on the pore water loss, concrete temperature, shrinkage and plastic shrinkage cracking of concrete. The following conclusions can be drawn from this study:

- The evaporation of free pore water is primarily depended on the environmental conditions in the few hours after placement. The effect of cement content, type, particle size and concrete mixture is minimal during this time.
- Fresh concrete has a much higher free pore water loss when exposed to the sun than the shade. The difference in water loss between the sun and shaded specimen is inversely proportional to cloud cover and wind speed and proportional to GHI.
- Exposure to direct solar radiation can significantly increase the concrete temperature. The difference in concrete temperature between the specimen exposed to the sun and shade is inversely proportional to the cloud cover.
- Plastic concrete has a much higher shrinkage when exposed to the sun than the shade. The shrinkage is proportional to the evaporation. The difference in shrinkage between the sun and shade specimen is inversely proportional to cloud cover and proportional to GHI.
- Plastic shrinkage cracking was more severe when exposed to the sun than the shade. The results indicate that if the loss in pore water of two specimens is equal, the specimen with the lower concrete temperature is more likely to crack. However, exposing the concrete to direct radiation increases the loss in pore water to such an extent that a higher concrete temperature and, consequently, a higher rate of tensile strength development did not prevent or reduce the severity of PSC in the test conditions.
- For the specimens exposed to the sun, a better correlation was noted between radiation and crack area than wind speed and crack area. For shaded specimens, wind speed and the crack area had a better correlation than radiation and crack area.
- Several radiation-based evaporation estimation models were evaluated. The feasible Jansen-Haise model was recommended to estimate the pore water evaporation from concrete placed in moderate to high solar radiation. Under these conditions, the Uno and Al-Fadhala-Hover models significantly underestimated the evaporation rate of pore water.

- When concrete is placed in the shade, the Uno model provides the best estimate for the actual evaporation rate with a slight underestimation.

To conclude, this study indicates that solar radiation significantly increases the concrete temperature, the evaporation of free pore water, shrinkage and severity of plastic shrinkage cracking. Therefore, a model that accounts for solar radiation is proposed to estimate pore water evaporation in moderate to high solar radiation. Failure to eliminate or reduce solar radiation exposure can result in severe plastic shrinkage cracking in concrete.

Chapter 5

Plastic shrinkage cracking in 3D printed concrete

Abstract

In concrete, early age pore water evaporation results in volumetric shrinkage that, when restrained, can cause plastic shrinkage cracking (PSC). 3D printed concrete (3DPC) is vulnerable to PSC due to a lack of formwork, minimal bleeding water, low aggregate to binder ratio and high quantities of fines in the mixture. A novel experimental method was developed to determine the PSC risk, evaluating the efficacy of PSC prevention measures and understanding the behaviour of PSC in early age 3DPC. This study evaluated the free shrinkage of 3DPC specimens as well as identified and systematically introduced sources of restraint to induce PSC. The free shrinkage results showed a rate of strain gain and peak strain significantly higher than commonly found in ordinary concrete. Severe cracking was observed when the shrinkage was restrained under a moderate evaporation rate. Cracks formed within the first two hours after printing, earlier than in ordinary concrete. The proposed method was employed to study the fundamental behaviour of crack formation and propagation in 3DPC. The unique filament interlayer plane has a notable effect on the transfer of shrinkage deformation in the specimen. Differential horizontal deformation in consecutive layers and consequential interlayer slip was observed when the shrinkage was restrained. It is reasonable to conclude that interlayer slip caused by early age shrinkage has the potential to reduce the long-term interlayer bond strength and the durability of 3DPC.

Article information

Chapter 5 has been published as a journal article and can be cited as: **G.M. Moelich**, P.J. Kruger, R. Combrinck, Plastic shrinkage cracking in 3D printed concrete, Composites Part B: Engineering, vol. 200, November 2020. Online

Contribution declaration

With regard to this chapter, the nature and extent of the contributions of the candidate and the co-authors were as follow:

Name	Nature of contribution	Extent
G.M. Moelich (candidate)	Conceptualisation, Methodology, Validation, Formal analysis, Writing - original draft, Visualization, Investigation	90%
Dr P.J. Kruger (pjkruger@sun.ac.za)	Conceptualisation, Validation, Writing - review & editing	5%
Dr R. Combrinck (rcom@sun.ac.za)	Conceptualisation, Validation, Writing - review & editing, Supervision	5%

The undersigned hereby confirm that:

- The declaration above accurately reflects the nature and extent of the contributions of the candidate and the co-authors to this chapter.
- No other authors contributed to this chapter besides those specified above.
- Potential conflicts of interest have been revealed to all interested parties and that the necessary arrangements have been made to use the material in this chapter of the dissertation.

Signature of authors	Institutional affiliation	Date
	Department of Civil Engineering, Stellenbosch University	09/06/2021
	Department of Civil Engineering, Stellenbosch University	09/06/2021
	Department of Civil Engineering, Stellenbosch University	09/06/2021

5.1 Introduction

3D printing of concrete, also known as digital construction, has the potential to revolutionise the construction industry [156]. The additive manufacturing process of layer upon layer extrusion allows for concrete placement without conventional formwork, saving cost, time and materials [157, 30]. However, the absence of formwork as well as various other attributes, predisposes 3DPC to plastic shrinkage cracking (PSC) [13, 19, 158]. These cracks, as seen in Figure 5.1, are aesthetically unpleasing, can result in corrosion of steel reinforcement, increase carbonation of concrete and, if 3DPC is unreinforced, diminish tensile capacity.

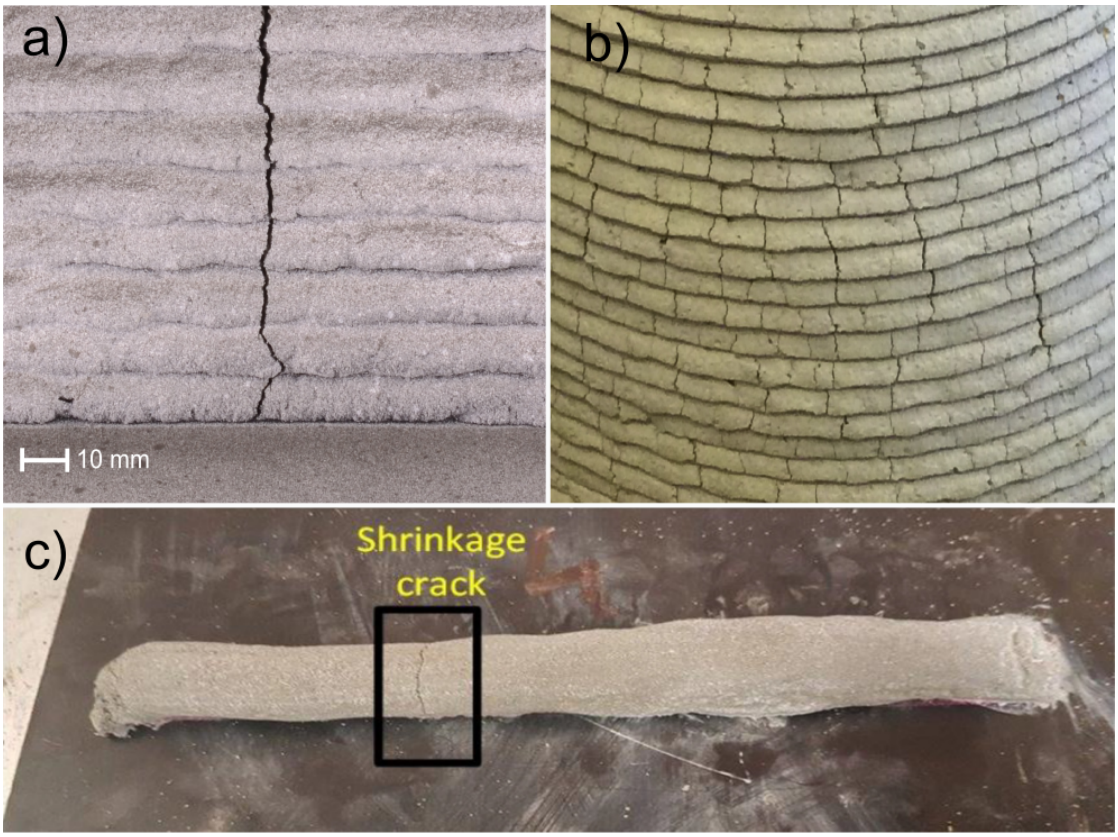

Figure 5.1: a) Crack produced in this study by exposing 3DPC to a moderate evaporation rate for the first two hours after printing. b) Excessive cracking due to early age shrinkage [19]. c) Crack noticed after one day of curing at laboratory temperature [159].

PSC occurs in freshly placed (plastic) concrete due to the evaporation of pore water that induces a negative pressure in the pore system and results in a three-dimensional volume reduction (shrinkage) [88, 56, 58]. Restraining this shrinkage results in tensile strain development that, if it exceeds the tensile strain capacity

of the plastic concrete, can result in cracking [91, 133]. In conventional construction, concrete elements with a high surface area to volume ratio (such as slabs, pavements and bridge decks) placed in a highly evaporative environment without sufficient curing are prone to PSC [42, 47]. 3DPC is even more vulnerable to PSC than ordinary concrete due to the reasons discussed here.

In ordinary formwork construction, the accumulation of bleeding water on the top surface prevents the evaporation of pore water and reduces horizontal shrinkage [55]. It is presumed that 3DPC would generally produce less bleeding water than ordinary concrete due to the large quantity of fines and low water to cement (w/c) ratio [73]. The pore water would therefore be exposed to evaporation for a longer time period resulting in more pore water loss and shrinkage [47]. On the contrary, less bleeding is synonym with less vertical settlement [155].

Immediately after placement, 3DPC is exposed to environmental factors such as the ambient temperature, humidity and wind due to the lack of formwork. These factors not only control the evaporation of pore water but can also increase the rate of the hydration reaction, especially higher temperatures [95]. Rapid hydration has many adverse consequences, including; thermal and chemical volumetric changes, higher long-term permeability and reduced compressive strength [40, 53, 97]. Excessive pore water evaporation is the driving force of plastic shrinkage cracking. The high surface area to volume ratio of 3DPC elements can result in excessive pore water evaporation from the sides of the element, where bleeding water provides less protection, increasing the risk of PSC [74].

The mix proportions of 3DPC is notably different from ordinary concrete. The low aggregate content in 3DPC (aggregate to binder ratio of about 1.3-1.6 in 3DPC and 4-6 in ordinary concrete mixes) and absence of coarse aggregates (maximum particle size in the order of 2 mm) can increase shrinkage, both in the plastic and hardened (dry) state [42, 43, 16]. A lower w/c ratio tends to have a secondary role, by controlling the bleeding rate and the fine particle quantity, but can significantly increase autogenous shrinkage [40]. The high proportion of extenders, in particular silica fume, can also increase PSC by producing a smaller pore size that increases the capillary build-up [160, 61, 65]. Some literature [62, 161] have shown that the addition of superplasticizers can reduce the severity of PSC, while others [162] have argued that the retarding effect of some superplasticizers can increase the severity. That being said, the mix proportions used for 3DPC are vital to the pumpability and buildability.

Other than bleeding, lack of formwork and mix proportions, it is likely that the interlayer and extrusion-induced shearing will also have an effect on PSC but in a way that cannot be foreseen without further experimental research. It is possible for the interlayer to affect the pore water exchange between layers or the transfer of shrinkage from one layer to the next. The pore shape and size distribution are

different in 3DPC due to extrusion and can also affect shrinkage [74].

In regard to relevant 3DPC literature, Le et al. [13] monitored the drying shrinkage of specimens cast into a mould from 2 to 180 days to demonstrate the efficacy of curing measures on 3DPC mixes according to EN 12617 [163]. Slavcheva [164] and Kim et al. [165] followed, also casting printable concrete into moulds and monitoring the drying shrinkage over 28 days according to ASTM C596 [166]. Van Zijl et al. [167] cast a printable 3DPC mixture into plastic shrinkage moulds to show that polypropylene fibres can reduce early age shrinkage. De Coensel [168] was the first to measure the early age shrinkage of concrete extruded through a nozzle. The shrinkage of a one-layer specimen was exposed to a low evaporation rate (about 0.07 $kg/m^2/h$) to investigate superabsorbent polymers as an internal curing method. Saturated lightweight aggregates, expansive agents and shrinkage-reducing admixtures have also been suggested for reducing PSC in 3DPC but have not been tested [157]. Although many have cautioned against PSC in 3DPC, no literature could be found on the early age shrinkage or cracking of multi-layer extruded cementitious material elements.

To study plastic shrinkage cracking in ordinary concrete, either the ASTM test method [109] or the ring method is typically used. Some researchers [65, 62, 128, 101] prefer the former while others [162, 89] prefer the latter. Both have advantages and disadvantages, but it is clear that neither is suitable for evaluating early age shrinkage or cracking of a multi-layered printed specimen. The conventional free shrinkage test setup utilises the mould for fixing LVDTs. The ASTM and ring cracking moulds provide the restraint that inducing cracks. All the conventional methods only expose the top surface of the concrete specimen. In 3DPC, the layer-by-layer construction, exposed sides, lack of a mould and potential influence of the interlayer necessitate a new test method. The proposed test setup should be easy to construct, the test method should be easy to execute in a laboratory and provide repeatable and reliable results. Ultimately, the method should be suitable to evaluate and compare the efficacy of different 3DPC mixes, environments as well as PSC mitigating measures.

This brief literature review confirms the vulnerability of 3DPC to PSC and identifies potential differences in the early age behaviour as opposed to ordinary concrete. A lack of literature on PSC in 3DPC, as well as the need for a suitable test method, is clear. To address the aforementioned issues, this study proposes a method to experimentally test early age shrinkage as well as early age cracking in multilayer 3DPC specimens. The response of the specimens, exposed to a moderate evaporation rate, is monitored while considering the effect of the interlayer. In the future, the introduction of tensile reinforcement and higher on-site evaporation rates can further increase the risk and severity of PSC.

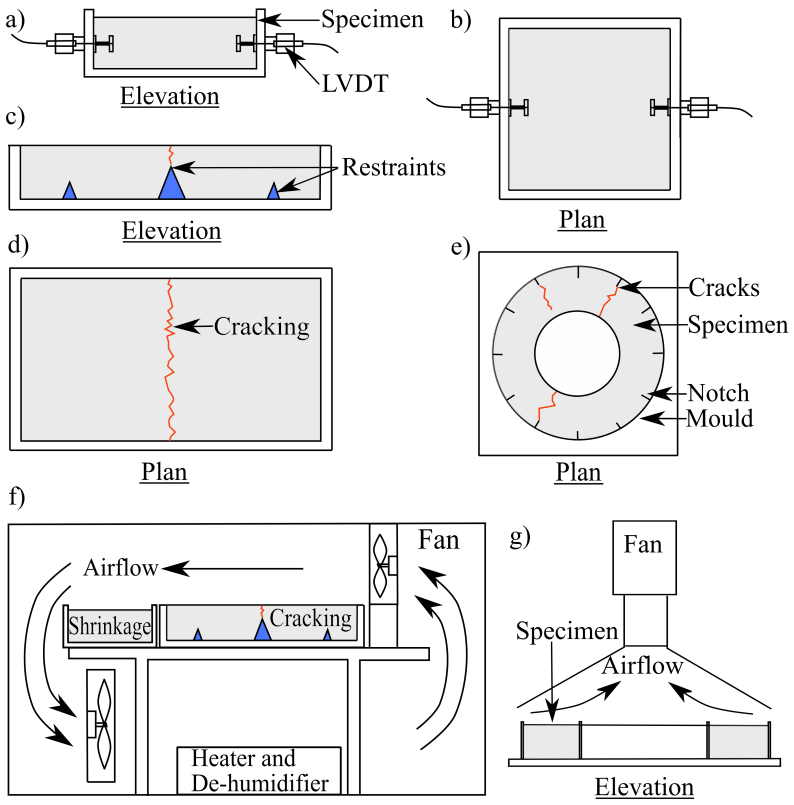

Figure 5.2: Methods of testing PSC in ordinary concrete: a) and b) elevation and plan view of standard free shrinkage mould [58], c) and d) elevation and plan of ASTM plastic shrinkage cracking mould [109], e) plan view of alternative ring test method for inducing cracks [89], f) typical test chamber for standard moulds, g) typical test chamber for alternative ring test method

5.2 Experiments

Extrusion of the concrete through the moving nozzle allows for layer-by-layer placement along a pre-programmed path. Mechanically controlling the nozzle movement ensures a consistent specimen geometry that improves the repeatability of the experiments. The 3D printer and the experimental setup used can be seen in Figure 5.3. More details on the experimental setup follow.

5.2.1 Materials and mix proportions

The mix proportions, as seen in Table 5.1, were modified from Kruger et al. [38]. A CEM II 52.5N cement that contains between 6 and 20% limestone extender was used. Fly-ash (DuraPozz Class F) and silica fumes (Chryso DSF) were added to obtain the required rheological properties. A natural, continuously graded and

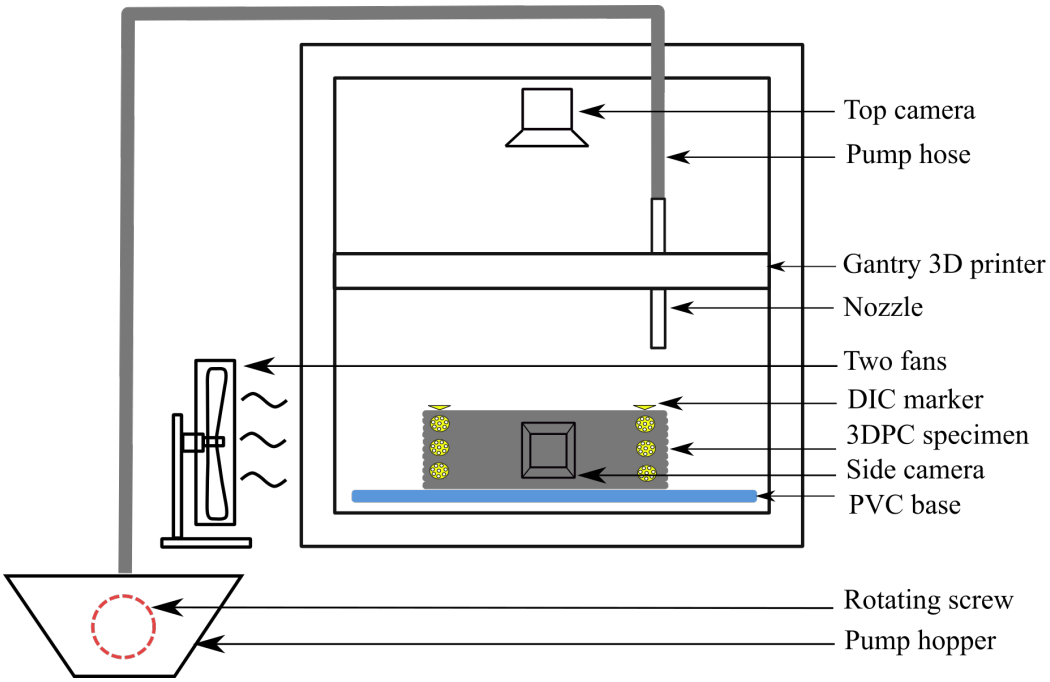

Figure 5.3: The experimental setup used in this study.

locally sourced quarry sand, with a maximum particle size of 4.75 mm, was used as fine aggregate. Superplasticizer (Chryso Fluid Premia 310), a modified polycarboxylate polymer, was added as a percentage of binder mass (mb). A small quantity of synthetic iron oxide (Sika) colour pigment was added in Mix 2 to dye the concrete black. The addition of a pigment had a negligible effect on the rheological properties and printability of the concrete. Mix 2 was only used in the one speckled pattern experiment where black concrete was beneficial to the accuracy of the deformation results.

Other researchers have used 3DPC mixtures with an aggregate to binder (a/b) ratio in the 1.3-1.7 range [16]. Typically, the a/b ratio of ordinary concrete is in the 4-6 range, self-compacting concrete (SCC) is in the 3-3.75 range and for high-performance concrete (w/b = 0.2-0.3) in the 2-3 range [61, 43, 169]. The incompressible aggregates provide stability to the binder in the plastic and hardened state. Consequently, the low a/b is concerning in terms of plastic and long-term shrinkage.

5.2.2 Material properties

In order to characterise the mix, the static (τ_s) and dynamic yield (τ_d) stresses, as well as the re-flocculation (R_{thix}) and structuration rates (A_{thix}) were determined with an ICAR rheometer as recommended by Kruger et al. [38]. The shear rate

Table 5.1: Mix proportions.

Constituent	Mix 1 [kg]	Mix 2 [kg]
Cement	579	579
Fly-ash	169	169
Silica fume	83	83
Fine aggregate	1167	1167
Water	261	261
Superplasticizer	1.204% mb	1.204% mb
Black pigment	0	16.67
Water/cement	0.45	0.45
Aggregate/binder	1.40	1.40

of 1 s^{-1} (0.2 rpm) and test duration of 60 seconds were based on the screw speed and geometry of the concrete pump and the extrusion time of the material [170]. The rheology and setting time results can be seen in Table 5.2. A Vicat needle test [**?**] was conducted on three samples to determine the initial (T_i) and final setting (T_f) times of the 3DPC mortar.

Table 5.2: Material properties of the mix.

Material parameter	Mix 1
τ_s [Pa]	1891
τ_d [Pa]	969
R_{thix} [Pa/s]	2.26
A_{thix} [Pa/s]	0.522
T_i [minutes]	210
T_f [minutes]	430

5.2.3 Mixing and test procedure

The mixing and test procedure, as seen in Table 5.3, was followed meticulously. The 25 ℓ two-blade pan mixer required additional interim hand mixing to prevent some of the materials sticking to the pan's bottom. Before printing, the pump was primed with the mixture. The print was activated to extrude concrete in a layer-by-layer fashion on the predefined path without any intervention. Time-zero was defined as the time when the print path has reached its end. Measurement targets and/or crack inducing shrinkage restraining rods were inserted immediately after the print was completed. After 10 minutes, the mixture attained adequate

stiffness to cut the specimens without affecting the filament shape. A steel putty knife was used to divide the printed concrete into specimens of the desired length. If the specimens were cut a few minutes too early, a minor deformation occurred in the filaments that did not result in any cracks. The specimens were not moved from their original position. Care was taken to not induce vibration or movement in the base. Any excess material was removed from the print bed to prevent any disruption in the airflow. Once the specimen has been cut to the desired length, the observations could start. Free shrinkage observations were started exactly 12 minutes after printing was completed where crack monitoring started a few minutes later. In order to reduce the time between the first observation and time-zero the specimen should be cut earlier which will result in the deformation of the filament.

Table 5.3: Timeline of the mixing and test procedure.

Step	TAP*	Duration	Details
1			Test trail run
2			Setup of measurement equipment
3			Weigh materials
4			Coat PVC printing base with mould oil
5		60 s	Mix all dry materials in mixer
6		45 s	Gradually add water for duration
7		45 s	Gradually add superplasticizer for duration
8		120 s	Additional interim mixing with steel trowel
9		120 s	Continue mechanical mixing
10		30 s	Transport concrete to printer
11		5 min	Prime concrete pump
12		5-7 min	Print test specimen
13	Time-zero	3 min	Insert restraints and/or DIC markers
14	3 min	7 min	Calibrate measurement equipment
15	10 min	1 min	Cut specimens to length and remove excess
16	11 min	1 min	Activate fans to produce airflow
17	12 min	3/24 h	Start observations
18	20 min	1 min	Spray surface pattern if required

TAP* - Time after print

5.2.4 Concrete printing

A 1 m^3 gantry printer with a 25 mm diameter circular nozzle was used to place concrete filaments with a cross-section of approximately 40 x 10 mm (width x

height). For more detail on the 3D concrete printer used in this study, Kruger [24] can be consulted. A print speed of 90 mm/s was selected. Thereafter the extrusion rate was adjusted to obtain a 40 mm filament width. The pass time was never more than 42 seconds.

5.2.5 Evaporation condition

All experiments were conducted in a climate-controlled room with an air temperature of $25 \pm 1°C$ and relative humidity of $60 \pm 5\%$. Two free-standing fans were used to produce a uniform wind speed of $13 \pm 1\ km/h$ over the printed specimens. The Beaufort wind speed guide describes this wind speed as a gentle to moderate breeze [50]. These evaporation conditions resulted in an evaporation rate of approximately 0.412 $kg/m^2/h$ [100]. This evaporation rate is fairly moderate and is less than half of that used for testing PSC in ordinary concrete [171].

5.2.6 Monitoring deformation with digital image correlation

The digital image correlation (DIC) technique compares the greyscale intensity of pixels in two images to calculate the displacement of high contrasting targets on the specimen. Signatures in the targets are identified in the undeformed image and then located in the deformed image. The signature can be the grey-value, the derivative or, most often, the signature of the neighbouring pixels. The "neighbourhood" of pixels is called a subset. The displacement of the subset is the average displacement of the pixels in the subset [172, 173].

In this study, two types of targets were used: a marker embedded in the specimen to measure free shrinkage (seen in Figures 5.3, 5.4 and 5.5) and a speckled pattern sprayed onto the specimen's surface for the restrained shrinkage (seen in Figure 5.1 a). Each marker consists of eight white dots with a diameter of 2.4 mm as seen in Figure 5.4. The software identifies an ellipse in the pixels on the dot's perimeter and then calculates the displacement of the ellipse's centre during deformation [173]. Here, the ellipse is the "neighbourhood" of pixels on the perimeter of the white dot. The displacement of the marker is defined as the average displacement of the ellipsis corresponding to the eight dots. With the speckled pattern target, only the subset size and deformation area is user-defined. The software identifies the unique signatures in the subsets of the undeformed image and finds them, using correlation, in the deformed image to calculate a displacement field.

For 2D applications, only one camera is required. Many [67, 114, 65] have used DIC to measure plastic shrinkage in concrete. DIC provides a non-contact alternative to conventional Linear Variable Differential Transformers (LVDTs).

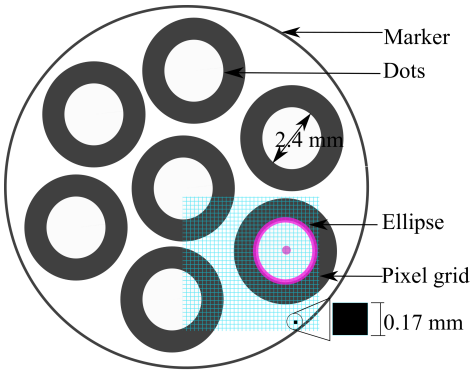

Figure 5.4: DIC markers used to measure free shrinkage.

DIC limits the disruption of airflow around the specimens and allows the accurate tracking of more points on the specimen.

Two identical optical cameras were used to monitor in-plane deformation (only 2D) of the specimens. Two fluorescent lamps, producing a white colour, were attached to the camera stand to provide sufficient light. A constant light source during the experiment is critical to the success of this technique. GOM correlate (2019) was used to process the image series.

5.2.6.1 Using markers

Two markers were embedded 10 mm into the layer (top or side) and 25 mm from the ends of the specimen (Figure 5.5). Using markers rather than a surface pattern is beneficial for measuring free shrinkage since it: does not alter the evaporation and bleeding characteristics of the concrete surface, represents the internal deformation of the layer (not just the surface) and is unaffected by bleeding.

Figure 5.5: A 300 mm long, 20 layered printed specimen with DIC markers embedded.

All the images are compared to the first image, taken 12 minutes after the print is complete. It is assumed that the deformation before the first image is negligible compared to the absolute deformation. Images were captured at an interval of 2 minutes with a camera placed 835 mm from the markers. A 25 mm focal length was used. Each 4928 x 3264 pixels image had a pixel size of 0.175 x 0.175 mm. This produced a 16 x 16 pixels ellipse over each dot on the marker and a displacement resolution smaller than 0.01 mm.

All images were compared to the first image to calculate the change in position of the markers. The displacement, measured in the print direction, of two markers were added to calculate the deformation over a specific length (L). The nominal strain is then calculated by dividing the change in length (ΔL) by the original length (L) where shrinkage is defined as positive. The scale was defined by placing a steel ruler in the same plane as the targets. The scale has no effect on the dimensionless strain results.

5.2.6.2 Using a surface pattern

The concrete surface appeared relatively dry 20 minutes after the print due to the absence of bleeding water and moderate evaporation rate. Once dry, a speckled pattern was created on the surface of the black concrete (Mix 2) specimen using white and black chalk-based spray paint as seen in Figure 5.6. The success of the surface pattern DIC is dependent on the contrast between the applied pattern and the surface background that was improved by using black concrete (Mix 2). The DIC software was used to verify that the quality of the pattern is acceptable. Bertelsen et al. [67] showed that chalk-base paint does not influence the evaporation of pore water like acrylic-base paint does. The absence of surface water 20 minutes after printing and the use of chalk-based paint permitted the use of a surface pattern.

The first image was taken 24 minutes after print completion, before which some deformation may have occurred. The time between the first observation and time-zero is dependent on the drying time of the concrete. In this experiment, the absolute displacement is not as relevant as the change and transfer of displacement. A delayed start was therefore acceptable.

Images (4928 x 3264 pixels) were captured at an interval of 2 minutes. The spray paint produced speckles much smaller than the dots on the marker and required a smaller pixel size. By placing the camera at 700 mm from the specimen and using a 50 mm focal length a pixel size of 0.065 x 0.065 mm was obtained. The pixel size is in accordance with Bertelsen et al. [67] and Zhao et al. [114] who used sizes of 0.087 x 0.087 mm and 0.058 x 0.058 mm, respectively. A subset size of 23 pixels and a point-to-point distance of 14 pixels were selected to obtain a

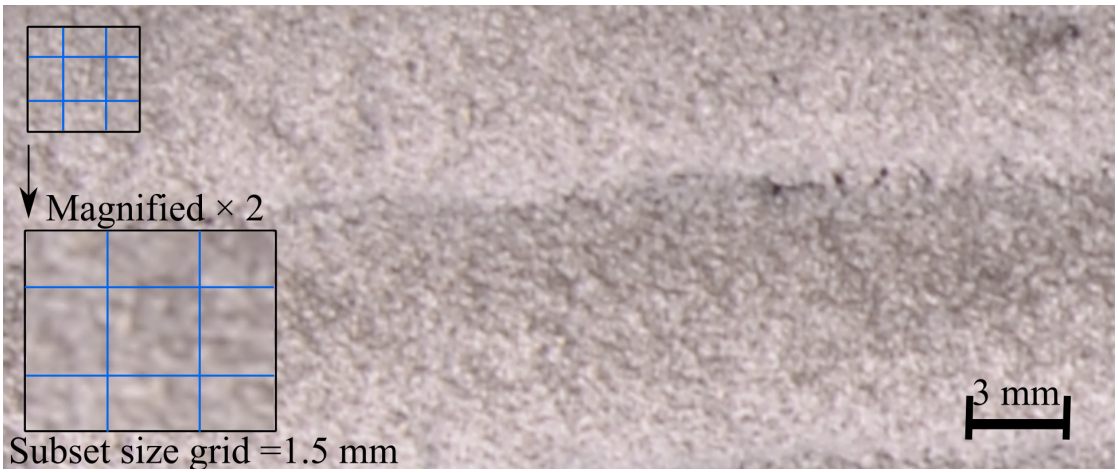

Figure 5.6: DIC speckled pattern on the surface of the concrete specimen.

density greater than 3 speckles per subset. A resolution smaller than 0.001 mm was obtained.

5.2.7 Crack growth analysis

A Matlab algorithm was developed to measure the crack size from an image series. This approach reduces computational time and improves accuracy by reducing human error. Using image processing software in combination with DIC is beneficial since many of the prerequisites, such as a constant light source, small pixel size and the camera setup, are already met. A similar technique has also been used by others in the field [60, 109]. A short description follows.

Firstly, the scale is defined. Here, a pixel size of 0.065 x 0.065 mm was used. The image is cropped to show only the crack under consideration. The cropped image is then transformed to greyscale and converted to a binary image (each pixel as a 1 or 0 in a matrix), using the "imbinarize" function, at a defined threshold (more on this later). Morphological operations are performed to clean the binary image using the "bwmorph" function's "clean", "fill" and "spur" operations. All the 1s in the resulting matrix are summed and scaled to the actual size (mm^2) to obtain the crack area. The procedure is repeated for all the images of the series to obtain the crack growth. In the case of a specific layer, the images are cropped to only show the crack of that layer.

The methodology of selecting a threshold value has been disputed in the past. The binary conversion function classifies each pixel as a 1 (crack) or 0 (concrete) based on the greyscale value. Some surface pores or other irregularities can occasionally be classified as part of the crack (referred to as impurities below). To prevent this misidentification, the following simple procedure is proposed.

All the images in the series are cropped to depict the area where the crack forms. The image of the fully developed crack is converted to a binary image at different thresholds as seen in Figure 5.7. The absence of impurities (Th=0.2) can mean that the algorithm is not sensitive enough and underestimates the total crack area. Too high a threshold (Th=0.4) can overestimate the actual crack area by being oversensitive to the greyscale value and any changes in lighting. The threshold was selected from Figure 5.7 as the image with the lowest threshold with at least some visible impurities. Here, a threshold of 0.3 was selected. This threshold is low enough to minimise the impurity area but high enough to maximise the crack area.

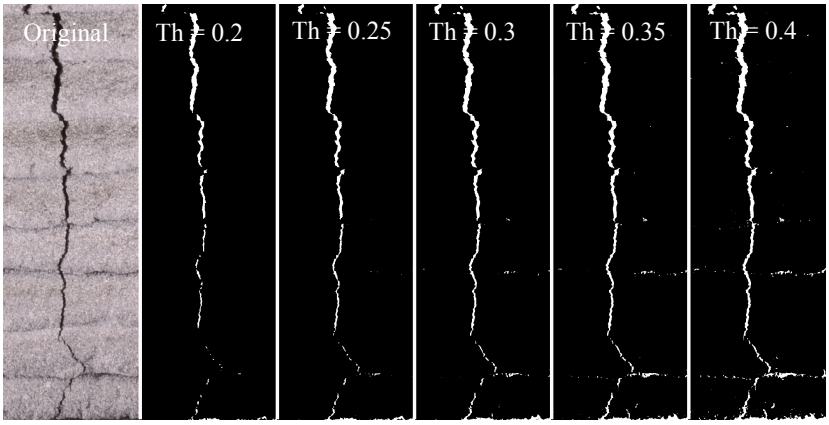

Figure 5.7: Original and binary images of the crack at different threshold values (Th).

The impurity area is then determined by calculating the mean area in all the uncracked images where the area should be zero. All the images are then analysed at the 0.3 threshold and the impurity area is subtracted from the calculated area to obtain the actual crack area.

5.2.8 Experimental setup

Either the experimental setup of free shrinkage or cracking was used in each experiment. In both cases, care was taken to apply an even coat of mould release oil to the PVC print bed in order to reduce base friction between the bed and bottom layer of the specimen as permitted by ASTM C1579 [109].

5.2.8.1 Free shrinkage

Three experiments were conducted to evaluate the influence of the specimen's length and number of layers on the free shrinkage strain result. Initially, a specimen length of 200 or 300 mm with a height of one or three layers were considered. The

shrinkage in the print direction was monitored from the top with markers as seen in Figure 5.8. The three-layer, 300 mm long specimen was also monitored from the side. To further investigate the influence of restraint and layer height, two 300 mm, 20 layer specimens were monitored from the side for the first 24 hours (Figure 5.5).

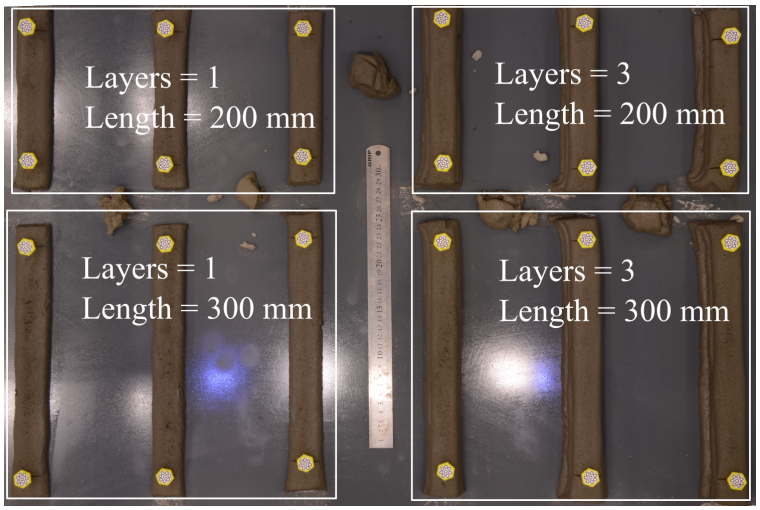

Figure 5.8: Printed specimens with lengths of 200 or 300 mm with one or three layers.

5.2.9 Restrained shrinkage and cracking

PSC occurs due to a restraint of horizontal plastic shrinkage. Three forms of restraint were identified in 3DPC, namely: print geometry, base friction and reinforcement. Five restraint combinations were evaluated experimentally (Figure 5.9). The specimen's dimensions were selected from the free shrinkage results as 300 mm long with 10 layers. A height of 100 mm was selected to agree with the crack forming moulds used for studying ordinary and fibre reinforced concrete [109]. Curved specimens were not considered due to the complexities of crack area monitoring. The specimens, each with a different restraint combination, were placed under the evaporation load and observed for 3 hours to see if cracking was induced.

Restraint Combination A utilises the geometry of the ends to induce cracking in the 300 mm straight section. Combination B utilises the restraint caused by the base friction (specimen printed on two pieces of 40-grid sandpaper with a smooth surface in-between) to induce a crack originating from the base and propagating to the top of the specimen. Combination C, D and E utilises the restraint caused by reinforcement-like vertical restraints. For Combination D, four stiff steel rods (diameter 6 mm, length 50 mm) were inserted from the top into the concrete

immediately after the printing was finished. Combination C and E followed a similar procedure with two 100 mm long steel rods. In addition to Combination C, Combination E had a 2 mm steel plate inserted (15 mm into the specimen) to act as a notch for crack formation. The rigid element was not in contact with the specimen and did not provide additional surface friction to the top of the specimen.

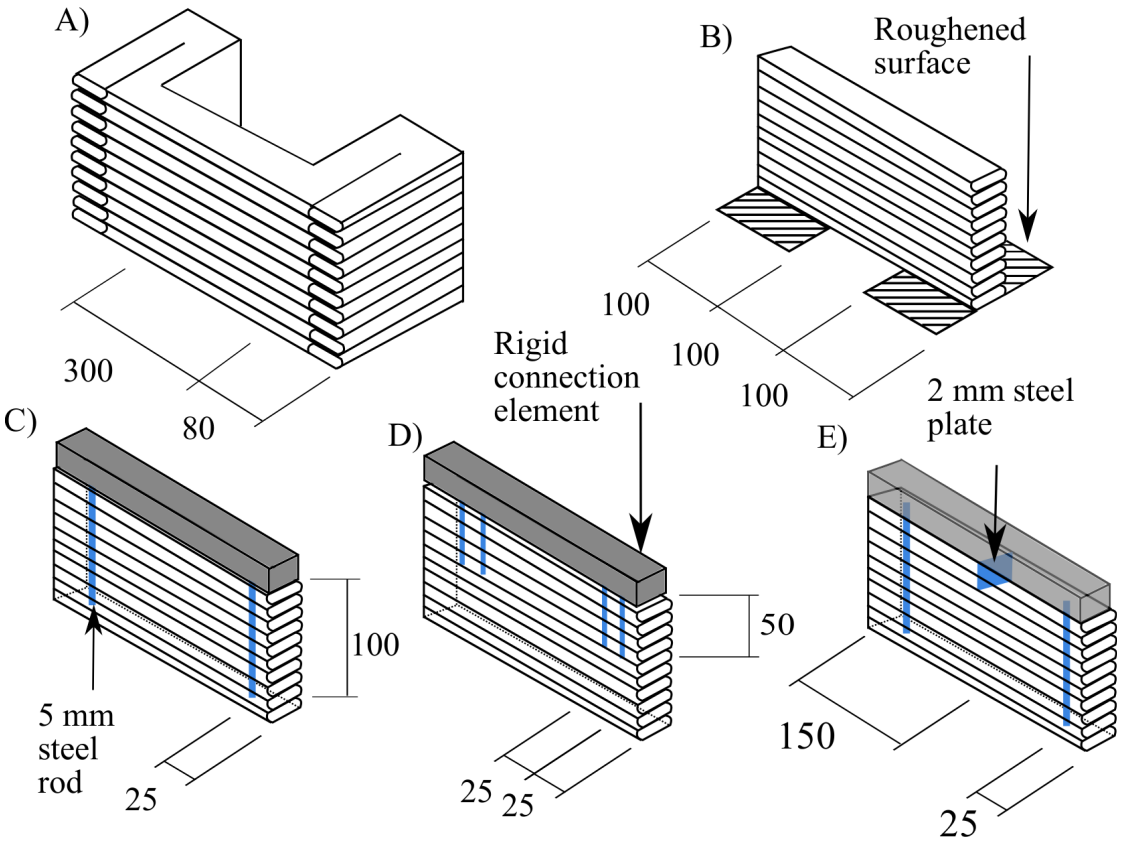

Figure 5.9: The combinations of print geometry, base friction and reinforcement used to induce PSC in 3DPC. A) Restrained by the print geometry. B) Restrained by base friction. C) Restrained by two 100 mm steel rods connected with a rigid element. D) Restrained by four 50 mm steel rods connected with a rigid element. E) Restrained by two 100 mm steel rods connected with a rigid element in combination with a notch midway between the restraints.

5.2.10 Recommendations

Although the results show good repeatability in the experiments, the following improvements are recommended to reduce variability in the results:

- A free-standing fan is used in this study and by many others [67, 114] to create an evaporation load. However, the geometry of the 3DPC specimens can result in a turbulent state of airflow and inconsistencies in the evaporation load through the testing chamber. A wind tunnel is recommended to produce more laminar and uniform airflow. ASTM C1579 [109] should be consulted for recommendations on the wind tunnel.

- The crack inducing apparatus should be constructed from an unabsorbent material, unlike wood. PVC is recommended. Here, care was taken to prevent contact between the concrete and the wood (rigid connection element in Figure 5.9). Any contact would induce undesired additional restraint and affect cracking.

- To improve the free shrinkage experiment, the base friction can be further reduced by covering the PVC base with a layer of wax paper or plastic sheeting.

- ASTM C490 [174] suggests a resolution of 0.004 mm to measure drying shrinkage. It is recommended that a smaller pixel size is used for measuring the free shrinkage to obtain a even lower resolution than used here. This can be achieved by placing the camera closer to the specimen. Nonetheless, the resolution used was deemed sufficient for the purpose of the study.

- A random pattern on each marker is recommended to prevent the software from misidentifying the markers in the preceding images. In this study, misidentification, detected by plotting the results, occurred occasionally and was in all cases corrected by interpolation.

- Although a 15 mm notch is used, it is recommended that the notch height corresponds with the filament height which is 10 mm in this study. This would be advantageous for studying the effect of the interlayer on cracking as well as decrease the notch to crack length ratio and, therefore, reduce the effect of the notch on cracking.

- The concrete temperature can have a significant influence on the rate of static yield stress development and, consequently, the shape retention and buildability of 3DPC [175, 38, 170]. Care should be taken when testing PSC at different ambient temperatures.

5.3 Results and discussion

5.3.1 Free shrinkage and the specimen dimensions

The mean nominal strain of 200 or 300 mm long, one (L1) or three-layer (L3) specimens can be seen in Figure 5.10 where shrinkage strain is defined as positive. The rate of nominal strain development was higher in the L1 specimens compared to the L3 specimens. The surface area to volume ratios of L1 and L3 are about 15% and 8.3%, respectively. The higher surface to volume ratio can cause an increase in the pore water loss and the rate of strain development. The peak strain occurred earlier in the L1 specimens but the magnitude was not significantly different from the L3 specimens. If the strain data of the maximum L3 200 mm and the minimum L3 300 mm specimen were removed, the peak strain of all the specimens was between 6.3 and 7.1 μm/mm.

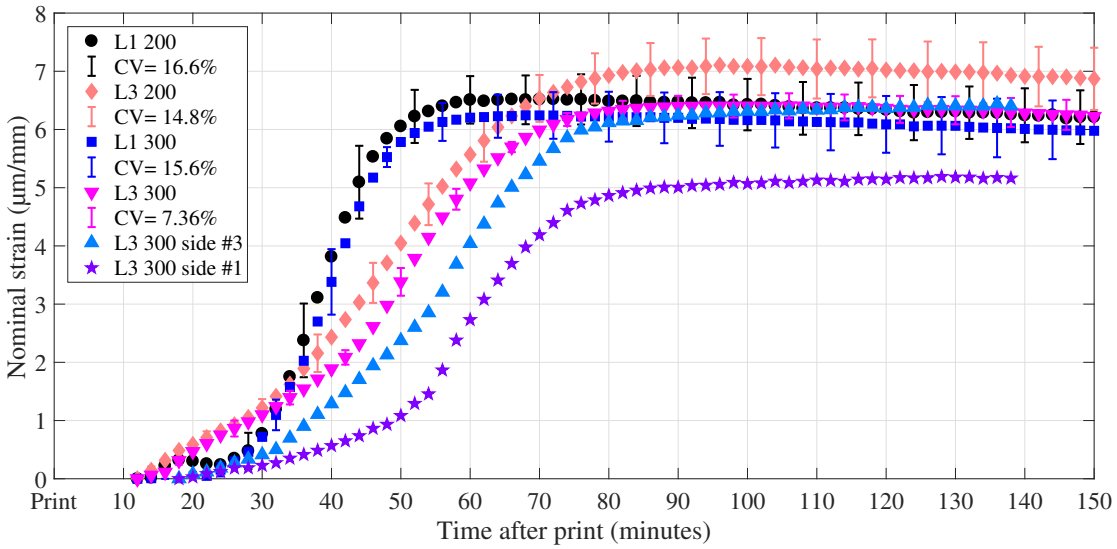

Figure 5.10: Nominal strain development of 200 and 300 mm specimens with one (L1) or three (L3) layers. Specimen L3 300 was also monitored from the side with #3 and #1 corresponding to the top and bottom layer, respectively.

In all the experiments conducted, the 200 mm specimens had a higher rate of strain gain than their 300 mm counterpart. As the concrete develops stiffness with time the shrinkage decreases. Therefore, a higher rate of strain gain is likely to result in a higher peak strain. A one-way analysis of variance (ANOVA) was conducted to evaluate the effect of the specimen length on the mean and peak strain. The results showed that there is no statistically significant difference in the mean strain ($F(1, 18)=2.1$, $p=0.16$) or peak strain ($F(1, 18)=1.77$, $p=0.20$) at

a significance level of 0.05. Since neither the length nor the number of layers of the specimen made a statistically significant difference in the peak or mean strain results, the coefficient of variation (CV) was used to select a specimen length and height for the test setup.

The mean CV measured over the test period was higher (16.6% and 14.8% for L1 and L3, respectively) in the 200 mm specimens and the lowest in the L3 300 mm specimens (7.36%). The variability in cross-section area and base friction over the shorter 200 mm length may be the cause of the higher CV. Any defects in the cross-section area or bottom layer restraint would have a more significant effect on the strain development of a shorter specimen with fewer layers than the alternative. These factors, as well as a realistic surface to volume ratio and layer-on-layer rather than layer-on-base interaction commissioned the use of longer specimens with more layers.

The peak strain result of the L3 300 specimen, monitored from the top, is in agreement with the L3 300 side specimen's top layer (#3). The strain in the bottom layer (#1) of the L3 300 specimen is significantly less than any of the other specimens. A reduced strain in the bottom layer is expected due to an increase in base restraint which is a function of mass.

The influence of the base on the restraint of the bottom layer is even greater in a 20 layer specimen. The nominal strain can be seen in Figure 5.11 b) where #20 is the top layer.

The peak strain of the bottom layer is 25% lower in L20 than in L3. The decrease is relatively small considering that the mass on the bottom layer of L20 is 8.5 times that of L3. This behaviour is expected where the base friction is low.

It is clear from Figure 5.11 b) that the peak nominal strain increases with distance from the base layer, with the exception of the top layer (#20). As the distance from the base layer increases, the influence of the base restraint decreases together with an increase in shrinkage of the layers below, resulting in a higher strain at the upper layers. The mean strain difference between #2 and #4 is more than 2.7 times that of #4 and #6, giving an indication to the influence of the base restraint on the strain development. Although the surface to volume ratio is three times higher in #20 than #18, #20 has a strain lower than #18, a phenomenon also observed in other specimens. This phenomenon may be due to the rise of the bleeding water through the layers to the top but more experiments are required to confirm this hypothesis.

Surprisingly, the magnitude of strain is only marginally higher in the L20 specimen when compared to the L1 and L3 specimens. An increase in peak strain was expected as the number of layers increased due to a reduced influence of the base restraint. Instead, additional layers increased the mass of the specimen that increased the base restraint and resulted in no significant increase in the peak

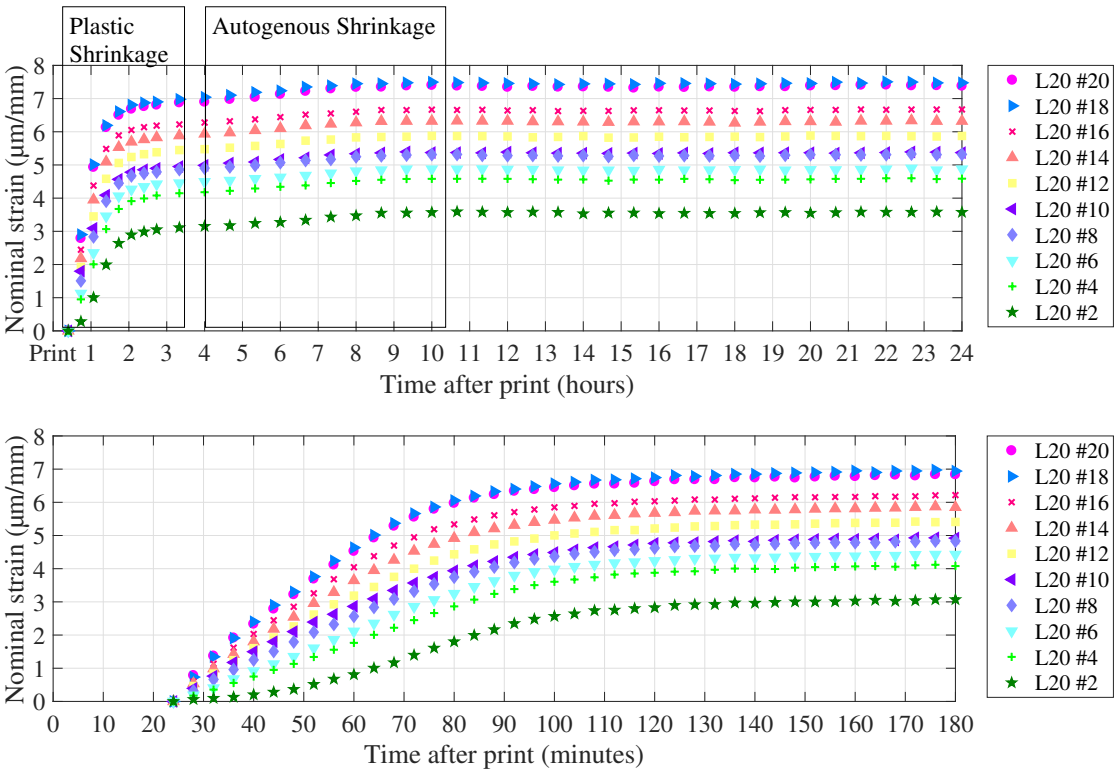

Figure 5.11: Nominal strain of a 300 mm, 20 layer specimen: a) measured over 24 hours and b) 3 hours.

strain of the top layers. More layers are therefore likely to result in a similar free shrinkage, but more severe cracking due to a higher base restraint.

All the layers have a second increase in nominal strain occurring between 4 and 10 hours as seen in Figure 5.11 a). The time-frame, mix composition and magnitude of strain increase suggests autogenous shrinkage. A similar increase was also observed by De Coensel [168] and identified as autogenous shrinkage.

Turcry and Loukili [62] measured a plastic shrinkage strain in the 1.8-4 μm/mm range for ordinary concrete and 2.1-4.5 for SCC under an estimated evaporation rate of about 0.5 $kg/m^2/h$. Combrinck et al. [155] showed a similar strain range in ordinary concrete. Holt and Leivo [40] stated that at a free shrinkage strain of 1 μm/mm there is a high risk of PSC in ordinary concrete. The strain measured in 3DPC is approximately twice that measured by others in ordinary concrete and SCC, and many times higher than 1 μm/mm even at a moderate evaporation rate. The peak strain is also reached earlier in 3DPC, at about 90-120 minutes, compared to the 3-6 hours of ordinary concrete and SCC.

From the results and observations from the experiments conducted, the following deductions can be made for further experiments:

- The repeatability of the experiments were evaluated with the coefficient of variation (CV) of the measurements. A lower CV was observed in the longer specimens with more layers. This study recommends a specimen length of 300±10 mm with a gauge length of 250±10 mm. This gauge length produced the lowest CV and is in agreement with ASTM C490 [174].
- The surface area to volume ratio is similar (<5% difference) for a specimen with 6 layers or more. Therefore, a specimen with more than 6 layers is recommended.
- The influence of the base restraint on the strain seems to decrease with an increase in the number of layers. More layers would, therefore, decrease the sensitivity of the experimental setup.
- However, too many layers can increase the base restraint by increasing the mass of the specimen. A free shrinkage specimen with 10 layers is recommended.

5.3.2 Restraint combinations for inducing a crack

For Restraint Combination A and B, no cracking was observed in two separate experiments. The restraint created by the print geometry and base friction was not enough to cause cracking. The print geometry and base friction can, however, result in cracking under more severe evaporation rates and should not be excluded as a cause of cracking. Moulds with a ring geometry have been used in the past to induce early age cracking in conventional concrete [162].

Combinations C and D resulted in cracking at the restraining rods as seen in Figure 5.12 a) and b). When a notch (2 mm steel plate, 15 mm into the specimen) was added to Combination D the crack also formed at the restraining rods as seen in Figure 5.12 c). For both Combinations C and D, the cracks started to form approximately 50 minutes after printing and was not due to the specimen preparation procedure.

Combination E formed a crack that propagated from the notch to the base as seen in Figure 5.13. The crack first appeared 56 minutes after print and continued to grow in length until it divided the entire specimen at 104 minutes. Figures 5.1 a) and 5.15 depict a similar crack formed with Restraint Combination E in different specimens.

It is hypothesised that the different crack patterns in Combination D with the notch and Combination E are due to the different restraining rod penetration depths (reinforcement length). Combination D had a rod length of 50 mm that resulted in cracks at the restraining rods where Combination E had a rod length of 100 mm (from the top layer to the base) that resulted in a crack at the notch.

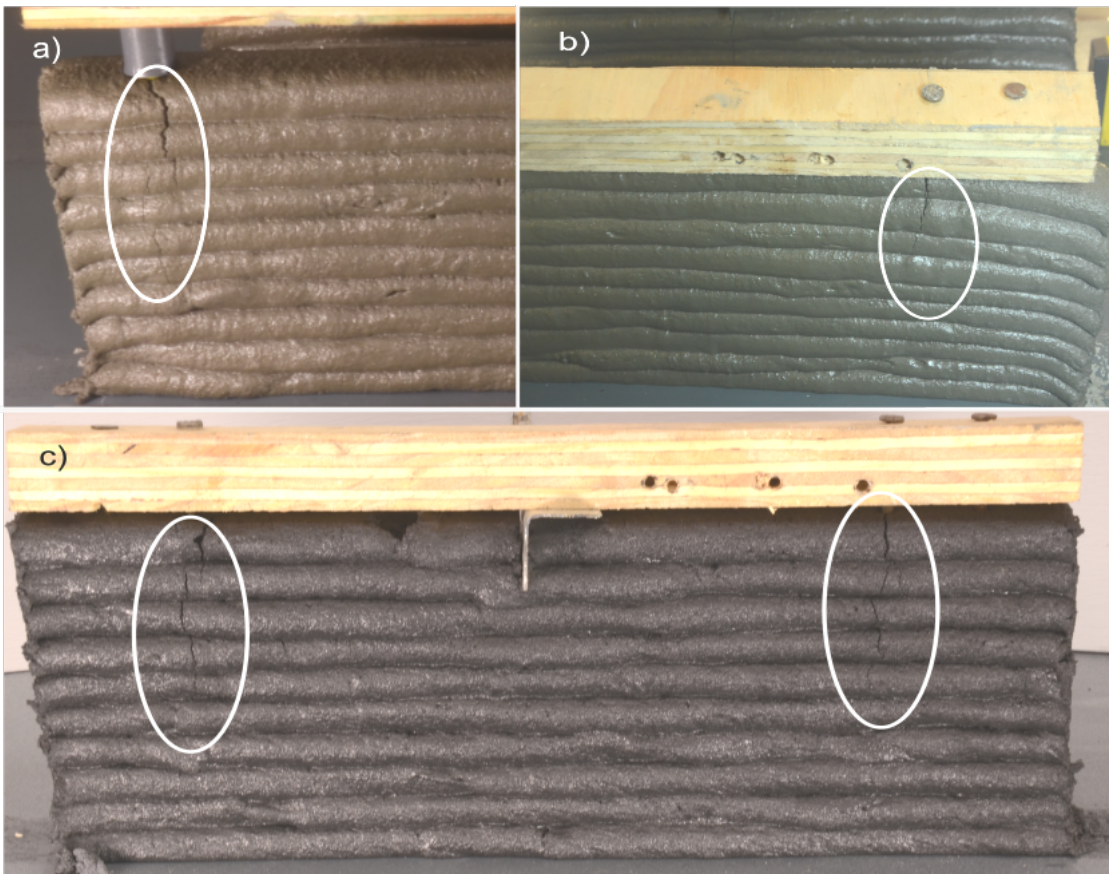

Figure 5.12: Cracks that tend to form due to a) Combination C (camera at 60° angle to specimen), b) Combination D (camera at 45° angle to specimen) and c) Combination D when a notch is inserted (camera at 90° angle to specimen). These cracks started to form approximately 50 minutes after printing.

Restraint Combination E is discussed next, followed by a discussion on the crack pattern in Combination D.

5.3.3 Deformation in the Restraint Combination E specimen

To confirm that the crack induced by Restraint Combination E is a result of plastic shrinkage, two shrinkage markers were placed midway between the crack and the restraining rod, with a gauge length of 130 mm (L) measured over the crack, as seen on Figure 5.13. The change in length (ΔL) between two markers can be seen in Figure 5.14. A positive ΔL corresponds to an inward (towards the crack or centre) displacement of the shrinkage markers. When the layer is uncracked, and therefore connected to both restraints, a small positive ΔL is observed due to the

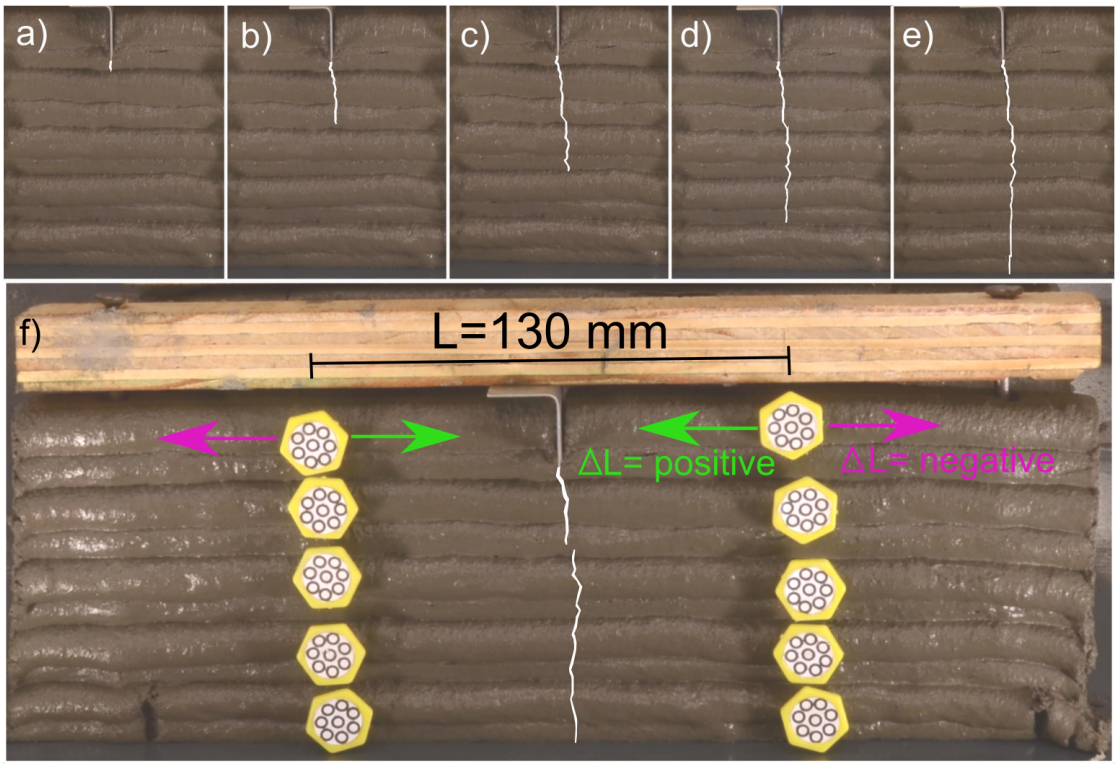

Figure 5.13: Crack (indicated in white) created by Restraint Combination E at a) 64, b) 86, c) 96, d) 98, e) 104 minutes after print. f) Combination E with shrinkage markers placed at a gauge length of 130 mm (L), midway between the crack and restraining rods.

shrinkage between the two markers. After a few minutes ΔL changes direction, meaning that the markers are being displaced outwards, away from the crack. Soon after the change in direction the layer starts to crack. Once the crack propagates through a particular layer, an increase in the rate of negative ΔL is observed in the top layers due to the shrinkage between the crack and restraints. It should be noted that at 50 minutes, the deformation is more than four times as large in the free shrinkage specimens as in this restrained shrinkage specimen. The results are as expected and in agreement with our understanding of plastic shrinkage crack propagation [89, 155].

It can be confirmed that Restraint Combination E resulted in a true plastic shrinkage crack. Combination E is therefore recommended for future experimental research on PSC in 3DPC. Combination E mitigates the contribution of plastic settlement cracking to plastic shrinkage cracking by avoiding reinforcement that induces differential settlement [155]. The crack position, at the midpoint between restraints, also eliminates other sources of mechanical induced cracking.

It was also observed that the failure is more ductile in the upper layers with the

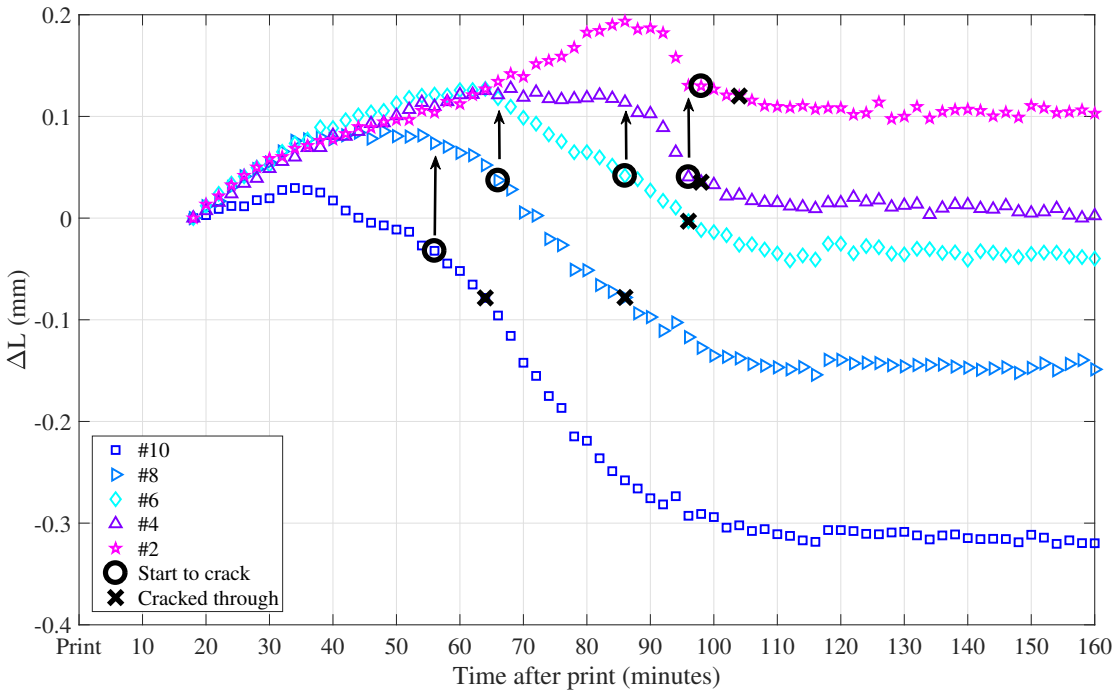

Figure 5.14: The change in length (ΔL) between two shrinkage markers shown in Figure 5.13.

crack appearing on the surface about 20 minutes after the markers have changed direction. As the stiffness of the fresh concrete increases the brittleness of the failure is likely to increase. As the crack propagates through the specimen the area connecting the left-hand and right-hand sides is reduced resulting in a concentration of the tensile forces which accelerates crack propagation. It appears that the formation of a crack in one layer has a significant influence on the displacement in the layer below, as shown by the arrows in Figure 5.14. As soon as the crack appears on the surface of layer #9, the ΔL in layer #8 changes direction. Similar for #8 and #6 and #6 and #4.

Our understanding of the evolution and distribution of deformation and cracking is key to the design of tensile reinforcement and selection of PSC mitigating measures for 3DPC in the future.

5.3.4 Understanding the deformation that results in cracking

The deformation of the entire specimen can be evaluated by conducting a speckled pattern DIC analysis. The horizontal displacement of multiple points on the surface for the Restraint Combination E specimen can be seen in Figure 5.15.

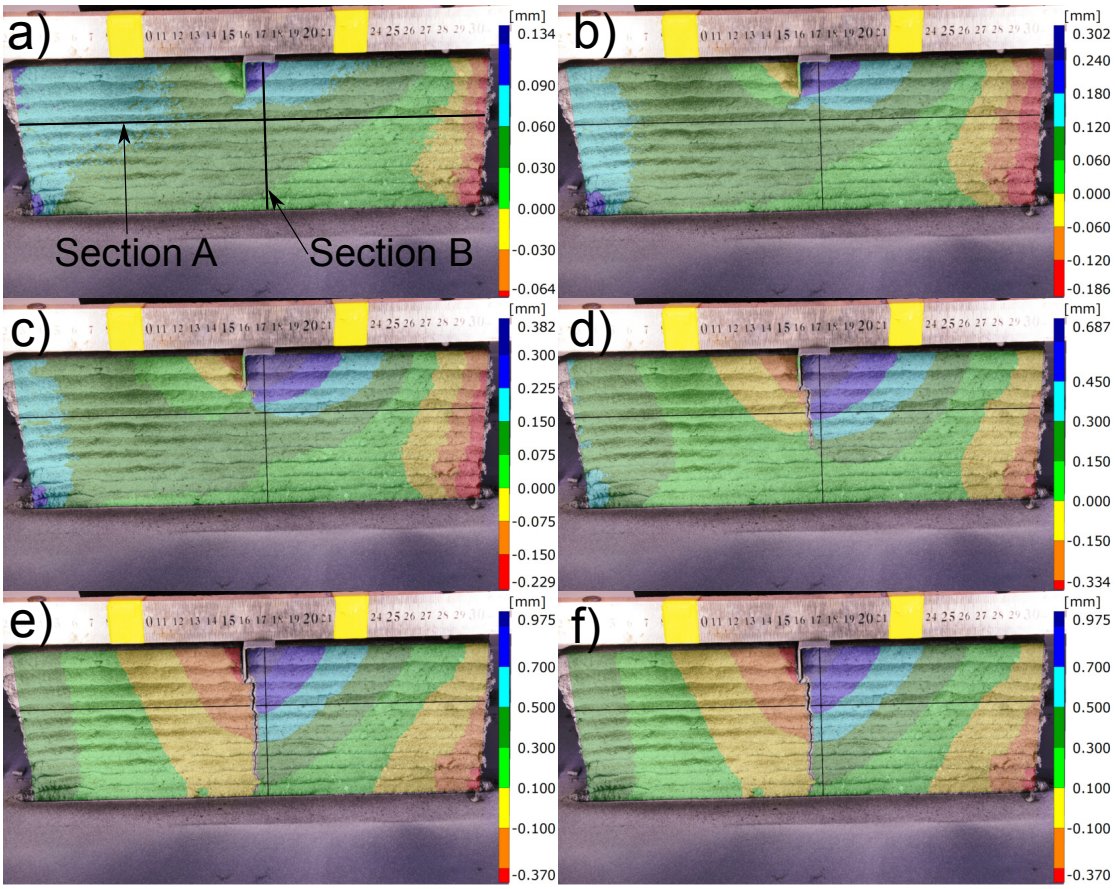

Figure 5.15: Restraint Combination E horizontal displacement in the DIC specimen at a) 34, b) 46, c) 50, d) 64, e) 80 and f) 122 minutes after print. Zero displacement is defined at 24 minutes after print. Positive displacement correspond to a rightward movement of the points on the specimen.

Initially (Figure 5.15 a), the peak displacements occur on the outsides of the restraints as well as at the notch since the concrete is free to displace at these locations. The deformation near the notch, in layer #10 and #9 (Figure 5.15 b), is transferred to layer #8. The negative displacement on the one side and positive displacement on the other creates a crack in layer #8 (Figure 5.15 c). The crack propagates through the specimen (Figure 5.15 d) resulting in a displacement increase. It appears that the deformation of one layer transfer fairly uniformly to the one below (Figures 5.15 d and e). Once the crack has developed fully, the displacement reaches a peak (Figure 5.15 f). On the left-hand side, the deformation of layer #10 and #1 are fairly similar with the contour line being almost perpendicular to the base. Such behaviour would suggest a low base friction and complete transfer of deformation over the interlayer. On the right-hand side, the

contour lines have a 45° angle to the base, suggesting a high base friction or 50% transfer of displacement over the interlayer.

5.3.4.1 Deformation and cracking of different layers

The crack width and deformation (L=18 mm measured across the crack) of each layer in the Restraint Combination E specimen can be seen in Figure 5.16. ΔL increases with layer height and proceeds the formation of the crack in the layers, indicated for layer #8 by the arrow in the Figure 5.16. The increase of ΔL is proportional to the crack width increase for the different layers after the crack has formed. The top layers deform more, also seen in the free shrinkage specimens, resulting in a higher ΔL and larger crack width.

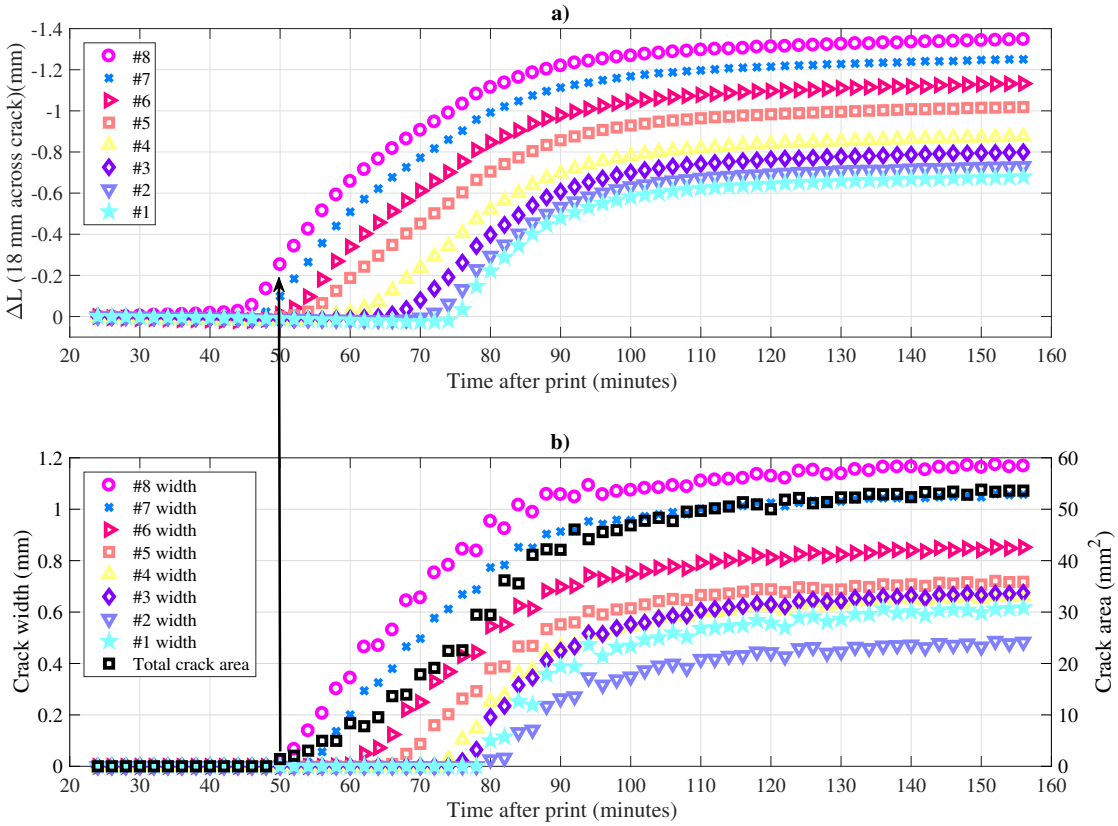

Figure 5.16: Length change (ΔL) and crack width of each layer in a Restraint Combination E specimen. a) The change in length where L is 18 mm measured across the crack and b) the crack width in the layer seen in Figure 5.15.

The development of the total crack area can be seen in Figure 5.16 b). The cracking started at 52 minutes and increased at a constant rate until about 90

minutes whereafter the growth rate decreased. The crack in this experiment started to form slightly earlier and propagated quicker than in the other experiments.

5.3.4.2 Deformation along a horizontal plane of layer 7

The ΔL along Section A in Figure 5.15 at different lengths (L) spanning the crack can be seen in Figure 5.17. To enhance the explanation the expected uncracked free shrinkage result is also shown on Figure 5.17. For the free shrinkage (FS) specimen, ΔL is linear between the maximum at the specimen's edge and zero at the centre. The negative gradient indicates a contraction.

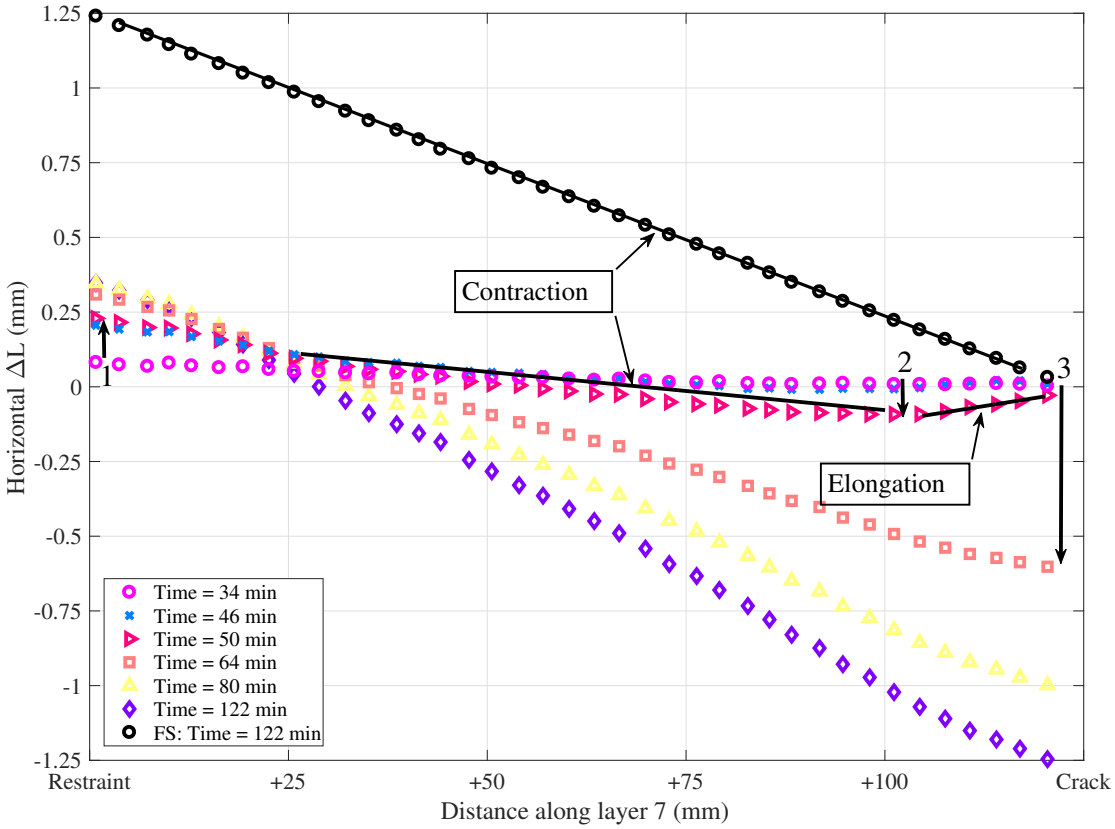

Figure 5.17: The horizontal change in length (ΔL) of Section A in Figure 5.15 measured at different distances from the crack to the restraint at 34, 46, 50, 64, 80 and 122 minutes after print.

For the restrained shrinkage, ΔL is fairly small for the first 34 minutes whereafter the positive (towards the crack) displacement near the restraint starts to increase (Arrow 1), similar to what is expected in the free shrinkage specimen.

With the increase in stiffness of the plastic concrete the deformation at the restraint declines due to the increasing effect of the restraining rods. At 50 minutes, the restraining rods prevent deformation at the restraints to such an extent that the continuous shrinkage deformation is concentrated to the centre of the specimen (Arrow 2). The internal shrinkage results in a contraction (negative gradient) from the restraint to about 100 mm along the length of the layer and elongation (positive gradient) from there to the centre of the specimen where the layer is still connected to the opposite side (uncracked). This elongation results in tensile stress in the 50 mm spanning the crack. The notch reduces the specimen's area to increase the tensile force at a selected location. At 55 minutes, when the tensile force exceeds the tensile capacity, the crack propagates and releases the built-up elastic energy. After the layer has cracked, the negative deformation is distributed linearly along the length of the layer and continues for the next hour (Arrow 3).

This behaviour was observed in each layer on both sides of the crack and is in agreement with the results in Figure 5.14. A similar contraction and resulting elongation is expected in the absence of a notch but in this hypothetical case the crack pattern might be different. The cracking of the layers above definitely has an effect on the deformation in the layer but the contraction and resulting elongation will still be present in a single layer specimen if shrinkage is restrained.

The initiation of cracking in the specimen can be described in four stages: 1⇒ the development of deformation constraint due to the stiffening of the concrete (Arrow 1); 2⇒ contraction due to the plastic shrinkage mechanism (Arrow 2); 3⇒ resulting elongation and 4⇒ crack formation.

5.3.4.3 The evolution of cracking, free shrinkage and restrained shrinkage

The crack width, L20 specimen free shrinkage and the restrained shrinkage measured over various lengths across the crack can be seen in Figure 5.18. The free shrinkage at 50 minutes is between 0.6 and 0.8 mm greater than the restrained shrinkage. An inward deformation is observed for L=126 mm before crack formation, similar to the results in Figure 5.14. This is due to the fact that the concrete has not yet attained the stiffness so that the restraint can prevent positive deformation.

In Figure 5.18 b) at 44 minutes, the negative deformation at L=126 mm and L=54 mm starts to increase together. Stage 1 is therefore complete and Stage 2 is under way. The contraction (Stage 2) due to internal shrinkage induces elongation (Stage 3). Consequently, the negative deformation at L=18 mm only starts 4 minutes after L=54 mm where L=2 mm starts 10 minutes after L=54 mm. It appears that the contraction is transferred along the length of the layer to induce

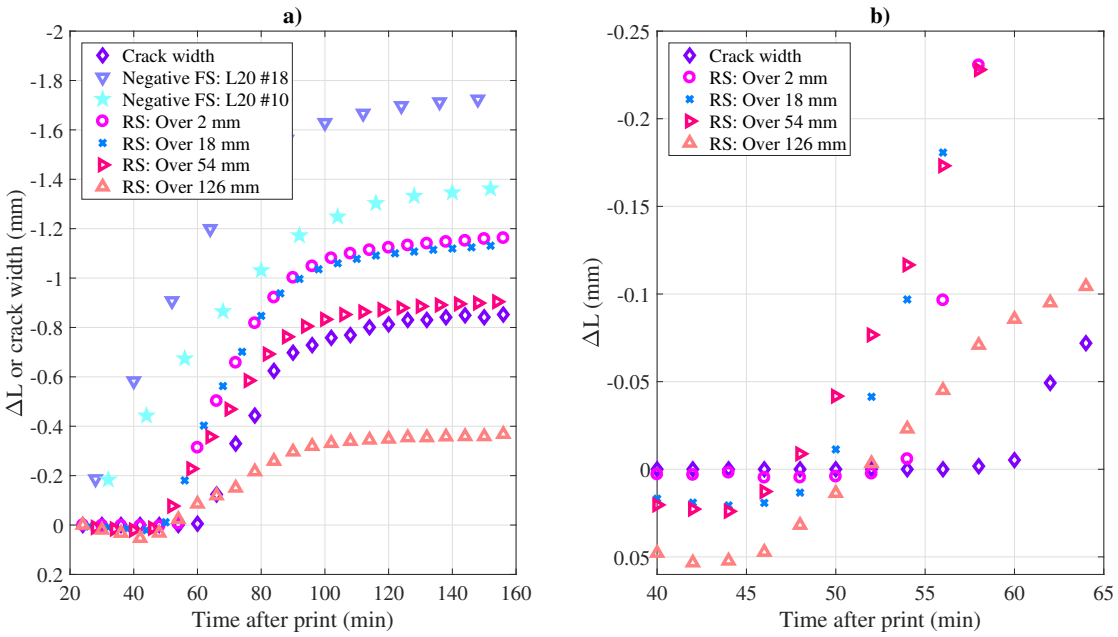

Figure 5.18: Layer 6 crack width, free shrinkage (FS) and restrained shrinkage (RS) measured over (L=) 2, 18, 54 and 126 mm across the crack. a) For the first 160 minutes after printing. b) For the period of crack formation.

elongation with time. After the crack has formed, the 2 and 18 mm deformation is proportional to the increase in crack width.

5.3.4.4 Displacement along a vertical plane

The horizontal displacement of points on a vertical plane parallel to the crack (Section B in Figure 5.15) can be seen in Figure 5.19. As expected, the displacement of the top layers is first to increase. Initially (46 minutes), displacement is small and locally distributed in the top layers (#10 to #7). At 50 minutes, the top of layer (ToL) #8 starts to crack and the displacement in the layers below increases. An irregularity in the displacement is observed at the interlayer of layer #7 and #8 and can be attributed to localised interlayer slip. For the next 14 minutes, the interlayer slip at the ToL #7 is reduced. As the crack propagates through the specimen the lower levels start to deform. At 64 minutes, when layer #4 starts to crack, interlayer slip is observed again at the top of layer #4. At 80 minutes, the specimen has cracked through to the base and the displacement increases uniformly to 122 minutes where the interlayer slip at the ToL #4 is still noticeable. The interlayer slip plane extends along the length of the layer and is even more noticeable further from the crack. The interlayer at ToL #4 was not visibly any different from other layers where minimal interlayer slip occurred.

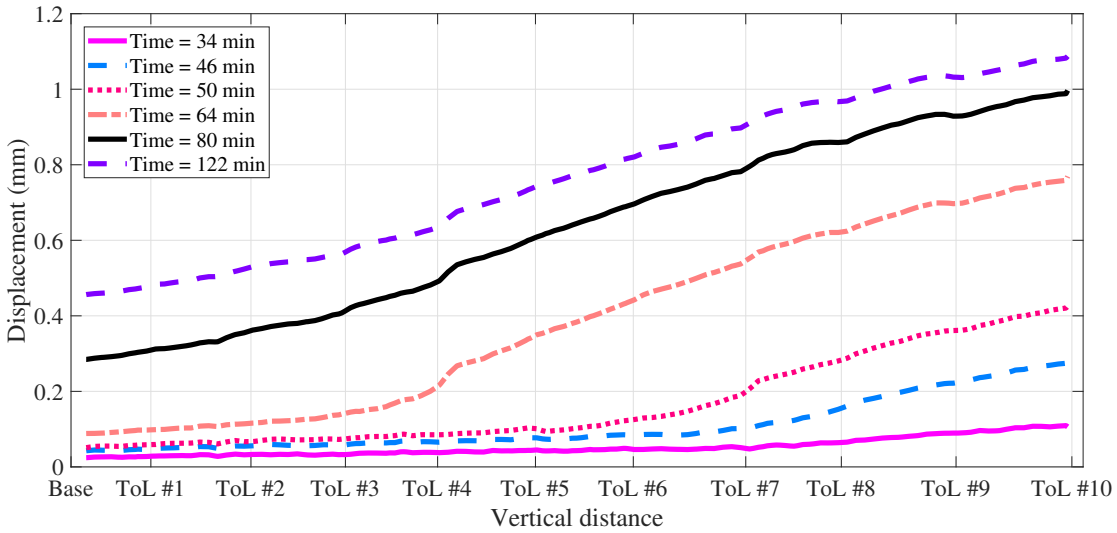

Figure 5.19: Horizontal displacement of points on Section B in Figure 5.15 at 34, 46, 50, 64, 80 and 122 minutes after print.

Slipping occurs on the interlayer plane (i.e., between two filaments) due to the reduced cross-section width and increased porosity [74, 176]. Interlayer slip can be beneficial for PSC mitigation by reducing the transfer of early age deformation between layers. However, the magnitude of the interlayer slip observed here is not sufficient for preventing deformation transfer. In fact, the observation of interlayer slip due to the early age shrinkage of concrete is problematic in terms of long-term interlayer bond strength and the durability of 3DPC.

5.3.5 The hypothesised relationship between interlayer bond strength and interlayer slip

The crack pattern caused by Restraint Combination D in Figure 5.20 is particularly interesting considering that the only two differences between Combination D and E are the number of, and penetration depth of the restraining rods. It is believed that the penetration depth (50 mm) is responsible for this crack pattern.

The hypothesised displacements of the layers in a Restraint Combination D specimen with a notch can be seen in Figure 5.20. The bottom layers (#1 to #5) are free to deform in a positive direction (to the centre of the specimen) but the layers above (#6 to #10) are constrained by the restraining rods. This results in a tensile stress concentration forming at the ends of the restraining rods. The tensile stress surpasses the tensile capacity at this discontinuity resulting in the crack forming. This occurs before the tensile capacity is reached at the notch. Once the cracks have formed at the restraints the tensile stress between the restraints

are released by the widening of the cracks. As a result of the discontinuity, a differential displacement plane is created between the bottom and top layers on the outside of the restraining rods (dotted line in Figure 5.20).

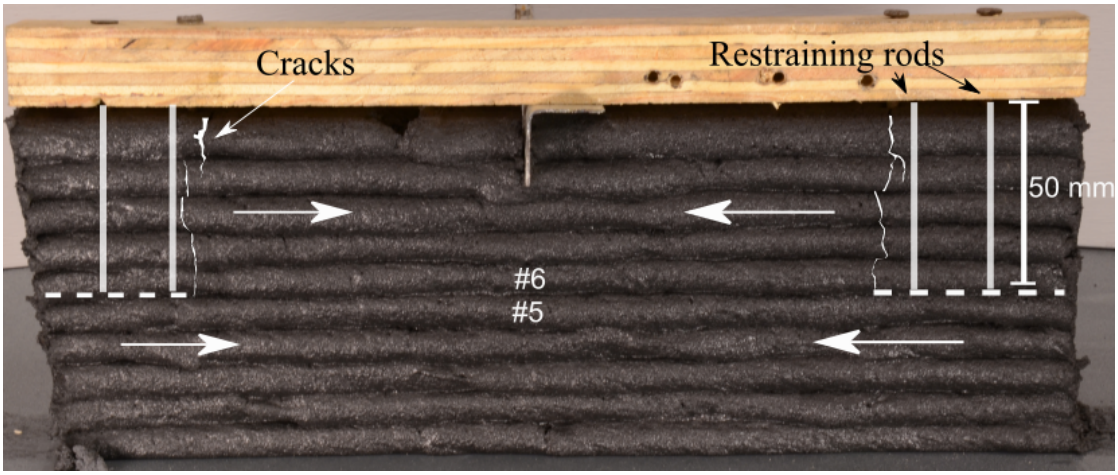

Figure 5.20: Displacement required to form the crack pattern in Restraint Combination D with a notch.

Earlier in this study, slip was observed along the interlayer in an experiment where uniform shrinkage occurred. Restraint Combination D caused differential displacement in two layers, increasing the likelihood of interlayer slip.

The crack pattern that occurred when demoulding the specimen can be seen in Figure 5.21. The specimen cracked horizontally along the differential displacement plane almost exactly on the interlayer. No horizontal cracking occurred between the restraining rods, where minimal differential displacement occurred.

This result indicates that plastic shrinkage and discontinuities in the restrain thereof can adversely affect the long-term interlayer bond strength of 3DPC. An interlayer slipping plane has the potential to reduce the long-term bond strength and allow for the intrusion of harmful agents between layers to reduce the durability of reinforced 3DPC. Complementary experiments are currently being conducted to shed light on this phenomenon.

5.4 Conclusion

3D printed concrete is extremely susceptible to plastic shrinkage cracking as demonstrated in this study. Digital image correlation was used to evaluate the unrestrained (free) early age deformation of 3DPC specimens when exposed to a

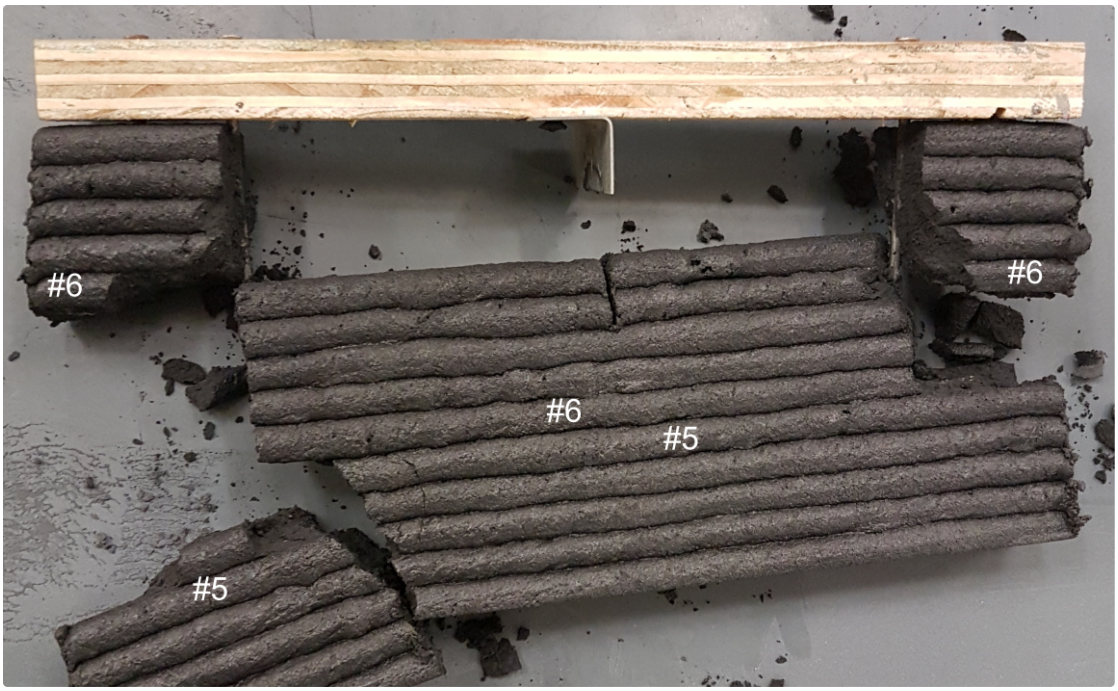

Figure 5.21: The cracking pattern observed during demoulding of the specimen in Figure 5.20.

moderate evaporation rate. Different forms of restraint were evaluated to propose a technique for inducing plastic shrinkage cracking in 3DPC. The following conclusions can be drawn from this study:

- The proposed experimental method is suitable for evaluating the risk of plastic shrinkage cracking, developing and evaluating prevention measures and improving the understanding of crack propagation in 3DPC. The technique was justified by evaluating the deformation response of a restrained 3DPC specimen exposed to a moderate evaporation rate.
- A substantial amount of free shrinkage occurs within the first two hours after printing due to a moderate evaporation rate. The rate of strain gain, as well as the peak strain, were several times higher than in ordinary concrete.
- The introduction of reinforcement-like shrinkage restraints resulted in severe cracking in the 3DPC specimens. Cracking started approximately 50 minutes after printing and increased in width for the next hour.
- An understanding of the fundamental behaviour of early age crack formation in 3DPC was developed by monitoring the deformation during plastic shrink-

age. The crack initiation can be described in four stages: the development of deformation constraint, contraction, elongation and crack formation.

- For the first time, interlayer slip was observed in the transfer of shrinkage deformation from one layer to the next. Both continuous and discontinuous restraints resulted in interlayer slip. Early age interlayer slip is unique to 3D printed concrete and the lack of understanding thereof necessitates complementary research.
- It is reasonable to believe that the observed interlayer slip has the potential to reduce the long-term interlayer bond strength and durability of 3DPC. More experiments are required to confirm this.

Perhaps most importantly, this study brings to light many unanswered questions on the response of 3DPC to early age shrinkage. The urgency of this matter is augmented by an increase in on-site applications, where the evaporation rate may be higher, and the introduction of tensile reinforcement that would increase the tendency of plastic shrinkage cracking in 3DPC.

Chapter 6

Mitigating early age cracking in 3D printed concrete using fibres, superabsorbent polymers, shrinkage reducing admixtures, B-CSA cement and curing measures

Abstract

3D printed concrete is vulnerable to severe early age shrinkage-related cracking due to the absence of formwork and coarse aggregates. To address this, several potential mitigation measures are compared based on their ability to reduce free shrinkage and cracking severity at dosages which do not adversely affect the printability or buildability of a well-developed 3DPC mix. The results show that a low dosage of short polypropylene microfibres eliminates early age cracking. The external application of a curing agent and multiple applications of misting water are less effective. Calcium sulfoaluminate-belite cement is used to accelerate structuration and proves beneficial in crack mitigation while enhancing buildability. Internal curing, with superabsorbent polymers, is less effective in mitigating plastic cracks but reduces autogenous shrinkage and increases the rate of stiffening. At the dosage used in this study, the shrinkage reducing admixture is relatively ineffective in crack mitigation, with higher dosages adversely affecting the buildability.

Article information

Chapter 6 has been submitted as a journal article and can be cited as: **G.M. Moelich**, P.J. Kruger, R. Combrinck, Mitigating early age cracking in 3D printed concrete using fibres, superabsorbent polymers, shrinkage reducing admixtures, B-CSA cement and curing measures, Submitted to Cement and Concrete Research.

Contribution declaration

With regard to this chapter, the nature and extent of the contributions of the candidate and the co-authors were as follow:

Name	Nature of contribution	Extent
G.M. Moelich (candidate)	Conceptualisation, Methodology, Validation, Formal analysis, Writing - original draft, Visualization, Investigation	90%
Dr P.J. Kruger (pjkruger@sun.ac.za)	Conceptualisation, Validation, Writing - review & editing	5%
Dr R. Combrinck (rcom@sun.ac.za)	Conceptualisation, Validation, Writing - review & editing, Supervision	5%

The undersigned hereby confirm that:

- The declaration above accurately reflects the nature and extent of the contributions of the candidate and the co-authors to this chapter.
- No other authors contributed to this chapter besides those specified above.
- Potential conflicts of interest have been revealed to all interested parties and that the necessary arrangements have been made to use the material in this chapter of the dissertation.

Signature of authors	Institutional affiliation	Date
	Department of Civil Engineering, Stellenbosch University	09/06/2021
	Department of Civil Engineering, Stellenbosch University	09/06/2021
	Department of Civil Engineering, Stellenbosch University	09/06/2021

6.1 Introduction

3D printing concrete allows for formwork-free construction, saving time, cost and material. This advantage leaves this new construction technique vulnerable to shrinkage-related cracking, since elements are exposed to the drying conditions of the environment from immediately after placement. Many experts [19, 157, 16, 158] have expressed concern since these cracks are aesthetically unpleasing, can allow for the ingress of corrosive agents and diminish mechanical strength if left unattended.

Concrete undergoes unavoidable volumetric changes throughout its lifespan. Three shrinkage mechanisms prevail, namely: pore water evaporation causing plastic shrinkage in the early age (<24 h) and drying shrinkage thereafter, cement hydration causing chemical shrinkage and self-desiccation causing autogenous shrinkage [40, 177]. Of these mechanisms, 3D printable concrete (3DPC) is particularly susceptible to: 1) plastic shrinkage cracking (PSC) due to the lack of formwork and coarse aggregates, minimal bleeding water, high quantities of fines and high surface to volume ratio, as well as 2) autogenous shrinkage due to the low water to binder ratio. Some commercial additive manufacturing companies, such as Apis Cor, prefer to print at night while others, such as CyBe, prints inside temporary structures to avoid the rapid drying associated with plastic shrinkage cracking [178].

Fortunately, various admixtures and curing measures are capable of mitigating early age shrinkage-related cracking. Fibres, superabsorbent polymers, shrinkage reducing admixtures and accelerators as well as externally applied moisture curing are often used as mitigation measures in conventional concrete. Nevertheless, their effectiveness in 3DPC is in doubt due to the magnitude of shrinkage. Moelich et al. [131] showed that the maximum plastic shrinkage strain in 3DPC is at least twice ($> \times 2$) that of conventional concrete at similar conditions. Furthermore, incorporating some of the aforementioned admixtures can be time-consuming since they can adversely affect the rheological properties, while some moisture curing techniques, such as ponding and plastic covers, are not feasible for early age 3DPC.

Only a few studies have been conducted to address early age shrinkage cracking in 3DPC. Moelich et al. [131] proposed a testing method to monitor and induce free plastic shrinkage and related cracking in multilayered 3DPC specimens. Federowicz et al. [179] had moderate success in reducing plastic shrinkage with a shrinkage reducing admixture while Van Der Putten et al. [180] successfully reduced the autogenous shrinkage, but not the plastic shrinkage, with superabsorbent polymers. Both the aforementioned studies [179, 180] extruded a single-layered specimen in an indoor environment where the pore water evaporation is minimal. No other literature could be found on this topic.

Some research groups [13, 181, 36] have incorporated synthetic fibres in their 3DPC mixes to mitigate plastic and drying shrinkage cracking. In conventional

concrete, a low volume of synthetic fibres (LVSF) has been used to reduce the width of early age cracks [113, 47]. LVSF increase the tensile strain capacity, redistribute tensile stresses and increases the post-cracking tensile strength to reduce crack widths [182, 183]. It is well known that the efficacy of fibres is related to its orientation. Extrusion-based placement can be beneficial in this regard since most fibres are orientated in the flow direction and, hence, aligned in the print direction (longitudinally). Incidentally, this is also the direction vulnerable to shrinkage cracking (PSC) [131, 158, 184]. Theoretically, a printed specimen would have more aptly orientated fibres to span the critical region than a cast specimen with a similar dosage of randomly orientated fibres. Ogura et al. [185] made a similar argument, and provided microscopic images as evidence, to explain the superior performance of extruded strain-hardening cement-based composites compared to mould-cast specimens. In conventional concrete, a low volume (0.1-0.2%) of monofilament or fibrillated fibres, mainly polypropylene, with a length of 12-18 mm is typically recommended for PSC [113, 47, 186]. Fibres with a diameter smaller than 0.1 mm and a relatively high aspect ratio are recommended [187]. Based on the orientation argument, even lower fibre dosages can potentially show PSC reducing capability when extruded. The efficacy of fibres in preventing early age cracking has not been investigated in 3DPC.

Superabsorbent polymers (SAPs) act as an internal reservoir that gradually releases water into the cementitious matrix and has been used to alleviate plastic settlement, plastic shrinkage [101, 102, 188] and autogenous shrinkage [189, 190], as a PSC test method [191], to alter the rheological properties [192, 193], increase freeze/thaw resistance [194] and promote self-healing [195]. SAPs can reduce the rate of capillary pressure build-up by releasing retained water to, ultimately, reduce plastic shrinkage and the crack severity [101, 188, 189]. Similarly, autogenous shrinkage is reduced through the release of retained water to reduce the drop in internal relative humidity during self-desiccation [190, 71]. A minor reduction in compression strength can be expected due to the premature release of water, increasing the w/c ratio. However, in 3DPC, SAPs can possibly increase the interlayer bond strength by increasing the surface moisture and/or reducing the early age differential shrinkage strain. Van Der Putten et al. [196] showed an increase in interlayer bond strength due to the addition of an SAP with a small sample size (three samples). More experiments are required to validate this hypothesis. SAPs can be characterised by their sorptivity kinetics as retentive or self-releasing. The retentive type releases water as a response to an external trigger (capillary suction or internal humidity drop) where the self-releasing type releases water continuously. Literature shows that the retentive type with a smaller diameter ($< 150\ \mu m$) is more effective in reducing early age shrinkage [102]. SAP dosages of 0.15-0.3% by mass of cement are recommended [197, 188].

Shrinkage reducing admixtures (SRAs) reduce the surface tension of the pore solution to decrease the rate of capillary pressure build-up in the pore system as well as the pore water evaporation [57, 66]. In conventional and self-compacting concrete, SRAs have been employed to eliminate PSC, reduce autogenous and long-term drying shrinkage without adversely affecting workability [198, 128, 199]. However, an increased setting time and a minor reduction in compressive strength can be expected at high dosages [200]. Various chemical structures have been identified as suitable for SRAs, namely: glycols, glycol ethers and amino terminated poly(ethylene-propylene) glycols [201]. These SRAs are commercially available and effective at dosages of 1-4% by weight of cement [66, 128, 199].

Calcium sulfoaluminate cement (CSA) is promoted as a Portland cement alternative because of its lower energy consumption and reduced CO_2 emission during production [202]. CSA has the additional benefit of accelerating the early age strength gain which can be beneficial for the buildability of 3DPC [203]. CSA form large quantities of ettringite and aluminum hydroxide through the hydration of ye'elimite [204]. The formation of ettringite results in a volumetric expansion that some researchers have used to compensate for the shrinkage of Portland cement concrete [205, 206]. Ettringite formation relates to the amount of gypsum in the system as well as the pore structure density and the presence of water (external and internal) [204]. If insufficient water is available in the early age (low w/c), external water from the environment (e.g. moisture curing, precipitation) can lead to the formation of secondary ettringite and cracking in the hardened state [202, 206]. Care should be taken when using CSA in high-performance 3DPC mixes, because of this expansive behaviour. In this study, the CSA was not used as a shrinkage-compensator, but rather to accelerate stiffening. This was accomplished by replacing a low quantity of Portland cement with calcium sulfoaluminate-belite. Increasing the rate of stiffening can mitigate PSC by reducing the amount of pore water that evaporates [47] and the shrinkage response. No literature could be found where CSA was used as an accelerator to reduce PSC.

Fibres, SAPs and SRAs are added directly to the concrete and can influence the printability, buildability (rheological properties) as well as the long-term strength development of 3DPC. On the other hand, curing agents are applied onto the concrete's surface and can, therefore, be employed without influencing the rheological properties.

Curing agents (CAs) are one of the most frequently used shrinkage mitigation measures on-site. CAs form a mono-membrane to reduce pore water evaporation. If CAs' application can be incorporated in the printing process, the aforementioned negative consequences can be avoided. CAs are not as effective in reducing autogenous shrinkage [71] but paraffin oil-based and petroleum resin emulsion curing agents have been employed to reduce and eliminate PSC [61, 64, 207].

In this study, the efficacy of the aforementioned mitigation measures is evaluated. The aim is to give guidance on the application of mitigation measures in an extensively developed thixotropic 3DPC mix. The research question is, *"What should be added/done to a 3DPC mix/element to prevent early age cracking, without adversely affecting the rheological properties?"* The mechanisms of these mitigation measures are well defined in the literature and are not under dispute here. It is also beyond the scope to redesign the reference mix for a specific admixture.

6.2 Experiments

The standard 3DPC mix of Stellenbosch University's research group was used in this study. Five admixtures were added separately to the reference mix at a dosage which did not significantly affect the pumpability. A curing agent and two water curing regimes were applied externally to the reference mix. Each mix was printed and exposed to a highly evaporative environment for 3 h. The free shrinkage and crack growth were monitored. A rheometer was also used to quantify the printability and buildability of the respective mixes.

6.2.1 Materials, mix design and mitigation measures

Portland cement (CEM II 52.5N) with between 6 and 20% limestone extender (chemical composition given in Table 6.2), fly-ash (DuraPozz Class F) and silica fume (Microfume by Silicon Smelters) were selected as binders. A natural, continuously graded quarry sand, with a maximum particle size of 4.75 mm, was used as aggregate. The proportions of binders, water and aggregate were adopted from Kruger et al. [38] and kept constant for the different mixes, as seen in Table 6.1. These mixes can be classified as high-performance concrete with a w/c ratio of 0.45, w/b ratio of 0.31 and 28-day compressive strength of approximately 65 MPa.

Table 6.1: Mix proportions.

	REF	FIBRE	SAP SR	SAP RET	SRA	CSA
Cement $[kg/m^3]$	568	568	568	568	568	523
Fly-ash $[kg/m^3]$	162	162	162	162	162	162
Silica fume $[kg/m^3]$	81	81	81	81	81	81
Aggregate $[kg/m^3]$	1175	1175	1175	1175	1175	1175
Water $[kg/m^3]$	256	256	256	256	256	256
Superplasticizer [% mass of binder]	0.6	0.6	0.6	0.6	0.6	0.6
Fibres [% volume of mix]	-	0.3	-	-	-	-
SAP SR [% mass of binder]	-	-	0.3	-	-	-
SAP RET [% mass of binder]	-	-	-	0.3		-
Additional water $[kg/m^3]$	-	-	17.88	38.25		-
SRA [% mass of cement]	-	-	-	-	1	-
CSA [% cement replacement]	-	-	-	-	-	8

Table 6.2: Chemical composition of the binders as % of weight, determined with a major element XRF analysis.

	CEM II	Fly-ash	Silica fume	B-CSA
CaO	62.85	4.29	0.66	46.35
SiO_2	18.60	54.76	84.39	13.46
Al_2O_3	3.47	33.09	0.60	15.32
Fe_2O_3	2.64	3.16	3.28	0.69
K_2O	0.47	0.67	3.46	0.54
Na_2O	0.24	0.26	0.64	0.10
P_2O_5	0.14	0.43	0.14	0.09
TiO_2	0.16	1.61	0.02	0.62

In the mix design phase, the admixture dosages were selected based on the printability (as a combination of pumpability, extrudability and buildability), with mini-slump-flow test results as an indication [208]. Cho et al. [26] dropped the flow table 15 times to recommend a slump-flow target range of 150-160 mm. Mixes in this slump-flow range have shown excellent printability in the past [209]. The simple mini-slump-flow test was preferred for the design phase since conducting a complete rheology test for all the different admixture dosages would be time-consuming and is not the aim of this study. The mini-slump-flow results for the different mixes can be seen in Fig. 6.1.

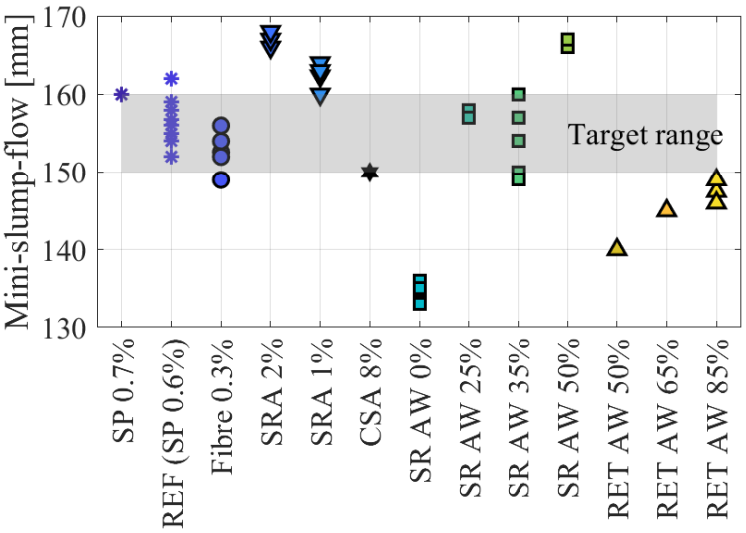

Figure 6.1: The mini-slump-flow results for different mixes. Each marker represents the mean of three consecutive tests conducted immediately after mixing.

A modified polycarboxylate polymer superplasticizer (SP) (Commercial name: Fluid Premia 310) was selected and added at a dosage of 0.6% of mass of binder to achieve a mini-slump-flow value in the target range.A monofilament polypropylene microfibre with a length of 6 mm and diameter of 30-40 μm was selected (Commercial name: Corehfil). More on the fibre's properties can be find elsewhere [210]. In conventional concrete, fibre lengths of 12 to 18 mm are typically recommended for mitigating early age cracking. Here, a shorter fibre was preferred to reduce the likelihood of pump blockage during printing [210]. A dosage of 0.3% had a minor effect on the mini-slump-flow result and is a relatively high dosage for shrinkage crack mitigation [187]. As shrinkage reducing admixture, a glycol ether-based SRA (Commercial name: Serenis) was selected. A dosage of 1% was preferred to reduce the adverse effect on the buildability. Increasing the dosages beyond 1% would require a redesign of the reference mix.

Calcium sulfoaluminate-belite (B-CSA with chemical composition in Table 6.2) was selected and 8% of the original Portland cement was replaced for the CSA mix, similar to Khalil et al. [203]. This mix is labelled as CSA henceforth. A dosage of 8% resulted in a stiffening so significant that cleaning the pump 60 min after mixing became challenging. Increasing the dosage beyond 8% is therefore not recommended, from a practical viewpoint. At this dosage, CSA resulted in a minor reduction in the mini-slump-flow and was therefore deemed suitable for pumping.

Self-releasing (SR) and retentive (RET) type superabsorbent polymers were obtained from a commercial supplier and used as delivered. The SR SAP is a covalently cross-linked polyacrylate similar to SAP 1 of [188], SAP 1 of [197], SAP 2 in [211] and SAP B of [192]. The RET SAP is a covalently cross-linked poly (acrylate-co-acrylamide) with a lower cross-linking density than the SR SAP. The RET SAP was similar to SAP 2 of [188], SAP 2 of [197], SAP 1 in [211] and SAP DN of [192]. Literature [211] can be consulted for SEM images, the particle size distribution and the absorption kinetics of these SAPs. A SAP dosage of 0.3% was selected based on the results of Boshoff et al. [188]. The standardised "tea-bag method" [211] was performed as a pre-test with a filtrated cement slurry to determine the sorptivity of the received SAPs. The test was conducted twice with the mean in Fig. 6.2. The addition of SAPs had a significant effect on the rheology which was mitigated by adding additional water on top of the mixing water, as done in Boshoff et al. [188] and others [190, 197]. It took approximately 10 min from adding the SAPs until placement. The sorptivity values (S) at 10 min were 21 and 18.5 g/gSAP for the SR and RET SAPs, respectively. The amount of additional water (AW) was calculated with $AW = ASap.S$ where ASap is the amount of SAP [gSAP]. The percentage of additional water was determined experimentally based on the mini-slump-flow test results. 35% AW was selected for the SR SAP

and 85% AW for the RET SAP. However, future research will use 100% AW for the RET SAP since the 85% AW resulted in a very stiff mix.

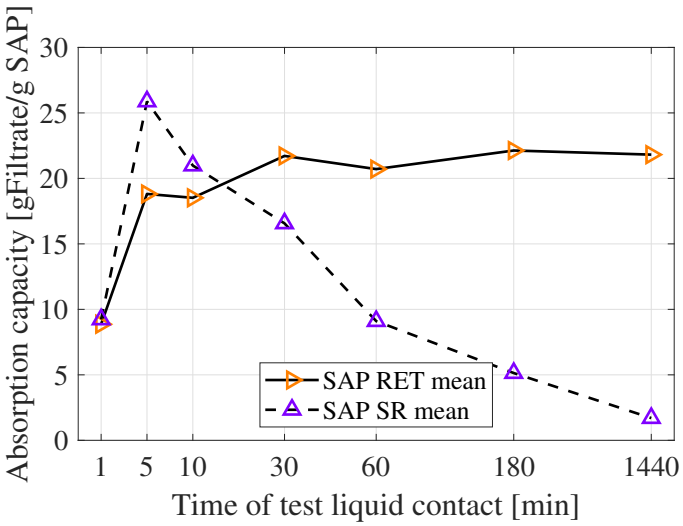

Figure 6.2: The cement filtrate absorption of the self-releasing (SR) and retentive (RET) type superabsorbent polymers obtained with the tea-bag test.

As a curing agent (CA), a low viscosity white pigmented wax emulsion (Commercial name: Cure WB) was selected and applied to the concrete surface of REF at 0.2 l/m^2 at the start of the test, based on the supplier's recommendations. Two different water curing regimes were implement using only tap water: 1) 1 mm^3/mm^2 was applied to REF once, at the start of the evaporation condition (denoted as S-WATER) and 2) 1 mm^3/mm^2 of tap water was applied to REF at 20-min intervals (denoted as MULTI-W). An interval of 20 min was selected based on the free shrinkage development of the reference mix as suggested by Visagie [207].

6.2.2 Mixing, printing and specimen preparation

The materials were batch-mixed in a 50 ℓ two-blade pan mixer at a constant mixing velocity. The dry materials were mixed before the addition of mixing water for 1 min. The water, additional water (for SAP mixes) and superplasticizer were added and mixed in for 1 min each. Additional interim hand mixing was conducted to ensure uniformity. After another 1 min of mechanical mixing, the specific admixture was added and mixed in for 2 min.

The specific mix was used to prime the pump and hose whereafter the print was activated. A 1 m^3 gantry-type 3D concrete printer with a 25 mm (diameter) circular nozzle was used to extrude $35 \pm 3 \times 10 \pm 1$ mm (width×height) filaments.

No intervention was required during printing. The REF printed element can be seen in Fig 6.3 a. The print speed of 75 mm/s resulted in an 82 s pass time that was kept constant throughout the study. Since the rheological properties varied depending on the mix, the pump speed had to be adjusted to maintain a constant flow rate and extrude a 35 mm wide filament.

Immediately after printing, the printed shape was cut into shorter specimens, as seen in Fig. 6.3 b. The excess material was removed whereafter the restraining rods and shrinkage measurement markers were inserted, as discussed later. The evaporation condition was activated 30 min after printing. In this study, time-zero is defined as the moment the “wind" (airflow) is activated. Any deformation before time-zero can be neglected due to the low evaporation rate in the climate controlled room.

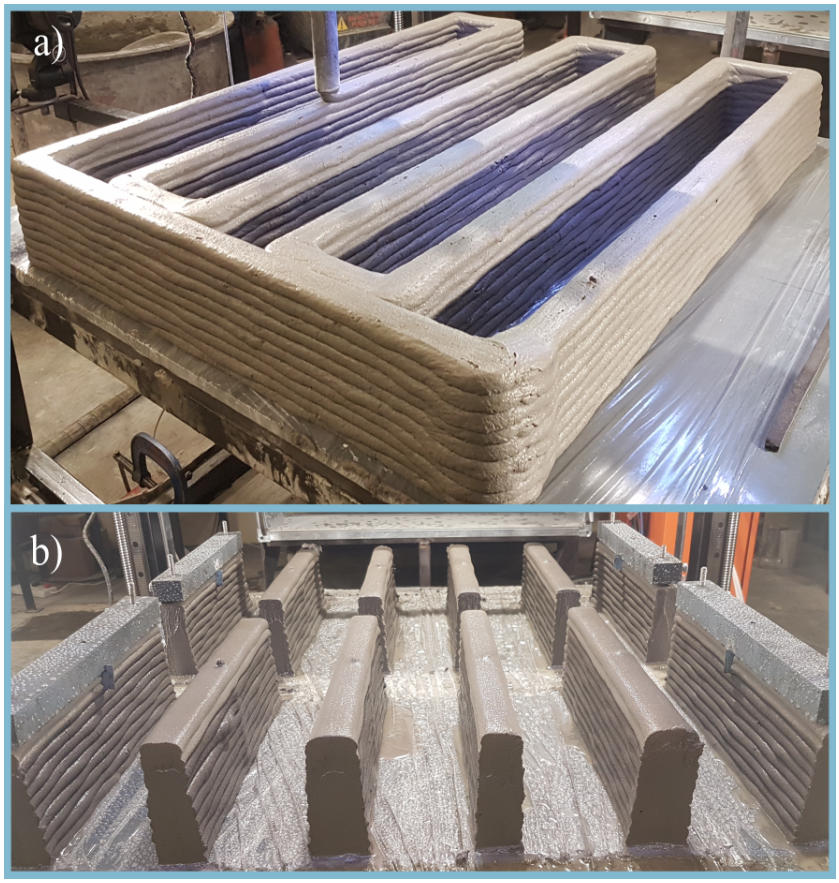

Figure 6.3: The print path executed for each of the mitigation measures. (a) The printed element. (b) The 300 mm long specimens, six for free shrinkage and four for cracking.

6.2.3 Evaporation condition

As per the recommendation of Moelich et al. [131], an evaporation control chamber was used to evaporate the pore water from the printed specimens in a repeatable way. The parallel study [132] can be consulted for more on the evaporation control chamber used here. A relatively high, but not uncommon evaporation rate of 0.74 $kg/m^2/h$ was used in this study [171, 212, 109]. The concrete was placed at a temperature of 21°C and exposed to an ambient temperature of 23±0.5°C and relative humidity of 50±3%. The airflow was increased from 0 to 10.5±0.3 m/s, at time-zero, in order to activate the severe drying condition. The climatic conditions were kept constant for the next 3 h.

Thereafter, the airflow was deactivated, but the ambient temperature and relative humidity were maintained. This decreased the drying condition's evaporation rate from 0.74 $kg/m^2/h$ (henceforth referred to as the severe drying condition) to 0.07 $kg/m^2/h$ (henceforth referred to as the benign drying condition).

6.2.4 Free shrinkage measurements

The free shrinkage specimen was printed on a PVC base covered with plastic film and mould release oil to mitigate the base friction. The free shrinkage measurement method proposed by Moelich et al. [131] was followed with one modification. A restraining rod was inserted at the centre of the specimen and connected to the base to prevent asymmetrical deformation and reduce statistical variability. A 10 layered, 300 mm long specimen was used similar to Moelich et al. [131]. The displacement of target (DIC) markers, embedded in the specimens, were monitored from the top to determine the shrinkage. This configuration allowed for monitoring multiple specimens simultaneously, and increases the feasible sample size of each test. The free shrinkage specimen can be seen in Fig. 6.4 a.

Digital image correlation (DIC) was implemented to monitor the displacement of markers placed in the specimens from a series of images. This technique is preferred above conventional LVDTs since airflow is not disrupted in any way [131]. The following literature provided valuable information on the DIC technique [213, 214].

Two identical monochrome machine vision cameras (Basler acA2040) were used to generate a series of 2048×1536 pixels TIFF images. A 36 mm fixed focal length lens (Edmund Optics) was used in combination with the camera. The cameras were placed at a working distance of 1800 mm to obtain a field-of-view of 350×260 mm (width×height). A pixel size of 0.17×0.17 mm was deemed adequate since a displacement resolution of 0.002 mm was attainable. This resolution is less than the 0.004 mm recommended by ASTM C490 [174]. The DIC markers were inserted into the free shrinkage specimen, as seen on Fig. 6.4 c and d. Each DIC marker

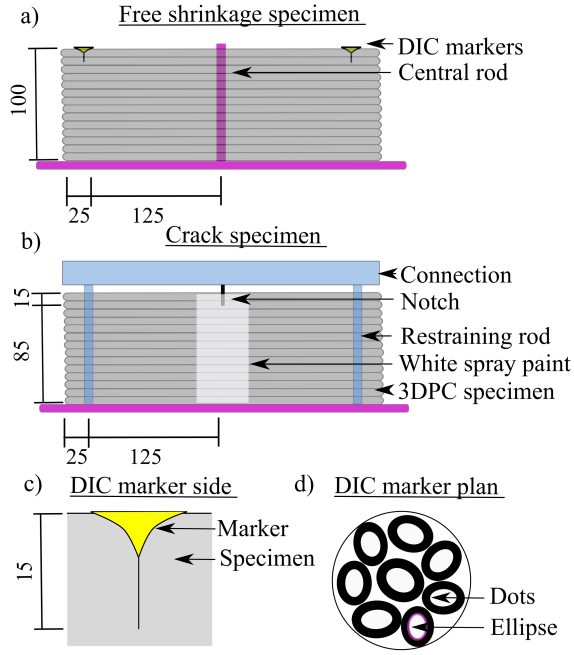

Figure 6.4: (a) Free shrinkage specimen. (b) Crack specimen. (c) DIC marker side view. (d) DIC marker plan view. Units in mm.

is unique and consisted of 8 elliptical dots, each with an internal diameter of approximately 10 ± 2 pixels [173]. The image taken at time-zero (activation of airflow) was used as a reference for the rest of the series. The markers were imaged every 3 min for the next 3 h and, thereafter, every 10 min for the next 21 h. A series of uncompressed TIFF images were processed with GOM Correlate 2019. It was unnecessary to define a scale since nominal strain was used in this study. Here, shrinkage is defined as a positive strain.

6.2.5 Crack growth measurements

Plastic shrinkage cracks were induced in a 10 layered, 300 mm long specimen with the method proposed by Moelich et al. [131]. The crack inducing method can be seen in Fig. 6.4 b. A Matlab algorithm [131] was used in this study with a constant binarize threshold of 0.35. To improve the contrast between the surface and the crack, white chalk-based spray paint was evenly applied to the 70×100 mm area under the notch in a repeatable way (Fig. 6.4 b). Bertelsen et al. [67] recommended using chalk-based paint to study plastic shrinkage cracking since it does not influence pore water evaporation or the PSC phenomena.

Two identical optical cameras (4928 x 3264 pixels) monitored the crack specimens. The working distance of 700 mm and a focal length of 24 mm produced a

530 mm wide field-of-view and a 0.11×0.11 mm pixel. The crack was imaged at a 3-min interval to produce a sampling noise less than 5% of the total crack area.

6.2.6 Rheology

A rotational rheometer (German ICAR RHM-3005/3009) was used to quantify the printability and buildability as well as the stiffening of the different mixes. A stress growth test was performed at a shear rate of 1 s^{-1} (0.2 revolutions per second) for 60 s. The rheometer test parameters were based on the screw speed and geometry of the concrete pump as well as the selected extrusion rate [170]. The mix was pre-sheared at a shear rate of 1 s^{-1} (0.2 revolutions per second) for 60 s, and time-zero was noted. A single-batch approach was followed with resting intervals of 30 s, 60 s, 90 s, 120 s for the re-flocculation rate (R_{thix}) and 15 min, 30 min and 45 min for the structuration rate (A_{thix}) [38, 37].

6.2.7 Measurements

Nine 32 ℓ prints were conducted, one for each mitigation measure. Each print generated six free shrinkage and four cracking test specimens. After the 3 h of severe evaporation, the airflow was deactivated and the free shrinkage measurements were continued for the next 21 h. The printed specimens were imaged to evaluate the surface finish. The penetration resistance was not determined in this study since the static yield stress development rate provided an adequate, if not better, quantification of setting.

6.2.8 Variability and reproducibility

Error bars were used to indicate the maximum and minimum of each data set. The variability of the free shrinkage results was small, with a CoV of 5.5% in the reference set. The cracking results were more variable with a CoV of 8.9% in the reference set. This is due to the inherent variability of the cracking phenomena and is also found in the literature [101, 191, 109]. Conclusions were made based on the outcome of a one-way ANOVA between the reference and the mitigation measure's data set. For conciseness, the ANOVA results were not reported if the two groups were notably different, and this was mostly the case.

After mixing, three mini-slump-flow tests were conducted. If the result deviated more than 5 mm from previous batches' mean, the mix was discarded. Six cubes were cast from each mix. The REF, FIBRE, SRA and CSA cubes were cured in a curing tank while six SAP RET, SAP SR and REF cubes were left exposed to the benign drying condition. The compressive strength was determined 56 days after printing.

6.3 Results and discussion

6.3.1 Mitigation of plastic shrinkage

The first step towards mitigating cracking is to reduce the shrinkage. The free shrinkage development due to early age pore water evaporation can be seen in Fig. 6.5. The reference (REF) shows a similar shrinkage curve than Moelich et al. [131] with a high shrinkage rate in the first 60 min that declines after 80 min. The shrinkage starts immediately after the evaporation condition is activated, indicating the absence of bleeding water protection. The 3 h strain magnitude of 11 mm/m is very high, and much higher than the 6 mm/m of Moelich et al. [131] due to the higher evaporation rate (0.74 $kg/m^2/h$ vs 0.41 $kg/m^2/h$ in [131]). With conventional concrete containing coarse aggregates, Combrinck et al. [161] and Olivier et al. [101] measured a 7 h free shrinkage strain of 4.5 mm/m and 3 mm/m at an evaporation rate of 1 $kg/m^2/h$.

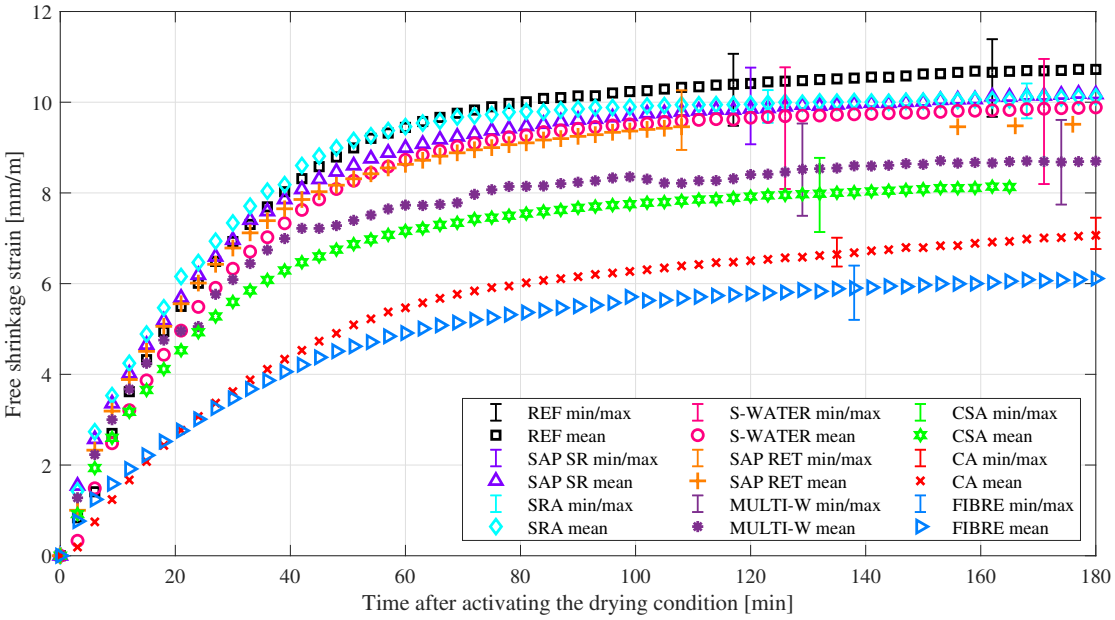

Figure 6.5: The free plastic shrinkage strain development of the various mitigation measures.

The addition of a shrinkage reducing admixture (SRA) results in a 6% decrease in the 3 h shrinkage strain with no reduction in the rate. There is no statistically significant difference between SRA and REF. Federowicz et al. [179] showed a similar result with 2% SRA in 3DPC. SRA reduces the surface tension (γ) of the pore solution, to reduce the capillary pressure (P) according to the Young-Laplace equation [57, 56]:

$$P = \frac{-2\gamma cos\theta}{r} \tag{6.1}$$

where θ is the contraction angle and r is the radius of the menisci. Reducing the surface tension would reduce the capillary pressure. In conventional concrete this has proven to be an effective method of reducing plastic shrinkage and cracking [57, 198, 128]. However, in high-performance concrete, where the particles are smaller, the absolute capillary pressure is higher due to the small radii of the menisci (r) [56, 58]. A minor reduction in the surface tension may not be sufficient to mitigate shrinkage significantly. This necessitates the used of a higher dosage than recommended for conventional concrete. Federowicz et al. [179] also recommended increasing the SRA dosage above 4% from experimental results. However, this would significantly influence the rheological properties if the mix is not redesigned.

The self-releasing (SR) SAP reduces the 3 h shrinkage strain by 5% with no reduction in the shrinkage rate. The released water had a minor effect on the shrinkage with no statistically significant difference between SAP SR and REF. According to Fig. 6.2, the SR SAP releases between 3.13 and 4.53 $kg/m^3/h$ of additional water during the 3 h period. This translates to 3.29-4.77 g/h additional water per specimen. The drying condition evaporates 27.9 g/h pore water from the specimen (this has been experimentally validated). The evaporated water is, therefore, more than 5 times that of the replaced water. Van Der Putten et al. [180] also showed no significant reduction in the free plastic shrinkage when adding SAPs to 3DPC.

The retentive (RET) SAP performed better, reducing the 3 h shrinkage by 10%. The amount of released water is unknown since the desorption of retentive SAPs are demand controlled, but it is likely that the matrix's shrinkage influences desorption [197]. If all the absorbed water is released in the first 3 h, which is unlikely, 13.4 g/h would be released in the specimen. This is approximately half that of the evaporated water. Nonetheless, additional water release explains the statistically significant difference between REF and SAP RET as determined by a one-way ANOVA ($F(1,10) = 14.2$, $p = 0.003$).

Spraying the specimens with water before activating the evaporation condition reduces the 3 h free shrinkage by 6%. The initial (first 5 min) shrinkage rate also reduces by 21%. However, 12 min after water application, the shrinkage rate is again equal to that of the reference due to the evaporation of the applied water. There was no statistically significant difference between S-WATER and REF. Applying the water at 20 min intervals (MULTI-W) results in a 19% reduction of the 3 h shrinkage strain. Every application reduces the shrinkage rate to approximately zero for 9 to 12 min whereafter the rate returns to that of the reference. Ultimately, there is a statistically significant difference between REF and MULTI-W as determined by one-way ANOVA ($F(1,10) = 30.76$, $p = 0.00024$). It remains

surprising how effective simple moisture curing is in mitigating shrinkage. That being said, the large variability in S-WATER and MULTI-W data sets should be noted with most of the applied water running down the vertical face soon after application.

Replacing the Portland cement with 8% CSA reduces the 3 h shrinkage strain by 24%. The shrinkage rate only started deviating from REF 10 min after time-zero (40 min after mixing). Thereafter the shrinkage rate is lower, resulting in the reduction of the 3 h shrinkage. There is a statistically significant difference between REF and CSA as determined by a one-way ANOVA ($F(1,10) = 45.1$, $p = 0$). The curing agent is, however, more effective in reducing free shrinkage.

Applying the curing agent (CA), reduces the 3 h free shrinkage by a statistically significant 34%. The shrinkage rate also decreases significantly. The CA mitigates pore water evaporation resulting in a shrinkage curve different to all the other mitigation measures. The curing agent has a higher viscosity than water which prevented it from dripping down the vertical concrete surface when applied. This reduces the variability of results.

The FIBRE mix performs best of all the mitigation measures with a 43% reduction of the 3 h shrinkage strain. This is surprising since the majority of the literature shows only a decrease in the crack size and not necessary in the free shrinkage [182, 113, 187]. Mangat and Azari [215] and Branston et al. [216] also noticed a reduction in the free shrinkage and attributed it to the higher frictional-force between the fibre and matrix that restrains the shrinkage movement. Bertelsen et al. [183] showed a 25% reduction of free shrinkage with polypropylene fibres but attributed this to the fibres' ability to redistribute localised strains and cited Banthia and Gupta [113]. It is hypothesised that the latter mechanism is responsible for the free shrinkage reduction noticed here. Moelich et al. [131] showed that the top layer of a printed specimen could experience a shrinkage strain more than double that of the bottom layer due to the base friction. The free shrinkage specimen is, in fact, partially restrained even if the base friction is minimised. It is believed that the fibres redistribute the restraint of the bottom layers to the top layers in order to reduce the shrinkage displacement of the top layer where it is measured. This hypothesises is supported by the findings of Bertelsen et al. [183] but should be investigated in future research. Currently, it is the best explanation of this result.

6.3.2 Prevention of plastic cracking

The main goal of this study is to mitigate and ultimately prevent plastic shrinkage cracking. The plastic shrinkage crack area development can be seen in Fig. 6.6. REF starts cracking between 18 and 21 min after the evaporation condition is activated. The crack propagates rapidly for the next 60 min whereafter the growth

rate declines. The crack growth proceeds the free shrinkage with a lag of about 20 min. The crack development curve is similar to Moelich et al. [131]. A typical (median) crack as well as the corresponding binary equivalent, for each of the mitigation measures, can be seen in Fig. 6.7.

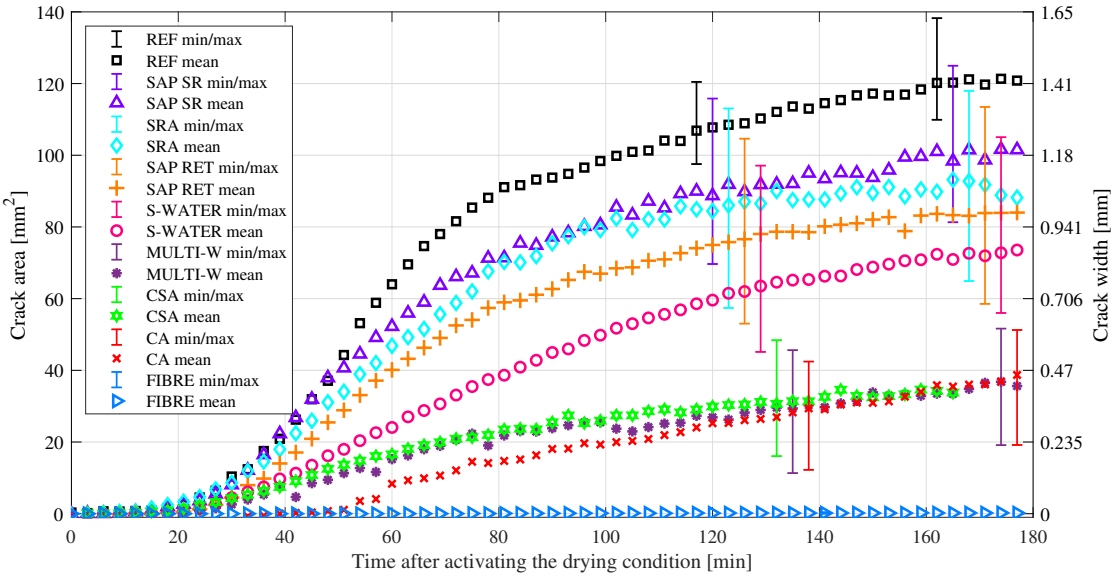

Figure 6.6: The crack area development of the various mitigation measures over a period of 3 h.

The self-releasing (SR) SAP reduces the crack area by 18% while the retentive (RET) SAP performs better with 31%. There is no statistically significant difference between the SAP SR and REF ($F(1,6) = 3.7$, $p = 0.10$) while the difference between SAP SR and REF is statistically significant ($F(1,6) = 7.9$, $p = 0.03$). The amount of evaporated water is, however, multiple times more than the released water. This limits the efficacy of SAP to lower evaporative environments. It was observed that the area around the crack was still moist, long after the rest of the surface has dried. This was only observed in the SAP RET specimens and can be seen in Fig. 6.7 k. In conventional concrete, Boshoff et al. [188] reduced the crack area by 52% with SAP SR and 44% with SAP RET, at a similar dosage.

The addition of SRA reduces the total crack area by 26%. The SRA is surprisingly effective in reducing the crack area, considering that it only marginally reduced the free shrinkage. There is a statistically significant difference between the SRA and REF as determined by a one-way ANOVA ($F(1,6) = 6.5$, $p = 0.043$). This result agrees with that shown by the literature [57, 66, 198, 128, 199].

Water curing performs well with a crack area reduction of 38% for a single application (S-WATER) and 70% for multiple applications (MULTI-W). There is

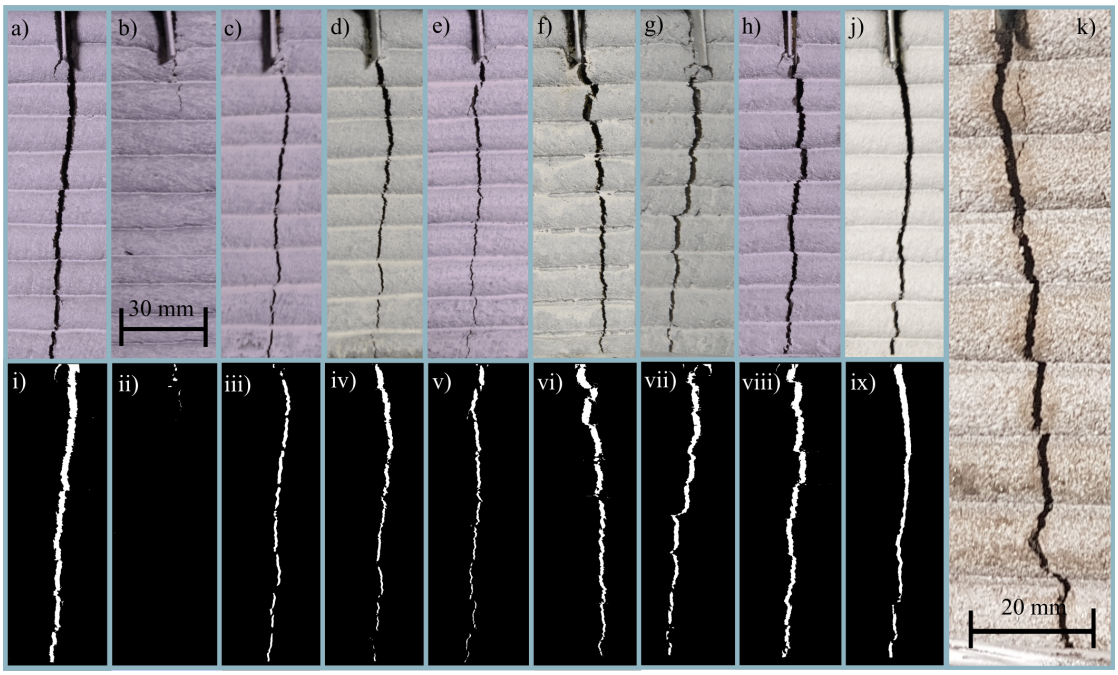

Figure 6.7: The median plastic shrinkage crack in REF (a), FIBRE (b), CSA (c), MULTI-W (d), CA (e), S-WATER (f), SAP RET (g), SAP SR (h) and SRA (j). The surface colour relates to the age at which the image was captures and these image were taken at different ages. The binary equivalent of (a) is in (i), (b) in (ii) etc. (k) SAP RET crack with moist perimeter.

no statistically significant difference between S-WATER and REF ($F(1,6) = 13.6$, $p = 0.10$) while the difference between MULTI-W and REF is statistically significant ($F(1,6) = 75$, $p = 0.0001$). Again, the variability is concerning and largely due to uneven, vertically orientated concrete surface. The higher viscosity of the curing agent is beneficial in this regard.

The curing agent (CA) delays cracking by about 30 min whereafter the crack growth rate is similar to that of MULTI-W and much less than REF. Ultimately, CA reduces the crack area by 66% but some of the cracks were still growing at the end of the test. The majority of free shrinkage, in the CA specimen, occurs in the first 80 min with a slow shrinkage rate thereafter. It is therefore unlikely that the crack size would increase significantly beyond 180 min.

Replacing 8% of the cement with CSA reduces the crack area by 72%. The crack starts at the same time as the other mixes indicating that the tensile capacity, at the time of cracking, is not significantly more than the other mixes due to the rapid strength gain provided by CSA. After crack formation, the crack growth rate is significantly lower, compared to REF. A significant reduction in the free shrinkage rate is also noticed between 20 and 40 min. The rapid stiffness gain

reduces the shrinkage response and crack growth in the CSA specimen.

The addition of short polypropylene microfibres prevents (100% reduction) cracking in three of the four specimens and significantly reduces the area of the forth specimen as seen in Fig. 6.7 b. Fibres reduce the crack size in three phases: 1) the total plastic shrinkage is reduced by redistribution stress concentrations [113, 183], 2) the early age tensile strength is increased to prevent cracking [182, 216] and 3) the peak stress elongation and post-crack tensile strength is increased to control crack growth [187].

6.3.3 Post-plastic free shrinkage

After the severe drying condition was deactivated, the specimens' free shrinkage strain continued to increase for the next 7 h under the benign drying condition ($0.07\ kg/m^2/h$) as seen in Fig. 6.8. The reference specimen experiences a $0.5\ mm/m$ increase in the free shrinkage. Moelich et al. [131] also showed a secondary shrinkage increase of about $0.5\ mm/m$ in the presence of a $0.412\ kg/m^2/h$ drying condition. This secondary shrinkage increase is, therefore, not related to the drying condition's evaporation rate. It is likely that this secondary shrinkage has components of both chemical shrinkage, caused by the hydration reaction, as well as autogenous shrinkage, caused by self-desiccation. This would also explain why the secondary shrinkage started later in Moelich et al. [131] —the higher superplasticizer dosage delayed the hydration reaction and, therefore, the secondary shrinkage. However, the magnitude of the secondary shrinkage strain is only a fraction of that experienced during the first 3 h under the severe drying condition.

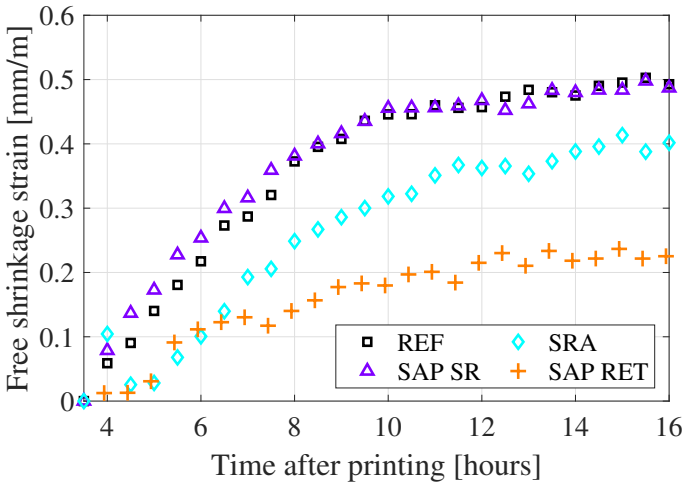

Figure 6.8: The secondary shrinkage strain development, of the various mitigation measures, in the early age period.

SAP SR followed a similar trend as REF since most of the additional absorbed water is released in the first 3 h as seen in Fig. 6.2. The SRA reduces the secondary shrinkage by 17% while the SAP RET results in a 44% reduction. The retentive (RET) SAP could still release its absorbed water to mitigate secondary shrinkage. This after the severe drying condition of the first 3 h evaporated a large portion of the free pore water. Van Der Putten et al. [180] also reported a reduction in autogenous shrinkage with SAPs.

6.3.4 Pumpability

All mixes were successfully printed without clogging the hose or any noticeable segregation. The pump speed required adjustment, depending on the mix, to control the flow rate. This was necessary to maintain the constant filament width, of 35 mm, for each of the different mixes used in this study. The SRA mix requires a pumping speed 11% lower than REF due to the low initial static and dynamic yield stress. SAP SR requires a similar speed than REF while FIBRE and CSA requires a slightly (5%) higher pumping speed due to the higher initial static yield stress. SAP RET required a 45% higher pump speed than REF and had the highest initial static yield stress of all the mixes. That being said, the RET mix was still able to print the 10 layers without clogging the pump or hose. The pumpability of RET can be improved by adding more additional water which does not require a redesign of the reference mix. These results agree with the mini-slump-flow values, which relates to the dynamic yield stress seen in Fig. 6.9.

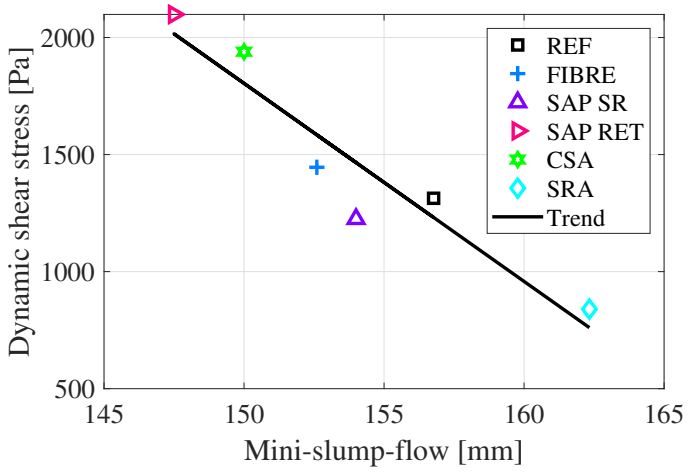

Figure 6.9: The mini-slump-flow results against the dynamic yield stress for different mixes.

6.3.5 Buildability

The development of the static yield stress can be seen in Fig. 6.10 with the re-flocculation (R_{thix}) and structuration (A_{thix}) rates in Table 6.3. REF shows a moderate re-flocculation rate while SRA and FIBRE have a slightly lower R_{thix}. A discontinuity can be noticed between the 0 s and 30 s static yield stress of the FIBRE mix. For the first stress growth test (0 s), the fibres are still spanning the shearing plane (on the perimeter of the vane's rotational path), resulting in a high static yield stress. Since no agitation is applied during the resting time, the first test's continuous shearing orientates the fibres for the second test, resulting in a lower static yield stress. Thereafter, R_{thix} is similar to REF. The CSA has a higher R_{thix} compared to REF.

SAP RET has a significantly higher R_{thix} than REF while SAP SR has a negative R_{thix}. The SAP SR releases water inherently, throughout the test, to reduce the static yield stress as the resting times increases, as explained by Mechtcherine et al. [192]. On the other hand, SAP RET continued adsorbing the free water in the early stages of the test, as seen in the "tea-bag" results (Fig. 6.2). This increases the rate of yield stress development and results in a higher R_{thix}. Mechtcherine et al. [192] showed similar results and provided the same explanation, also showing the SAP RET increases the rate of plastic viscosity development over time. SAP RET's R_{thix} value of 7.03 Pa/s is very high and similar to the nanoparticle 3DPC mix of Kruger et al. [38].

An A_{thix} value of 0.5 Pa/s, as shown for REF, is common in 3DPC literature. A_{thix} of REF, FIBRE, SAP RET and SRA are all similar, with SAP SR having a significantly lower A_{thix}. Again, this is due to the intrinsic releasing attributes of SAP SR. In the SAP RET mix, the yield stress continued to increase rapidly up until 30 min, due to the absorption of additional water. The CSA mix had a significantly higher A_{thix} due to the rapid formation of calcium aluminate hydrates and ettringite. For the CSA mix, the rheometer was near maximum torque at a 30 min resting time so the 45 min test was not performed for safety reasons.

The buildability model proposed by Kruger et al. [217] was used to estimate the number of layers printed before plastic collapse due to plastic yielding of the critical bottom layer. Kruger's model performed well compared to other models, as shown by Jayathilakage et al. [34]. A circular hollow column with a 250 mm diameter was selected as the print shape with print speeds of 60 and 120 mm/s. The results are presented in Table 6.3. The model is influenced by the initial static and dynamic yield stresses which are different for the mixes. To ensure equal comparison of buildability, the dynamic yield stress of all the mixes were adjusted to that of REF while the difference between the static and dynamic yield stress of each mix was maintained. In reality, this can be achieved by adjusting the superplasticizer dosage.

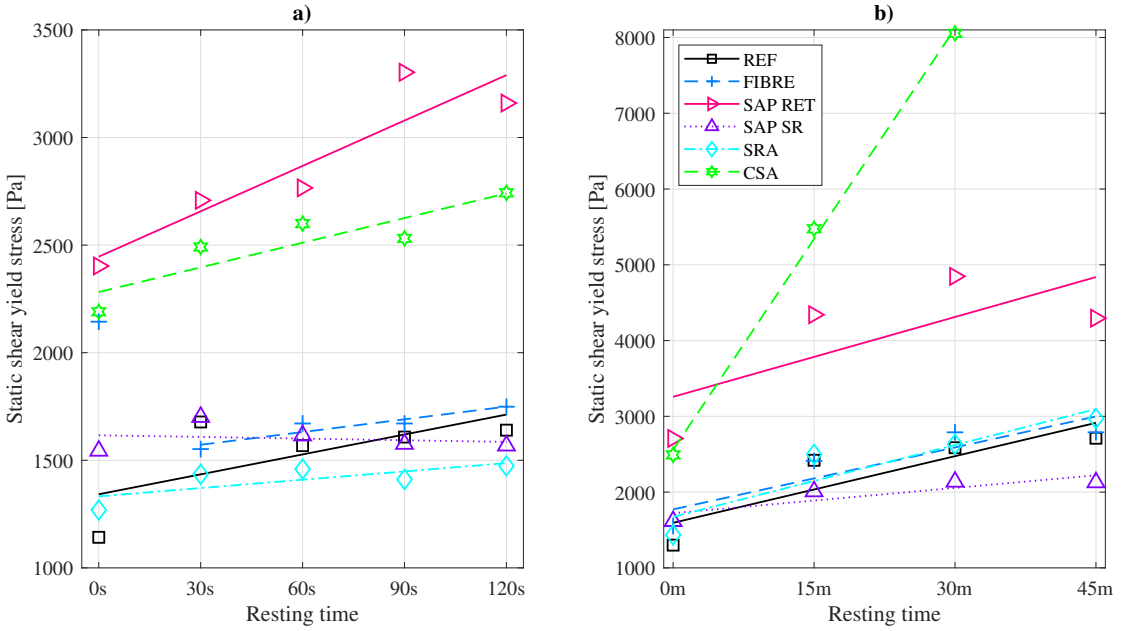

Figure 6.10: The static yield shear stress development due to the re-flocculation (a) and structuration (b) mechanisms for the of the various mixes. The rate of re-flocculation (R_{thix}) and structuration (A_{thix}) can be seen in Table 6.3

The model estimates that REF, FIBRE and SRA would collapse at a very similar height at the 60 mm/s print speed. The height of collapse reduces about 30% for the SAP SR mix when compared to REF. The SAP RET mix has a notably higher buildability due to the absorption of free water causing higher rate of stiffening. Adding CSA also improves the buildability significantly due to the rapid chemical structuration at longer resting times. The SAP RET had a better

Table 6.3: The re-flocculation (R_{thix}) and structuration (A_{thix}) rates for the respective mixes as well as the estimated buildability [217] at print speeds of 60 and 120 mm/s. The different yield stresses for the various mixes were accounted for in the buildability estimation.

	R_{thix} [Pa/s]	A_{thix} [Pa/s]	Layer of failure [217]: 60 mm/s	120 mm/s
REF	3.09	0.49	31 (A_{thix})	29 (A_{thix})
FIBRE	1.97	0.45	30 (A_{thix})	26 (R_{thix})
SAP RET	7.03	0.59	43 (A_{thix})	40 (A_{thix})
SAP SR	-0.26	0.19	20 (R_{thix})	20 (R_{thix})
SRA	1.29	0.52	29 (R_{thix})	24 (R_{thix})
CSA	3.92	3.09	73 (A_{thix})	35 (R_{thix})

buildability than CSA at a high print speed. Of course, the R_{thix} provided by SAP REF is reversible while the CSA provides permanent stiffening. SAP RET is therefore more suited for batch mixing compared to CSA. Without the adjustment in yield stress values, the SRA significantly reduces the buildability. Increasing the SRA dosage should reduce the buildability even further.

6.3.6 Surface finish

The surface finish of the mitigation measures is similar to the reference with the exceptions of MULTI-W and SAP RET, as seen in Fig. 6.11. Multiple water applications erode the paste from the surface while the SAP RET mix has an uneven surface finish due to the pores the SAPs leave behind.

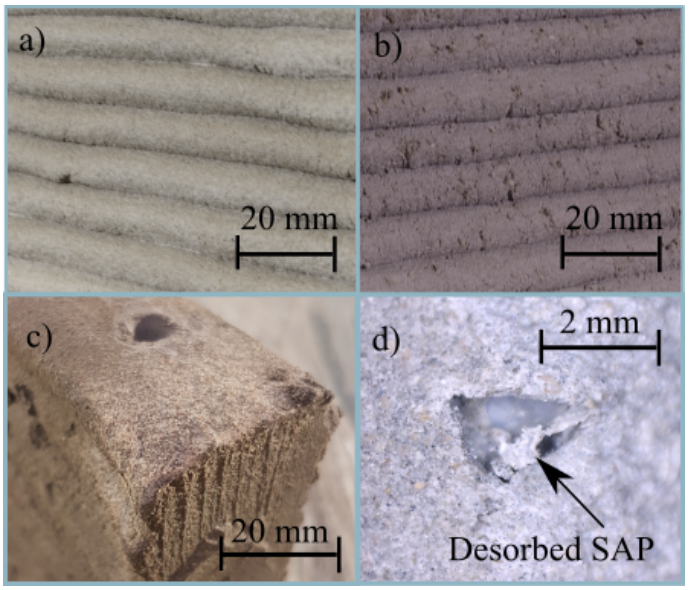

Figure 6.11: The surface finish of: (a) REF, (b) SAP RET, (c) MULTI-W, (d) the desorbed retentive SAP in the resulting pore.

6.3.7 Compressive strength

The 56-day compressive strength results were similar for the various mixes, as seen in Fig. 6.12. There is no statistical significant difference between the REF and any of the other groups according to a one-way ANOVA. This result can be expected for the low dosages used in this study. When curing the CSA cubes in water, no expansion cracks were observed and the compressive strength did not differ

from REF. It can therefore be concluded that incorporating a low quantity of calcium sulfoaluminate-belite cement in this mix does not result in severe expansion cracking.

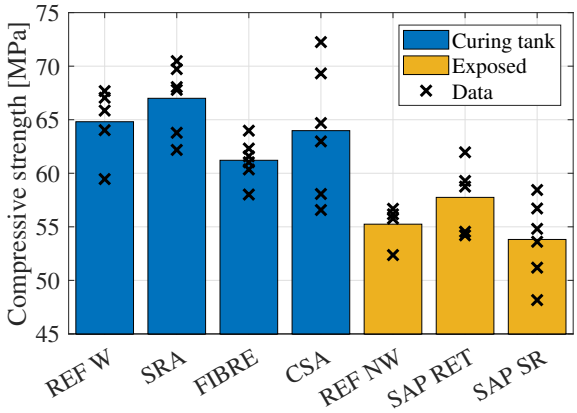

Figure 6.12: Mean 56-day compressive strength for the various mixes.

6.4 Conclusion

This research employed early age shrinkage mitigation measures to eliminate plastic shrinkage cracking and reduce early age shrinkage in 3D printed concrete. Admixture dosages were selected to have no adverse effect on the pumpability or buildability of the 3DPC. Based on the results of this study, the following recommendations can be made:

- Short polypropylene microfibres were the most effective in preventing plastic shrinkage cracking, eliminating the visible cracks in most specimens. A low dosage ($< 0.3\%$) did not adversely affect the printability or buildability. For this reason, microfibres is the recommended mitigation measure.
- The curing agent was also effective in shrinkage and crack mitigation. Using a curing agent has the added benefit of not affecting the rheological properties or strength gain since it is applied to the concrete's surface. The application can be automated by attaching a spraying device to the end-effector.
- Multiple applications of water is effective in shrinkage and crack mitigation but can erode the cement paste from the surface.
- Incorporating shrinkage reducing admixture affected the rheological properties so significantly that only a low dosage was feasible. At this dosage, the

SRA was not effective in crack mitigation. A lower superplasticizer dosage is recommended for higher SRA dosages but it is also possible that SRA's are not viable for 3DPC due its adverse effect on the buildability.

- Using calcium sulfoaluminate-belite cement as an accelerator is effective in crack mitigation. CSA also improved the buildability significantly without adversely affecting the pumpability. For larger elements, continuous mixing is recommended to prevent pumping issues.
- The retentive SAP was less effective in plastic shrinkage mitigation but performed best with regards to autogenous shrinkage. The retentive SAP can also be used to achieve high vertical building rates in 3DPC. However, determining the amount of additional water can be time-consuming.

This study establishes a foundation for the following future research:

- The fibre dosage should be optimised, and the efficacy of other fibre types should be investigated for 3DPC. The redistribution of shrinkage-related strains should be investigated as a potential cause of the reduction in free shrinkage seen here.
- A 3DPC mix should be optimised for higher dosages of shrinkage reducing admixtures, and the efficacy on 3DPC mixes should be investigated.
- A slow absorbing SAP can improve the rate of stiffening of 3DPC and should be investigated further.

Chapter 7

A plastic shrinkage cracking risk model for 3D printed concrete exposed to different environments

Abstract

The absence of formwork leaves early age 3D printed concrete vulnerable to excessive pore water evaporation. This study investigates the fundamental behaviour of the resulting plastic shrinkage cracking by exposing printed specimens to six drying conditions at concrete ages of 0, 1, 2 and 4 h (delay times). The results show that the rate of concrete mass loss is equal to the drying condition's free water evaporation rate for the first few hours, causing significant desiccation and plastic shrinkage. A moderate evaporation rate removed 24% of the total mixing water from the specimen in only 2 h. The minimal surface moisture and low bleeding rate provide limited protection against pore water evaporation. Therefore, increasing the evaporation rate results in an immediate and direct shrinkage response in the concrete. Delaying the evaporation to the initial setting time decreases the shrinkage magnitude by 56%. If cracking risk is defined as the product of the crack area and crack probability, the risk reduces with an evaporation rate decrease and delay time increase. An empirical model for cracking risk is proposed based on the evaporation rate, delay time and stiffening rate. The experimental results of other studies are used as validation.

Article information

Chapter 7 has been improved and submitted as a journal article: **G.M. Moelich**, P.J. Kruger, R. Combrinck, A plastic shrinkage cracking risk model for 3D printed concrete exposed to different environments.

Contribution declaration

With regard to this chapter, the nature and extent of the contributions of the candidate and the co-authors were as follow:

Name	Nature of contribution	Extent
G.M. Moelich (candidate)	Conceptualisation, Methodology, Validation, Formal analysis, Writing - original draft, Visualization, Investigation	90%
Dr P.J. Kruger (pjkruger@sun.ac.za)	Conceptualisation, Validation, Writing - review & editing	5%
Dr R. Combrinck (rcom@sun.ac.za)	Conceptualisation, Validation, Writing - review & editing, Supervision	5%

The undersigned hereby confirm that:

- The declaration above accurately reflects the nature and extent of the contributions of the candidate and the co-authors to this chapter.
- No other authors contributed to this chapter besides those specified above.
- Potential conflicts of interest have been revealed to all interested parties and that the necessary arrangements have been made to use the material in this chapter of the dissertation.

Signature of authors	Institutional affiliation	Date
	Department of Civil Engineering, Stellenbosch University	09/06/2021
	Department of Civil Engineering, Stellenbosch University	09/06/2021
	Department of Civil Engineering, Stellenbosch University	09/06/2021

7.1 Introduction

One of the most noteworthy attributes of 3D concrete printing is the absence of formwork since it allows for significant savings in material, construction time and costs. However, this advantage leaves the concrete vulnerable to rapid pore water evaporation immediately after printing [16].

For the low w/c mixes typically used in 3D printed concrete (3DPC), severe pore water loss reduces the amount of water available to hydrate the cementitious particles, adversely affecting the mechanical and durability performance [16, 218]. Furthermore, early age pore water evaporation causes a rise in the internal negative capillary pore pressure that results in a volumetric contraction, a phenomenon known as plastic shrinkage [88, 91, 56, 58]. When this shrinkage is restrained, plastic shrinkage cracks (PSC) form, as presented in Fig. 7.1. 3DPC is particularly susceptible to PSC due to the absence of coarse aggregates, minimal bleeding water, high quantities of fines, and high surface area to volume ratio [131].

Figure 7.1: A typical plastic shrinkage crack in 3D printed concrete. This printed specimen had a height of 100 mm and length of 700 mm. The base provided the only shrinkage restraint. The crack formed midway, long before the initial setting time. The concrete water evaporation rate was 0.33 $kg/m^2/h$.

The main mechanisms of PSC in conventional concrete has been identified, and various models have been proposed. Radocea [219] investigated the capillary pore pressure development in saturated granular mixes exposed to rapid drying. The study showed that the pressure development depends on the geometry of

the particles near the surface, the availability of surface water and the amount of evaporated water. It was concluded that the total volumetric shrinkage mainly relates to the amount of evaporated water. Holt and Leivo [40] proposed a linear relationship between the amount of evaporated water two hours after the initial set and the magnitude of plastic shrinkage strain. Boshoff and Combrinck [47] went further and used the amount of evaporated water at the initial set, subtracted the amount of bleeding water and linked the result to the severity of plastic shrinkage cracking. The bleeding film protects against cracking by delaying the pore water evaporation [55, 46]. The basis of Boshoff's model is that the cracking severity is related to the amount of evaporated pore water at the initial setting time. Sayahi et al. [68] related the crack severity to the product of the initial setting time and the amount of pore water that has evaporated at that time. Therefore, multiplying Boshoff's model with the initial setting time. In this way, tensile capacity was accounted for. In a different approach, Ghourchian et al. [220] adapted Terzaghi's consolidation equation for saturated soils to model the volumetric shrinkage of concrete due to drying. Ghourchian et al. [221] then proposed a model for plastic shrinkage cracking, using the Bresler-Pister and Rankine failure criteria. The study used X-ray radiography to monitor crack formation from the side of the specimen.

Literature indicates the tensile strain capacity of plastic concrete decreases from the placement to about the final setting time, whereafter it starts increasing gradually [40, 47], as seen in Fig. 7.2. This explains why cracking becomes visible between the initial and final setting time in conventional concrete [63]. However, in 3DPC, plastic shrinkage cracking appears much earlier, long before the initial setting time [131]. Furthermore, in 3DPC, the shrinkage starts immediately after printing, opposed to conventional concrete where the shrinkage typically starts after the bleeding and settlement period. The magnitude and rate of plastic shrinkage is also several times higher in 3DPC. This fundamentally different behaviour renders the available models inadequate in predicting the plastic shrinkage cracking in 3DPC.

Only a few researchers have studied PSC in 3DPC. Federowicz et al. [179] and Van Der Putten et al. [180] printed single layer specimens and exposed them to an indoor environment to test the efficacy of shrinkage reducing admixture and superabsorbent polymers, respectively, in mitigating plastic shrinkage. Hoffmann et al. [226] noticed plastic shrinkage cracks above a rigid lintel of a 3D printed building wall model. Moelich et al. [131] proposed a method of testing plastic shrinkage and related cracking in multi-layered printed concrete. The specimens were exposed to a more severe drying condition, and the fundamental behaviour of plastic shrinkage and crack development was discussed. Moelich et al. [227] followed and used the test method to evaluate the efficacy of various PSC mitigating measures. The study showed that short polypropylene microfibres could

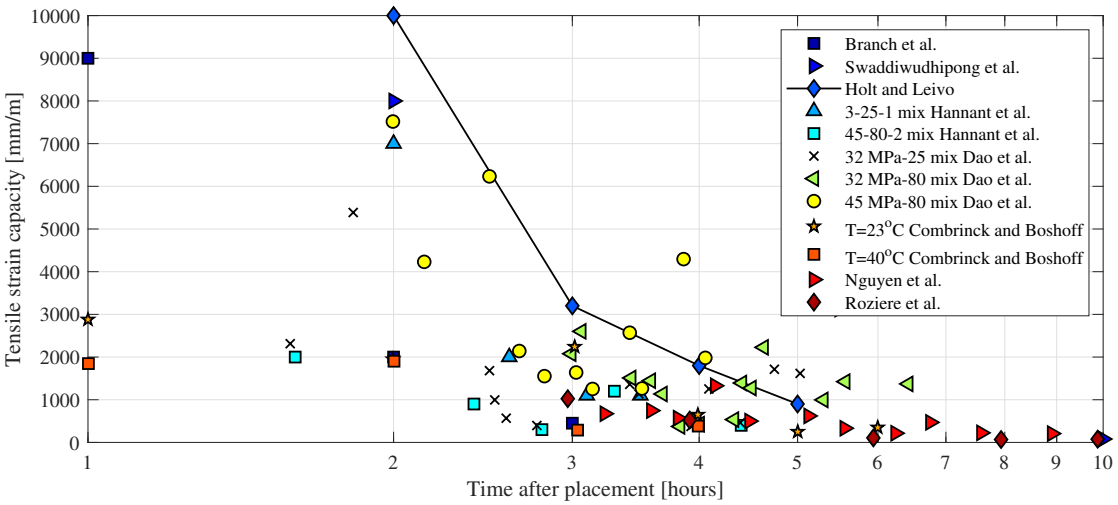

Figure 7.2: The development of the tensile strain capacity for plastic concrete. Updated from Boshoff and Combrinck [47], featuring the results from Branch et al. [222], Swaddiwudhipong et al. [223], Holt and Leivo [40], Hannant et al. [224], Dao et al. [134], Combrinck and Boshoff [133], Nguyen et al. [92], Roziere et al. [225].

eliminate plastic cracking at a severe drying condition. Furthermore, Moelich's testing method allows for the monitoring of the early age cracking at its point of failure and while it propagates, unlike the ASTM C1579 [109] method, which only monitors the resulting surface crack. Monitoring the crack propagation contributes to our understanding of plastic cracking in early age concrete. To achieve this with the ASTM C1579 [109] method X-ray radiography is required as done by Ghourchian et al. [221].

Several topics regarding the fundamental behaviour of plastic shrinkage cracking in printed concrete are yet to be addressed. This study investigates the bleeding gradient, the effect of different drying conditions and delay times on the concrete water evaporation rate, free shrinkage and plastic shrinkage cracking. The aim is to elaborate on the behaviour of plastic shrinkage and related cracking in printed concrete. The mechanism that causes the decline in the shrinkage rate of 3DPC is identified. Ultimately, an empirical model is proposed to quantify the risk of plastic shrinkage cracking in 3D printed concrete and results from literature are used to validate the model.

7.2 Experiments

3D printed concrete test specimens were exposed to five different drying conditions at four different delay times. The free shrinkage strain, plastic shrinkage crack area, concrete water evaporation and bleeding rate were determined.

7.2.1 Materials

The standard mix proportions of the Stellenbosch University 3DPC research group was used Kruger et al. [38]. Portland cement (CEM II 52.5N) with between 6 and 20% limestone extender was added at 579 kg/m^3. Fly-ash (FA, Commercial name: DuraPozz Class F) and silica fume (SF, Commercial name: Microfume by Silicon Smelters) were added at 169 kg/m^3 and 83 kg/m^3, respectively. The main chemical components of these binders are presented in Table 7.1. As aggregate, a natural, continuously graded quarry sand, with a Fineness Modulus of 2.19, was added at 1167 kg/m^3. Municipal tap water was added at 261 kg/m^3. A modified polycarboxylate polymer superplasticizer (SP, Commercial name: Fluid Premia 310) was added at 0.68% of binder mass. The mix had a w/c ratio of 0.45, a w/b ratio of 0.314 and aggregated to binder ratio of 1.4. The mix proportions and materials were constant during the course of this study and resulted in a Vicat needle initial and final setting time of 230 min and 460 min, respectively.

Table 7.1: Chemical composition (percentage of weight) for the Portland cement (CEM II), fly-ash (FA) and silica fume (SF) used in this study, as determined with a major element XRF analysis.

	CEM II	Fly-ash	Silica fume	B-CSA
CaO	62.85	4.29	0.66	46.35
SiO_2	18.60	54.76	84.39	13.46
Al_2O_3	3.47	33.09	0.60	15.32
Fe_2O_3	2.64	3.16	3.28	0.69
K_2O	0.47	0.67	3.46	0.54
Na_2O	0.24	0.26	0.64	0.10
P_2O_5	0.14	0.43	0.14	0.09
TiO_2	0.16	1.61	0.02	0.62

7.2.2 Mixing and printing procedure

The materials were batch-mixed in a two-blade pan mixer at a constant mixing velocity. The dry materials were mixed for 1 min before the mixing water was added and mixed in for another 1 min. Thereafter, a superplasticizer was added and mixed in for 1 min. Additional interim hand mixing was conducted to ensure uniformity; whereafter, mechanical mixing continued for 3 min.

The printer's transport system was primed with the concrete mix. Thereafter, a 1 m^3 build volume gantry-type 3D concrete printer with a 25 mm (diameter) circular nozzle was used to extrude $36 \pm 3 \times 10 \pm 1$ mm (width×height) filaments

without any intervention. A print speed of 75 mm/s was selected and produced an 82 second pass time for the print path in Fig. 7.3 a. The print speed, print path, pass time and extrusion rate was kept constant for the experiments.

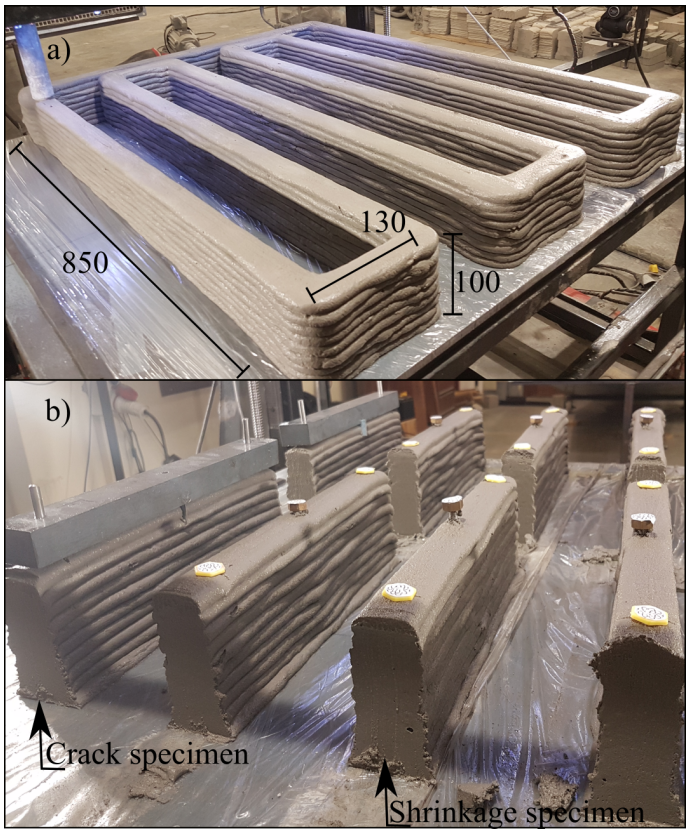

Figure 7.3: a) The printed element. b) The crack and shrinkage specimens.

The friction between the bed and specimen was minimised by covering the PVC print bed with a thin plastic film (Clingwrap) and mould release oil before printing [109]. Once the printing was completed, a steel putty knife was used to cut 300 mm long specimens from the printed element. The restraining rods were then inserted to create the free shrinkage or crack specimens, but a more detailed discussing follows later. The digital image correlation (DIC) markers were inserted, and then the test chamber was closed. Time-zero is defined at 25 min after completing the print since cutting the specimen and inserting the DIC markers took about 20 min.

7.2.3 Drying conditions

After time-zero, the specimens were exposed to different drying conditions. The climatic conditions used to produce these drying conditions can be seen in Ta-

ble 7.2. The parallel study [132] can be consulted for more on the evaporation control chamber used to produce these climatic conditions.

The evaporation rate (denoted by ER) of the drying condition was quantified by measuring the free water mass loss from a water-pan for 3 h, as specified by ASTM C1579 [109]. Henceforth, the water-pan evaporation rate is used to label the drying condition, as seen in Table 7.2. The evaporation rate from the water-pan is referred to as the free water evaporation rate.

The concrete specimen's rate of water evaporation is henceforth referred to as the concrete evaporation rate. The measured concrete evaporation rate is also presented in Table 7.2. The distinction between the concrete evaporation rate and free water evaporation rate should be noted.

ER0.01 resembles an indoor/laboratory climate. ER0.2, ER0.3 and ER0.45 resemble benign outdoor Mediterranean climate. The evaporation rate of ER0.2 and ER0.3 can be expected daily in the winter months of a Mediterranean climate, while ER0.45 is more common in summer months [171]. ER0.6S combines the effect of a low wind speed and high solar radiation to produce a higher evaporation rate. The 1110 W/m^2 radiation, provided by infrared lights, is a typical irradiance in the summer months of a Mediterranean climate [212]. ER0.56 is a drier climate with a similar wind speed and temperature as ER0.45, and was selected to represent the on site evaporation rate of a Mediterranean climate [171]. The ACI 305.1 [100] and ASTM C1579 [109] recommend testing PSC in ordinary concrete at 1 $kg/m^2/h$, which is common in Southern Africa, U.S.A., Australia and the Middle East. However, an evaporation rate of 1 $kg/m^2/h$ would not provide scientific value for this study.

Table 7.2: The different drying conditions used in this study.

	ER0.01	ER0.2	ER0.3	ER0.45	ER0.56	ER0.6S
Initial concrete temperature [$°C$]	21± 0.5	21	21	21	21	21
Ambient temperature [$°C$]	21± 0.3	21	21	21	21	21
Relative humidity [%]	60± 5	60	60	60	50	60
Wind speed [m/s]	0± 0.3	3.5	7.5	10.5	10.5	3.5
Radiation [W/m^2]	0	0	0	0	0	1110
Measured free water ER [$kg/m^2/h$]	0.01	0.2	0.3	0.45	0.56*	0.6
Measured concrete ER [$kg/m^2/h$]	0.02	0.2	0.33	0.42	0.56*	0.3

ER = Evaporation rate
*ER0.56 estimate with Uno [50]

7.2.4 Free shrinkage test

The 10 layered, 300 mm long free shrinkage specimen, used in this study can be seen in Fig. 7.3 b. The test method proposed by Moelich et al. [131] was used throughout this study. Moelich et al. [227] later improved the original method by suggesting that a central rod should be inserted to minimize asymmetrical deformation, as seen in Fig. 7.4 a. The central rod was also used in this study.

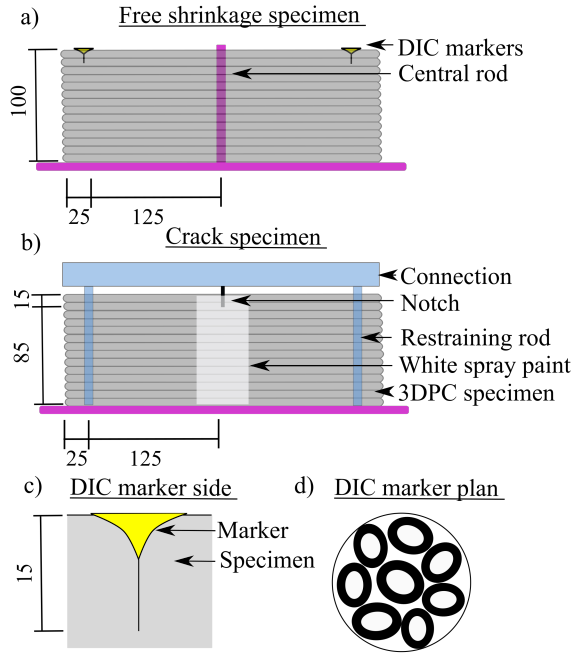

Figure 7.4: a) Free shrinkage specimen and b) crack specimen. c) DIC marker plan view. d) DIC marker side view. Units in mm. Figure from Moelich et al. [227].

To determine the free shrinkage strain, digital image correlation (DIC) was implemented to monitor the displacement of the embedded marker from a series of images. The images were generated at an interval of 3 min and stopped 3 h after activating the airflow. The markers are presented in Fig. 7.4 c and d. Here, shrinkage is defined as a positive strain. Each test produced six free shrinkage specimens from which the mean shrinkage strain was calculated.

Fig. 7.5 shows the graphical meaning of the relevant shrinkage terms used in this study. The shrinkage magnitude was defined as the shrinkage value at 120 min after printing. The shrinkage period was the time until the shrinkage magnitude is equal to 97% of its final value. The shrinkage rate was defined over the first 20 min. The time at which layers 1 (L1), 4 (L4) and 8 (L8) crack was also indicated on the free shrinkage curve.

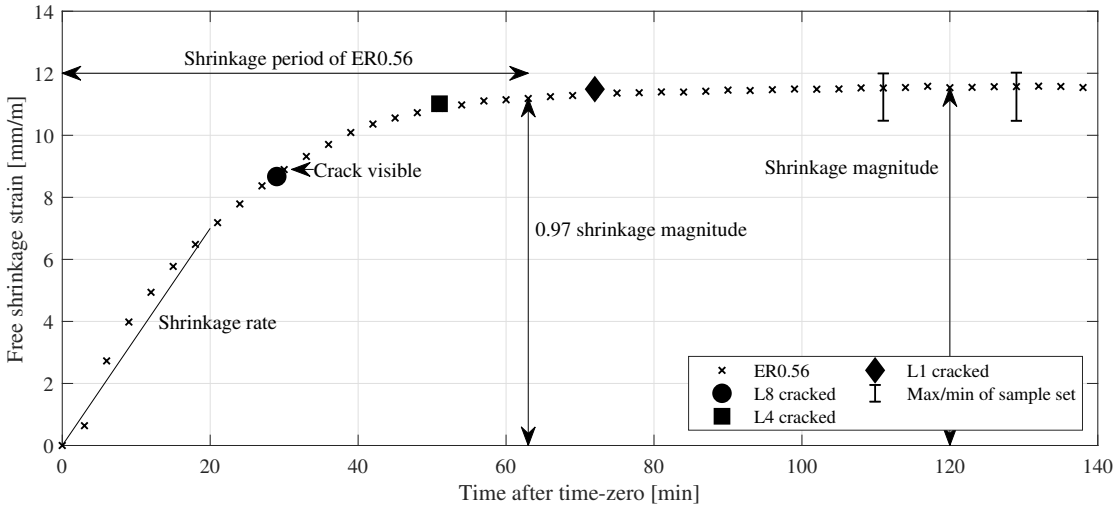

Figure 7.5: Free shrinkage-related terms used in this study.

7.2.5 Cracking test

Plastic shrinkage cracks were induced with the method proposed by Moelich et al. [131]. The crack inducing method can be seen in Fig. 7.4 b. The cracks were imaged at 3 h after activating the airflow, and the image was used to determine the crack area. A Matlab algorithm was used with a constant binarize threshold of 0.35 [131]. Each test produced four crack specimens from which the mean crack area, the time of cracking and the probability of cracking were calculated. The latter was calculated by dividing the number of cracked specimens by the total number of test specimens.

7.2.6 Concrete specimen evaporation rate

Four 36×100×700 mm (width×height×length) printed specimens were weighed every second for 24 hours using a calibrated load cell to determine the continuous mass loss. Data noise, produced by the airflow, were removed by plotting the mean 1 minute mass loss. The concrete evaporation specimens can be seen in Fig. 7.6.

7.2.7 Surface moisture and bleeding tests

The surface moisture and bleeding rate were determined by placing sheets of blotting paper on the printed specimen, similar to the method used by Sanjayan et al. [73]. The blotting paper were placed over the top four layers of a 4, 7 and 10 layered printed specimen, as presented in Fig.7.6. Sheets were also placed on the sides of the 10 layered specimen. The 60×100 mm sheets were placed on each location for 3 min at 10, 30 and 60 min after printing. A sample size of 3 was

deemed acceptable. The bleeding rate was calculated as the mass gain during the respective time periods. Any solid particles were removed from the sheet before the measurement, but this was uncommon. The test was conducted at the low evaporation rate of ER0.01 and the amount of evaporated water was accounted for.

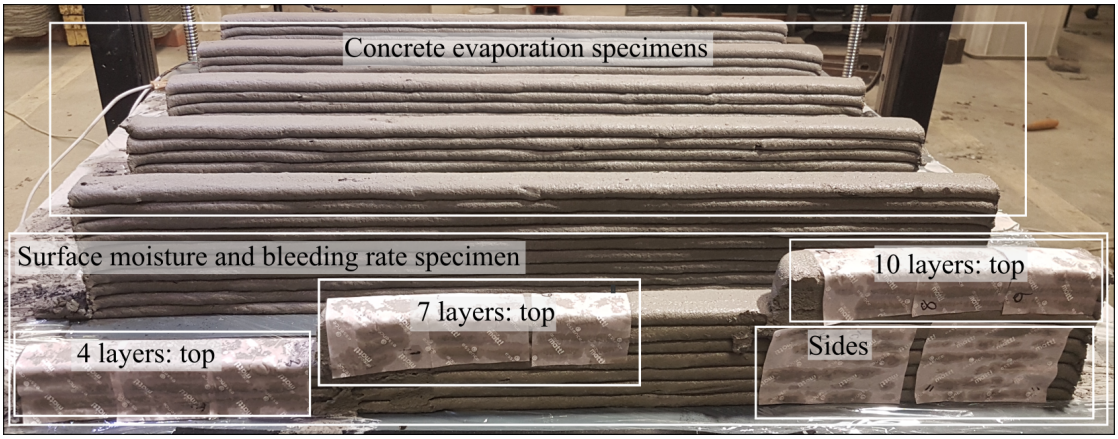

Figure 7.6: The concrete evaporation rate specimens and the bleeding specimen 60 min after printing.

7.2.8 Experimental program

The free shrinkage and crack tests were performed at the different drying conditions of ER0.01, ER0.2, ER0.3, ER0.45, ER0.6S and ER0.56, respectively. In three separate tests, activation of the ER0.56 drying condition was delayed by 1, 2 and 4 h after time-zero for ER0.56D1h, ER0.56D2h and ER0.56D4h, respectively. The nomenclature can be summarised as follows:

- **ER** = Free water **E**vaporation **R**ate measured for a specific drying conditions (e.g. **ER**0.56 had a free water evaporation rate of 0.56 $kg/m^2/h$).
- **D** = **D**elay time (e.g. for ER0.56**D**2h the measured free water evaporation rate of 0.56 $kg/m^2/h$ was activated 2 h after printing).

7.3 Results

7.3.1 Surface moisture and bleeding rate development

The surface moisture development and bleeding rate on the top of layers 4, 7 and 10 are similar, as seen in Fig. 7.7. This implies that the upward migration of bleeding water from the bottom layers is minimal.

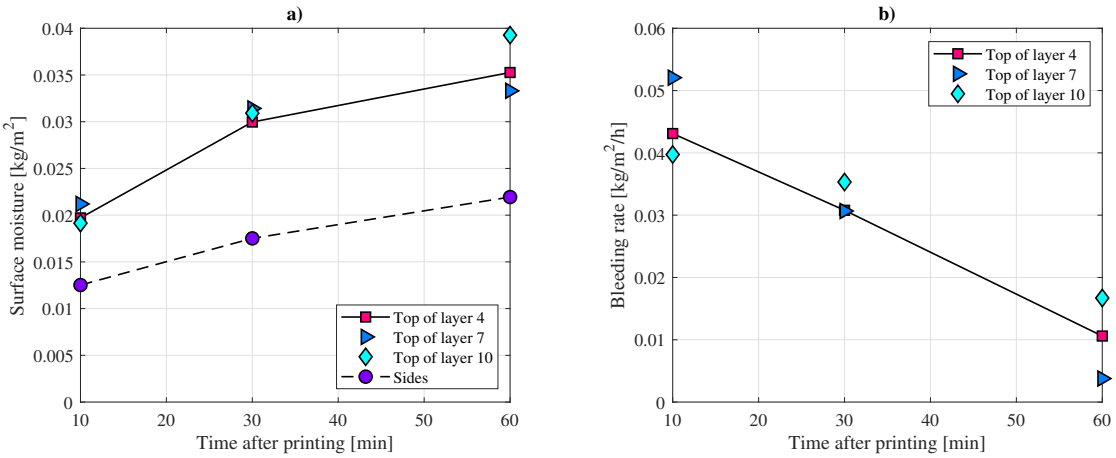

Figure 7.7: The surface moisture (a) and bleeding rate (b) on the top of layers 4, 7 and 10 as well as on the sides of a printed specimen.

The results also show that the elements' lateral sides have lower surface moistures than the top of the filament. It is likely that the top surface gains surface moisture during the first 10 min after printing due to the settlement of the filament under gravitation—the bleeding phenomenon. It can therefore be argued that the sides mainly indicate the amount of moisture on the surface of the concrete, while the development of the top surface moisture indicates the amount of bleeding.

The low w/b ratio and high fines content of the 3DPC mix result in the low bleeding rate. The bleeding rate is much lower than that of conventional concrete, which shows bleeding rates between 0.2 and 1 $kg/m^2/h$ for the first 30 to 60 min, depending on the mix proportions and materials [220, 63, 161, 228].

The lack of surface moisture and low bleeding rate leave printed elements vulnerable to pore water loss immediately after printing. To quantify, a moderate evaporation rate of 0.3 $kg/m^2/h$ evaporates the initial surface moisture of 0.02 kg/m^2 in 4 min. Thereafter, the bleeding rate is insufficient to replace the evaporated surface moisture, and the pore water evaporates.

7.3.2 The rate of concrete specimen evaporation

For about the first 2 h, defined as Stage 1 in Fig. 7.8, the concrete water evaporation rate is equal to the rate of free water evaporation. Therefore, the rate of concrete evaporation is controlled by the drying conditions. To be exact, the ER0.2 drying condition evaporates the concrete water at 0.2 $kg/m^2/h$ for the first 2 h, ER0.3 at 0.33 $kg/m^2/h$ and ER0.45 at 0.42 $kg/m^2/h$. ER0.6S is the exception, with a free water evaporation rate of 0.6 $kg/m^2/h$ producing a concrete evaporation rate of 0.3 $kg/m^2/h$. This is due to the way the radiation is applied to the specimen. For the flat water surface, the radiation heated the surface evenly, but this was not practically achievable in this study for the three-dimensional printed specimens.

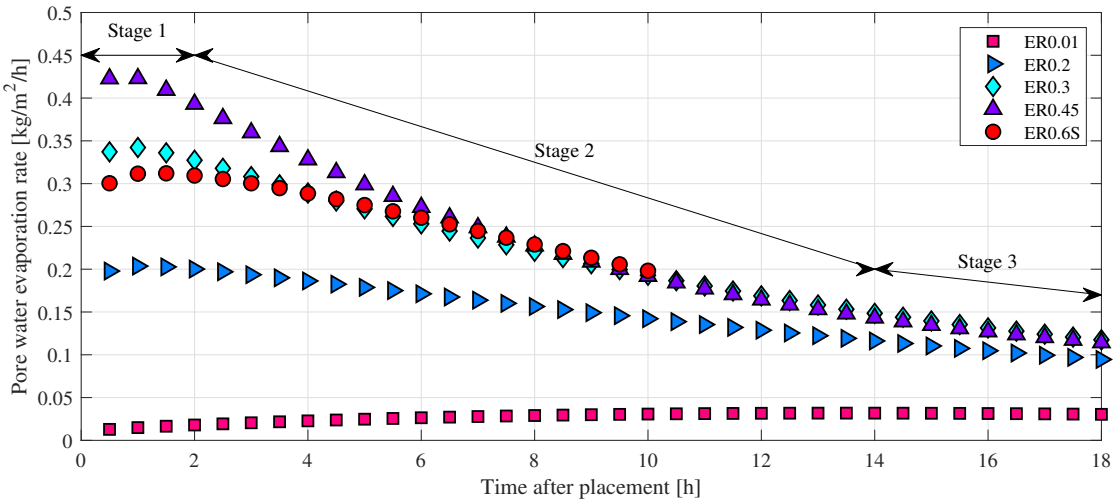

Figure 7.8: The rate of evaporation from the printed concrete specimens at different drying conditions.

After the first 2 h, defined as Stage 2 in Fig. 7.8, the rate of concrete evaporation starts to decrease. It is clear that the concrete evaporation rate of ER0.45 reduces more rapidly than ER0.2. This is because the supply of the surface water decreases, mainly due to the stiffening of the concrete caused by hydration and evaporation as well as the desiccation of the concrete specimen [54].

At the end of the test period, defined as Stage 3 in Fig. 7.8, the drying condition has a minor effect on the rate of evaporation from the concrete specimen. In this stage, the concrete surface is desiccated to such an extent that the pore water evaporation is supply controlled—water migrates by the slow process of vapour diffusion [54].

The amount of pore water that can evaporate from 3DPC is concerning. Initially each printed test specimen contained 0.62 kg of mixing water. The ER0.45 drying condition evaporates 0.15 kg, 24%, only in the first 2 h and 0.35 kg, 56%, in

18 h. ER0.2, a benign drying condition, evaporates 10% in the first 2 h and 46% in 18 h. 3DPC loses large quantities of pore water, even at low to moderate evaporation rates, due to the high surface area to volume ratio. Early age water loss causes plastic shrinkage and reduces the amount of water available for hydration. Losing this amount of pore water can have a significant effect on the long-term mechanical and durability performance. The effect should be quantified in future research.

7.3.3 Free shrinkage

The free shrinkage rate and magnitude increase with the evaporation rate, as seen in Fig. 7.9. Increasing the evaporation rate from 0.01 to 0.2 $kg/m^2/h$ produces a significantly higher rate of free shrinkage and a 457% higher shrinkage magnitude. From ER0.2 to ER0.45, the shrinkage rate increases incrementally with the evaporation rate, resulting in a higher shrinkage magnitude.

It is noted that the length of the shrinkage period corresponds to Stage 1 of the concrete evaporation, presented in Fig. 7.8. This would imply that the mechanisms decreasing the rate of concrete water loss contribute to the decrease in shrinkage rate. These mechanisms are the concrete stiffening due to hydration and evaporation and the exhaustion of available concrete water.

The length of the shrinkage period decreases from ER0.2 to ER0.45. This is because the significant concrete water evaporation stiffens the concrete. The more severe drying condition evaporates more concrete water, resulting in a higher degree of evaporation-induced stiffening and a shorter shrinkage period.

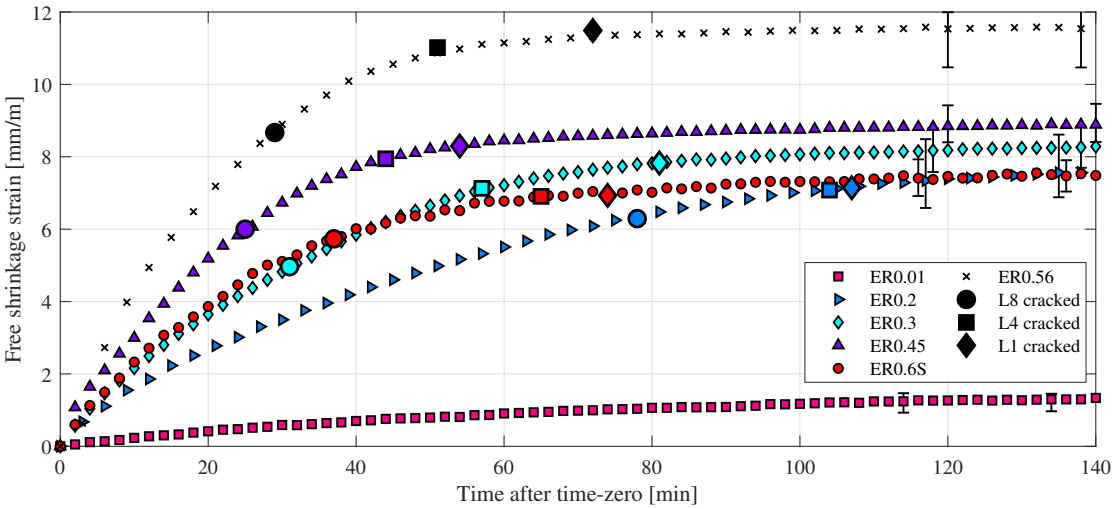

Figure 7.9: Free shrinkage at different drying conditions and its plastic shrinkage crack propagation.

From ER0.45 to ER0.56, the increase in the shrinkage magnitude can be attributed to the higher first 10 min shrinkage rate. The lengths of the shrinkage periods do not decrease, suggesting that there is a limit to the amount of evaporation-induced stiffening. If it was just the availability of concrete water that controlled the length of the shrinkage period, the length would have shortened from ER0.45 to ER0.56 which is not the case.

ER0.6S shows a similar initial shrinkage rate as ER0.3 due to the similar rates of concrete water evaporation. However, at about 50 min, the shrinkage rate of ER0.6S decreases below that of ER0.3. The behaviour is attributed to the applied radiation increasing the concrete temperature (by about $3°C$) and, consequently, the rate of hydration-induced stiffening. Ultimately, the shrinkage magnitude of ER0.6S is 10% lower than ER0.3 even though the rates of concrete water loss were similar (the difference between the ER0.6S and ER0.3 shrinkage results are statistically significant according to a one-way ANOVA with $F(1,9) = 6.02$ and $p = 0.03$).

The significant influence of the evaporation on the free shrinkage is clear from Fig. 7.10. As soon as the drying condition is activated, the specimen starts to undergo plastic shrinkage, indicating the low surface moisture and bleeding rate. Furthermore, delaying the concrete evaporation influences the rate and magnitude of the free shrinkage. A 1 h, 2 h and 4 h delay results in a 14.4%, 31.5%, 56% reduction in the shrinkage magnitude. This is due to the hydration reaction stiffening the concrete with time.

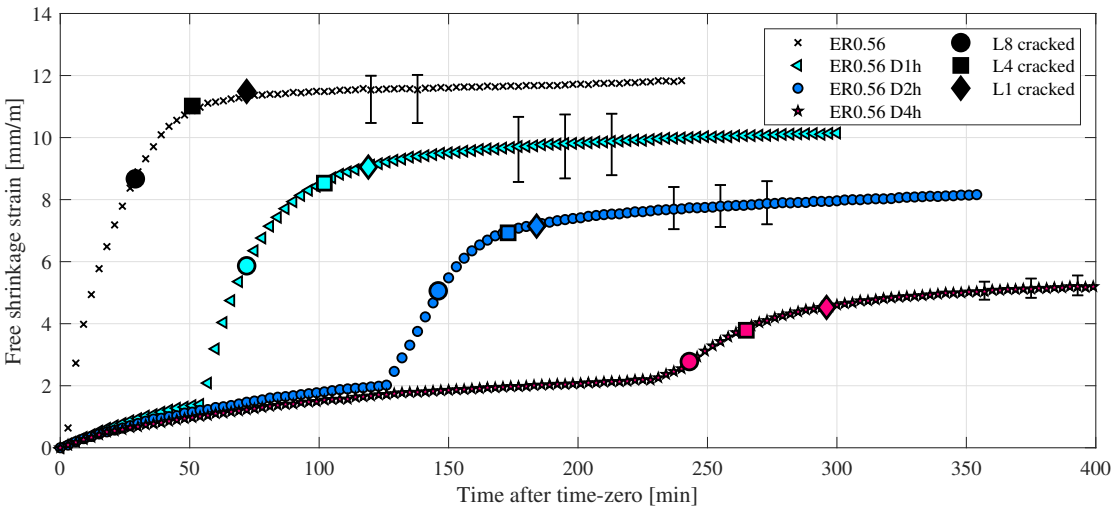

Figure 7.10: Free shrinkage at different delay times and the plastic shrinkage crack propagation.

Literature indicates that the Young's modulus of plastic concrete starts increas-

ing significantly between the initial and final setting time [133, 92]. This explains the reduction in shrinkage magnitude for increased delay times. The increase in Young's modulus is due to the hydration reaction and its development is further referred to as stiffening.

7.3.4 Crack propagation

The time at which layers 1 (L1), 4 (L4) and 8 (L8) cracked is indicated on the free shrinkage curves of Fig. 7.9. The figure shows that the specimens do not crack at a specific strain magnitude. This is due to various factors, including the rate of shrinkage, stress relaxation and the hydration and evaporation-dependent tensile capacity playing an influential role [92, 133].

From ER0.2 to ER0.45, the time of crack formation reduces. However, from ER0.45 to ER0.56, the cracking times does not decrease for the more severe drying condition. This finding debunks one of the initial hypotheses, that the evaporation rate relates linearly to the time of cracking.

Fig. 7.10 shows that the fresher concrete can resist a higher tensile strain before cracking. Delaying the evaporation with 4 h resulted in a cracking strain magnitude of 2.78 mm/m which is 211% lower than without the delay. The result agrees with the literature, which shows that the tensile strain capacity reduces from placement until a point between the initial and final setting time before it starts increasing [40, 47, 133].

7.3.5 Crack risk

The crack area and crack probability results are presented in Fig. 7.11 a. Here, the risk of cracking is used to quantify the cracking potential, and defined as the product of the crack area and the crack probability:

$$Crack\ Risk = Crack\ Area \times Crack\ Probability \tag{7.1}$$

The crack risk is presented in Fig. 7.11 b. It is clear from the results that the crack risk is related to the evaporation rate. The results are consistent with the concrete evaporation rates and the free shrinkage results.

Furthermore, the crack risk reduces as the delay time increases. This is surprising, considering that the tensile capacity decreases from placement to a point between the initial and final setting time. If the tensile capacity controlled the crack risk, the risk would have increased with the delay time, but this is not the case. Rather, the shrinkage magnitude and rate controls the crack risk. Without shrinkage, the tensile strain would be insufficient to form and widen cracks. The stiffening of the concrete controls shrinkage, as mentioned in Section 7.3.3. It can

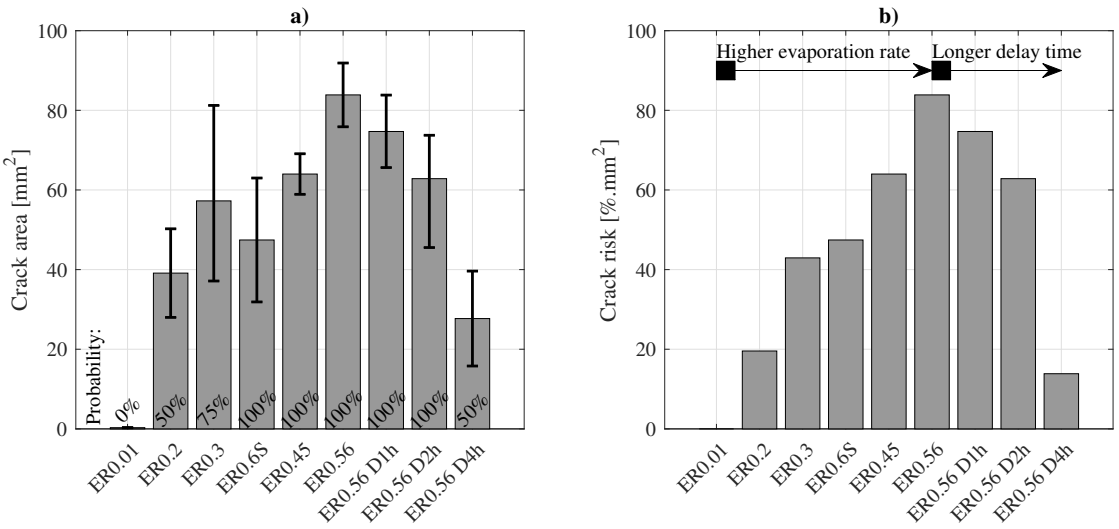

Figure 7.11: The crack area (a) and crack risk (b) for the different evaporation rates and delay times. In a) the crack probability is indicated at the bottom of the bars and the error bars indicate the quartiles.

therefore be concluded that the stiffening of the concrete is one of the main factors controlling the crack risk. The drying condition's evaporation rate is equally important since it controls the shrinkage.

7.4 Modelling and verification

Literature and the results presented here clearly indicate that crack risk increases as the evaporation rate increases [40, 47, 68]. This is particularly true for 3D printed concrete due to the high surface area to bulk volume ratio. If a linear relationship is assumed a regression R^2 value of 0.98 is obtained, as presented in Fig. 7.12 a.

The crack risk decreases as the delay time increases. This is due to the reduction in the shrinkage magnitude and rate, a product of the concrete stiffening with time. If the crack risk is assumed to have a linear relationship with the delay time, a regression R^2 value of 0.95 is obtained, as presented in Fig. 7.12 b. A second-degree polynomial improves the fit marginally.

If the crack risk (CR in $\%.mm^2$) increases linearly with the evaporation rate (EvR in $kg/m^2/h$) and decreases linearly with the delay time (T_d in h) until between the initial (T_i in h) and final setting time (T_f in h), the crack risk can be estimated with:

$$CR \propto EvR\left(1 - \frac{2T_d}{T_i + T_f}\right) \tag{7.2}$$

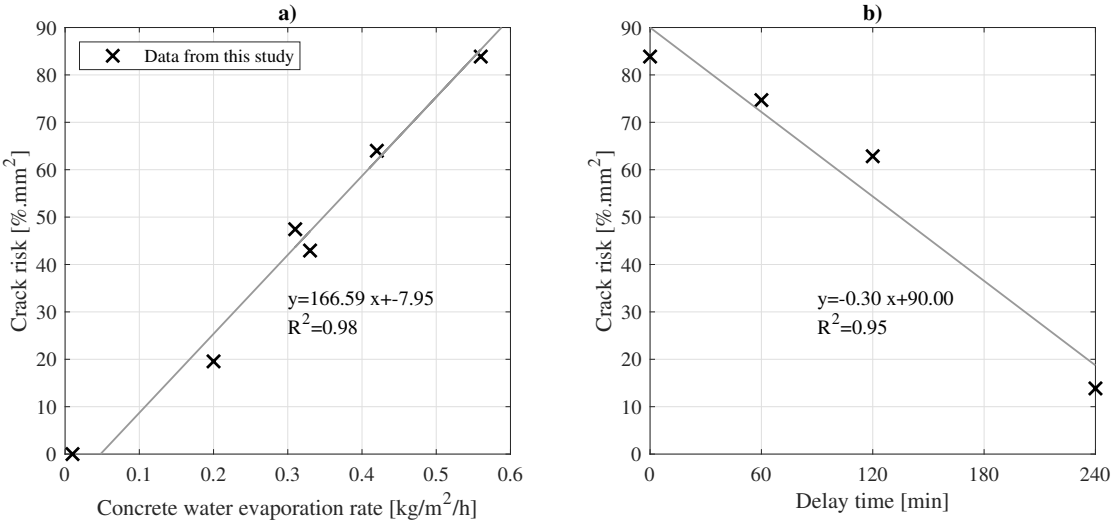

Figure 7.12: The crack risk against the concrete evaporation rate for different mixes.

Relating the estimated crack risk and the actual crack risk produces a regression R^2 value of 0.96, as presented in Fig. 7.13. The regression value is high compared to the PSC models proposed by others for cast concrete. This is mainly because of the significant loss of concrete water that governs the plastic shrinkage cracking behaviour in 3DPC. The model accounts for the evaporation rate, the delay time and the decrease in crack risk due to the concrete stiffening with time. The underlying principles hold for printed concrete regardless of the mix proportions.

Nonetheless, the model was validated with Mix 1 from Moelich et al. [131] and REF from Moelich et al. [227], as presented in Fig. 7.13. The mixes used different fine aggregates and superplasticizer dosages, but the mix proportions and w/c ratio were similar. The proposed model overestimates the crack risk with 12% for Mix 1 and underestimates with 2% for REF. Errors of this magnitude can be deemed acceptable.

The PSC testing method used by researches is the worst-case scenario. Therefore, a crack risk below 10 $\%.mm^2$ can be regarded as acceptable in actual printed elements. This means that the probability of cracking and the width thereof are likely to be small. This recommendation is based on engineering judgment and the results of this study and others [131, 227].

The empirical model implies that for mixes with similar proportions, an evaporation rate below 0.1 $kg/m^2/h$ results in an acceptable cracking risk. For this material, the model shows that an evaporation rate of 0.5 $kg/m^2/h$ should be reduced below 0.1 $kg/m^2/h$ for 280 min after printing to avoid cracking. For drying conditions more severe than 0.6 $kg/m^2/h$, the evaporation rate should be reduced to below 0.1 $kg/m^2/h$ until the final setting time.

The physical interpretation of the crack risk is presented in Fig. 7.14. The

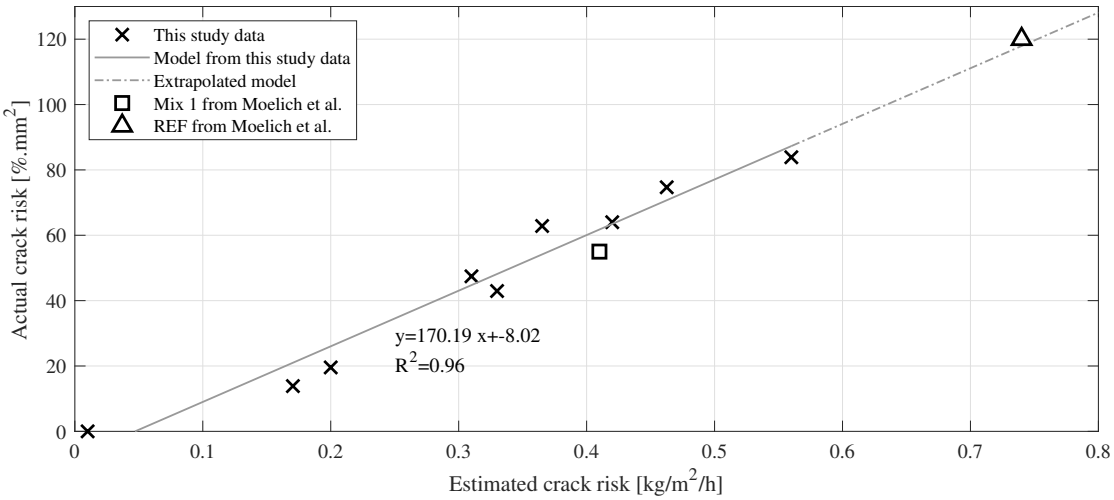

Figure 7.13: The empirical model for the risk of plastic shrinkage cracking in 3D printed concrete. Mix 1 of from Moelich et al. [131] and REF from Moelich et al. [227] are used as validation.

crack risk values can also be divided by the length (85 mm) for the approximate crack width.

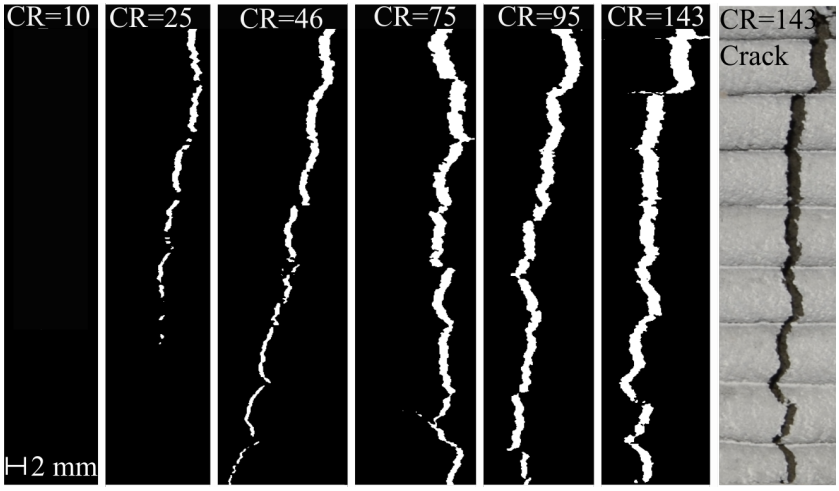

Figure 7.14: Typical cracks observed in different specimens for different crack risk (CR) values. The original image of CR=143 $\%.mm^2$ is presented on the right.

7.5 Conclusion

This study investigated the effect of the environment's evaporation rate and its time of application on the early age concrete water loss, free plastic shrinkage and cracking of 3D printed concrete. The following conclusions can be drawn from this study:

- 3DPC shows a significantly lower bleeding rate than conventional concrete, predisposing it to pore water loss and plastic shrinkage cracking. The sides of the printed specimen show a lower amount of surface moisture than the top of the filament and the bleeding gradient, from the bottom to the top layers, is minimal.
- For the first few hours after printing, the concrete evaporation rate was similar to the environment's free water evaporation rate. A moderate evaporation rate ($0.45\ kg/m^2/h$) can evaporate 24% of the total mixing water in the first 2 hours, resulting in significant plastic shrinkage and desiccation of the specimen.
- The magnitude of the free plastic shrinkage decreases with the evaporation rate and decreases 56% as the delay time is increased from after printing to 4 h. The latter is attributed to the gain in concrete stiffness.
- The mechanism that causes the decline in the shrinkage rate was identified as the hydration and evaporation-induced stiffening of the concrete.
- Plastic shrinkage cracking can be prevented if evaporation is delayed for long enough that the concrete can gain stiffness. This reduces the shrinkage magnitude and rate, and therefore, the crack area.

An empirical model was proposed for the plastic shrinkage cracking risk, based on the evaporation rate, delay time and concrete stiffness rate. It is recommended that the environment's evaporation rate is reduced to below $0.1\ kg/m^2/h$ until the final setting time to reduce the risk of cracking in printed elements.

Chapter 8

The effect of restrained early age shrinkage on the interlayer bond and durability of 3D printed concrete

Abstract

3D printed concrete exhibits a high magnitude and rate of plastic shrinkage (early age drying-induced shrinkage) compared to conventional cast concrete. This study investigated if restraining this shrinkage adversely affects the long-term durability and mechanical performance. Shrinkage was restrained by inserting reinforcement-like rods into the fresh concrete and exposing the specimen to a moderate evaporation rate. The interlayer bond strength, permeability and ion penetration of the unrestrained and restrained specimens were then compared. The results shows that shrinkage causes shear strain concentrations at the interlayers due to a lack of particle interlocking and non-uniform pore water evaporation from the undulated evaporation face. Consequently, discrepancies in the transfer of shrinkage between layers occur, a phenomenon coined as interlayer slip. Evidence is presented of a 12% reduction in interlayer bond strength, a 70% higher permeability and 17% higher chloride ion penetration. These adverse consequences were due to interlayer slip and microcracking. Nonetheless, the durability of uncracked printed concrete is satisfactory, even with localised interlayer slip and microcracking.

Article information

Chapter 8 has been accepted for publication as a journal article and can be cited as: **G.M. Moelich**, P.J. Kruger, R. Combrinck, The effect of restrained early age shrinkage on the interlayer bond and durability of 3D printed concrete, Journal of Building Engineering, vol. 43, November 2021. Online

Contribution declaration

With regard to this chapter, the nature and extent of the contributions of the candidate and the co-authors were as follow:

Name	Nature of contribution	Extent
G.M. Moelich (candidate)	Conceptualisation, Methodology, Validation, Formal analysis, Writing - original draft, Visualization, Investigation	90%
Dr P.J. Kruger (pjkruger@sun.ac.za)	Conceptualisation, Validation, Writing - review & editing	5%
Dr R. Combrinck (rcom@sun.ac.za)	Conceptualisation, Validation, Writing - review & editing, Supervision	5%

The undersigned hereby confirm that:

- The declaration above accurately reflects the nature and extent of the contributions of the candidate and the co-authors to this chapter.
- No other authors contributed to this chapter besides those specified above.
- Potential conflicts of interest have been revealed to all interested parties and that the necessary arrangements have been made to use the material in this chapter of the dissertation.

Signature of authors	Institutional affiliation	Date
	Department of Civil Engineering, Stellenbosch University	09/06/2021
	Department of Civil Engineering, Stellenbosch University	09/06/2021
	Department of Civil Engineering, Stellenbosch University	09/06/2021

8.1 Introduction

3D concrete printing is an additive manufacturing technique that shows potential to facilitate automation in the construction industry. The layer upon layer extrusion of thixotropic cementitious mortar allows for formwork free construction, reducing material waste, costs and allows for increased design freedom.

When early age concrete is exposed to rapid pore water evaporation, negative capillary pressure develops in the pore network, which leads to a three-dimensional volume reduction known as plastic shrinkage [56, 58]. Restraining plastic shrinkage can result in both visible and microcracks. These cracks allow for the ingress of degradation agents, causing the corrosion of reinforcement, carbonation of the matrix and, ultimately, premature deterioration of the element [229, 230].

The absence of formwork and bleeding water leaves 3D printed concrete (3DPC) vulnerable to the drying environment soon after deposition. In the first 2 h, 3DPC exhibits a high rate and large magnitude of shrinkage when exposed to even a moderate evaporation rate [131]. This is due to the lack of coarse aggregates, high quantities of fines and high surface to volume ratio of typically thin-walled 3DCP elements. Moelich et al. [131] used digital image correlation to investigate the shrinkage strain development and redistribution of restrained 3DPC specimens exposed to rapid early age drying. Discontinuities in the transfer of shrinkage from one layer to the next were noticed. It was hypothesised that the introduction of restraint, through reinforcement, can cause differential shrinkage and result in these discontinuities. The current study investigates this hypothesis and the effect on the long-term interlayer bond strength and durability performance of 3DPC.

Rigid building components, connected to freshly printed concrete can restrains the early age shrinkage. Hoffmann et al. [226] noticed visible plastic shrinkage cracking when new filaments were placed on a lintel. Others [131] have used vertical reinforcement-like rods to restrain shrinkage and study plastic shrinkage cracking in 3DPC. External restraint can also result from a rough print bed or connections to more mature layers. Internal sources include geometrical changes and non-uniform stiffening. On the other hand, increasing the structuration rate can potentially mitigate plastic shrinkage and several set-on-demand methods have been proposed to facilitate rapid stiffening after extrusion [231–234, 227].

In 3DPC, a long print path combined with a slow nozzle speed can result in a long pass time [217]. During this time, the surface moisture evaporates, causing a weak long-term interlayer bond [73, 78]. Air entrapment, high plastic viscosity and lack of surface roughness can also significantly influence the bond strength [75, 74, 76, 79]. The filaments can also undergo a significant amount of shrinkage, causing shear stress on the interlayer at an early age, which may weaken the long-term bond [16]. Nerella et al. [76] postulated that shrinkage of the newly extruded layer can cause relaxation in the bond. For high evaporation rates and a weak

early age interlayer bond, plastic shrinkage can also cause debonding of layers [235]. Except for the aforementioned literature, the effect of early age differential shrinkage on the interlayer bond strength of 3DPC has not been investigated.

The interlayer can also have a significant effect on the durability of 3DPC [79]. It has been reported that the interlayer region has a higher porosity and air content as well as higher void interconnectivity than the filament [74, 176, 76]. μCT scans also show that printing elongates the filament's pores, in the printing direction, increasing permeability [80]. Differential shrinkage can contribute to the impaired durability [236]. Van Der Putten et al. [237] explains that the shrinkage of a newly deposited layer is partially restrained by the previous layer and can result in microcracks at a longer pass time. A few studies [236–238] have investigated the durability of the interlayer but more research is required. This study also aims to contribute in this regard.

Literature from cast concrete reports three mechanisms in which rapid drying can induce microstructural damage in cementitious materials: 1) the emptying of large pores to increase the volume and connectivity of the pore network, 2) dehydration and partial collapse of the Calcium-Silicate-Hydrate (CSH) sheets to increase the size of capillary pores and result in a "coarsening" of the microstructure, and 3) shrinkage-related microcracks induced by internal or external restraint [72]. These mechanisms occur simultaneously with differential shrinkage and are difficult to decouple. It is reasonable to assume that increasing the evaporation rate activates all the mechanisms, but the introduction of external restraint focuses on the damage caused by microcracks and differential shrinkage.

This study aims to show the adverse long-term consequences of differential early age shrinkage in 3DPC, other than visible cracking. External restraints were used to induce differential shrinkage while the pass time was kept constant. The focus was not on the effects of interlayer surface moisture evaporation or air entrapment.

8.2 Experiments

A 3D printer was used to extrude concrete in a layer-by-layer fashion along a predefined path (Fig. 8.1 a) at a constant pass time of 60 s. Thereafter, a rapid drying condition was used to induce early age shrinkage in the specimens (Fig. 8.1 b). This shrinkage was either restrained (Fig. 8.1 d) or unrestrained (Fig. 8.1 c). In the former, deformation was prevented in the top half of the specimen. In the latter, the entire specimen was allowed to deform freely. In this way, the magnitude of differential shrinkage between consecutive layers was controlled. Deformation was monitored using digital image correlation (DIC). The interlayer bond strength (IBS) and the durability performance were evaluated.

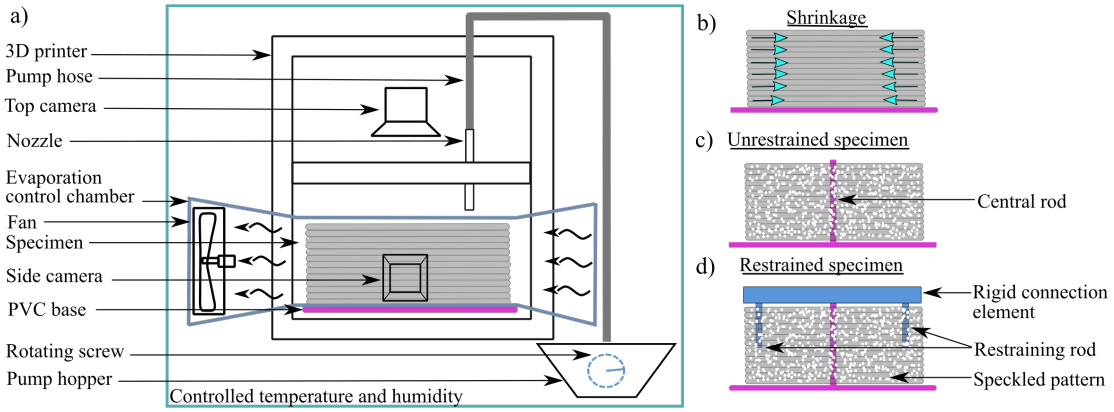

Figure 8.1: The experimental arrangement used in this study. a) 3D concrete printer, axial fan and deformation monitoring equipment. b) The resulting early age shrinkage due to pore water loss. c) Unrestrained shrinkage specimen. d) Configuration of steel rods for restrained shrinkage.

8.2.1 Materials, mixing and printing procedure

The standard mix proportion of Stellenbosch University's 3DPC research group was adopted [38]. A CEM II 52.5N cement that contains between 6 and 20% limestone extender was added to the batch-mixer at 579 kg/m^3. Fly-ash (DuraPozz Class F) and silica fume (Chryso DSF) was added at 169 and 83 kg/m^3, respectively. As fine aggregate, a natural, continuously graded and locally sourced quarry sand with a maximum particle size of 4.75 mm was added at 1167 kg/m^3. All the dry materials were then mixed for 60 s. Tap water was added at 261 kg/m^3 and mixed for 45 s. A modified polycarboxylate polymer superplasticizer (Chryso Fluid Premia 310), at 0.652% of binder mass, was gradually added and mixed for 45 s. Interim hand mixing was performed for 120 s to ensure uniformity. Thereafter, mechanical mixing continued for another 120 s. Theses proportions resulted in a w/c ratio of 0.45 and aggregate/binder ratio of 1.4. The mix was then transported to the printer. The pump was primed with the mix whereafter extrusion was activated to print the concrete on the bed without any intervention.

A 1 m^3 gantry-type 3D concrete printer with a circular nozzle (25 mm diameter) was used to place 40×10 mm (width×height) filaments. More detail on this 3D concrete printer can be found elsewhere [36, 210]. A print speed of 90 mm/s was selected whereafter the extrusion rate was adjusted to obtain a 40 mm filament width. A constant pass time of 60 s was selected. The mix was extruded on a smooth PVC base, with an even coat of mould release oil, to reduce friction between the bed and bottom layer.

After printing, the concrete was allowed to structurate for 30 min before the

restraining rods were inserted. Thereafter, the specimens were cut to the desired length of 300 mm. The drying condition was then activated, and time-zero was recorded.

8.2.2 Evaporation conditions and control

To control the pore water evaporation rate, an evaporation control chamber was designed and built according to the guidelines provided by ASTM C1579 [109]. The device, seen in Fig. 8.1 a, produced uniform airflow over the printed specimens while the ambient temperature and relative humidity were controlled.

The test specimens were exposed, for 3 hours, to either the LAB or SITE drying conditions. Both LAB and SITE had an ambient temperature of $22.5 \pm 0.5°C$ and relative humidity of $60 \pm 3\%$. The concrete temperature at placement was $21.5 \pm 0.5°C$. An airflow of $6.3 \pm 0.3\ m/s$ was generated for SITE while no airflow was generated for LAB. These drying conditions resulted in a water evaporation rate of 0.02 $kg/m^2/h$ for LAB and 0.36 $kg/m^2/h$ for SITE. LAB, used as the reference condition, imitates a indoor environment where SITE imitates an outdoor environment with a more severe evaporation rate. The drying conditions of SITE is benign compared to a common Mediterranean climate [171] and much less than the 1 $kg/m^2/h$ suggested for testing PSC in conventional concrete [100]. During printing, the evaporation rate was kept constant at LAB. Here, the emphasis was not on the pore water that evaporates during printing but rather on the pore water evaporation for the first 3 hours thereafter.

8.2.3 Inducing differential shrinkage

Shortly after print completion, pointed steel rods with a diameter of 6 mm were inserted into the 3DPC to produce either an unrestrained or restrained specimen. For the unrestrained specimen (Fig. 8.1 c), a single steel rod, connected to the base, was inserted in the middle of the specimen from below to prevent asymmetrical deformation. The shrinkage was allowed to deform the specimen freely. For the restrained specimen (Fig. 8.1 d), two additional restraining rods were inserted from the top and connected to the central rod. The two outer rods prevent deformation in the top half of the specimen to invoke differential shrinkage between the top and bottom halves. The configuration of the restraining rods and the dimensions of the specimens for each test conducted can be seen in Fig. 8.2.

The restraint arrangement was strategicly selected to induce differential shrinkage at the centre of the test samples. This unrealistic configuration is used to exacerbate differential shrinkage and study the phenomenon.

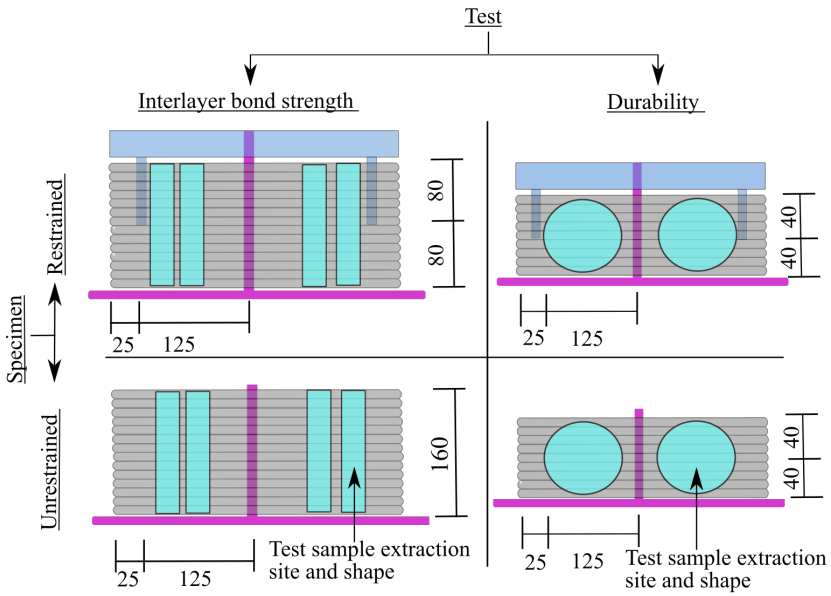

Figure 8.2: The configuration of the restraining rods and dimensions of the specimens for each test conducted in this study. The locations of extraction and specimen shape, used for the hardened state tests, are also indicated.

8.2.4 Monitoring deformation with DIC

The speckled pattern digital image correlation (DIC) technique was used to monitor the early age deformation. After 40 min, the concrete surface was dry enough to apply a speckled pattern. Black chalk-base spray paint was applied to the concrete surface to produce speckles with a suitable diameter, between 3 and 5 pixels [213]. Thereafter, deformation monitoring started and continued for the next 3 hours.

Two identical optical cameras (4928 × 3264 pixels) were used to monitor in-plane deformation of the specimens. The cameras were placed 700 mm from the specimen with a focal length of 50 mm to produce a pixel size of 0.081 × 0.081 mm similar to Bertelsen et al. [67]. To reduce edge effects, the region-of-interest (300 × 60 mm) was positioned at the centre of a bigger field-of-view (400 × 265 mm). The first image was taken 40 min after print completion (time-zero) and every 3 min thereafter for the next 3 h. GOM correlate (2019) was used to process a series of images. A subset size of 21 pixels and a point-to-point distance of 11 pixels were selected to obtain a density greater than 3 speckles per subset [213].

8.2.5 Strain definition

In this study, shrinkage strain (ε) is defined as positive and elongation as negative. The gauge length varied depending on the results' application but is provided with the result. ε_x is defined as the horizontal strain and was defined over a larger gauge length, typically 125 mm. ε_y is defined as the vertical strain and calculated over the interlayer, at a shorter gauge length, typically a few millimetres.

8.2.6 Interlayer bond strength

After 3 h of the drying condition, all the interlayer bond strength (IBS) specimens were covered with plastic wrap to prevent further pore evaporation. The test samples were then collected from the 3DPC specimen on the positions seen in Figure 8.2. The printed specimens were saw-cut into 160 × 40 × 40 mm (L × W × H) samples, 24 h before each test. To determine the IBS, 7 and 28-day four-point bending tests were conducted [239]. The filament layers are aligned transversely (orientation O-III), parallel to the applied load, to induce normal stress in the interlayer. This orientation was selected since it is the weakest of orthotropic 3DPC [79]. As a reference, the same batch concrete used for printing was cast into the EN 196-1 [239] flexural test moulds, vibrated at a moderate intensity for 2 min and exposed to the same drying condition as the printed specimen. The IBS reduction (S_R) was determined with the following equation [79]:

$$S_R(\%) = 100\left(1 - \frac{S_{III}}{S_M}\right) \tag{8.1}$$

where S_{III} is the flexure strength of the printed specimen and S_M is the flexure strength of the cast specimen.

Recently, Kruger and Van Zijl [79] reviewed the testing methods used to quantify the lack of interlayer adhesion observed in printed concrete. Of these, the four-point bending test is preferred for its simplicity, minimal specimen preparation and saw-cutting. The short testing time allows for a larger sample size and a better characterisation of the variability and central tendency. Four-point bending also produces a constant bending moment and no internal shear force over a large central region of the test specimen, unlike three-point bending. Others have used a similar test method [210, 78, 76].

8.2.7 Durability

The durability performance of the concrete is quantified using two indicators: Oxygen Permeability Index (OPI) and Chloride Conductivity Index (CCI) [85, 86, 84]. OPI reports the gas permeability that indicates the degree of pore connectivity

while CCI reports the resistance to chloride ion penetration of the concrete. 21 days after printing, the test samples were collected from the printed specimen on the positions seen in Figure 8.2. 70 mm diameter concrete disk samples were saw-cut from the various 3DPC specimens. The same saw-cutting procedure was used on all the specimens to avoid causing additional microstructural damage. The 40 mm thick disks were saw-cut for a second time to produce a smooth face on the one side, and reduce the thickness to 30 mm. Thereafter the disk samples were dried in an oven for 7 days at $50 \pm 2°C$. As a reference, the same batch concrete used for printing was cast into cube moulds and exposed to the same drying conditions as the printed specimens. The cubes were not vibrated, for equal comparison to the printed samples.

At 28 days after printing, the samples were removed from the oven. The samples were placed in the falling head permeameter, after which oxygen is passed through at an initial pressure of 100 ± 5 kPa. The rate of pressure drop was recorded to determine the D'Arcy permeability coefficient and the OPI [84]. To simulate reality, the disks were orientated that the oxygen enters through the undulated face.

The CCI samples were oven-dried with the OPI samples. Thereafter, the CCI samples were vacuum saturated with a NaCl solution and placed in a two-cell conduction arrangement. A 10 V potential difference was applied across the sample to accelerate the movement of chloride ions. The current and voltage readings were recorded, and the CCI was calculated. More details on these tests are available in literature [84].

8.2.8 Experimental program

Literature reports a large coefficient of variation (CoV) in IBS results [79]. Localised differential shrinkage is likely to increase the CoV even more. To determine if the results between the two groups were statistically significant, a large number of samples were tested and a one-way analysis of variance (ANOVA) was conducted. The samples size is reported with the ANOVA result (F(BG,WG) = F, p = PV) as (WG+2)/2. A standard box and whiskers plots are used throughout this study to present the data with its variability.

Seven 38 ℓ prints were conducted from different batches of the same concrete mix. Fig. 8.3 shows the freshly printed element without any fixtures. In each print, there were restrained (R), unrestrained (U) and mould-cast (M) specimens. Prints 1 to 4 produced the IBS samples while Prints 5 to 7 produced the durability samples. Prints 1, 2 and 5 were exposed to LAB while Prints 3, 4, 6 and 7 were exposed to SITE. For each combination of restrained/unrestrained and LAB/SITE, 20 IBS samples were tested on 7 days while 12 were tested on 28 days. For the durability tests, at least 4 samples were tested for each of the combinations

[84]. A set of durability samples were cured in a EN 196-1 [239] standard curing tank (water curing, denoted as W) until 21 days after printing. The majority of durability samples and all the IBS samples were not water cured (no water curing, denoted as NW). The nomenclature can be summarised as follows:

- I7 or I28: **I**nterlayer bond strength on a concrete age of **7** or **28** days.
- Mould, U or R: Mould-cast, **U**nrestrained or **R**estrained specimen.
- LAB or SITE: Benign or severe drying condition with evaporation rates of 0.02 $kg/m^2/h$ and 0.36 $kg/m^2/h$, respectively.
- NW or W: **N**ot cured in **W**ater or cured in a **W**ater curing tank.

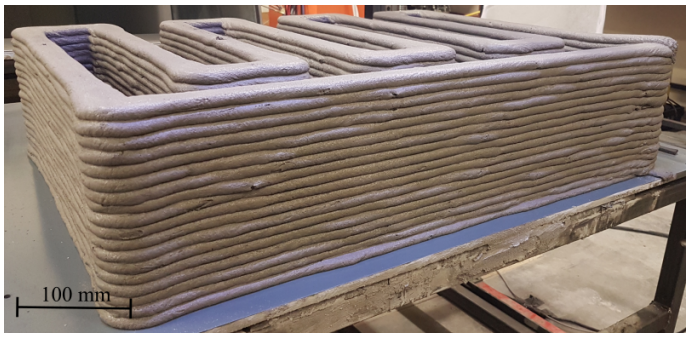

Figure 8.3: The printed element from which the IBS samples were extracted.

8.3 Results

8.3.1 Digital image correlation analysis

The aim of this section is to find discontinuities in the transfer of shrinkage from one layer to the next. For this reason, the results were not average for multiple cross-section. The authors verified that the data presented here is representative of the entire specimen.

8.3.1.1 The unrestrained specimen

ε_x was calculated over 125 mm, from the central rod to Section A, as seen in Fig. 8.4. The positions of the interlayers were also measured on Section A. A gauge length of 1.3 mm was selected for ε_y to show the ε_y concentrations on

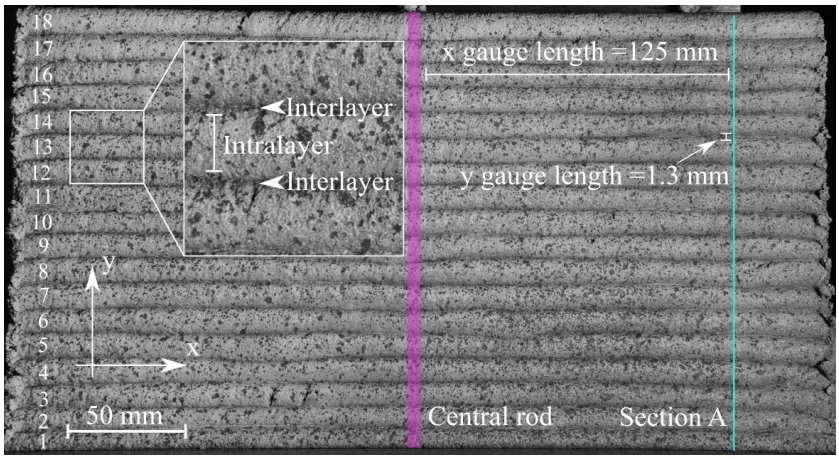

Figure 8.4: The unrestrained shrinkage specimen.

the interlayer. Fig. 8.4 also indicates the difference between the interlayer and intralayer.

The ε_x and ε_y results for an unrestrained printed specimen, exposed to the LAB drying condition, can be seen in Fig. 8.5. The low evaporation rate results in a small ε_x with the majority of the shrinkage occurring in the top half of the specimen. In the 3 h of monitoring, the specimens experienced a maximum ε_x of 2.4 mm/m in the top layer which correspond to a displacement of 0.3 mm. The shrinkage strain increases with time, as expected, with the shrinkage rate decreasing after 120 minutes. The maximum ε_x at 120 minutes is 6.6 mm/m with no distinct trend in the data.

The ε_x and ε_y results for the unrestrained specimen, exposed to the SITE drying conditions, can be seen in Fig. 8.6. Again, ε_x was calculated over 125 mm and ε_y over 1.3 mm, as seen in Fig. 8.4.

Exposing the unrestrained specimen to the SITE drying condition increases the ε_x more than five times with the ε_x of 14 mm/m corresponds to a displacement of 1.75 mm at the ends. Similar to LAB drying, the shrinkage strain increases with the distance from the base with the majority of shrinkage occurring in the first 2 h.

Discrepancies, in the transfer of shrinkage from on layer to the next, is barely noticeable at 30 min but becomes more distinct as time progress. The development is clear for interlayer 9, as indicated with arrows in Fig. 8.6. At 180 min, discrepancies are noticeable on multiple interlayers as indicated by circles in Fig. 8.6.

The shrinkage strain increases linearly within the specific layer but does not transfer uniformly to the layer below causing a discontinuity that coincides with the interlayer. In a distance of 2-3 mm over the interlayer the shrinkage decreases significantly before it starts increasing again in the intralayer. Moelich et al. [131]

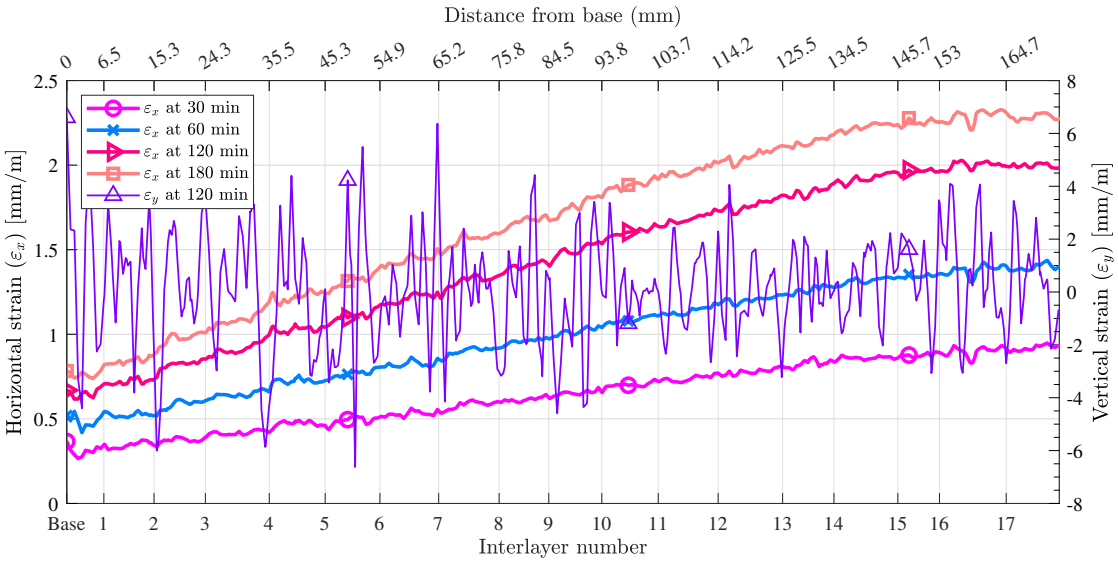

Figure 8.5: The ε_x and ε_y of a unrestrained specimen exposed to the LAB drying condition. The position of the interlayer was measured from this specific specimen, at Section A seen in Fig. 8.4. In these plots, markers were used to clearly distinguish between the different lines.

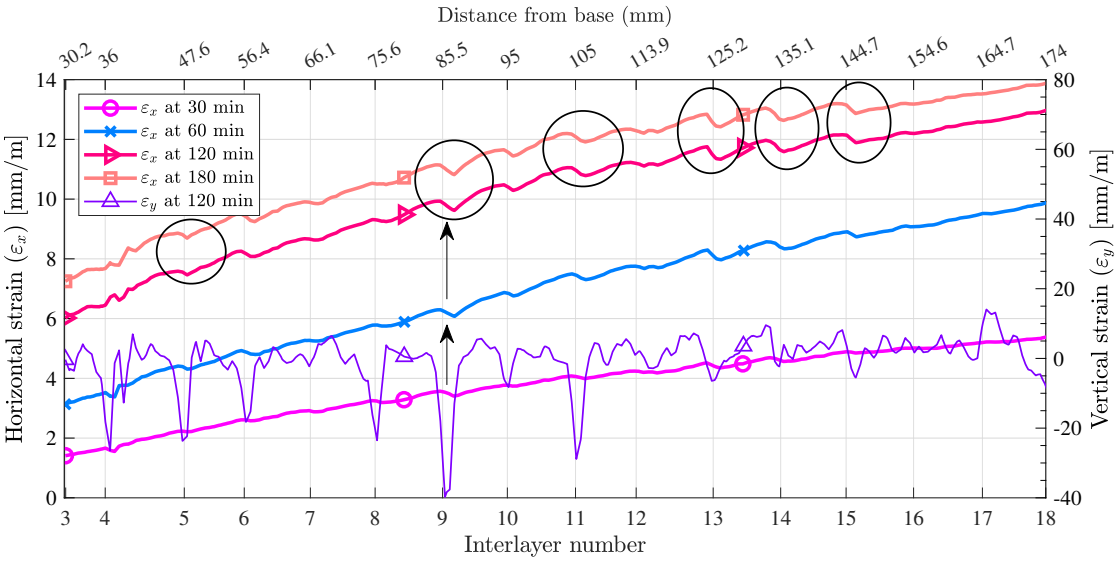

Figure 8.6: The ε_x and ε_y of a unrestrained specimen exposed to the SITE drying condition. The positions of interlayer slip are indicated with a circle. The positions of the interlayers were measured from the specific specimen, at Section A seen in Fig. 8.4.

also noticed these discontinuities and attributed it to slip between layers. However, it is not a complete debonding at the interlayer, but rather a region of reduced

shrinkage transfer. In this specimen, interlayer slip is particularly noticeable at the top of layer 5, 9, 11, 13, 14 and 15 with the magnitude being approximately 0.44 mm/m (minimum strain subtracted from the maximum strain in the layer below). This value is significant when compared to the LAB condition's results. Interlayer slip is also noticed on the left-hand side and at section other that Section A.

No interlayer slip occurs between layer 16 to 18. The effect of the base restraint decreases as the element's height increases. Theoretically, there is a height at which the base restraint has no effect on the shrinkage. Above this height the shrinkage is uniform, meaning that the gradient of the strain curve is approximating zero, and no interlayer slip occurs.

The ε_y results, also seen in Fig. 8.6, can now be considered. Elongation ($-\varepsilon_y$) is noticed over the interlayer plane that coincides with the slippage planes. Fig. 8.7 a shows the vertical deformation of this specimen at 120 min. The layers tend to remain parallel while undergoing a greater magnitude of ε_x in the top layers than in the bottom layers. This results in an upward displacement of the specimen's ends and a decrease in the radius of curvature of the global element. The ε_y is however not distributed evenly over each filament, as seen in Fig. 8.7 b. The strain is concentrated at the interlayer, resulting in elongation peaks shown in Fig. 8.6. This is due to the reduced cross-section area on the interlayer plane.

The distribution of shear strain (ε_{xy}) in the specimen is presented in Fig. 8.7 c. The shear strain concentrations on the interlayer are clear. The magnitude of interlayer ε_{xy} increases from the centre to the unconnected ends. No visible cracks were noticed on the interlayer plane. Ultimately, the ε_{xy} explains the discontinuities in the ε_x transfer.

The magnitude of slip increases as the distance from the centre increases as seen in Fig. 8.8. Furthermore, the ε_x line is near linear at 37 and 75 mm from the centre, but this is not the case at 125 mm from the centre.

8.3.1.2 The restrained specimen

Two additional restraining rods were introduced to concentrate the interlayer slip along a single interlayer plane as seen in Fig. 8.9. These restraining rods prevent deformation in the top layers and promotes interlayer slip in layers 8 to 10.

The ε_x and ε_y strain of the restrained specimen, exposed to the SITE drying condition, can be seen in Fig. 8.10. The introduction of restraints reduces the magnitude of ε_x significantly with a maximum strain of 5.2 mm/m, after 3 h, occurring near the bottom of the restraining rod. The restraining rod ends in layer 10, and the rigidity thereof causes interlayer slip at the top of layer 10, as expected. The magnitude of this interlayer slip is however surprisingly low at

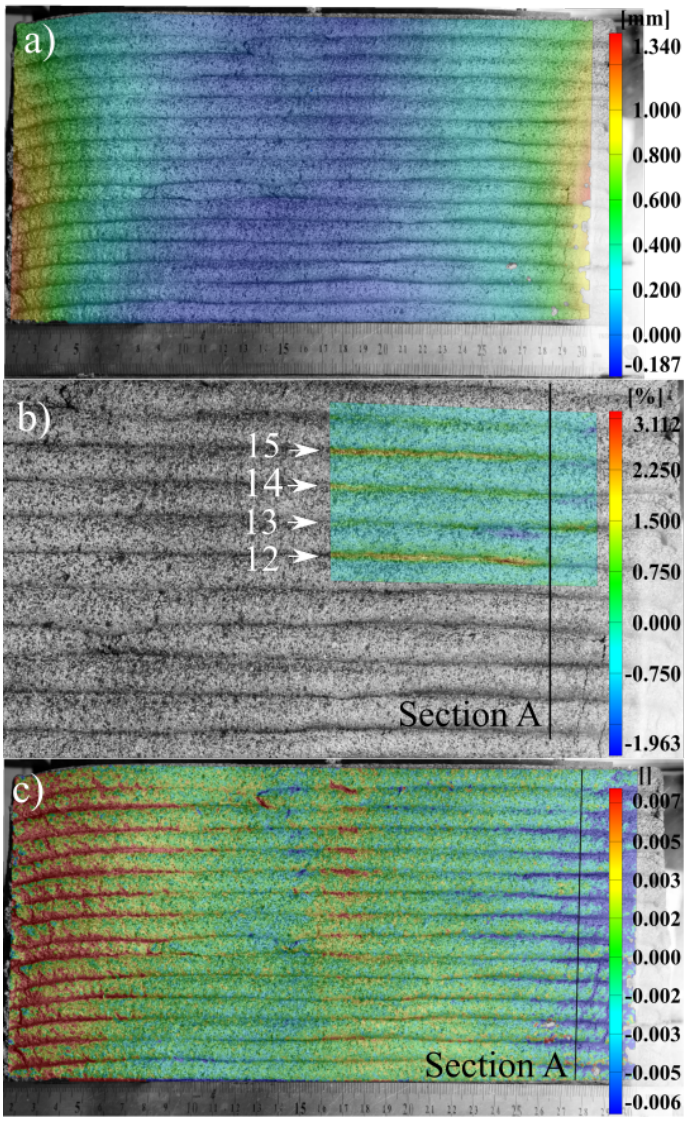

Figure 8.7: a) Vertical deformation due to horizontal shrinkage, with positive as upward displacement, 120 min after activating the SITE drying condition. b) The ε_y ($\% \times 10$ for mm/m) at 120 min. c) The shear strain ε_{xy} at 120 min ($unit \times 1000$ for mm/m).

0.257 mm/m. In fact, the interlayer slip at the top of layer 3, which is due to the base restraint, has a similar magnitude.

The magnitude and frequency of slip, as well as the magnitude of ε_{xy}, is much lower in the restrained specimen compared to the unrestrained specimen. This is explained by the lower shrinkage curve gradient observed in the restrained specimen. The gradient in the unrestrained specimen (0.045 m^{-1}) is twice that of the restrained specimen (0.02 m^{-1}). As with the unrestrained specimen, the ε_y peaks

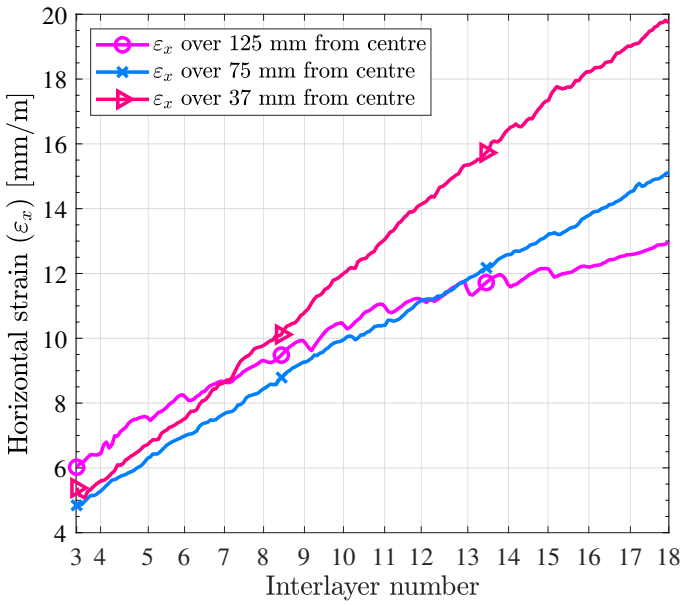

Figure 8.8: The ε_x at a distance of 125, 75 and 37 mm from the central restraining rod. The specimen was unrestrained and exposed to the SITE drying condition for 120 min. The position of the interlayer was measured at 125 mm and differs for 75 and 37 mm.

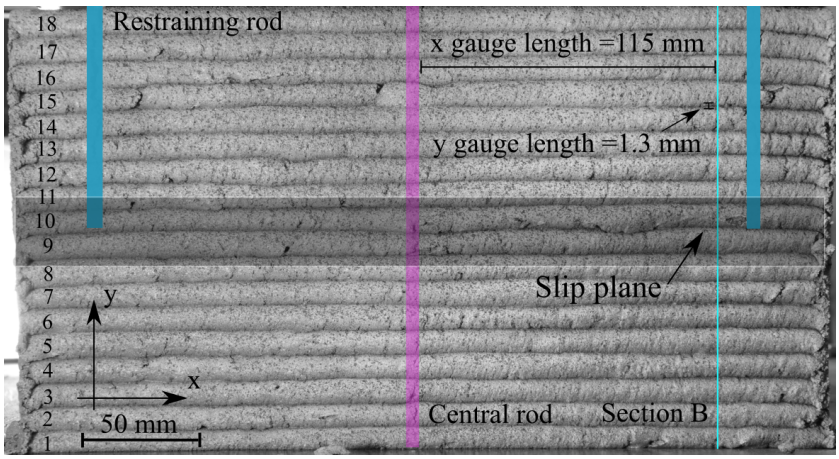

Figure 8.9: The restrained shrinkage specimen with induced slip plane.

on the slipping interlayer plane.

8.3.2 Interlayer bond strength results

The flexural strength (O-III) of the mould-cast and printed samples are presented in Fig. 8.11 a. The flexural strength of the mould-cast samples increases 20% for 7 to 28 days, while the printed samples only increase 9%. Every printed sample

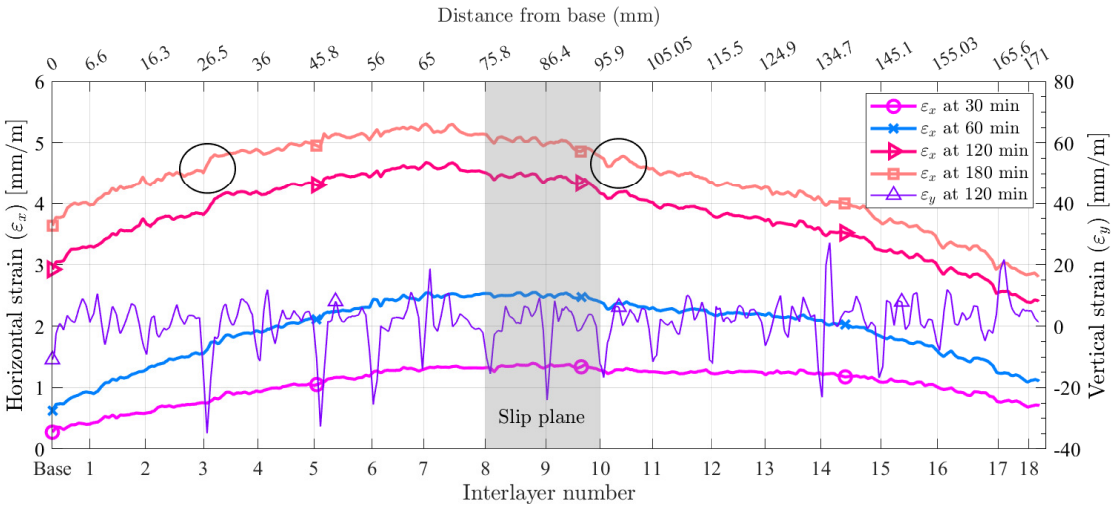

Figure 8.10: The ε_x and ε_y of a restrained specimen exposed to the SITE drying condition. The positions of interlayer slip are indicated with a circle. The positions of the interlayers were measured from the specific specimen, at Section B as seen in Fig. 8.9.

tested in this study failed on an interlayer. Fig. 8.11 b shows the 28-day IBS reduction (S_R) with similar values reported in literature [79].

On average, the samples which were exposed to SITE have a lower flexural strength than samples exposed to LAB, but this result is not statistically significant according to a one-way ANOVA ($F(1,42) = 0.93$, $p = 0.34$). The restrained samples exposed to SITE have a lower flexural strength than the LAB samples, and this difference is statistically significant according to a one-way ANOVA ($F(1,34) = 4.24$, $p = 0.047$). When the restrained and unrestrained data sets from SITE are compared, the mean flexural strength reduced 12% due to the restraint, but the difference is not statistically significant according to a one-way ANOVA ($F(1,18) = 2.35$, $p = 0.14$). For the 7-day S_R, the restrained and unrestrained samples from SITE show similar values.

When the 7 and 28-day results are combined, the restrained SITE samples show a 7% higher third quartile S_R compared to unrestrained SITE, with similar first quartiles. This suggests that not only is the S_R of restrained samples are more variable that the unrestrained samples, but also that the variability on the upper-end of the S_R distribution is larger. The CoV's support this result with 13% for the unrestrained and 15.4% for the restrained specimen. For design, this implies larger partial factors and less economic buildings.

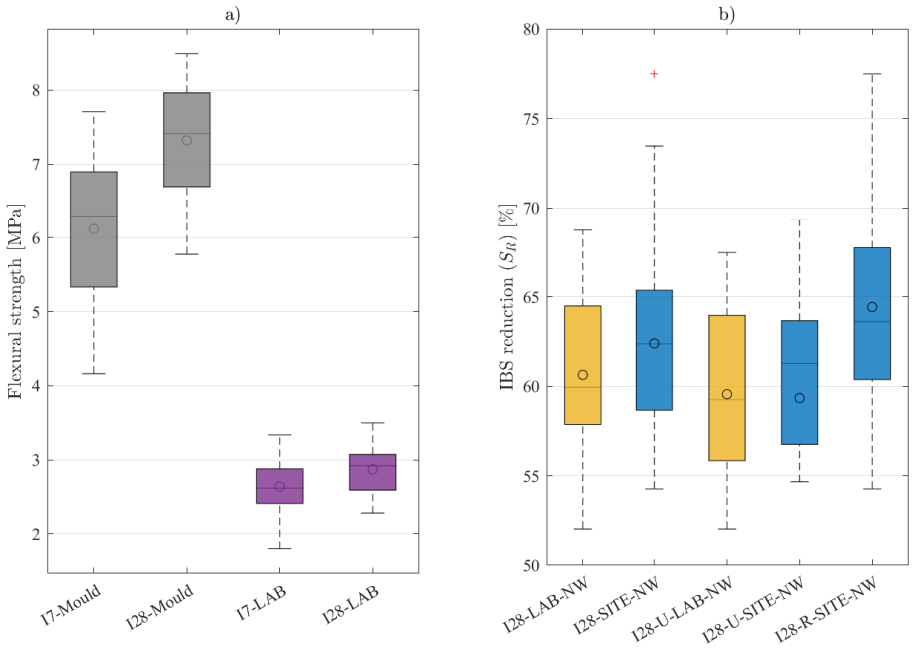

Figure 8.11: A box and whisker plot of the a) 7 and 28-day flexural strength of mould-cast and printed samples and b) the reduction in IBS (S_R) at 28 days for the different drying condition and restraint combinations. Means are indicated with a circle.

8.3.3 Durability

8.3.3.1 Oxygen permeability

To indicate the pore interconnectivity, the Oxygen Permeability Index (OPI) and D'Arcy permeability coefficient results are presented in Fig. 8.12. The permeability of the printed samples is marginally higher (5%) that the mould-cast samples, but the difference between the two groups are statistically insignificant. Exposing the samples to SITE resulted in a 23% higher permeability than LAB, with no statistically significant difference between the two groups according to a one-way ANOVA ($F(1,10) = 0.64$, $p = 0.44$). When the SITE specimens were restrained, the permeability is 109% higher than LAB, with a statistically significant difference between the two groups according to a one-way ANOVA ($F(1,10) = 13.2$, $p = 0.005$). The restrained samples of SITE have a 70% higher permeability that the unrestrained samples from SITE, with a statistically significant difference between the two groups according to a one-way ANOVA ($F(1,6) = 6.4$, $p = 0.044$). Water curing (W) decreases the permeability, as expected. The restrained SITE samples show a higher permeability than the unrestrained SITE samples, but there is no statistically significant difference between the two groups according to a one-way ANOVA ($F(1,6) = 0.32$, $p = 0.6$).

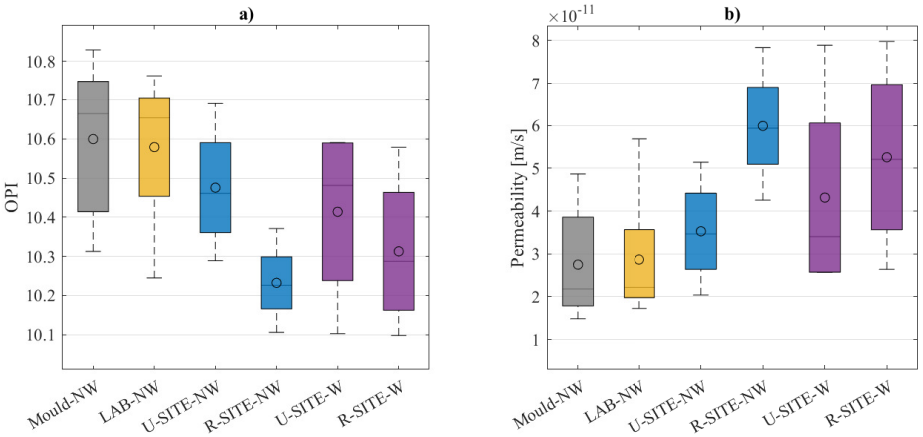

Figure 8.12: A box and whisker plot of the a) Oxygen Permeability Index (OPI) and b) D'Arcy permeability coefficient for samples from different drying condition and restraint combinations. The mean is indicated with a circle.

To put this result in perspective, a reduction in permeability of about 3×10^{-11} m/s is reported when increasing the w/c from 0.4 to 0.5 in a plain OPC mortar [229]. The mould-cast permeability results shown here are marginally higher than those shown by Githachuri and Alexander [85] but this is due to the shorter curing period, absence of water during curing and vibration.

8.3.3.2 Chloride conductivity and porosity

To indicate the resistance to chloride ion penetration, the Chloride Conductivity Index (CCI) results are presented in Fig. 8.13 a. The mould-cast samples show a 20% lower CCI than the printed samples with a statistically significant difference between the two groups according to a one-way ANOVA ($F(1,14) = 4.9$, $p = 0.044$). The unrestrained SITE samples have a 25% lower CCI than the LAB samples. The restrained SITE samples have a 17% higher CCI than the unrestrained SITE samples, and the difference between the two groups is statistically significant according to a one-way ANOVA ($F(1,6) = 13.2$, $p = 0.011$). For the water cured samples, the CCI of the restrained SITE samples is 14% higher than the unrestrained SITE samples, but the difference between the two groups is not statistically significant according to a one-way ANOVA ($F(1,6) = 2.7$, $p = 0.15$).

The chloride resistant shown here is high compared to more conventional mortars due to the high quantities of cement and supplementary cementitious materials (SCMs), such as fly ash and silica fume, found in 3DPC. Githachuri and Alexander [85] explains that the finer particle size of SCMs improves pore filling ability to reduce the penetration of chloride ions.

The porosity results are presented in Fig. 8.13 b. The mould-cast samples have

a 14% lower porosity than the printed LAB samples with a statistically significant difference between the two groups according to a one-way ANOVA ($F(1,28) = 13.9$, $p = 0.0009$). Kruger et al. [80] also showed a higher porosity in printed samples, compared to mould-cast. The samples exposed to SITE have a lower porosity than LAB and the difference is statistically significant according to a one-way ANOVA ($F(1,21) = 11.06$, $p = 0.003$). The porosity may be related to the magnitude of early age shrinkage, with a higher magnitude reducing the porosity. Curing the samples in water reduced the porosity significantly, as expected. These results correspond well with the CCI results.

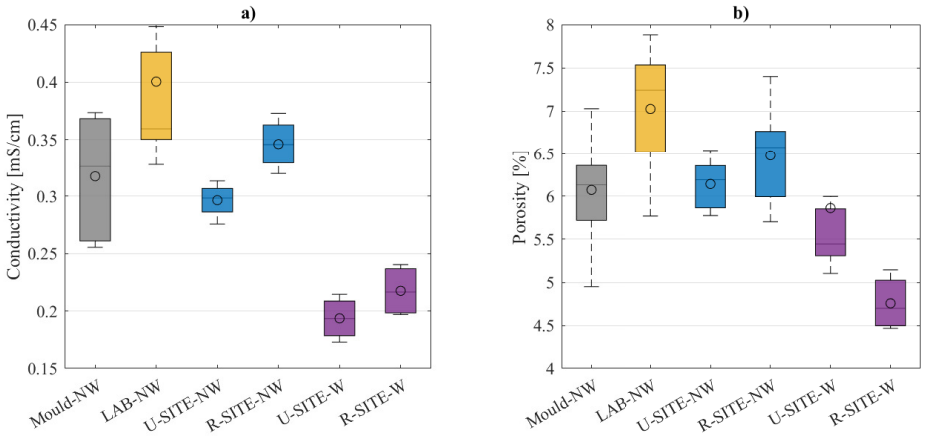

Figure 8.13: A box and whisker plot of the a) Chloride Conductivity Index (CCI) and b) the porosity for samples from different drying condition and restraint combinations. The mean is indicated with a circle.

8.4 Discussion

The discontinuities noticed on the interlayer plane, so-called interlayer slip, can be attributed to the inhomogeneous particle size distribution within the filament due to the pumping process. During pumping, the shear stress occurring near the pipe wall forces larger particles to the centre of the pipe, a phenomenon known as flow-induced particle migration [32]. This migration leaves behind the rich paste and results in an inhomogeneous particle size distribution within the filament [79]. The extent of particle interlocking near the interlayer is therefore different from that of the bulk material. The intralayer is also more exposed to the evaporation load due to the undulations of the concrete face. The higher evaporation at the intralayer and reduced interlocking at the interlayer result in interlayer slip.

The introduction of the two restraining rods was not as successful at concentrating the differential shrinkage on a single interlayer, as the authors expected. The plastic concrete responds to the induced rigidity by reducing the magnitude of deformation and distributing it evenly to the bottom layer. Nonetheless, discontinuities did occur in the middle of the specimen due to the restraints. In the unrestrained specimen, the magnitude of these discontinuities was twice that of the restrained specimen, and also more frequent. This can be attributed to the larger gradient of horizontal shrinkage, which caused high shear strain concentrations on the interlayer.

Restraining the early age shrinkage cause a reduction in the 28-day interlayer bond strength of the printed samples. It was initially hypothesised that the differential shrinkage damages the early age CSH bridges on the interlayer to impair the bond strength. However, this could not be confirmed as the sole mechanism since the magnitude of slip was larger in the unrestrained specimen. Microcracks, also caused by restrained shrinkage, is a potential cause. A statistically significant result could only be produced when the effects of the empty pores, dehydration, microcracks and differential shrinkage were combined (when comparing samples of LAB to restrained SITE). External restraint also increases the variability of the interlayer bond strength, especially, at the weaker end of the distribution.

The printing process smears voids into more ellipsoidal shapes, increasing the interconnectivity in the printing direction, as explained by Kruger et al. [80]. In this study, the printed samples' permeability was not significantly higher than the mould-cast. This is because the direction of oxygen penetration is transverse to the printing direction. Increasing the pore water evaporation increased the permeability of the 3DPC, as expected. However, the effect of restraining the shrinkage was much more significant than the effect of pore water evaporation. This can be due to the formation of microcracks, which increases in severity because of the external restraint.

Printing increases the rate of chloride ion penetration. Restraining the early age shrinkage also increased the penetration rate. However, the chloride ion penetration resistance is high compared to conventional concrete, due to the high quantities of supplementary cementitious materials [85]. Ultimately, water curing promotes further pozzolanic and hydration reaction or "self-healing" to reduce the difference between the restrained and unrestrained samples and decrease permeability and chloride ion penetration.

8.5 Conclusion

This study set out to show the long-term consequences of restrained early age shrinkage on 3D printed concrete. The results were not what the authors expected

since interlayer slip not only occurred in the restrained specimens but also in the unrestrained specimens. Nonetheless, the study presents the following noteworthy conclusions:

- Shear strain concentrations form on the interlayer due to the lack of particle interlocking at the interlayer region and higher evaporation from the intralayer, products of pumping and undulations in the evaporation face. These shear strain concentrations can cause interlayer slip.
- Interlayer slip occurs gradually and is a self-induced phenomenon which is more dependent on the magnitude and gradient of the shrinkage-to-height curve than on the external restraint. The phenomenon is common near the unconnected ends of printed specimens and is expected to prevail near geometrical changes of continuously printed elements.
- Restraining the early age shrinkage reduced the interlayer bond strength, and increased the permeability and chloride ion penetration. These adverse consequences were not attributed to interlayer slip alone since microcracks could have a similar effect.
- In terms of durability, 3DPC with a short pass time performed well due to the large quantities of cement and supplementary cementitious material in the mix.

Chapter 9

Modelling the interlayer bond strength of 3D printed concrete with surface moisture

Abstract

Providing additional water to the hydrating cementitious particles is essential to achieve the optimal mechanical performance of the low w/b concrete mixes preferred for 3D printing. This study incorporates superabsorbent polymers (SAP) and additional water in 3D printed concrete (3DPC) to promote the hydration process through delayed internal water release. The study shows that a retentive SAP modifies the rheological development by absorbing the pore fluid for a short period after printing. The absorption-induced stiffening increases the thixotropy and buildability by 49% and 25%, respectively. A retentive SAP increases the flexural strength and interlayer adhesion by 19% and 10%, respectively. This is due to the internal water release that promotes hydration. Evaporation of the interlayer moisture during the pass time has the opposite effect—evaporation reduces the interlayer adhesion. Based on this assumption, an analytical model is proposed. The model accounts for the pass time, bleeding, and the environmental evaporation rate to estimate the surface moisture and predict the lack of interlayer adhesion. In this study, the model accurately (RMSE=2.5%) predicted an interlayer adhesion reduction from 30% to 50%. The interlayer adhesion results of other studies could also be predicted.

Article information

Chapter 9 has been submitted as a journal article and can be cited as: **G.M. Moelich**, P.J. Kruger, R. Combrinck, Modelling the interlayer bond strength of 3D printed concrete with surface moisture, Cement and Concrete Research, vol. 150, December 2021. Online

Contribution declaration

With regard to this chapter, the nature and extent of the contributions of the candidate and the co-authors were as follow:

Name	Nature of contribution	Extent
G.M. Moelich (candidate)	Conceptualisation, Methodology, Validation, Formal analysis, Writing - original draft, Visualization, Investigation	90%
Dr P.J. Kruger (pjkruger@sun.ac.za)	Conceptualisation, Validation, Writing - review & editing	5%
Dr R. Combrinck (rcom@sun.ac.za)	Conceptualisation, Validation, Writing - review & editing, Supervision	5%

The undersigned hereby confirm that:

- The declaration above accurately reflects the nature and extent of the contributions of the candidate and the co-authors to this chapter.
- No other authors contributed to this chapter besides those specified above.
- Potential conflicts of interest have been revealed to all interested parties and that the necessary arrangements have been made to use the material in this chapter of the dissertation.

Signature of authors	Institutional affiliation	Date
	Department of Civil Engineering, Stellenbosch University	09/06/2021
	Department of Civil Engineering, Stellenbosch University	09/06/2021
	Department of Civil Engineering, Stellenbosch University	09/06/2021

9.1 Introduction

In the past 10 years, 3D concrete printing has received increasing attention in academia and the construction industry. The technology promises more design freedom, less waste material, faster construction time, reduced cost and, most importantly, increased workplace safety [156, 16].

High-performance concrete mixes (HPCM) with water to binder ratios between 0.21 and 0.41 are typically preferred for printing [16]. Low w/b mixes require additional curing water to complete the hydration process and achieve optimal long-term durability and mechanical performance [88, 218]. However, conventional techniques such as ponding and misting are ill-suited for larger 3D printed concrete (3DPC) structures. Superabsorbent polymers (SAP) or pre-wetted light-weight aggregates provide a passive solution that can automate water supply. Typically, unsaturated SAP and additional water are added during the mixing phase. Ideally, the SAP absorbs the additional water to gradually release it into the bulk of the cementitious matrix when the hydration process requires it.

SAPs are characterised by their water releasing kinetics as retentive or self-releasing. The retentive type releases water as a response to an external trigger (capillary suction or internal humidity drop), while the self-releasing type releases water inherently with time [197, 192].

Jensen and Hansen [218] first used SAPs to prevent autogenous shrinkage in concrete mixes with low water to binder ratios. In the past 20 years, SAP's applications have expanded to include plastic shrinkage cracking mitigation [101, 102, 188], improving freeze/thaw resistance [194] and promoting self-healing [195]. Studies on mechanical performance come to different conclusions, with testing age, amount of additional water, mix and constituents, SAP type, dosage and size as well as curing conditions influencing the outcome. A reduction in compressive strength is typically noted in literature, and attributed to the empty voids left by the dehydrated SAP (increased macropores) or to the premature release of water by the SAP resulting in a higher w/c ratio [240, 169, 241]. Some studies show an increase in compressive strength, and attribute the result to a higher degree of hydration [242].

SAPs can also have a significant effect on the rheological properties of concrete. Mechtcherine et al. [192] attributed this change in rheology to the SAP's water absorption and releasing kinetics in 0.3-0.5 w/b mortars. The retentive SAP showed a steadily and more pronounced increase in yield stress and plastic viscosity with time compared to the reference. Others showed similar results and confirmed the explanation [243–245, 242]. Schröfl et al. [197] added that the retentive SAP releases water as the cementitious particles start to hydrate, after the dormant period. Recently, Ma et al. [246] added that the increase in static yield stress is also linked to the structural evolution of the SAP itself and/or the colloidal interaction

between the SAP and cementitious particles. However, adding saturated SAPs did not show the same increase in static yield stress, contradicting the previous hypothesis. The study also showed that excessive mixing induces a minor amount of water release.

Only a few studies have used SAPs as an internal curing agent for low w/b 3D printed concrete mixes. Schröfl et al. [238] used neutron radiography to study the capillary water intake of 3DPC specimens with different pass times (deposition intervals). The water intake clearly preferred the interlayers with longer pass times with SAPs increasing the capillary intake. Van Der Putten et al. [236] followed to show no preferential water intake for short pass times but confirmed that SAPs increase the capillary water intake by increasing the porosity. In terms of mechanical performance, Van Der Putten et al. [196] showed that SAP increases the interlayer bond strength and attributed the result to less plastic and autogenous shrinkage as well as a higher surface moisture. On the contrary, the same authors, in a different study [180], reported that SAP decrease the interlayer bond strength even with a surface moisture increase. Ma et al. [247] successfully demonstrated that cellulose fibres could improve the bond strength of 3DPC through internal curing by hydrating the anhydrous cement particles near the interlayer. In terms of early age shrinkage, Van Der Putten et al. [180] used SAPs to mitigate autogenous shrinkage in 3DPC. The influence of early age shrinkage on the interlayer bond strength of 3DPC has not been confirmed experimentally, with Moelich et al. [132] reporting inconclusive results.

In this study, the terms flexural strength and interlayer adhesion are used distinctively. The former refers to absolute strength and the latter to the bond between two printed layers (expressed in term of the flexural strength of the mould-cast specimens), as suggested by Kruger and Van Zijl [79].

Due to a lack of literature and the notable advantages of a higher degree of hydration, this study investigates the effect of SAP on the rheological and mechanical properties of high-performance 3DPC further. The lack of interlayer adhesion, also called the "Achilles heel of 3D printed concrete structures" [76], is discussed extensively. It is hypothesised that SAPs can improve the adhesion between layers by 1) hydrating the anhydrous cementitious particles in the interlayer region and/or 2) providing additional surface moisture, on the interlayer, after extrusion. The effect of the latter is investigated further with a novel analytical model, developed in this research. The model stems from the current theoretical understanding of the interlayer adhesion, with surface moisture being one of the main parameters. Experiments were also conducted to validate the model.

9.2 Modelling the reduction in interlayer adhesion

The literature identifies the main mechanisms responsible for the lack of interlayer adhesion in 3DPC as A) a lack of interlayer surface moisture [73–75], B) air entrapment [76, 77], C) adverse thixotropy [39, 79] and D) a lack of surface roughness [74]. Of these mechanisms, the former (A) has been identified as the dominant mechanism for the lack of interlayer adhesion and is the focus of this study [76, 73, 75, 79, 78].

At an early age, an increased time between layer deposition (pass time) is not the root cause of the lack of interlayer adhesion. It is the evaporation and bleeding rates which controls the surface moisture during the pass time which leads to the loss of interlayer adhesion. This is the foundation of the proposed model.

At extrusion, the aggregates and cementitious particles are interconnected with pore fluid. In this state, the filament's surface has an initial amount of moisture (Phase 1 in Fig. 9.1) [58]. With time, the concrete settles under gravitation forces to increase the thickness of the surface moisture film, a process known as bleeding (Phase 2 in Fig. 9.1) [88]. Surface moisture is lost to the environment, through evaporation, due to the vapour pressure difference, a phenomenon described by Dalton's Law [49]. This evaporation gradually reduces the water film with time until the film reaches the solid particles (Phase 3 in Fig. 9.1). Further evaporation cause water menisci to form between the solid particles. The radii of these water menisci become smaller as more pore fluid is lost to the environment. At some stage, the radii becomes too small to bridge the gap between the solid particles, causing air to penetrate the pore system locally (Phase 4 in Fig. 9.1) [58, 75]. If a subsequent filament (overlay) is placed on this surface (substrate), any air inside the pore system is entrapped. The drier substrate filament absorbs the surface moisture of the overlayer filament, and the entrapped air rises into the overlay filament due to its lower density [79, 248]. The lack of moisture explains the higher amount of anhydrous cementitious particles near the bottom of the overlayer filament for longer pass times [74, 248]. Furthermore, the entrapped air explains the higher amount of larger pores noticed in the bottom of the overlayer filament for longer pass times [74, 77, 80]. Ultimately, the entrapped air and anhydrous cementitious particles explain the decrease in interlayer adhesion that occurs with longer pass times [79].

Sanjayan et al. [73] showed an increase in interlayer bond adhesion when increasing the pass time from 20 to 30 min. This was attributed to an increase in surface moisture due to bleeding. Keita et al. [75] and Roussel [39] noted that 3DCP specimens, protected from drying, only showed a noteworthy decrease in the interlayer bond when the pass time was increased beyond the final setting

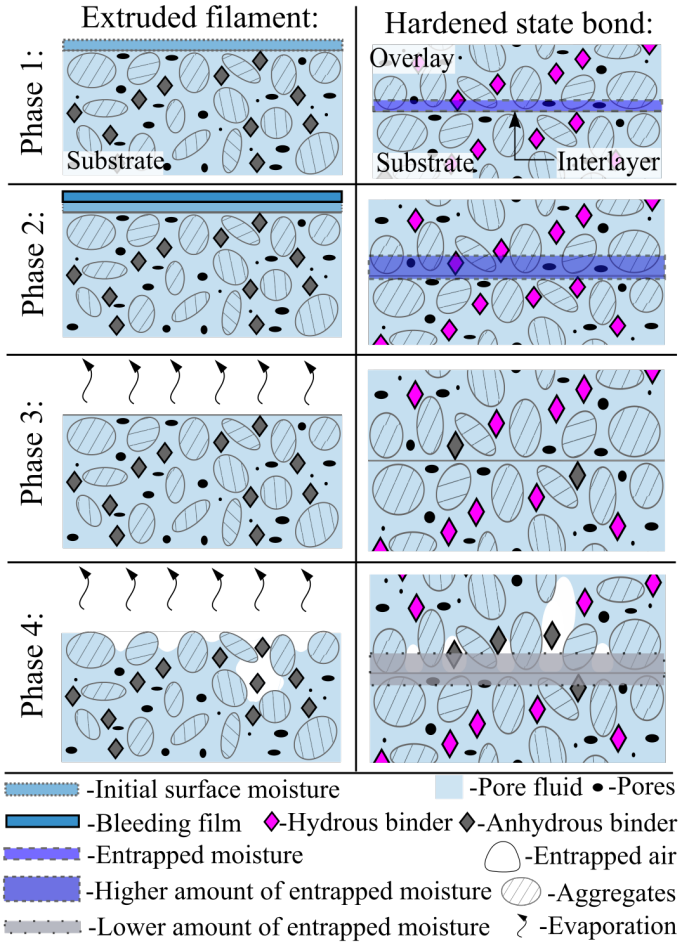

Figure 9.1: The changes in surface moisture of 3DPC. Left: The phases of surface moisture development of the bottom filament (substrate) after extrusion. Right: The hardened state bonded filaments and the consequence of surface moisture loss in the particular phase. Recreated from Kruger and Van Zijl [79] and Slowik et al. [58].

time. The specimens exposed to drying (higher evaporation rate) showed a significant decrease in the bond strength when increasing the pass time from 7 to 60 min. This result and other literature suggest that mechanisms other than the amount of available surface moisture can have a significant effect when the pass time exceeds the initial setting time [76, 248, 235]. Furthermore, in proximity of the initial setting time the pore water evaporation rate becomes supply controlled and can differ significantly from the environment's evaporation load, but exactly when this occurs depends on the evaporation rate and w/c ratio [51, 54, 249, 75].

Many parameters, including the extrusion and printing methods, the lubrication layer, whether shear or plug flow is achieved, the mix proportions and the printing speed, affect the surface moisture at extrusion [73]. However, from once

the filament is placed until the initial setting time, the change in surface moisture mainly depends on the bleeding and evaporation processes [88, 47]. Between placing filaments (pass time), bleeding and evaporation can change the amount of surface moisture on the substrate filament. When the overlayer filament is placed, the system closes. This understanding can be expressed mathematically as:

$$IA \propto SM_f = SM_i + B_{pt} - pt(ER_{pt}) \tag{9.1}$$

where IA is the lack of interlayer adhesion, SM_f $[kg/m^2]$ is the surface moisture at placement of the overlayer, SM_i $[kg/m^2]$ is the initial surface moisture of the substrate, pt $[h]$ is the pass time, B_{pt} $[kg/m^2]$ is the amount of bleeding at the pass time (extrusion of overlay) and ER_{pt} $[kg/m^2/h]$ is the rate of moisture evaporation. This analytical model is only valid if the following two a priori conditions are met:

1. The pass time is smaller than the initial setting time. Other processes, such as hydration and consolidation, have a more significant effect on the rate of pore water evaporation after the initial setting time.

2. The amount of moisture loss ($pt \times ER_{pt}$) is smaller than the amount of available moisture in and on the filament. As long as there is moisture available on the surface the rate of evaporation is controlled by the environment's evaporation load, and the model can estimate the surface moisture. Estimating outside this limit can result in errors.

The B_{pt}, ER_{pt} and SM_i should be determined experimentally. However, for the first few hours after printing, ER_{pt} is mainly dependent on the environmental conditions, namely: wind speed, relative humidity, air temperature, concrete temperature and solar radiation [51, 54]. For low solar radiation (shaded condition), the Uno [50] and Al-Fadhala and Hover [51] models can be used to estimate the evaporation load from the environmental conditions. When casting in direct sunlight (high solar radiation) the models by Penman [137] and Jensen-Haise [141] are recommended [212]. Models by Al-Fadhala and Hover [51] and Azenha et al. [249] can be used to convert the environment's evaporation load to the actual amount of moisture loss from the concrete. However, this is not necessary for pass times less than about an hour or two, since for the first few hours the actual rate of moisture loss from the concrete is equal to the environment's evaporation rate.

The relationship ($\propto$ in Eq. 9.1) between SM_f and IA is described in three stages, as presented in Fig. 9.2. Stage I represents the lack of interlayer adhesion if the surface moisture remains unchanged, e.g. a low evaporation rate and short pass time. In Stage I the initial air entrapment, thixotropic and surface roughness are dominant. Stage II represents the case where evaporation and bleeding control the surface moisture, e.g. longer pass times and moderate to high evaporation

rates. During Stage III, the moisture from within the pore system evaporates and air penetrates the pore network to decrease the interlayer adhesion even further. Whether or not the gradient decreases from Stage II to III remains a matter for future research. This research focusses on Stage I and II.

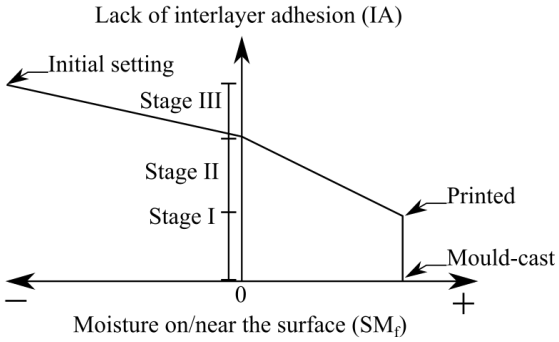

Figure 9.2: Lack of interlayer adhesion against the surface moisture of the substrate filament.

The authors do not deny that the thixotropy processes can have an effect on the interlayer adhesion of 3DPC. However, it is postulated that the loss of surface moisture governs the interlayer adhesion at moderate to high evaporation rates or longer pass times.

9.3 Experiments

Two mixes containing a self-releasing or retentive type SAP were designed for printing. The SAP mixes and a reference 3DPC mix were printed with a gantry-type 3D concrete printer. The interlayer evaporation was controlled during printing with two climatic conditions. The development of the rheological properties as well as the amount of surface moisture on the interlayer was evaluated immediately after printing. Specimens were cut from the printed element, and the flexural strength was evaluated at an age of 56 days with a four-point bending test. The compressive strength of the printed specimens was also evaluated at an age of 56 days. Additional experiments were conducted to validate the proposed model, and is discussed in Section 9.5.1.

9.3.1 Materials and mixes

As binders, Portland cement (CEM II 52.5N) with between 6 and 20% limestone extender, fly ash (FA, DuraPozz Class F) and silica fume (SF, SiliconSmelters: Microfume) were selected. The main chemical components of these binders are

presented in Table 9.1. A natural, continuously graded quarry sand, with a Fineness Modulus of 2.19, was used as aggregate. A modified polycarboxylate polymer superplasticizer (SP, Chryso: Fluid Premia 310) was selected.

The standard mix proportions of the Stellenbosch University 3DPC research group was used, as presented in Table 9.2 [38]. The superplasticizer dosage of the reference mix (REF) was determined using a mini-slump-flow test [208]. A dosage of 0.6% produced a flow diameter of 156 mm, which is in the 150-160 mm range recommended by Cho et al. [26]. Mixes in this range have shown acceptable pumpability and buildability properties in past studies at Stellenbosch University [209].

Table 9.1: Chemical composition, as a percentage of weight, for the Portland cement (CEM II), fly ash (FA) and silica fume (SF) used in this study as determined with a major element XRF analysis.

	CEM II	FA	SF
CaO	62.9	4.3	0.7
SiO_2	18.6	54.8	84.4
Al_2O_3	3.5	33.1	0.6
Fe_2O_3	2.6	3.2	3.3
K_2O	0.5	0.7	3.5

Table 9.2: Mix proportions of the reference (REF) and SAP mixes (SR35 and RET100).

Base mix proportions:	REF	SR35	RET100
Cement $[kg/m^3]$	568	568	568
Fly ash $[kg/m^3]$	162	162	162
Silica fume $[kg/m^3]$	81	81	81
Aggregate $[kg/m^3]$	1175	1175	1175
Water $[kg/m^3]$	256	256	256
Superplasticizer $[pmob]$	0.6	0.6	0.6
Added additionally ("on top") to base mix:			
SAP SR $[pmob]$	-	0.3	-
SAP RET $[pmob]$	-	-	0.3
Additional water $[kg/m^3]$	-	17.88	45

pmob - percentage mass of binder

Two types of SAPs were obtained from SNF Floerger France and used as delivered. A standardised "tea-bag" test was performed as a pre-test to determine the sorptivity of the received SAPs, as recommended by the RILEM TC 260-RSC [211, 250]. The test was conducted twice with the means presented in Fig. 9.3. According to their sorptivity kinetics, the SAPs were classified as either self-releasing (SR) or retentive (RET).

The SR type releases water intrinsically and is a covalently cross-linked polyacrylate similar to the SAP 1 of [188] and [197], SAP 2 in [211] and SAP B of [192]. The RET type releases water in response to an external trigger and is a covalently cross-linked poly (acrylate-co-acrylamide) with a lower cross-linking density than SR. RET was similar to SAP 2 of [188] and [197], SAP 1 in [211] and SAP DN of [192]. Literature can be consulted for SEM images and the particle size distribution of the SAPs used in this study, albeit from a different batch [211]. A SAP dosage of 0.3% was selected based on literature [192, 101, 188, 180].

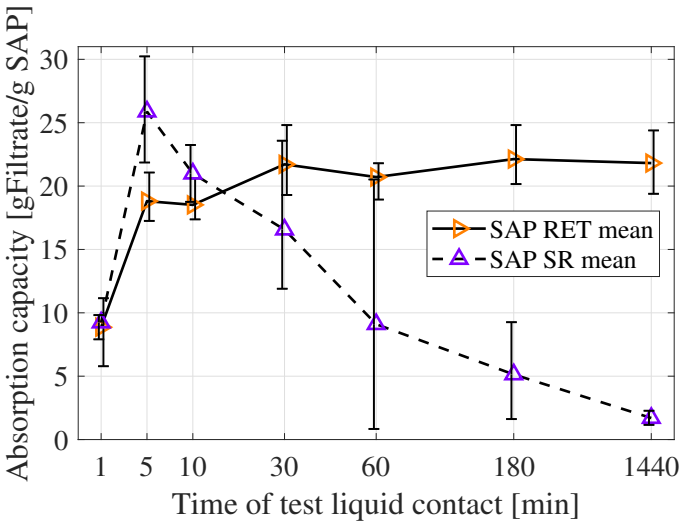

Figure 9.3: The cement filtrate absorption of the self-releasing (SR) and retentive (RET) type superabsorbent polymers obtained with the tea-bag test. The error bars indicate the lower and upper quantiles.

The amount of additional water (AW) was calculated as $AW = x.ASap.S$ where x [%] is the adjustment for the mini-slump-flow test result, $ASap$ is the amount of SAP [gSAP] and S is the SAP's sorptivity. The 10 min S values were used since it took approximately 10 min from SAP addition to extrusion. S values of 21 and 18.5 g/gSAP was therefore selected for SR and RET, respectively, from Fig. 9.3.

The amount of additional water was adjusted (x) to achieve the desired mini-slump-flow test result immediately after mixing. The aim was to produce a flow

diameter similar to the 156 mm of REF, as recommended by Cho et al. [26]. For the SR mix, with $x = 35\%$, a flow diameter of 157 mm was obtained. For the RET mix, with $x = 100\%$, a flow diameter of 154 mm was obtained. The SAP mix containing SR and 35% additional water ($x = 35\%$) is denoted as SR35, while the RET with 100% additional water ($x = 100\%$) is denoted as RET100.

9.3.2 Mixing and printing

The materials were batch-mixed in a two-blade pan mixer at a constant mixing velocity. The dry materials were mixed for 1 min before the mixing water, and additional water (for the SAPs) were added and mixed in for another 1 min. Thereafter, a superplasticizer was added and mixed in for 1 min. Additional interim hand mixing was conducted to ensure uniformity; whereafter, mechanical mixing continued for 1 min. The specific SAP was added and mixed in for 2 min. It took approximation 10 min to transport the mix to the hopper and prime the pump and hose, after which printing commenced. During this time, the SAPs could absorb more mixing water.

A 1 m^3 gantry-type 3D concrete printer with a 25 mm (diameter) circular nozzle was used to extrude $40 \pm 3 \times 10 \pm 1$ mm (width×height) filaments without any intervention. The print speed of 75 mm/s resulted in a 50 s pass time that was kept constant by using the same print path. Since the rheological properties varied depending on the mix, the pump speed had to be slightly adjusted to obtain the 40 mm filament width. The 200 mm high printed element can be seen in Fig. 9.4 a.

9.3.3 Evaporation and curing

The evaporation of the interlayer moisture was controlled by producing airflow over the interlayer during the 50 s pass time. Two drying conditions were used, W (wind) or N (no wind). For W, the airflow was channelled over the interlayer at a speed of 4 ± 0.3 m/s (measured on the interlayer of each sample) while printing. For both N and W; the ambient temperature was $23 \pm 0.3°C$, the relative humidity was $52 \pm 3\%$ and the concrete temperature, at placement, was $22°C$. The pore fluid evaporation rate was determined to be 0.07 $kg/m^2/h$ for N and 0.32 $kg/m^2/h$ for W. These values were determined by continuously monitoring the mass of a printed specimen, exposed to different drying conditions, for 90 min.

With a pass time of 50 s, the amount of evaporated water is 0.00097 kg/m^2 for N and 0.00444 kg/m^2 for W. This information is crucial for the comparability of studies on the effect of surface moisture loss on interlayer adhesion.

When the print was complete, the airflow was deactivated. 40 min after completion, the 40×40 mm (W×H) test specimens were cut, with a steel putty knife,

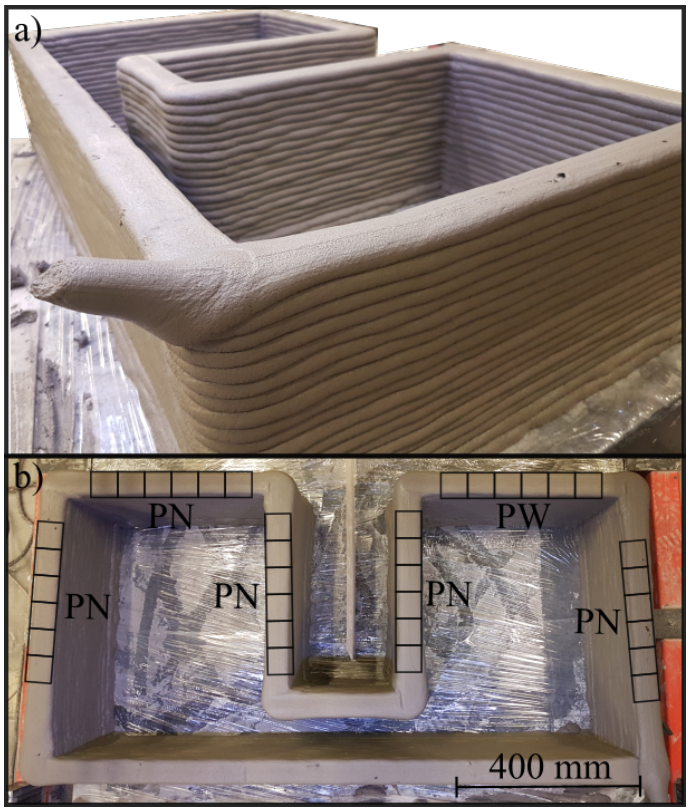

Figure 9.4: a) Perspective view of the element printed (image with REF). b) Plan view of the printed element and layout of the test specimens. The printed specimens exposed to the higher airflow speed are denoted as PW, while PN is used for the lower airflow speed.

from the larger element at the locations seen in Fig 9.4 b. Kruger and Van Zijl [79] recommended early age cutting above hardened state saw-cutting, arguing that the latter can possibly damage the interlayer and influence the results. After cutting, the specimens were cured at a constant ambient temperature of $23 \pm 0.3°C$ and relative humidity of $52 \pm 3\%$. To ensure uniform drying, the specimens were cured in an upright position, evenly spaced from one another with no protection against pore water evaporation. The cutting and handling processes were performed consistently for the different groups.

9.3.4 Rheology

A rotational type ICAR rheometer was used to determine the static and dynamic yield stresses. The mix was pre-sheared at a shear rate of 1 s^{-1} (0.2 revolutions per second) for 60 s, and time-zero was noted. The sample was allowed to rest for a defined interval before it was sheared again at a shear rate of 1 s^{-1} (0.2 revolutions

per second) for 60 s. These test parameters were based on the screw speed, the concrete pump's geometry, and the extrusion rate used in this study. The static value was taken as the peak yield stress while the dynamic value was taken as the minimum post-peak yield stress. Resting intervals of 30, 60, 90, 120 s and 15, 30 and 45 min were used to determine the re-flocculation (R_{thix}) and structuration rates (A_{thix}) in a single-batch approach [38, 37]. Kruger et al. [170] used similar rheological protocols. The thixotropy (λ_t) was defined as:

$$\lambda_t = \frac{\tau_0 - \tau_e}{\tau_e} \tag{9.2}$$

with τ_0 and τ_e the initial and equilibrium yield stresses at a specific time (t) [251, 252]. The rheometer test was conducted on two 23 ℓ samples of each mix and the mean is presented.

9.3.5 Buildability

The height of plastic collapse due to plastic yielding of the critical bottom layer was estimated with the buildability model proposed by Kruger et al. [217]. The model is only valid for thixotropic 3DPC mixes. Jayathilakage et al. [34] showed that Kruger's model estimates the height of plastic failure within 7% of experimental results while Kruger et al. [217] reported an error less than 10%. The estimations were based on a circular hollow column element with a 250 mm diameter at print speeds of 40 and 100 mm/s. The mix's initial static and dynamic yield stresses significantly influence the layer of failure. Therefore, the dynamic yield stress was adjusted to that of REF while the difference between the static and dynamic yield stress of each mix was maintained. The R_{thix} and A_{thix} were also maintained. In this way, the buildability results of the different mixes can be compared conservatively.

9.3.6 Initial surface moisture

The amount of initial surface moisture was determined by placing sheets of blotting paper on a printed layer immediately after extrusion, similar to Sanjayan et al. [73]. Three 60×100 mm sheets were spaced evenly and left for 1 minute to absorb the surface moisture. The test was repeated three times, and the mean was calculated. The CoV of the test was 12.4%.

9.3.7 Available surface moisture

To determine the amount of available surface moisture on the interlayer, an empty tea-bag was filled with approximately 0.3 g of the retentive type SAP [191]. Imme-

diately after printing, four tea-bags were spaced evenly on the printed element's top layer. The SAP was allowed to absorb the available water for 1 min. The unsaturated and saturated SAP mass and the tea-bag mass were recorded to calculate the amount of absorbed water. The CoV of the test was 10%. Meyer et al. [191] showed that placing SAP's on the surface can extract pore water, to mimic evaporation. This technique is therefore suited for estimating the amount of water available for evaporation.

9.3.8 Mechanical testing

Four-point bending tests were conducted at age of 56 days with a loading rate of 50 N/s [239, 253]. The arrangement is presented in Fig. 9.5 a. Prisms of 160×40×40 mm (L×W×H) were mould-cast from each mix, vibrated for 2 min and demoulded 24 h after casting. The printed specimens were longer, but this did not affect the result (200×40×40 mm, L×W×H). For the printed specimens, the filament layers were aligned transversely (O-III orientation), parallel to the applied load. In this way, normal tensile stress is induced in the bottom part of the specimen's interlayer. Literature recommends testing the O-III orientation in bending to quantify the interlayer bond's strength [78, 79]. The 18th interlayer was aligned with the left support for each test. The result is further referred to as the flexural strength (FS).

The lack of interlayer adhesion (IA) is quantified as a reduction in flexural strength from the mould-cast specimen, calculated as [79]:

$$IA = 100\left(1 - \frac{FS}{FS_M}\right) \tag{9.3}$$

with FS the flexural strength (O-III) of the 3DPC specimen and FS_M the mean mould-cast flexural strength. In this way, the flexural strength of the mix is ignored. An IA value of 0% is the casting equivalent bond strength while higher values indicate a weaker interlayer adhesion.

The prism halves were tested in compression with a loading rate of 2400 N/s [239, 253]. 40 × 40 mm steel plates were used to restrict the load area as seen in Fig. 9.5 b. The specimens were placed so that the interlayers align with the plate edges. The reduction in compressive strength ($CS_R(\%)$) due to printing was calculated as:

$$CS_R = 100\left(1 - \frac{CS}{CS_M}\right) \tag{9.4}$$

with CS the compressive strength of the 3DPC specimen and CS_M the mean mould-cast compressive strength.

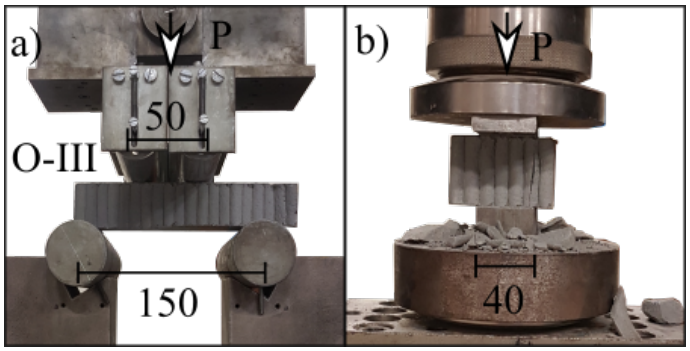

Figure 9.5: a) The four-point bending test of a printed specimen. b) The compression test of a printed specimen. Units in mm.

9.3.9 Experimental program

Three 32 ℓ prints were conducted, one for each mix. In total, 98 bending tests and 70 compression tests were conducted. For each mix, six mould-cast (MN), more than 18 PN (printed, no wind) and six PW (printed, wind) specimens were tested in bending. Similarly, six mould-cast (MN), more than 12 PN (printed, no wind) and six PW (printed, wind) specimens were tested in compression for each mix. The sample size used was deemed sufficient for this study. The nomenclature can be summarised as follows (e.g. MN FS the flexural strength of the no wind mould-cast specimens):

- **M** or **P** = **M**ould-cast or **P**rinted specimen
- **N** or **W** = exposed to **N**o wind or **W**ind
- **FS** or **CS** = **F**lexural or **C**ompressive **S**trength

9.4 Results and discussion

9.4.1 Rheological properties

The two SAPs (SR35 and RET100) have a distinct effect on the development of the rheological properties, as seen in Fig. 9.6.

The REF mix shows a moderate re-flocculation (R_{thix}) and structuration (A_{thix}) rate of 2.9 and 0.37 Pa/s, respectively. For the shorter resting time intervals ($\leq$120 s), the static yield stress increases rapidly due to re-flocculation. Thereafter, chemical structuration controls the rate of static yield stress increase [38]. Although higher rates are typically preferred for printing, the REF mix was deemed suitable for the purpose of this study. The dynamic yield stresses of REF remains

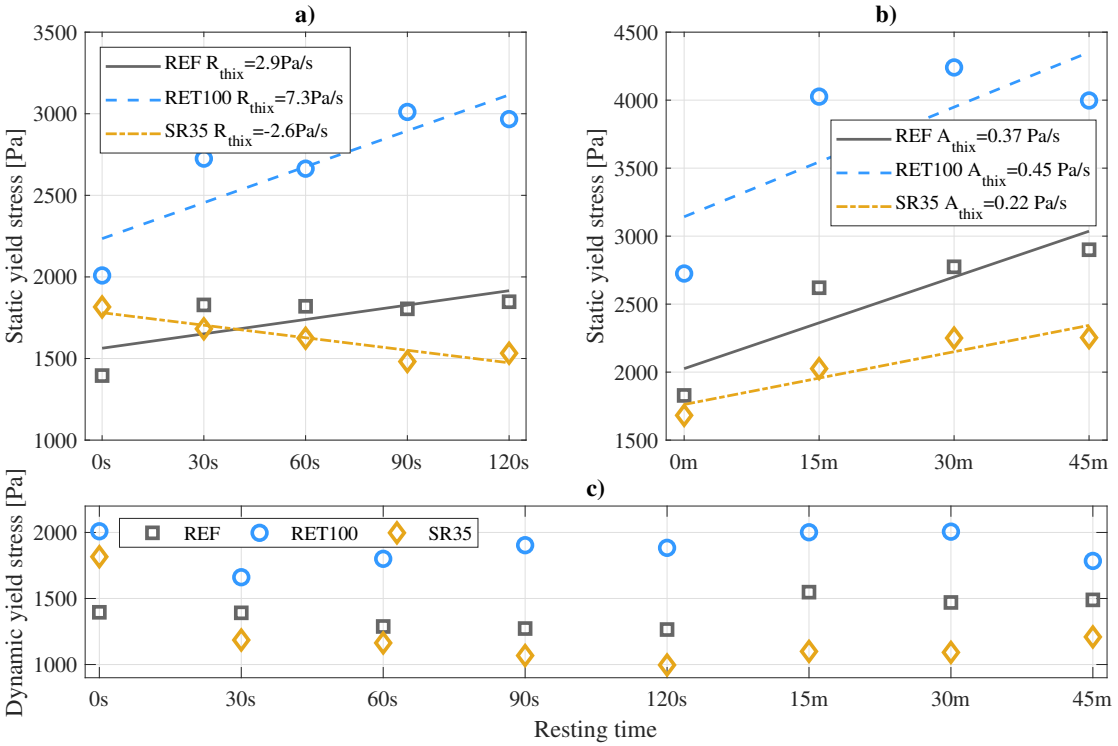

Figure 9.6: The static and dynamic yield stresses at different resting times for each of the three mixes. a) Resting times shorter than 120 s with the gradient of the trend line as R_{thix}. b) Resting times longer than 15 min the gradient of the trend line as A_{thix}. c) Dynamic yield stress development.

fairly constant for the shorter resting times, decreasing linearly from 1395 to 1265 Pa during this period.

The SR35 mix shows a decrease in the static yield stress for the short resting times and a negative R_{thix} value of -2.6 Pa/s. A 53% decrease in the dynamic yield stress from the first (0 s) to the second test (30 s) is also noticed. The behaviour can be attributed to the intrinsic releasing kinetics of the SR SAP. Fig. 9.3 shows that the self-releasing SAP starts releasing water intrinsically, 5 min after initial saturation, and confirms the hypothesis. This increases the water/particle ratio to reduce the static and dynamic yield stresses as the resting time interval increases. It is also possible that the test's shearing action prompts water release or that the saturated SAP acts as a ball-bearing to contribute to this behaviour. Perhaps the latter mechanism's effect is trivial since the static yield stress continues to decrease for each test.

Fig. 9.3 shows that the SR SAP releases minimal water for the longer rest intervals. The precipitation of ettringite, the formation of calcium silicate hydrate (C-S-H) and portlandite result in a gradual structuration of the material.

However, the additional water that has been released intrinsically and through excessive shearing results in an A_{thix} of 0.22 Pa/s which is 41% lower than REF. The literature agrees that the intrinsic release of additional water is the dominant mechanism of rheological control for self-releasing SAPs [197, 192, 245, 246].

The RET100 mix shows a R_{thix} of 7.3 Pa/s and an A_{thix} of 0.45 Pa/s which is 151% and 21% higher than REF. The 30 s test demonstrates a significant increase in static yield stress. The result suggests that the SAP absorbs water in the resting interval. The RET SAP continues to absorb the free water for short resting intervals, as seen in Fig. 9.3. Mechtcherine et al. [192] explained that the SAP absorbed the free water and the superplasticizer. However, when the mix is continuously sheared (dynamic) for a second time (30 s), the dynamic yield stress reduces 20%. Thereafter, the dynamic yield stress of the RET100 mix increases gradually, unlike the SR35 mix.

The static yield stress of the RET100 mix continues to increase even for the longer resting times due the hydration process and the absorption of the free water by the SAP. Fig. 9.3 indicates that the SAP can potentially absorb water until 30 min after initial saturation. Ultimately, the high static yield stress and relatively low dynamic yield stress of the RET100 mix results in a high thixotropy.

The rheological behaviour shown here is valuable for printing since the free water is absorbed to rapidly increase the stiffening rate once the filament is extruded. It also appears that continuous shearing reduces the dynamic yield stress to reduce the pump's strain.

The 1 and 30 min thixotropy indices for the three mixes are presented in Fig. 9.7. The RET100 mix has a 49% higher λ_{1min} and 33% higher λ_{30min} than REF. RET100's λ_{30s} is 75% higher than that of REF. As shown in Fig. 9.6, at 30 s, the dynamic yield stress decreases while the static increases.

For the SR35 mix, the λ_{1min} and λ_{30min} increase 10% from REF even though the R_{thix} and A_{thix} was lower. This is due to the reduction in dynamic yield stress caused by the SR SAP.

For 3DPC, the transportation system (pump and hose) limits the dynamic yield stress. A higher thixotropy (λ_t) means that a higher yield strength can be achieved immediately after placement from a fixed dynamic yield stress. Rapid reflocculation (R_{thix}) and structuration (A_{thix}) increase the shear strength to support the weight of successively deposited layers. Therefore, a higher λ_t, R_{thix} and A_{thix} yield a better buildability [217].

9.4.2 Buildability

The results are presented in Table 9.8. The REF element collapses at vertical build heights of 350 and 320 mm due to plastic yielding of the critical bottom filament layer, at a printing speed of 40 and 100 mm/s, respectively. The higher λ_t, R_{thix}

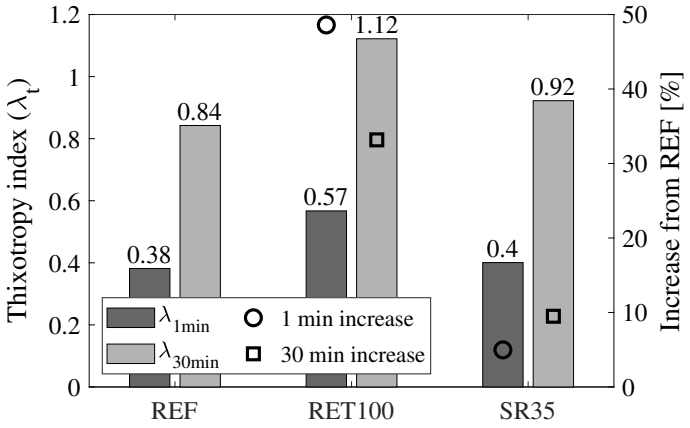

Figure 9.7: The thixotropy, as defined by λ_t, at 1 min and 30 min resting times for each of the three mixes. The secondary axis and markers indicate the percentage increase compared to REF.

and A_{thix} of RET100 increased the height of plastic collapse by 25% for both print speeds. The buildability could not be estimated for the SR35 mix since the mix violates the assumption of thixotropy (negative R_{thix}) required for Kruger's model [217].

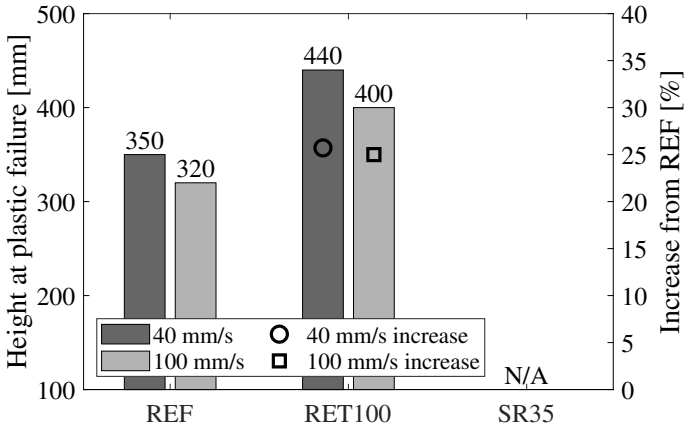

Figure 9.8: The vertical height at plastic failure for printing speeds of 40 and 100 mm/s for the REF and RET100 mixes, as estimated with Kruger's buildability model [217]. The secondary axis and markers indicate the percentage increase compared to REF.

9.4.3 Surface moisture

The initial (SM_i) and available (SM_a) surface moisture of the different mixes are presented in Fig. 9.9. The SR35 mix has a similar amount of SM_i and SM_a as

REF. On the other hand, the RET100 mix has a 10.6% and 12.6% higher amount of SM_i and SM_a. The differences between the SM_i and SM_a values of REF and RET100 are however not statistically significant.

A SM_i of 0.02 kg/m^2 corresponds to a water film thickness of approximately 20 μm. In Fig. 1, this value can be interpreted as the water film thickness of the Phase 1 state. If the porosity is considered, this corresponds to approximately 60 μm of moisture near the surface. Sanjayan et al. [73] measured an initial water film thickness of 51 μm and Van Der Putten et al. [74] measured 60 μm. Considering the different mixes and test methods used by the aforementioned studies and this study, the amount of surface moisture can be deemed to be in a similar range.

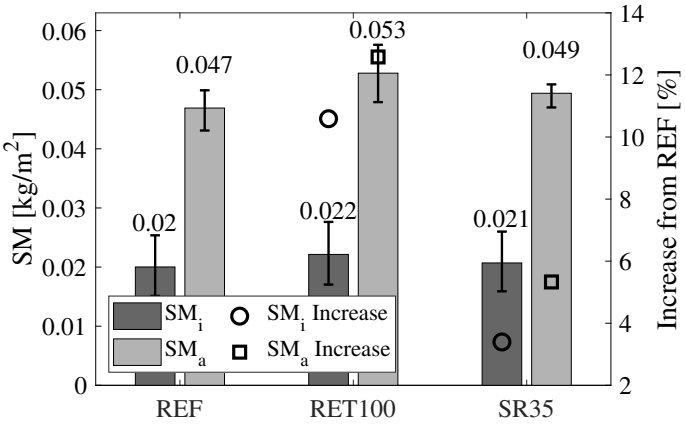

Figure 9.9: The initial (SM_i) and available (SM_a) surface moisture on the interlayer for each of the three mixes. The error bars indicate the lower and upper quartiles. The secondary axis and markers indicate the percentage increase compared to REF.

9.4.4 Flexural strength and interlayer adhesion

The flexural strength of the mould-cast and printed specimens are presented in Fig. 9.10 a. For all the mixes, the printed specimens show a significant lower flexural strength than the mould-cast samples. Exposing the printed specimens to a moderate evaporation rate also reduces the flexural strength.

The MN, PN and PW specimens of the RET100 mix show a 14%, 19% and 20% higher flexural strength than REF. For the MN, PN and PW specimens, the differences between the RET100 and REF mixes are statistically significant according to a one-way ANOVA (MN: $F(1,10) = 5.3$, $p = 0.04$; PN: $F(1,42) = 12.4$, $p = 0.001$; PW: $F(1,9) = 6.6$, $p = 0.03$). The failure pattern also differed for the printed specimens of REF and RET100. All the PN and PW specimens of REF

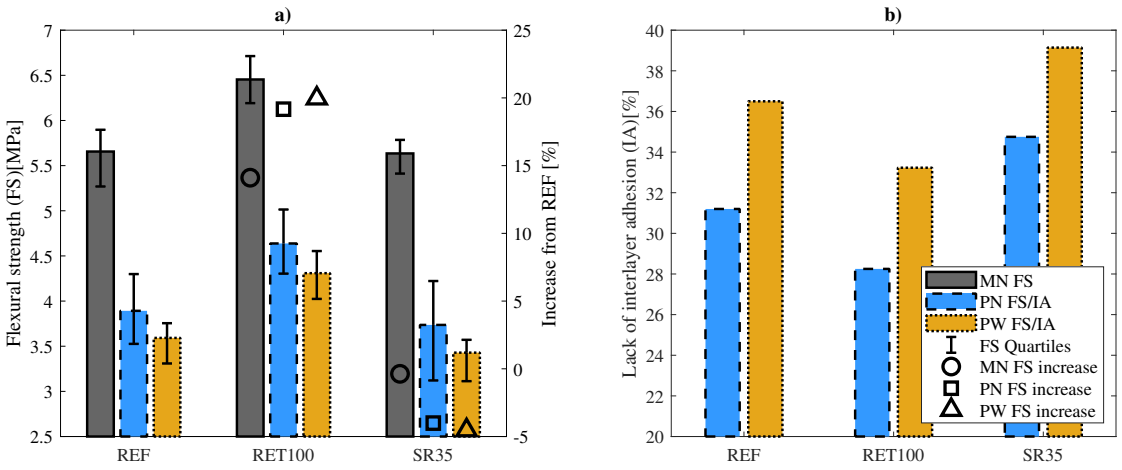

Figure 9.10: a) The mean 56-day flexural strength (FS) of the MN (mould-cast), PN (printed, no wind) and PW (printed, wind) specimens for each of the three mixes. The quartiles indicate the variability and markers on the secondary axis indicate the percentage increase compared to REF. b) The lack of interlayer adhesion (IA) for the PN and PW specimens of each mix. The legend is for both Plots a and b.

failed on the interlayer, while only 42% of the RET100 PN and PW specimens failed on the interlayer. The other 58% failed between the interlayers (in the filament layer), at least partially. The result implies that the tensile strengths of the filament and interlayer are similar, in some cases. The RET100 mix may have a higher amount of macropore in the filament which can reduce its tensile capacity. This, in combination with a higher degree of hydration on the interlayer, increasing the tensile capacity, explains the failure pattern noticed here. The different failure patterns are presented in Fig. 9.11. For this specimen orientation, a flexural strength value of 4.64 MPa is relatively high even at 56 days [79]. For cast concrete, others have also shown a mean flexural strength increase due to SAP [254].

On the other hand, the MN, PN and PW specimens of the SR35 mix show similar (0%, -5%, -5%) flexural strength than REF. According to a one-way ANOVA, the differences between the MN, PN and PW specimens of SR35 and the REF counterpart are not statistically significant. Of the SR35 specimens, only 4% failed in the layer, with the other 96% failing on the interlayer.

Fig. 9.10 b shows the lack of interlayer adhesion (IA), calculated with Eq. 9.3. The RET100 mix shows a higher interlayer adhesion than the REF mix. Therefore, the RET100 mix did not only have a higher flexural strength; it also promoted interlayer adhesion. This can possible be attributed to two mechanisms: 1) the released water, which promotes the hydration of anhydrous cementitious particles near the interlayer, and 2) the initial surface moisture on the interlayer which is

Figure 9.11: The different flexure failure pattens. REF fails on the interlayer while SR35 and RET100 fail in the layer. The difference in surface finish should be noted.

slightly higher. The SR35 mix shows lower interlayer adhesion than REF.

The effect of plastic shrinkage on the interlayer adhesion was mitigated by selecting a short pass time and low post-printing evaporation rate. The influence of plastic and autogenous shrinkage on interlayer adhesion is not the focus of this study, but it should be investigated in the future.

Roussel [39] and, more recently Weng et al. [255], stated that a reduction in the thixotropy (particularly with reference to A_{thix}) of a mix corresponds to an increase in the interlayer bond strength. However, the results presented here show the opposite. The SR35 mix shows a lower R_{thix} and A_{thix}, and similar λ_t than REF but shows a reduced interlayer adhesion. The RET100 mix shows a higher R_{thix}, A_{thix} and λ_t but improved interlayer adhesion.

On the other hand, Keita et al. [75] stated that the influence of thixotropy on the interlayer adhesion is not as dominant as the evaporation of the interlayer's surface moisture. The flexural strength results presented in Fig. 9.10 agree, with a clear reduction in flexural strength and interlayer adhesion due to the higher environmental evaporation rate. For the REF, RET100 and SR35 mixes the flexural strength decreased 7.1%, 6.9% and 6.7% when the evaporation rate increased from 0.07 $kg/m^2/h$ for N to 0.32 $kg/m^2/h$ for W. Similarly, the interlayer adhesion reduced by 5.3%, 5.03% and 5%.

To investigated the relationship between the loss of surface moisture through evaporation and the interlayer adhesion further, the median lack of interlayer adhesion is plotted against the estimated amount of surface moisture (Eq. 9.1) as presented in Fig.9.12.

The amount of surface moisture clearly relates to the interlayer adhesion. For each mix, exposure to a moderate wind speed evaporates the surface moisture

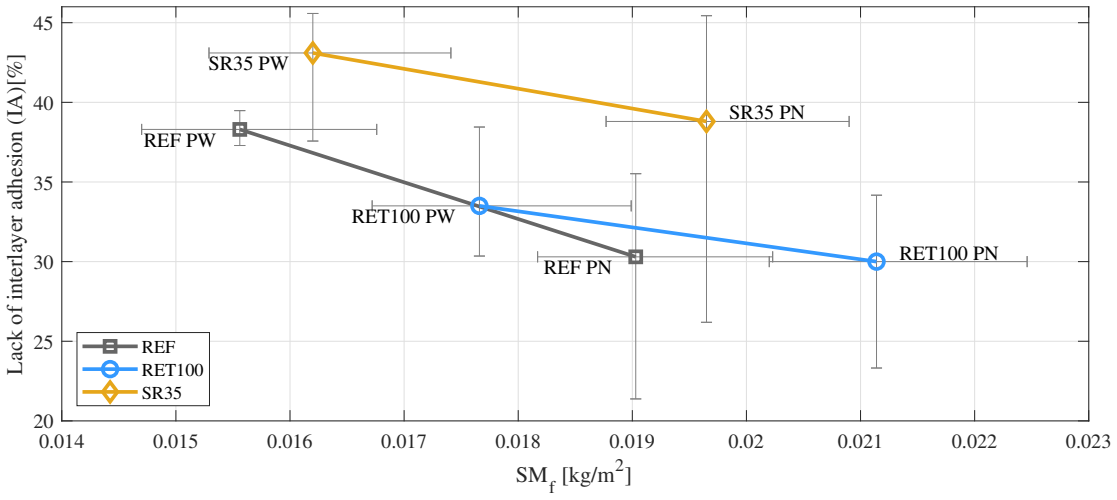

Figure 9.12: Amount of surface moisture against the median lack of interlayer adhesion of the REF, RET100 and SR35 mixes. As before, the PW specimens were exposed to W (wind) while the PN were exposed to N (no wind). Here, the median is used to measure the central tendency. This reduces the effect of the extreme values.

during the pass time to reduce the interlayer adhesion. In the case of REF, the increase in evaporation rate resulted in the largest reduction in interlayer adhesion. For RET100, the SAP provides water to the anhydrous cementitious particles to promote adhesion when some of the surface moisture was removed by evaporation.

It can be concluded that the RET SAP (RET100) increases the interlayer adhesion by releasing water, which promotes the hydration of anhydrous cementitious particles near the interlayer. This mechanism reduces the adverse effect of surface moisture evaporation during the pass time.

9.4.5 Compressive strength

The compressive strengths of the mould-cast and printed specimens are presented in Fig. 9.13 a. As with the flexural strength, the printed specimens show a lower compressive strength than the mould-cast specimens, and exposing the printed specimens to a moderate evaporation rate reduces the compressive strength. However, the effects of printing and evaporation were not as significant for the compressive strength as for the flexural strength.

The mean compressive strength of the MN, PN and PW specimens of the RET100 mix were similar (0%, -10% and -11%) to REF. The variability in the MN, PN and PW results are noteworthy, and the difference between the RET100 and REF mixes were not statistically significant according to a one-way ANOVA.

On the other hand, the MN, PN and PW specimens of the SR35 mix show a 10%, 19%, 19% lower compressive strength that the REF mix. The difference is

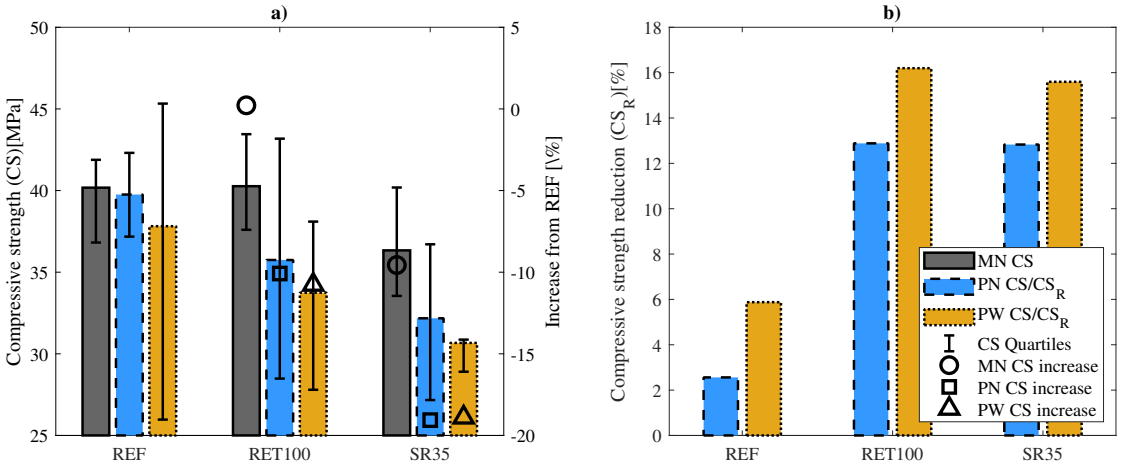

Figure 9.13: a) The 56-day compressive strength (CS) of the MN, PN and PW specimens for each of the three mixes. b) The reduction in compressive strength (CS_R) when the printed specimens are compared to the mould-cast specimens, for the PN and PW specimens of each mix.

only statistically significant if the PN specimens for SR35 and REF are compared, according to a one-way ANOVA (PN: F(1,21) = 6.515, p = 0.02). The MN specimens of SR35 show a lower compressive strength than REF. Literature attributes this to the increased amount of air voids left by the dehydrated SAP [241].

Fig. 9.13 b shows the reduction in compressive strength (CS_R), expressed as a function of the mould-cast specimen of the specific mix, as calculated with Eq. 9.4. The presence of the interlayer has a minor effect on the compressive strength of the REF mix (CS_R: 3% and 6%, for PN and PW). For the RET100 and SR35 mixes, the effect of the interlayer was more significant than for REF (CS_R for PN and PW: RET100, 13% and 16%; SP35, 13% and 16%). The increased CS_R of RET100 and SR35 can possibly be attributed to the to shearing during pumping, which causes the premature release of additional water from the SAPs. This increases the w/c ratio and reduces the compressive strength. The effect is more pronounced in the compressive strength test since failure occurs in the bulk of the filament, unlike the FC test where the interlayer fails. Some literature suggests that the effect of premature water release is minor, but this depends on the dosage and type of SAP [246].

For REF, RET100 and SR35, the compressive strength reduced 3.3%, 3.3% and 2.8% when the evaporation rate was increased from 0.07 $kg/m^2/h$ for N to 0.32 $kg/m^2/h$ for W.

9.5 Validating the proposed model

9.5.1 Experiments

To validate the proposed model, additional experiments were conducted. The REF mix was printed at pass times of 2, 3 and 4 min. Each printed element was exposed to a wind speed of either 2 or 4 m/s, a relative humidity of 53% and ambient temperature of 23.6 ^oC. These conditions produced an evaporation rate of either 0.14 or 0.25 $kg/m^2/h$. The initial surface moisture was determined experimentally and the final surface moisture (SM_f), at extrusion of the overlay filament, was calculated with Eq. 9.1. Six prisms were cast from each mix and more than 12 prisms were extracted from each printed element for each drying condition. Four-point bending tests were conducted at a concrete age of 28 days and the lack of interlayer adhesion was calculated with Eq. 9.3.

9.5.2 Validation

Firstly, the a priori conditions should be evaluated: 1) the pass time is shorter than the initial setting time and 2) the amount of evaporated water is less than the amount of available water. The model is valid for an SM_f of about -0.03 kg/m^2 and a pass time of 210 min (initial setting time). Furthermore, the contribution to the surface moisture through bleeding was assumed negligible due to the short pass time and low bleeding rate of the mixes.

The estimated final surface moisture against the resulting interlayer adhesion is presented in Fig. 9.14. The surface moisture clearly relates to the interlayer adhesion. Assuming a linear relationship produces a R^2 value of 0.81 and a root mean square prediction error (RMSE) of 2.5%. The regression analysis produces a p-value of 0.006, which is smaller that 0.05, meaning that the relationship between the final surface moisture and interlayer adhesion is statistically significant.

9.5.3 Practical implications of the model

Earlier in this study, the mechanisms of Stage I were identified as air entrapment, thixotropy and a lack of surface roughness which is related to the mix and printing parameters. For the REF mix, the combined effect the Stage I mechanisms is a 32% reduction in interlayer adhesion, as presented in Fig. 9.14. The Stage I reduction can be determined experimentally for the specific mix and print setup by using a short pass time and low evaporation rate.

For Stage II, the loss of surface moisture controls the interlayer adhesion. For the RET mix, estimating the surface moisture accurately predicted the lack of interlayer adhesion from 30% to 50%. The Stage II reduction, for any pass time,

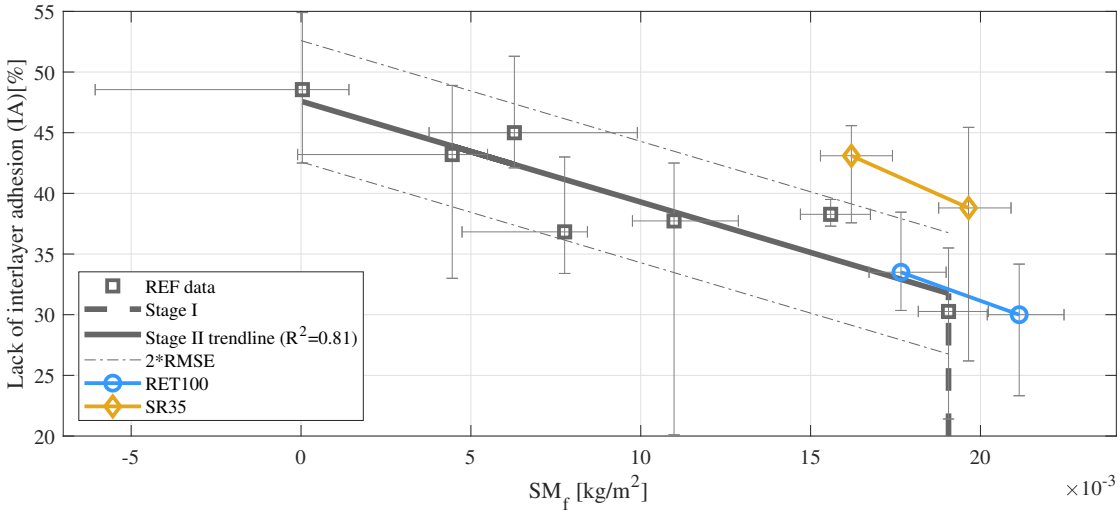

Figure 9.14: The surface moisture at extrusion of the overlay filament (SM_f) against the median lack of interlayer adhesion (IA). The error bars indicate the IA quartiles and the maximum and minimum SM_f.

bleeding and evaporation rate, can be predicted if the magnitude of Stage I and another point on the Stage II line is known. Interpolating between the two points is recommended.

When the SM_f becomes negative (Stage III) the gradient of the prediction line is likely to change. A data point in Stage III could allow for linear prediction to the zero SM_f point, however, this has not been validated.

9.5.4 A case study

As stated before, Keita et al. [75] exposed the 3DPC test specimens to a moderate evaporation rate and tested the interlayer adhesion for different pass times. In Fig.9.15 the reduction in interlayer adhesion is plotted against the estimated final surface moisture for pass times of 7, 10, 35 and 60 min. Since not all the modelling parameters are available in the paper, it is assumed that the bleeding rate is negligible and that the ambient and concrete temperature is 20^oC. The SM_i is assumed to be 0 or 0.03 kg/m^2 and the SM_f is estimated.

For zero SM_i and a linear gradient for Stage III, a R^2 of 0.974 is obtained. In this case, the 7 and 60 min strength values can be used to estimate the 10 and 35 min interlayer adhesion reduction with a root mean square error of 4.15%. The prediction line gradient differs from that in Fig. 9.14 since a different specimen orientation was used during mechanical testing.

If a SM_i of 0.03 kg/m^2 is assumed, the 10 min interlayer adhesion value coincides with zero SM_f. Stage II can then be defined from 38% to 48% and Stage III

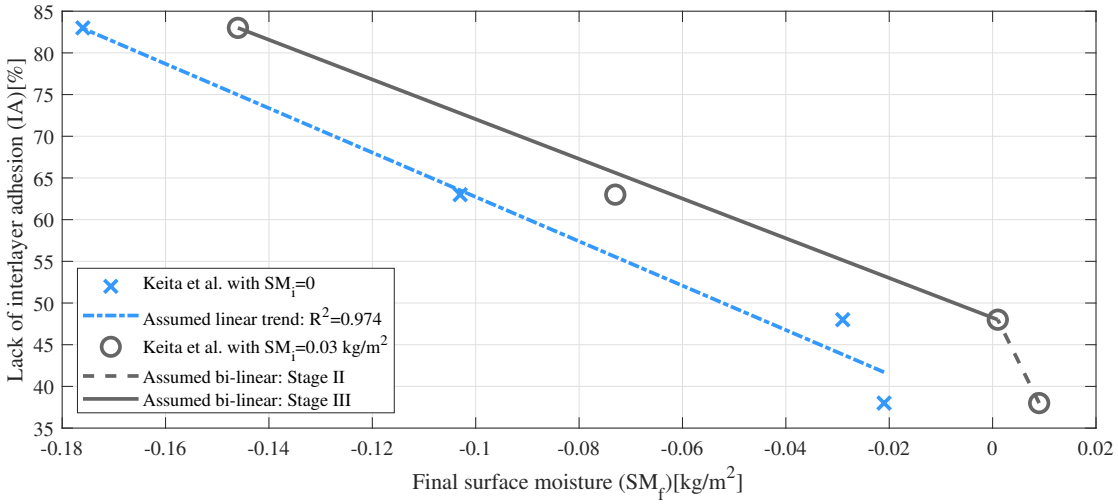

Figure 9.15: The estimated surface moisture (SM_f) against the lack of interlayer adhesion (IA) from the 7, 10, 35 and 60 min pass time data of Keita et al. [75].

from 48% to 83%. The different gradients of Stage II and III are clear, and the bi-linear model is revealed.

9.6 Conclusion

This study aimed to investigate the effect of superabsorbent polymers, as a method of internal curing, on the rheological and mechanical performance of high-performance 3D printed concrete. Two 3DPC mixes containing a retentive and self-releasing SAP were designed and evaluated. The following key advantages were identified:

- A retentive type SAP absorbed the pore water to increase the rate of static yield stress development without significantly affecting the dynamic yield stress. This behaviour is advantageous for the thixotropy and rate of stiffness gain, which improved the buildability of 3DPC by 25%.
- A retentive type SAP released curing water internally to hydrate the anhydrous cementitious particles and increase the flexural strength by 19% and the interlayer adhesion by 10%.

The effect of the magnitude of surface moisture on the interlayer adhesion was investigated further using a proposed analytical model. The model was based on the change in surface moisture during the pass time due to bleeding and evaporation rates. The reduction in interlayer adhesion was accurately (RMSE of 2.5%) predicted from 30% to 50% using the proposed model.

The relationship between surface moisture and interlayer adhesion should be investigated further. Specifically, the effect of different w/b ratios, the effect of the thixotropic development, the Stage III interlayer adhesion reduction, and the limits of the proposed model should be challenged in future research.

Chapter 10

Conclusion

10.1 Research summary

This dissertation aimed to address the adverse consequences of rapid pore water evaporation from early age printed and cast concrete. To achieve this, several objectives were defined. Each chapter addressed an objective and provided a conclusion. To summarise briefly:

- In Chapter 3 the expected on-site evaporation rate was characterised with a proposed weather data analysis method for four different locations. The results clearly indicated the benefit of selecting an appropriate placement time (time of day or month of the year) in reducing plastic shrinkage cracking risk. Active prevention measures were recommended based on the risk of cracking.
- In Chapter 4 the accuracy of the currently available pore water evaporation estimation equations is evaluated and the Jansen-Haise model is recommended for high levels of solar radiation exposure. The severity of plastic shrinkage cracking in cast concrete was also evaluated and the results showed that solar radiation significantly increases the severity of plastic shrinkage cracking.
- In Chapter 5 a test method is proposed to measure free plastic shrinkage in 3D printed concrete by evaluating different specimen dimensions. Several crack induction methods were evaluated, and a recommendation was made. Moreover, the study explains why and how plastic cracks form in 3D printed concrete. The high magnitude free shrinkage 3DPC exhibits, even at a moderate evaporation rate, is concerning. Slippage in the transfer of shrinkage was noticed and coined interlayer slip.

- In Chapter 6 the aforementioned test method was used to evaluate the efficacy of several mitigation measures for early age cracking in 3DPC. At a low dosage, short polypropylene microfibres prevent the formation of PSC without adversely affecting the printability or buildability. Decreasing the setting time with calcium sulfoaluminate-belite cement was also an effective method of crack mitigation. Superabsorbent polymers improves the buildability by increasing the stiffening rate through pore water absorption.
- Chapter 7 investigated the fundamental behaviour of PSC in printed concrete by increasing the evaporation rate and delay time. An empirical model was proposed for the risk of plastic cracking based on the results. The risk of PSC is estimated to be more than three times higher in 3DPC compared to cast concrete.
- Chapter 8 showed that restraining the early age shrinkage has an adverse effect on the long-term durability and mechanical performance of printed concrete. The interlayer bond strength reduced by 12% when the shrinkage was restrained, but the results were not statistically significant. The reduction was attributed to interlayer slip and the formation of microcracks. Even with these defects, the permeability and ion penetration of the visibly uncracked specimens remained relatively low, indicating a good durability for short pass times.
- Chapter 9 is the final content chapter. A retentive SAP improved the buildability through continuous absorption of the pore water and improved the interlayer bond strength by promoting the hydration of anhydrous cementitious particles. Evaporation of interlayer moisture, during printing, has the direct opposite effect. A model for interlayer adhesion was proposed based on the amount of surface moisture on the interlayer at the deposition of the subsequent filament. The surface moisture was estimated from the initial surface moisture, the pass time, bleeding rate and evaporation rate. The analytical model was validated for an interlayer bond strength reduction from 30% to 50%. However, applying the model to the experimental results of other researchers suggests that this range is likely to be extended in future research.

10.2 Enforceable findings

The following enforceable findings were presented:

- From Chapter 3, making a information-based decision on the concrete placement time should be the first step in preventing plastic shrinkage cracking.

- From Chapter 4, using sunshades or windbreaks can be a cost-effective solution for plastic shrinkage cracking. The effect of solar radiation should not be underestimated.
- From Chapter 5, 3D printed concrete is extremely susceptible to plastic shrinkage cracking.
- From Chapter 6, a low dosage of short polypropylene microfibres mitigates plastic shrinkage cracking in 3D printed concrete without a notable reduction in printability or buildability.
- From Chapter 7, the risk of PSC is low if the evaporation rate is reduced to below 0.1 $kg/m^2/h$ until the final setting time for similar 3DPC mixes.
- From Chapter 8, the durability and mechanical performance is adversely affected by early age pore water evaporation but, as long as the concrete is uncracked, this effect is minor.
- From Chapter 9, the interlayer bond strength reduces as the pass time increases, mainly due to the evaporation of the surface moisture. Therefore, reduce the pass time and evaporation rate to maximise the interlayer bond strength.

10.3 Application of findings

In the past decade, many cementitious mixes have been successfully printed using various additive manufacturing techniques. The printing approach and material behaviour, particularly in the fresh state, may differ from this study. It is expected the following findings hold, irrespective of the mixes or additive manufacturing technique used:

- The formfree nature of 3D printed concrete leaves it vulnerable to rapid pore water evaporation and consequential plastic shrinkage cracking.
- The climate in which the concrete is printed controls the rate of pore water evaporation. Solar radiation, air and concrete temperature, wind speed and relative humidity are relevant parameters in this regard.
- Reducing the pore water evaporation rate until the final setting time reduces the likelihood of early age cracking significantly.
- A low dosage of fibres is effective in mitigating the severity of plastic shrinkage cracking.

- Moderate post-printing pore water evaporation does not significantly affect the durability and mechanical performance of printed concrete as long as the specimen remains uncracked.
- The evaporation of the interlayer's surface moisture reduces the hardened state bond strength of printed concrete.

10.4 Recommendation for future research

Many material science-related challenges remain for construction-scale additive manufacturing. The following future research is recommended:

- Stage III of the interlayer bond strength model, proposed in Chapter 9, and the influence of thixotropy on Stage I and II should be investigated. The interlayer is unique to 3DPC and poses a novel challenge.
- Microfibre's mechanism of reducing plastic shrinkage and cracking, discussed in Chapter 6, should be investigated with digital image correlation.
- From Chapter 6, a shrinkage reducing admixture should be incorporated in 3DPC by redesigning the mix. The effect of the admixture on the plastic shrinkage, early age cracking, printability and buildability should be evaluated.
- The effect of the 3DPC element geometry (curves, openings, size) on the transfer of plastic shrinkage and severity of cracking should be investigated with digital image correlation. An alternative method of inducing cracks, without the use of restraining rods, should be proposed.
- Lastly, applications of using additive manufacturing to address African infrastructure challenges should be explored, e.g. housing in urban areas, resilience to natural disasters, food, water and energy security. Locally sourced alternative binding materials for additive manufacturing should also be identified.

The 3DPC research group of Stellenbosch is well-suited to address many of the material science challenges this technology is facing. The following key strengths should be utilised: the facilities available for experimental research on 3DPC, the foundation of cement-based material science and the knowledge of other 3DPC experts. Combining these strengths with a problem that is unique to 3DPC can produce world-class research.

Appendices

Appendix A

A guide to Digital image correlation

Digital image correlation (DIC) is a non-invasive method used for measuring surface displacements. The method offers a relatively simple experimental setup for a large number of data points. LVDT's are more reliable and is recommended if only a few measurement points are required. DIC is recommended for applications where conventional LVDT's are unsuitable. In this study, DIC was used to measure the shrinkage displacement since LVDT's obstructed the airflow in the evaporation chamber used to induce plastic shrinkage. DIC proved beneficial in understanding the development of early age shrinkage deformation in the presence of restraint and the development of cracks. To assist future researchers, this section briefly discusses the implementation of this method. More information is available elsewhere [213, 214].

A.1 Hardware

For two-dimensional displacements, a single camera is required to generate images at a predefined acquisition rate. Stellenbosch University's Structural Engineering laboratory has three suitable monochrome machine vision cameras, two of the Basler acA2040-55um models (A) and one Basler acA1920-150um model (B). The former model (A) captures images with 2048×1536 pixels at a maximum frame rate of 55/s. The latter model (B) captures images with 1920×1200 pixels at a maximum frame rate of 150/s. Since Camera A has more pixels per frame, it is recommended for general use. Camera B is recommended for high-speed application. The cameras can be controlled simultaneously with Basler's Pylon software. The exposure time (time the shutter is open) should be adjusted to obtain a clear image on connection. Saving the images in the TIFF format is recommended, and the record function can be used to save images directly to the PC for lower frame rates. Both Cameras A and B are compatible with the one

Edmund Optics Lens CFFL F1.4 f16mm 2/3" (A) and two Edmund Optics Lens CFFL F1.7 f36mm 2/3" (B) fixed focal length (no zoom) lenses. The 36 mm focal length lens (B) is recommended for general use. The focus should be adjusted on the lens to obtain a clear image.

A.2 Setup

First, a field-of-view (the actual area the camera monitors in mm×mm) is selected based on the object's dimensions. If possible, the field-of-view should be slightly (10-20%) larger than the object. From the field-of-view and lens focal length (36 mm), the distance from the camera to the object (working distance) can be calculated with Basler's lens selector tool. The 16 mm lens should be used if the working distance is practically too large. A constant light source that illuminates the field-of-view uniformly is essential, and additional lighting with a cool colour temperature (>5000K) is recommended. Securely fixing both the light and camera is imperative.

A.3 Resolution

The size of a single pixel can be calculated by dividing the field-of-view by the number of pixels in the image. With a DIC point component (target marker), a resolution of 70 to 100 times smaller than the pixel size was attained in this research.

For example, if the target markers are in a 300×100 mm (length×height) area, a 350×260 mm field-of-view is appropriate. With Camera A and Lens B, this results in a 1.8 m working distance, 0.17×0.17 mm pixel size and a displacement resolution between 0.0017 and 0.002 mm.

A.4 Software

GOM Correlate software (free) provides the means of obtaining displacement results from the series of images. Tutorials on the operation of the software are available on YouTube, and Section 5.2.6 explains how displacements are obtained from the surface patterns. The software allows for the use of a point or surface component. More than five unique elliptical dots, each with an internal diameter of approximately 10 ± 2 pixels, are recommended for the point component (Fig. 5.4). A random arrangement of elliptical speckles, with a mean diameter between 3 and 5 pixels, is recommended for the surface pattern (Fig. 5.6) [173].

List of References

[1] Abimbola Olukemi Windapo and Keith Cattell. The South African construction industry: Perceptions of key challenges facing its performance, development and growth. *Journal of Construction in Developing Countries*, 18(2):65–79, 2013.

[2] R. A. Buswell, R. C. Soar, A. G.F. Gibb, and A. Thorpe. Freeform Construction: Mega-scale Rapid Manufacturing for construction. *Automation in Construction*, 16(2):224–231, 2007.

[3] South African Department of Employment and Labour. Labour on injuries and fatalities in SA construction sector, 2017. URL https://www.gov.za/speeches/sa-construction-sector-9-mar-2017-0000{#}.

[4] Tshilidzi Marwala. *Closing the Gap: The Fourth Industrial Revolution in Africa*. Pan Macmillan South Africa, Johannesburg, 2020.

[5] Boston Consulting Group. Industry 4.0, 2021. URL https://www.bcg.com/capabilities/manufacturing/industry-4.0.

[6] H. Amelia. The Importance of 3D Printing in Industry 4.0, 2021. URL https://www.3dnatives.com/en/3d-printing-in-industry-4-0-150220215/{#}!

[7] Statistics South Africa. General Household Survey. Technical report, Pretoria, 2017. URL https://www.statssa.gov.za/publications/P0318/P03182017.pdf.

[8] Charles W Hull. Apparatus for Production of Three-Dmensonal Objects By Stereo Thography, 1984.

[9] J. Flynt. A Detailed History of 3D Printing, 2020. URL https://3dinsider.com/3d-printing-history/.

[10] Richard D'Aveni. The 3-D Printing Revolution, 2015. URL https://hbr.org/2015/05/the-3-d-printing-revolution.

[11] Joseph Pegna. Exploratory investigation of solid freeform construction. *Automation in Construction*, 5(5):427–437, 1997.

[12] Behrokh Khoshnevis. Automated construction by contour crafting - Related robotics and information technologies. *Automation in Construction*, 13(1):5–19, 2004.

[13] T. T. Le, S. A. Austin, S. Lim, R. A. Buswell, R. Law, A. G.F. Gibb, and T. Thorpe. Hardened properties of high-performance printing concrete. *Cement and Concrete Research*, 42:558–566, 2012.

[14] T. T. Le, S. A. Austin, S. Lim, R. A. Buswell, A. G.F. Gibb, and T. Thorpe. Mix design and fresh properties for high-performance printing concrete. *Materials and Structures/Materiaux et Constructions*, 45(8):1221–1232, 2012.

[15] K.N. Jha. *Formwork for Concrete Structures*. Tata McGraw Hill Education Private Limited, New Dilhi, India, 2012.

[16] Suvash Chandra Paul, Gideon van Zijl, Ming Jen Tan, and Ian Gibson. A review of 3D concrete printing systems and materials properties: current status and future research prospects. *Rapid Prototyping Journal*, 24(4):784–798, 2018.

[17] Borja García de Soto, Isolda Agustí-Juan, Jens Hunhevicz, Samuel Joss, Konrad Graser, Guillaume Habert, and Bryan T. Adey. Productivity of digital fabrication in construction: Cost and time analysis of a robotically built wall. *Automation in Construction*, 92(May):297–311, 2018.

[18] Isolda Agustí-Juan, Florian Müller, Norman Hack, Timothy Wangler, and Guillaume Habert. Potential benefits of digital fabrication for complex structures: Environmental assessment of a robotically fabricated concrete wall. *Journal of Cleaner Production*, 154:330–340, 2017.

[19] Geert De Schutter, Karel Lesage, Viktor Mechtcherine, Venkatesh Naidu Nerella, Guillaume Habert, and Isolda Agusti-Juan. Vision of 3D printing with concrete: Technical, economic and environmental potentials. *Cement and Concrete Research*, 112:25–36, 2018.

[20] Nathalie Labonnote, Anders Rønnquist, Bendik Manum, and Petra Rüther. Additive construction: State-of-the-art, challenges and opportunities. *Automation in Construction*, 72(October 2017):347–366, 2016.

[21] P. Domone and J. Illston. *Construction Materials: Their nature and behaviour*. Spon Press, New York, fourth edition, 2010.

[22] Riaan Combrinck. *Cracking of Plastic Concrete in Slab-Like Elements*. PhD thesis, Stellenbosch University, 2016.

[23] John Temitope Kolawole. *Influence of rheology on the cracking of plastic concrete*. Phd, Stellenbosch University, 2020.

[24] Jacques Kruger. *Rheo-mechanics modelling of 3D concrete printing constructability.* Phd, Stellenbosch University, 2019.

[25] D. Lootens, P. Jousset, L. Martinie, N. Roussel, and R. J. Flatt. Yield stress during setting of cement pastes from penetration tests. *Cement and Concrete Research*, 39(5):401–408, 2009.

[26] Seung Cho, Jacques Kruger, Frederick Bester, Marchant van den Heever, Algurnon van Rooyen, and Gideon van Zijl. A Compendious Rheo-Mechanical Test for Printability Assessment of 3D Printable Concrete. In *RILEM International Conference on Concrete and Digital Fabrication*, pages 196–205. Springer, Cham, 2020.

[27] E.P. Koehler and D.W. Fowler. Development of a portable rheometer for fresh portland cement concrete. Technical report, University of Texas, Austin, 2004.

[28] G.M. Moelich, R Van Huffel, and R Combrinck. Used Oil as an Admixture to Improve the Rheological Properties of Concrete. In W.P. Boshoff, R. Combrinck, V. Mechtcherine, and M. Wyrzykowski, editors, *3rd International Conference on the Application of Superabsorbent Polymers (SAP) and Other New Admixtures Towards Smart Concrete. SAP 2019.*, pages 184–191. RILEM Bookseries, vol 24. Springer, Cham, 2019.

[29] V. Mechtcherine, F. P. Bos, A. Perrot, W. R.Leal da Silva, V. N. Nerella, S. Fataei, R. J.M. Wolfs, M. Sonebi, and N. Roussel. Extrusion based additive manufacturing with cement based materials: Production steps, processes, and their underlying physics: A review. *Cement and Concrete Research*, 132(December 2019):106037, 2020.

[30] R. A. Buswell, W. R. Leal de Silva, S. Z. Jones, and J. Dirrenberger. 3D printing using concrete extrusion: A roadmap for research. *Cement and Concrete Research*, 112:37–49, 2018.

[31] M. van den Heever, F. A. Bester, P. J. Kruger, and G. P.A.G. van Zijl. Effect of silicon carbide (Sic) nanoparticles on 3d printability of cement-based materials. In *Proceedings of the 7th International Conference on Structural Engineering, Mechanics and Computation*, number September, pages 1616–1621, 2019.

[32] Egor Secrieru, Jad Khodor, Christof Schröfl, and Viktor Mechtcherine. Formation of lubricating layer and flow type during pumping of cement-based materials. *Construction and Building Materials*, 178:507–517, 2018.

[33] A. V. Rahul, Manu Santhanam, Hitesh Meena, and Zimam Ghani. 3D printable concrete: Mixture design and test methods. *Cement and Concrete Composites*, 97 (December 2018):13–23, 2019.

[34] R Jayathilakage, P Rajeev, and J G Sanjayan. Yield stress criteria to assess the buildability of 3D concrete printing. *Construction and Building Materials*, 240: 117989, 2020.

[35] F.P. Bos, P.J. Kruger, S.S. Lucas, and G.P.A.G. van Zijl. Juxtaposing fresh material characterisation methods for buildability assessment of 3D printable cementitious mortars. *Cement and Concrete Composites*, 120(March):104024, 2021.

[36] Seung Cho, Jacques Kruger, Stephan Zeranka, and Gideon Van Zijl. 3D Printable Concrete Technology and Mechanics. *Concrete Beton*, (158):11–18, 2019.

[37] Nicolas Roussel. A thixotropy model for fresh fluid concretes: Theory, validation and applications. *Cement and Concrete Research*, 36(10):1797–1806, 2006.

[38] Jacques Kruger, Stephan Zeranka, and Gideon Van Zijl. An ab initio approach for thixotropy characterisation of (nanoparticle-infused) 3D printable concrete. *Construction and Building Materials*, 224:372–386, 2019.

[39] Nicolas Roussel. Rheological requirements for printable concretes. *Cement and Concrete Research*, 112:76–85, 2018.

[40] E Holt and M Leivo. Cracking risks associated with early age shrinkage. *Cement and Concrete Composites*, 26:521–530, 2004.

[41] Jurate Saltyte Benth, Fred Espen Benth, and Paulius Jalinskas. A spatial-temporal model for temperature with seasonal variance. *Journal of Applied Statistics*, 34(7): 823–841, 2007.

[42] C.A. Shaeles and K. C. Hover. Influence of mix proportions and Construction Operations on Plastic Shrinkage Cracking in Thin Slabs. *ACI Materials Journal*, 85:495–504, 1988.

[43] A.A. Almusallam, M. Maslehuddin, M. Abdul-Waris, and M. M. Khan. Effect of mix proportions on plastic shrinkage cracking of concrete in hot environments. *Construction and Building Materials*, 12:353–358, 1998.

[44] P.H. Morris and P.F. Dux. A review of ACI recommendations for prevention of plastic cracking. *ACI Materials Journal*, 102(5):307, 2005.

[45] P. K. Mehta and P. J. M. Monteiro. *Concrete: microstructure, properties, and materials.* McGraw-Hill, New York, third edition, 2006.

[46] H. G. Kwak and S. J. Ha. Plastic shrinkage cracking in concrete slabs. Part II: Numerical experiment and prediction of occurrence. *Magazine of Concrete Research*, 58(8):517–532, 2006.

[47] William P. Boshoff and Riaan Combrinck. Modelling the severity of plastic shrinkage cracking in concrete. *Cement and Concrete Research*, 48:34–39, 2013.

[48] C.A. Menzel. Causes and prevention of crack development in plastic concrete. *Portland Cement Association Annual Meeting*, pages 130–136, 1954.

[49] O. Z. Cebeci and A. M. Saatci. Estimation of evaporation from concrete surfaces. *Proceedings of Third International RILEM Conference: Concrete in Hot Climates*, pages 25–31, 1992.

[50] Paul J. Uno. Plastic shrinkage cracking and evaporation formulas. *ACI Materials Journal*, 95(4):365–375, 1998.

[51] M. Al-Fadhala and K. C. Hover. Rapid evaporation from freshly cast concrete and the Gulf environment. *Construction and Building Materials*, 15(1):1–7, 2001.

[52] M. Bakhshi, B. Mobasher, and M. Zenouzi. Model for Early-Age Rate of Evaporation of Cement-Based Materials. *Journal of Engineering Mechanics*, 138(11): 1372–1380, 2012.

[53] A. A. Almusallam. Effect of environmental conditions on the properties of fresh and hardened concrete. *Cement and Concrete Composites*, 23:353–361, 2001.

[54] M. Azenha, K. Maekawa, T. Ishida, and R. Faria. Drying induced moisture losses from mortar to the environment. Part I: Experimental research. *Materials and Structures*, 40(8):801–811, 2007.

[55] William. Lerch. Plastic shrinkage. *ACI Journal*, 53(8):797–802, 1957.

[56] F. H. Wittmann. On the action of capillary pressure in fresh concrete. *Cement and Concrete Research*, 6:49–56, 1976.

[57] Pietro Lura, Brad Pease, Guy B. Mazzotta, Farshad Rajabipour, and Jason Weiss. Influence of shrinkage-reducing admixtures on development of plastic shrinkage cracks. *ACI Materials Journal*, 104(2):187–194, 2007.

[58] Volker Slowik, Markus Schmidt, and Roberto Fritzsch. Capillary pressure in fresh cement-based materials and identification of the air entry value. *Cement and Concrete Composites*, 30:557–565, 2008.

[59] V. Slowik, T. Hübner, M. Schmidt, and B. Villmann. Simulation of capillary shrinkage cracking in cement-like materials. *Cement and Concrete Composites*, 31 (7):461–469, 2009.

[60] C. Qi, J. Weiss, and J. Olek. Characterization of plastic shrinkage cracking in fiber reinforced concrete using image analysis and a modified Weibull function. *Materials and Structures*, 36:386–395, 2003.

[61] I. Löfgren, O. Esping, O. Jensen, P. Lura, and K. Kovler. Early age cracking of self-compacting concrete. *International RILEM conference on volume changes of hardening concrete: testing and mitigation*, pages 251–260, 2006.

[62] Philippe Turcry and Ahmed Loukili. Evaluation of plastic shrinkage cracking of self-consolidating concrete. *ACI Materials Journal*, 103(4):272–279, 2006.

[63] Riaan Combrinck and William Peter Boshoff. Typical plastic shrinkage cracking behaviour of concrete. *Magazine of Concrete Research*, 65(8):486–493, apr 2013.

[64] Andreas Leemann, Peter Nygaard, and Pietro Lura. Impact of admixtures on the plastic shrinkage cracking of self-compacting concrete. *Cement and Concrete Composites*, 46:1–7, 2014.

[65] Sadegh Ghourchian, Mateusz Wyrzykowski, Luis Baquerizo, and Pietro Lura. Susceptibility of Portland cement and blended cement concretes to plastic shrinkage cracking. *Cement and Concrete Composites*, 85:44–55, 2018.

[66] Moghul Sirajuddin and Ravindra Gettu. Plastic shrinkage cracking of concrete incorporating mineral admixtures and its mitigation. *Materials and Structures/Materiaux et Constructions*, 51(2), 2018.

[67] I. M.G. Bertelsen, C. Kragh, G. Cardinaud, L. M. Ottosen, and G. Fischer. Quantification of plastic shrinkage cracking in mortars using digital image correlation. *Cement and Concrete Research*, 123:105761, 2019.

[68] Faez Sayahi, Mats Emborg, Hans Hedlund, Andrzej Cwirzen, and Marcin Stelmarczyk. The severity of plastic shrinkage cracking in concrete: A new model. *Magazine of Concrete Research*, 73(6):315–324, 2021.

[69] O.M. Jensen. Monitoring water loss from fresh concrete. In *RILEM-JCI seminar on concrete durability and service life planning (ConcreteLife006)*, pages 197–202, Ein-Bokek, Israel;, 2006.

[70] Gaurav Sant, Pietro Lura, and Jason Weiss. Measurement of Volume Change in Cementitious Materials at Early Ages: Review of Testing Protocols and Interpretation of Results. *The Transportation Research Record*, 1979:21–29, 2006.

[71] Viktor Mechtcherine, Michaela Gorges, C. Schröfl, Alexander Assmann, Wolfgang Brameshuber Ribeiro, AntoÂ´nio Bettencourt, Daniel Cusson, Joao Custodio, Eugenia Fonseca Da Silva, Kazuo Ichimiya, Shin-ichi Igarashi, Agnieszka Klemm, Konstantin Kovler, Anne Neiry de Mendonc Lopes, Pietro Lura, Van Tuan Nguyen Zhutovsky, Hans-Wolf Reinhardt Semion, Romildo Dias Toledo Filho, Jason Weiss, Mateusz Wyrzykowski, and Guang Ye. Effect of internal curing by using superabsorbent polymers (SAP) on autogenous shrinkage and other properties of a high-performance fine-grained concrete: Results of a RILEM round-robin test. *Materials and Structures/Materiaux et Constructions*, 47(3):541–562, 2014.

[72] Linmei Wu, Nima Farzadnia, Caijun Shi, Zuhua Zhang, and Hao Wang. Autogenous shrinkage of high performance concrete: A review. *Construction and Building Materials*, 149:62–75, 2017.

[73] Jay G. Sanjayan, Behzad Nematollahi, Ming Xia, and Taylor Marchment. Effect of surface moisture on inter-layer strength of 3D printed concrete. *Construction and Building Materials*, 172:468–475, 2018.

[74] Jolien Van Der Putten, Maxim Deprez, Veerle Cnudde, Geert De Schutter, and Kim Van Tittelboom. Microstructural characterization of 3D printed cementitious materials. *Materials*, 12(18), 2019.

[75] Emmanuel Keita, Hela Bessaies-Bey, Wenqiang Zuo, Patrick Belin, and Nicolas Roussel. Weak bond strength between successive layers in extrusion-based additive manufacturing: measurement and physical origin. *Cement and Concrete Research*, 123:105787, 2019.

[76] Venkatesh Naidu Nerella, Simone Hempel, and Viktor Mechtcherine. Effects of layer-interface properties on mechanical performance of concrete elements produced by extrusion-based 3D-printing. *Construction and Building Materials*, 205:586–601, 2019.

[77] Biranchi Panda, Nisar Ahamed, Noor Mohamed, Suvash Chandra Paul, G V P Bhagath Singh, Ming Jen Tan, and Branko Šavija. The Effect of Material Fresh Properties and Process Parameters on Buildability and Interlayer Adhesion of 3D Printed Concrete. *Materials*, 12:2149, 2019.

[78] R. J.M. Wolfs, F. P. Bos, and T. A.M. Salet. Hardened properties of 3D printed concrete: The influence of process parameters on interlayer adhesion. *Cement and Concrete Research*, 119:132–140, 2019.

[79] Jacques Kruger and Gideon Van Zijl. Additive Manufacturing A comprehensive review on lack-of-fusion in digital concrete fabrication A comprehensive review on lack-of-fusion in digital concrete fabrication. *Additive Manufacturing*, 37:101654, 2020.

[80] Jacques Kruger, Anton du Plessis, and Gideon van Zijl. An investigation into the porosity of extrusion-based 3D printed concrete. *Additive Manufacturing*, 37 (November 2020):101740, 2021.

[81] Martin Classen, Jan Ungermann, and Rahul Sharma. Additive Manufacturing of Reinforced Concrete: Development of a 3D Printing Technology for Cementitious Composites with Metallic Reinforcement. *Applied Sciences*, 10(11):3791, 2020. ISSN 20763417.

[82] Frederick Bester, Marchant van den Heever, Jacques Kruger, and Gideon van Zijl. Reinforcing digitally fabricated concrete: A systems approach review. *Additive Manufacturing*, 37(November 2020):101737, 2021.

[83] Taylor Marchment and Jay Sanjayan. Mesh reinforcing method for 3D Concrete Printing. *Automation in Construction*, 109(June 2019):102992, 2020.

[84] UCT/WITS. Durability Index Testing Procedure Manual. Technical report, University of Cape Town and University of the Witwatersrand, 2017. URL https://www.theconcreteinstitute.org.za/durability.

[85] Kung'u Githachuri and Mark G. Alexander. Durability performance potential and strength of blended Portland limestone cement concrete. *Cement and Concrete Composites*, 39:115–121, 2013.

[86] Z. Mukadam, M. G. Alexander, and H. D. Beushausen. The effect of drying preconditioning on the South African durability index tests. *Cement and Concrete Composites*, 69:1–8, 2016.

[87] A. M. Neville. *Properties of Concrete*. John Wiley & Sons, Inc., London, fourth edition, 1997.

[88] T. C. Powers. *Properties of fresh concrete*. John Wiley & Sons, Inc., New York, first edition, 1968.

[89] M. Kayondo, R. Combrinck, and W.P. Boshoff. State-of-the-art review on plastic cracking of concrete. *Construction and Building Materials*, 225:886–899, 2019.

[90] H.-G. Kwak and S.-J. Ha. Plastic shrinkage cracking in concrete slabs. Part I: a numerical model. *Magazine of Concrete Research*, 58(8):505–516, 2006.

[91] Dan Ravina and Rahel Shalon. Plastic Shrinkage Cracking. *ACI Materials Journal*, 65:282–292, 1968.

[92] Duy H. Nguyen, Vinh T.N. Dao, and Pietro Lura. Tensile properties of concrete at very early ages. *Construction and Building Materials*, 134:563–573, 2017.

[93] Erika E Holt. Early age autogenous shrinkage of concrete. Technical report, Technical Research Centre of Finland., Espoo, Finland, 2001.

[94] R Combrinck, L Steyl, and W. P. Boshoff. Influence of concrete depth and surface finishing on the cracking of plastic concrete. *Construction and Building Materials*, 175:621–628, 2018.

[95] B. H. Ahmadi. Initial and final setting time of concrete in hot weather. *Materials and Structures/Materiaux et Constructions*, 33(232):511–514, 2000.

[96] A K Schindler, J M Ruiz, R O Rasmussen, G K Chang, and L G Wathne. Concrete pavement temperature prediction FHWA HIPERPAV and case studies with the models. *Cement and Concrete Composites*, 26(5):463–471, 2004.

[97] J. Ortiz, A. Aguado, L. Agulló, and T. García. Influence of environmental temperatures on the concrete compressive strength: Simulation of hot and cold weather conditions. *Cement and Concrete Research*, 35(10):1970–1979, 2005.

[98] S. Ghourchian, M. Wyrzykowski, L. Baquerizo, and Pietro. Lura. Performance of passive methods in plastic shrinkage cracking mitigation. *Cement and Concrete Composites*, 91:148–155, 2018.

[99] ACI 308R. Guide to Curing Concrete. Technical report, American Concrete Institute, Farmington Hills, 2008.

[100] ACI 305.1. Specification for Hot Weather Concreting. Technical report, American Concrete Institute, 2007.

[101] Gerhard Olivier, Riaan Combrinck, Muzafalu Kayondo, and William P. Boshoff. Combined effect of nano-silica, super absorbent polymers, and synthetic fibres on plastic shrinkage cracking in concrete. *Construction and Building Materials*, 192: 85–98, 2018.

[102] D. Snoeck, L. Pel, and N. De Belie. Superabsorbent polymers to mitigate plastic drying shrinkage in a cement paste as studied by NMR. *Cement and Concrete Composites*, 93(March):54–62, 2018.

[103] CCAA. Hot-Weather Concreting. Technical report, Cement Concrete & Aggregates Australia, 2004.

[104] PCA. Design and Control of Concrete Mixtures. Technical report, Portland Cement Association, Illinois, USA, 2002.

[105] M. A. Kohler, T. J. Nordenson, and W. E. Fox. Evaporation from Pans and Lakes. Technical report, U. S. Department of Commerce, Washington, 1955.

[106] K.C. Hover. Evaporation of water from concrete surfaces. *ACI Materials Journal*, 103(5):384–389, 2006.

[107] WMO. Guide to Meteorological Instruments and Methods of Observation. Technical report, World Meteorological Organization, Geneva, 2008.

[108] ENV 206. Concrete: Performance, Production, Placing, and Compliance Criteria. Technical report, European Standard, 1990.

[109] ASTM C1579. Standard Test Method for Evaluating Plastic Shrinkage Cracking of Restrained Fiber Reinforced Concrete. Technical report, American Society for Testing and Materials, 2013.

[110] Z Berhane. Evaporation of water from fresh mortar and concrete at different environmental conditions. *ACI Materials Journal*, 81(6):560–565, 1978.

[111] Menashi D Cohen, Jan Olek, and William L Dolch. Mechanism of Plastic Shrinkage Cracking in Portland Cement and Portland Cement-Silica Fume Paste and Mortar. *Cement and Concrete Research*, 20:103–119, 1990.

[112] T. A. Hammer. Effect of silica fume on the plastic shrinkage and pore water pressure of high-strength concretes. *Materials and Structures/Materiaux et Constructions*, 34:273–278, jun 2001.

[113] Nemkumar Banthia and Rishi Gupta. Influence of polypropylene fiber geometry on plastic shrinkage cracking in concrete. *Cement and Concrete Research*, 36(7): 1263–1267, 2006.

[114] Pengfei Zhao, Attila M. Zsaki, and Michelle R. Nokken. Using digital image correlation to evaluate plastic shrinkage cracking in cement-based materials. *Construction and Building Materials*, 182:108–117, 2018.

[115] Ashley C. Carden and George E. Ramey. Weather exposure and its effect on bridge deck curing in alabama. *Practice Periodical on Structural Design and Construction*, 4(4):139–146, 1999.

[116] Douglas C. Montgomery and George C. Runger. *Applied Statistics and Probability for Engineers*. Wiley, Hoboken, NJ, 5th editio edition, 2011.

[117] Stuart Coles. *An Introduction to Statistical Modeling of Extreme Values*. Springer, London, 2001.

[118] Ana Ferreira and Laurens De Haan. On the block maxima method in extreme value theory: PWM estimators. *Annals of Statistics*, 43(1):276–298, 2015.

[119] Enrique Castillo, AS Hadi, N Balakrishnan, and JM Sarabia. *Extreme value and related models with applications in engineering and science*. 2005.

[120] T. W. Anderson and D. A. Darling. A Test of Goodness of Fit. *Journal of the American Statistical Association*, 49(265):765–769, 1954.

[121] F. J. Massey. The Kolmogorov-Smirnov Test for Goodness of Fit. *Journal of the American Statistical Association*, 46(253):68–78, 1951.

[122] E. Kostandyan and J.D. Sørensen. Structural reliability methods for wind power converter system component reliability assessment. In *Proceedings on the 16th IFIP WG 7.5 Conference on Reliability and Optimization of Structural Systems*, pages 135–142, Yrevan, Armenia, 2012.

[123] M. Holicky. *Reliability analysis for structural design*. SUN Press, Stellenbosch, 2009.

[124] South African Weather Service. Weather Questions, 2019. URL http://www.weathersa.co.za/learning/educational-questions/.

[125] SANS 10160-3. Basis of Structural Design and Actions for Buildings and Industrial Structures. Part 3: Wind Actions. Technical report, South African National Standard, 2011.

[126] G. S. Hasanain, T. A. Khallaf, and K. Mahmood. Water evaporation from freshly placed concrete surfaces in hot weather. *Cement and Concrete Research*, 19(3): 465–475, 1989.

[127] A.S. Al-Gahtani. Effect of curing methods on the properties of plain and blended cement concretes. *Construction and Building Materials*, 24:308–314, 2010.

[128] R Combrinck, M Kayondo, B D Roux, W I De Villiers, and W P Boshoff. Effect of various liquid admixtures on cracking of plastic concrete. *Construction and Building Materials*, 202:139–153, 2019.

[129] Hyo-Gyoung Kwak, Soojun Ha, and W. Jason Weiss. Experimental and Numerical Quantification of Plastic Settlement in Fresh Cementitious Systems. *Journal of Materials in Civil Engineering*, 22(10):951–966, 2010.

[130] M.A. Sanjuán and R.D. Filho Tolêdo. Effectiveness of crack control at early age on the corrosion of steel bars in low modulus sisal and coconut fibre-reinforced mortars. *Cement and Concrete Research*, 28(4):555–565, 1998.

[131] GM. Moelich, J. Kruger, and R. Combrinck. Plastic shrinkage cracking in 3D printed concrete. *Composites Part B: Engineering*, 200:108313, 2020.

[132] G. M. Moelich, P. J. Kruger, and R. Combrinck. The effect of restrained early age shrinkage on the interlayer bond and durability of 3D printed concrete. *Journal of Building Engineering*, 43:102857, 2021.

[133] Riaan Combrinck and William P. Boshoff. Tensile properties of plastic concrete and the influence of temperature and cyclic loading. *Cement and Concrete Composites*, 97:300–311, 2019.

[134] V. Dao, P.F. Dux, and P.H. Morris. Tensile Properties of Early-Age Concrete. *Proceedings of the International Conference: Concrete Durability: Achievement and Enhancement*, pages 469–480, 2008.

[135] D. P. Bentz. A compurter model to predict the surface temperature and Time-of-wetness of concrete pavements and bridge decks. Technical report, U.S. Department of Commerce, 2000.

[136] J. W. Finch and R. L. Hall. Estimation of open water Evaporation. Technical report, Enviroment Agency, 2001.

[137] H. L. Penman. Natural Evaporation from Open Water, Bare Soil and Grass. *Proceedings of the Royal Society of London. Series A, Mathematical and Physical*, 193 (1032):120–145, 1948.

[138] R.G. Allen, L.S. Pereira, D. Raes, and M. Smith. *FAO Irrigation and drainage paper.* Number 56. Food and Agriculture Organization of the United Nations, Rome, 1998.

[139] Thomas C. Winter, Donald C. Buso, Donald O. Rosenberry, Gene E. Likens, Alex M. Sturrock, and David P. Mau. Evaporation determined by the energy-budget method for Mirror Lake, New Hampshire. *Limnology and Oceanography*, 48(3):995–1009, 2003.

[140] Judy Z. Drexler, Richard L. Snyder, Donatella Spano, and Kyaw Tha Paw U. A review of models and micrometeorological methods used to estimate wetland evapotranspiration. *Hydrological Processes*, 18(11):2071–2101, 2004.

[141] Donald O Rosenberry and Gene E Likens. Comparison of 15 evaporation methods applied to a small mountain lake in the northeastern USA. *Journal of Hydrology*, 340(3-4):149–166, 2007.

[142] Jon Finch and Ann Calver. Methods for the quantification of evaporation from lakes. Technical report, World Meteorological Organization and Commission for Hydrology, Wallingford, 2008.

[143] E.R. Anderson. Energy-budget studies. *Water-Loss Investigations: Lake Hefner Studies, Technical Report*, pages 71–118, 1954.

[144] T.R. Oke. *Boundary layer climates.* Methuen & Co. Ltd, London, second edi edition, 1987.

[145] W. Brutsaert. On a derivable formula for longwave radiation from clear skies. *Water Resources Research*, 11(5):742–744, 1975.

[146] Henrique Ferro Duarte, Nelson Luís Dias, and Selma Regina Maggiotto. Assessing daytime downward longwave radiation estimates for clear and cloudy skies in Southern Brazil. *Agricultural and Forest Meteorology*, 139(3-4):171–181, 2006.

[147] J.D. Jacobs. Radiation climate of Broughton Island. In R. G Barry, editor, *Energy Budget Studies in Relation to Fast-ice Breakup Processes in Davis Strait: : climatological overview*, pages 105–120. University of Colorado, Institute of Arctic and Alphine Research, 1978.

[148] Minha Choi, Jennifer M. Jacobs, and William P. Kustas. Assessment of clear and cloudy sky parameterizations for daily downwelling longwave radiation over different land surfaces in Florida, USA. *Geophysical Research Letters*, 35(20), 2008.

[149] F. Giadrossich, M. Niedda, D. Cohen, and M. Pirastru. Evaporation in a Mediterranean environment by energy budget and Penman methods , Lake Baratz , Sardinia , Italy. *Hydrology and Earth System Sciences*, 19(5):2451–2468, 2015.

[150] R.B. Stewart and W.R. Rouse. A simple method for determining the evaporation from shallow lakes and ponds. *Water Resources Research*, 12(4):623–628, 1976.

[151] H.L. Penman. Vegetation and hydrology. *Soil Science*, 95(5):357, 1963.

[152] W. Brutsaert and H. Stricker. An advection aridity approach to estimate actual regional evapotranspiration. *Water resources research*, 15(2):443–450, 1979.

[153] H.A.R. De Bruin and J.Q. Keijman. The Priestley-Taylor evaporation model applied to a large, shallow lake in the Netherlands. *Journal of Applied Meteorology*, 18(7):898–903, 1979.

[154] C.H.B. Priestley and R.J. Taylor. On the assessment of surface heat flux and evaporation using large-scale parameters. *Monthly weather review*, 100(2):81–92, 1972.

[155] Riaan Combrinck, Lourens Steyl, and William P. Boshoff. Interaction between settlement and shrinkage cracking in plastic concrete. *Construction and Building Materials*, 185:1–11, 2018.

[156] Yi Wei Daniel Tay, Biranchi Panda, Suvash Chandra Paul, Nisar Ahamed Noor Mohamed, Ming Jen Tan, and Kah Fai Leong. 3D printing trends in building and construction industry: a review. *Virtual and Physical Prototyping*, 12(3):261–276, 2017.

[157] Delphine Marchon, Shiho Kawashima, Hela Bessaies-Bey, Sara Mantellato, and Serina Ng. Hydration and rheology control of concrete for digital fabrication: Potential admixtures and cement chemistry. *Cement and Concrete Research*, 112: 96–110, 2018.

[158] Victor Li, Freek Bos, Kequan Yu, Wes McGee, Tsz Yan Ng, Stefan Chaves Figueiredo, Karsten Nefs, Viktor Mechtcherine, Venkatesh Naidu Nerella, Jinlong Pan, Gideon van Zijl, and Jacques Kruger. On the emergence of 3D printable Engineered, Strain Hardening Cementitious Composites (ECC/SHCC). *Cement and Concrete Research*, 132:106038, 2020.

[159] Pshtiwan Shakor, Shami Nejadi, and Gavin Paul. A study into the effect of different nozzles shapes and fibre-reinforcement in 3D printed mortar. *Materials*, 12(10), 2019.

[160] Omar S.Baghabra Al-Amoudi, Mohammed Maslehuddin, and Taofiq O. Abiola. Effect of type and dosage of silica fume on plastic shrinkage in concrete exposed to hot weather. *Construction and Building Materials*, 18(10):737–743, 2004.

[161] R. Combrinck, M. Kayondo, B. D. le Roux, W. I. de Villiers, and W. P. Boshoff. Effect of various liquid admixtures on cracking of plastic concrete. *Construction and Building Materials*, 202:139–153, 2019.

[162] Faez Sayahi, Mats Emborg, Hans Hedlund, and Andrzej Cwirzen. Plastic Shrinkage Cracking of Self-compacting Concrete: Influence of Capillary Pressure and Dormant Period. *Nordic Concrete Research*, 60(1):67–88, 2019.

[163] EN 12617. Products and Systems for the Protection and Repair of Concrete Structures : Part 4: Determination of shrinkage and expansion. *British Standard*, 2002.

[164] G. S. Slavcheva. Drying and shrinkage of cement paste for 3D printable concrete. *IOP Conference Series: Materials Science and Engineering*, 481, 2019. ISSN 1757899X.

[165] Kwan Kyu Kim, Jaeheum Yeon, Hee Jun Lee, and Jung Heum Yeon. Dimensional stability of SBR-modified cementitious mixtures for use in 3D additive construction. *Applied Sciences*, 9(16), 2019.

[166] ASTM C596. Standard Test Method for Drying Shrinkage of Mortar Containing Hydraulic Cement, 2018.

[167] G. P. A. G. Van Zijl, P. J. Kruger, S. Cho, and S. Zeranka. 3D Printing Polymer Fibre Concrete. *Conference Proceedings IIBCC 2018. International Inorganic-Bonded Fiber Composites Conference (IIBCC).*, pages 5–14, 2018.

[168] Rens De Coensel. *Printability and early age shrinkage of cementitious materials with superabsorbent polymers.* Master's dissertation, Ghent University, 2019.

[169] Babatunde J. Olawuyi and William P. Boshoff. Influence of SAP content and curing age on air void distribution of high performance concrete using 3D volume analysis. *Construction and Building Materials*, 135:580–589, 2017.

[170] Jacques Kruger, Stephan Zeranka, and Gideon van Zijl. A rheology-based quasi-static shape retention model for digitally fabricated concrete. *Construction and Building Materials*, 254:119241, 2020.

[171] G. M. Moelich and R. Combrinck. A weather data analysis method to mitigate and prevent plastic shrinkage cracking. *Construction and Building Materials*, 253: 119066, 2020.

[172] D. Lecompte, A. Smits, Sven Bossuyt, H. Sol, J. Vantomme, D. Van Hemelrijck, and A. M. Habraken. Quality assessment of speckle patterns for digital image correlation. *Optics and Lasers in Engineering*, 44(11):1132–1145, 2006.

[173] GOM GmbH. GOM Aramis Software: Acquisition Basic. Technical report, GOM GmbH, Braunschweig, 2016. URL www.gom.com.

[174] ASTM C490. Standard Practice for Use of Apparatus for the Determination of Length Change of Hardened Cement Paste, Mortar, and Concrete. Technical report, ASTM International, 2007.

[175] Jean Yves Petit, Kamal H. Khayat, and Eric Wirquin. Coupled effect of time and temperature on variations of yield value of highly flowable mortar. *Cement and Concrete Research*, 36(5):832–841, 2006. ISSN 00088846.

[176] Antonio Cicione, Jacques Kruger, Richard S. Walls, and Gideon Van Zijl. An experimental study of the behavior of 3D printed concrete at elevated temperatures. *Fire Safety Journal*, (May):103075, 2020.

[177] D. P. Bentz. A review of early-age properties of cement-based materials. *Cement and Concrete Research*, 38(2):196–204, 2008.

[178] M. Molitch-Hou. World's Largest 3D Printed Building Unveiled in Dubai, 2020. URL https://3dprint.com/261978/worlds-largest-3d-printed-building-unveiled-in-dubai-d/.

[179] Karol Federowicz, Maria Kaszynska, Adam Zielinski, and Marcin Hoffmann. Effect of Curing Methods on Shrinkage Development in 3D-Printed Concrete. *Materials*, 13(2590), 2020.

[180] J. Van Der Putten, D. Snoeck, R De Coensel, G. De Schutter, and K. Van Tittelboom. Early age shrinkage phenomena of 3D printed cementitious materials with superabsorbent polymers. *Journal of Building Engineering*, 35:102059, 2020.

[181] Behzad Nematollahi, Praful Vijay, Jay Sanjayan, Ali Nazari, Ming Xia, Venkatesh Naidu Nerella, and Viktor Mechtcherine. Effect of polypropylene fibre addition on properties of geopolymers made by 3D printing for digital construction. *Materials*, 11:2352, 2018.

[182] Rishi Gupta and Nemkumar Banthia. Correlating plastic shrinkage cracking potential of fiber reinforced cement composites with its early-age constitutive response in tension. *Materials and Structures/Materiaux et Constructions*, 49(4):1499–1509, 2016.

[183] I. M.G. Bertelsen, L. M. Ottosen, and G. Fischer. Quantitative analysis of the influence of synthetic fibres on plastic shrinkage cracking using digital image correlation. *Construction and Building Materials*, 199:124–137, 2019.

[184] Biranchi Panda, Suvash Chandra Paul, and Ming Jen Tan. Anisotropic mechanical performance of 3D printed fiber reinforced sustainable construction material. *Materials Letters*, 209:146–149, 2017.

[185] Hiroki Ogura, Venkatesh Naidu Nerella, and Viktor Mechtcherine. Developing and testing of Strain-Hardening Cement-Based Composites (SHCC) in the context of 3D-printing. *Materials*, 11(8):1–18, 2018. ISSN 19961944.

[186] Fernando Pelisser, Almir Barros Da S.Santos Neto, Henriette Lebre La Rovere, and Roberto Caldas De Andrade Pinto. Effect of the addition of synthetic fibers to concrete thin slabs on plastic shrinkage cracking. *Construction and Building Materials*, 24(11):2171–2176, 2010.

[187] I. M.G. Bertelsen, L. M. Ottosen, and G. Fischer. Influence of fibre characteristics on plastic shrinkage cracking in cement-based materials: A review. *Construction and Building Materials*, 230:116769, 2020.

[188] William Boshoff, Viktor Mechtcherine, Didier Snoeck, Christof Schröfl, Nele De Belie, António Bettencourt Ribeiro, Daniel Cusson, Mateusz Wyrzykowski, Nikolajs Toropovsf, and Pietro Lura. The effect of superabsorbent polymers on the mitigation of plastic shrinkage cracking of conventional concrete, results of an interlaboratory test by RILEM TC 260-RSC. *Materials and Structures*, 53(79), 2020.

[189] L. Dudziak, V. Mechtcherine, and W. Brameshuber. Enhancing Early-Age Resistance to Cracking in High-Strength Cement-Based Materials by Means of Internal Curing Using Super Absorbent Polymers. *International RILEM Conference on Material Science*, III:129–139, 2010.

[190] D. Snoeck, O. M. Jensen, and N. De Belie. The influence of superabsorbent polymers on the autogenous shrinkage properties of cement pastes with supplementary cementitious materials. *Cement and Concrete Research*, 74:59–67, 2015.

[191] D. M. Meyer, W. P. Boshoff, and R. Combrinck. Utilising super absorbent polymers as alternative method to test plastic shrinkage cracks in concrete. *Construction and Building Materials*, 248:118666, 2020.

[192] Viktor Mechtcherine, Egor Secrieru, and Christof Schröfl. Effect of superabsorbent polymers (SAPs) on rheological properties of fresh cement-based mortars - Development of yield stress and plastic viscosity over time. *Cement and Concrete Research*, 67:52–65, 2015. ISSN 00088846.

[193] Egor Secrieru, Viktor Mechtcherine, Christof Schröfl, and Dmitry Borin. Rheological characterisation and prediction of pumpability of strain-hardening cement-based-composites (SHCC) with and without addition of superabsorbent polymers (SAP) at various temperatures. *Construction and Building Materials*, 112:581–594, 2016.

[194] Viktor Mechtcherine, Christof Schröfl, Mateusz Wyrzykowski, Michaela Gorges, Pietro Lura, Daniel Cusson, Jim Margeson, Nele Da Belie, Didier Snoeck, Kazuo Ichimiya, Shin-Ichi Igarashi, Vyacheslav Falikman, Stefan Friedrich, Jurgen Bokern, Patricia Kara, Alicja Marciniak, Hans-Wolf Reinhardt, Soren Sippel, Joao Custodio, Antonio Bettencourt Ribeiro, Guang Ye, Hua Dong, and Jason Weiss. Effect of superabsorbent polymers (SAP) on the freeze-thaw resistance of concrete: results of a RILEM interlaboratory study. *Materials and Structures/Materiaux et Constructions*, 50(1), 2017.

[195] Didier Snoeck, Kim Van Tittelboom, Stijn Steuperaert, Peter Dubruel, and Nele De Belie. Self-healing cementitious materials by the combination of microfibres and

superabsorbent polymers. *Journal of Intelligent Material Systems and Structures*, 25(1):13–24, 2014.

[196] J. Van Der Putten, D. Snoeck, and K. Van Tittelboom. 3D Printing of cementitious materials with superabsorbent polymers. In M. A. Pereira Gomes de Araújo, N. De Belie, and K. Van Tittelboom, editors, *Durable Concrete for Infrastructure under Severe Conditions - Smart Admixtures, Self-responsiveness and Nano-additions*, pages 86–89, Ghent, Belgium, 2019.

[197] Christof Schröfl, Viktor Mechtcherine, Peter Vontobel, Jan Hovind, and Eberhard Lehmann. Sorption kinetics of superabsorbent polymers (SAPs) in fresh Portland cement-based pastes visualized and quantified by neutron radiography and correlated to the progress of cement hydration. *Cement and Concrete Research*, 75: 1–13, 2015.

[198] José Mora-Ruacho, Ravindra Gettu, and Antonio Aguado. Influence of shrinkage-reducing admixtures on the reduction of plastic shrinkage cracking in concrete. *Cement and Concrete Research*, 39(3):141–146, 2009.

[199] Pei Zhan and Zhi He. Application of shrinkage reducing admixture in concrete: A review. *Construction and Building Materials*, 201:676–690, 2019.

[200] J. Saliba, E. Rozière, F. Grondin, and A. Loukili. Influence of shrinkage-reducing admixtures on plastic and long-term shrinkage. *Cement and Concrete Composites*, 33(2):209–217, 2011.

[201] J. Plank and M. Ilg. The Role of Chemical Admixtures in the Formulation of Modern Advanced Concrete. In W. Boshoff, R. Combrinck, V. Mechtcherine, and M. Wyrzykowski, editors, *3rd International Conference on the Application of Superabsorbent Polymers (SAP) and Other New Admixtures Towards Smart Concrete.*, pages 143–157. RILEM Bookseries, vol 24. Springer, Cham, 2019.

[202] Irvin A. Chen, Craig W. Hargis, and Maria C.G. Juenger. Understanding expansion in calcium sulfoaluminate-belite cements. *Cement and Concrete Research*, 42(1): 51–60, 2012.

[203] Noura Khalil, Georges Aouad, Khadija El Cheikh, and Sébastien Rémond. Use of calcium sulfoaluminate cements for setting control of 3D-printing mortars. *Construction and Building Materials*, 157:382–391, 2017.

[204] Julien Bizzozero, Christophe Gosselin, and Karen L. Scrivener. Expansion mechanisms in calcium aluminate and sulfoaluminate systems with calcium sulfate. *Cement and Concrete Research*, 56:190–202, 2014.

[205] Angus K.F. Cheung and Christopher K.Y. Leung. Shrinkage reduction of high strength fiber reinforced cementitious composites (HSFRCC) with various water-to-binder ratios. *Cement and Concrete Composites*, 33(6):661–667, 2011.

[206] Iman Mehdipour and Kamal H. Khayat. Enhancing the performance of calcium sulfoaluminate blended cements with shrinkage reducing admixture or lightweight sand. *Cement and Concrete Composites*, 87:29–43, 2018.

[207] Jurie Wynand Visagie. *Invloed van vloeibare kuringsmetodes op plastiese krimpkrake van beton (In Afrikaans)*. Master's dissertation, Universiteit Stellenbosch, 2019.

[208] ASTM C230 / C230M. Standard Specification for Flow Table for Use in Tests of Hydraulic Cement. Technical report, ASTM International, West Conshohocken, PA, 2020.

[209] Frederick A. Bester, Marchant Van Den Heever, P. J. Kruger, S. Zeranka, and Gideon P.A.G. Van Zijl. Benchmark structures for 3D concrete printing. In *fib Symposium 2019: Concrete - Innovations in Materials, Design and Structures*, number June, pages 305–312, 2019.

[210] Marchant van den Heever, Frederick Bester, Mohammad Pourbehi, Jacques Kruger, Seung Cho, and Gideon van Zijl. Characterizing the Fissility of 3D Concrete Printed Elements via the Cohesive Zone Method. In *RILEM International Conference on Concrete and Digital Fabrication*, pages 489–499. Springer, Cham, 2020.

[211] Viktor Mechtcherine, Didier Snoeck, Christof Schröfl, Nele De Belie, Agnieszka J. Klemm, Kazuo Ichimiya, Juhyuk Moon, Mateusz Wyrzykowski, Pietro Lura, Nikolajs Toropovs, Alexander Assmann, Shin ichi Igarashi, Igor De La Varga, Fernando C.R. Almeida, Kendra Erk, António Bettencourt Ribeiro, João Custódio, Hans Wolf Reinhardt, and Vyatcheslav Falikman. Testing superabsorbent polymer (SAP) sorption properties prior to implementation in concrete: results of a RILEM Round-Robin Test. *Materials and Structures/Materiaux et Constructions*, 51(1), 2018.

[212] Gerrit M Moelich, Juandre E Van Zyl, Nadia Rabie, and Riaan Combrinck. The influence of solar radiation on plastic shrinkage cracking in concrete. *Cement and Concrete Composites*, 123:104182, 2021.

[213] E.M.C. Jones and M.A. Iadicola. A Good Practices Guide for Digital Image Correlation. Technical report, International Digital Image Correlation Society, 2018.

[214] P. L. Reu, E. Toussaint, E. Jones, H. A. Bruck, M. Iadicola, R. Balcaen, D. Z. Turner, T. Siebert, P. Lava, and M. Simonsen. DIC Challenge: Developing Images and Guidelines for Evaluating Accuracy and Resolution of 2D Analyses. *Experimental Mechanics*, 58(7):1067–1099, 2018.

[215] P. Mangat and M. Azari. Plastic shrinkage of steel fibre reinforced concrete. *Materials and Structures*, 23(3):186–195, 1990.

[216] John Branston, Sreekanta Das, Sara Y. Kenno, and Craig Taylor. Influence of basalt fibres on free and restrained plastic shrinkage. *Cement and Concrete Composites*, 74:182–190, 2016.

[217] P. Kruger, S. Zeranka, and G Van Zijl. 3D concrete printing: A lower bound analytical model for buildability performance quantification. *Automation in Construction*, 106:102904, 2019.

[218] Ole Mejlhede Jensen and Per Freiesleben Hansen. Water-entrained cement-based materials - I. Principles and theoretical background. *Cement and Concrete Research*, 31(4):647–654, 2001.

[219] A. Radocea. A model of plastic shrinkage. *Magazine of Concrete Research*, 46 (167):125–132, 1994.

[220] Sadegh Ghourchian, Mateusz Wyrzykowski, and Pietro Lura. A poromechanics model for plastic shrinkage of fresh cementitious materials. *Cement and Concrete Research*, 109:120–132, 2018.

[221] Sadegh Ghourchian, Mateusz Wyrzykowski, Mathieu Plamondon, and Pietro Lura. On the mechanism of plastic shrinkage cracking in fresh cementitious materials. *Cement and Concrete Research*, 115(2019):251–263, 2019.

[222] J. Branch, A. Rawling, D. J. Hannant, and M. Mulheron. The effects of fibres on the plastic shrinkage cracking of high strength concrete. *Materials and Structures/Materiaux et Constructions*, 34:189–194, 2002.

[223] Somsak Swaddiwudhipong, Hai Rong Lu, and Tiong Huan Wee. Direct tension test and tensile strain capacity of concrete at early age. *Cement and Concrete Research*, 33:2077–2084, 2003.

[224] D.J. Hannant, J Branch, and M Mulheron. Equipment for tensile testing of fresh concrete. *Magazine of Concrete Research*, 51:263–267, 1999.

[225] Emmanuel Roziere, Rachid Cortas, and Ahmed Loukili. Tensile behaviour of early age concrete: New methods of investigation. *Cement and Concrete Composites*, 55:153–161, 2015.

[226] Marcin Hoffmann, Szymon Skibicki, Paweł Pankratow, Adam Zieliński, Mirosław Pajor, and Mateusz Techman. Automation in the construction of a 3D-Printed concrete wall with the use of a lintel gripper. *Materials*, 13(8), 2020.

[227] G. M. Moelich, P. J. Kruger, and R. Combrinck. Mitigating early age cracking in 3D printed concrete using fibres, superabsorbent polymers, shrinkage reducing admixtures, B-CSA cement and curing measures. *Submitted to Cement and Concrete Research*, 2021.

[228] Sadegh Ghourchian, Mateusz Wyrzykowski, and Pietro Lura. The bleeding test: A simple method for obtaining the permeability and bulk modulus of fresh concrete. *Cement and Concrete Research*, 89:249–256, 2016.

[229] B. G. Salvoldi, H. Beushausen, and M. G. Alexander. Oxygen permeability of concrete and its relation to carbonation. *Construction and Building Materials*, 85: 30–37, 2015.

[230] Z. Wu, H. S. Wong, and N. R. Buenfeld. Influence of drying-induced microcracking and related size effects on mass transport properties of concrete. *Cement and Concrete Research*, 68:35–48, 2015.

[231] Yaxin Tao, A. V. Rahul, Karel Lesage, Yong Yuan, Kim Van Tittelboom, and Geert De Schutter. Stiffening control of cement-based materials using accelerators in inline mixing processes: Possibilities and challenges. *Cement and Concrete Composites*, 119(February):103972, 2021.

[232] Vitoldas Vaitkevičius, Evaldas Šerelis, and Vidas Kerševičius. Effect of ultra-sonic activation on early hydration process in 3D concrete printing technology. *Construction and Building Materials*, 169:354–363, 2018.

[233] Shravan Muthukrishnan, Sayanthan Ramakrishnan, and Jay Sanjayan. Effect of microwave heating on interlayer bonding and buildability of geopolymer 3D concrete printing. *Construction and Building Materials*, 265:120786, 2020.

[234] Shravan Muthukrishnan, Sayanthan Ramakrishnan, and Jay Sanjayan. Effect of alkali reactions on the rheology of one-part 3D printable geopolymer concrete. *Cement and Concrete Composites*, 116(December 2020):103899, 2021.

[235] H. Beushausen and M. G. Alexander. Failure mechanisms and tensile relaxation of bonded concrete overlays subjected to differential shrinkage. *Cement and Concrete Research*, 36(10):1908–1914, 2006.

[236] J. Van Der Putten, M. Azima, P. Van den Heede, T. Van Mullem, D. Snoeck, C. Carminati, J. Hovind, P. Trtik, G. De Schutter, and K. Van Tittelboom. Neutron radiography to study the water ingress via the interlayer of 3D printed cementitious materials for continuous layering. *Construction and Building Materials*, 258:119587, 2020.

[237] Jolien Van Der Putten, Melissa De Volder, Philip Van den Heede, Geert De Schutter, and Kim Van Tittelboom. 3D Printing of Concrete: The Influence on Chloride Penetration. In F Bos, S Lucas, R Wolfs, and T Salet, editors, *International Conference on Concrete and Digital Fabrication*, number July, pages 500–507. RILEM, 2020.

[238] C. Schröfl, V.N. Nerella, and V Mechtcherine. Capillary Water Intake by 3D-Printed Concrete Visualised and Quantified by Neutron Radiography. In T Wangler and R Flatt, editors, *First RILEM International Conference on Concrete and Digital Fabrication - Digital Concrete 2018.*, pages 217–224, 2018.

[239] EN 196-1. Methods of testing cement Part 1: Determination of strength. Technical report, British Standards Institution, 2016.

[240] M.T. Hasholt, O.M. Jansen, K. Kovler, and S. Zhutovsky. Can superabsorent polymers mitigate autogenous shrinkage of internally cured concrete without compromising the strength? *Construction and Building Materials*, 31:226–230, 2012.

[241] Babatunde J. Olawuyi, Adewumi J. Babafemi, and William P. Boshoff. Early-age and long-term strength development of high-performance concrete with SAP. *Construction and Building Materials*, 267:121798, 2021.

[242] Viktor Mechtcherine, Mateusz Wyrzykowski, Christof Schröfl, Didier Snoeck, Pietro Lura, Nele De Belie, Arn Mignon, Sandra Van Vlierberghe, Agnieszka J. Klemm, Fernando C.R. Almeida, José Roberto Tenório Filho, William Peter Boshoff, Hans Wolf Reinhardt, and Shin Ichi Igarashi. Application of super absorbent polymers (SAP) in concrete construction–update of RILEM state-of-the-art report. *Materials and Structures/Materiaux et Constructions*, 54(2), 2021. ISSN 13595997.

[243] Xianwei Ma, Qiang Yuan, Jianhui Liu, and Caijun Shi. Effect of water absorption of SAP on the rheological properties of cement-based materials with ultra-low w/b ratio. *Construction and Building Materials*, 195:66–74, 2019.

[244] Jianhui Liu, Kamal H Khayat, and Caijun Shi. Effect of superabsorbent polymer characteristics on rheology of ultra-high performance concrete. *Cement and Concrete Composites*, 112:103636, 2020.

[245] Livia B Agostinho and De C Pereira Alexandre. Rheological study of Portland cement pastes modified with superabsorbent polymer and nanosilica. *Journal of Building Engineering*, 34:102024, 2021.

[246] Siwei Ma, Cihang Huang, Prince Baah, Tommy Nantung, and Na Lu. The influence of water-to-cement ratio and superabsorbent polymers (SAPs) on solid-like behaviors of fresh cement pastes. *Construction and Building Materials*, 275:122160, 2021.

[247] Guowei Ma, Nazar Muhammad Salman, Li Wang, and Fang Wang. A novel additive mortar leveraging internal curing for enhancing interlayer bonding of cementitious composite for 3D printing. *Construction and Building Materials*, 244:118305, 2020.

[248] Hans Beushausen, Björn Höhlig, and Marco Talotti. The influence of substrate moisture preparation on bond strength of concrete overlays and the microstructure of the OTZ. *Cement and Concrete Research*, 92:84–91, 2017.

[249] M. Azenha, K. Maekawa, T. Ishida, and R. Faria. Drying induced moisture losses from mortar to the environment. Part II: Numerical implementation. *Materials and Structures*, 40(8):813–825, 2007.

[250] Didier Snoeck, Christof Schröfl, and Viktor Mechtcherine. Recommendation of RILEM TC 260-RSC: testing sorption by superabsorbent polymers (SAP) prior to implementation in cement-based materials. *Materials and Structures/Materiaux et Constructions*, 51(5), 2018. ISSN 13595997.

[251] Jian Ouyang, Yiqiu Tan, David J. Corr, and Surendra P. Shah. The thixotropic behavior of fresh cement asphalt emulsion paste. *Construction and Building Materials*, 114:906–912, 2016.

[252] Biranchi Panda, Cise Unluer, and Ming Jen Tan. Investigation of the rheology and strength of geopolymer mixtures for extrusion-based 3D printing. *Cement and Concrete Composites*, 94:307–314, 2018.

[253] EN196-1. Cement: Determination of Strength, 2016.

[254] L. Senff, R. C.E. Modolo, G. Ascensão, D. Hotza, V. M. Ferreira, and J. A. Labrincha. Development of mortars containing superabsorbent polymer. *Construction and Building Materials*, 95:575–584, 2015.

[255] Yiwei Weng, Mingyang Li, Dong Zhang, Ming Jen, and Shunzhi Qian. Investigation of interlayer adhesion of 3D printable cementitious material from the aspect of printing process. *Cement and Concrete Research*, 143:106386, 2021.